INVESTIGATION OF STRESS-DILATANCY RESPONSE AT LOW STRESS LEVELS WITH EMPHASIS ON SIMPLE SHEARING CONDITIONS

by

Abdulkadir Genç

B.S., Civil Engineering, Boğaziçi University, 2017

Submitted to the Institute for Graduate Studies in
Science and Engineering in partial fulfillment of
the requirements for the degree of
Master of Science

Graduate Program in Civil Engineering

Boğaziçi University

2021

ACKNOWLEDGEMENTS

I would like to extend my sincere gratitude to my supervisor Assoc. Prof. Özer Çinicioğlu for his patience and guidance. His suggestions throughout the research and writing of this thesis have been invaluable.

I would like to express my sincere gratitude to member of the thesis committee, Prof. Dr. Mehmet Monkul and Asst. Prof. İrem Zeynep Yıldırım for their efficient comments.

My family members have in many ways been a great source of strength and support for me throughout my studies, as they always have.

I also thank my friends Mehmet Can Alphan and İbrahim Ertuğrul Yalçın for their continuous support during my study.

ABSTRACT

INVESTIGATION OF STRESS-DILATANCY RESPONSE AT LOW STRESS LEVELS WITH EMPHASIS ON SIMPLE SHEARING CONDITIONS

In the present work, the assessment of dilatancy angle of cohesionless soils under low confining pressures and its contribution to peak friction angle are investigated. For this purpose, 3 different types of tests are conducted to obtain peak angle of dilation, peak friction angle and critical state friction angle on Kilyos sand. Alternative methods are used because of triaxial test being a time-consuming procedure and the apparatus being relatively expensive. Besides, triaxial tests being not practical to conduct ay very low stress levels is another reason to use alternative methods. An equipment which would allow the computation of peak dilatancy in a very short period of time is designed together with its electronic components and the required Arduino code. The main philosophy behind the equipment is to impose uniform shearing strain and to measure the associated change in the volume of a sample. Later the correlation between shear and volumetric strains is considered to calculate rate of dilation. With the devised mechanism, peak dilation angles of sand specimens with relative densities ranging from 14% to 79% are determined under the pressure resulted solely from their own weights. The equipment has transparent sidewalls that allow capturing images. Images captured during the tests are used for particle image velocimetry analyses. With the results of PIV analyses, shear planes, slip surfaces and the associated strain fields are determined. The number and intensity of shear planes are inspected and it is noted that their numbers increase with increasing relative density. Besides, the angle that active shear band makes with the horizontal axis is observed to be increasing as the relative density increases. Furthermore, sample uniformity during shearing is studied by plotting volumetric strain – shear strain relationship for different positions within samples. This aided the investigation of shear localization response. Examining the graphs obtained from both the tests and the associated PIV analyses, it is realized that volumetric strain versus shear strain relationship can be represented very well with a 3^{rd} order polynomial. Moreover, for the same level of stress and density combinations, peak friction

angles of the soil are determined using a simple test that is available in literature. Lastly, critical state friction angle is obtained using a simple method. Having experimentally determining the magnitudes of ψ_p, φ'_p and φ'_{cs}, stress – dilatancy parameters r, Q and R are determined.

ÖZET

DÜŞÜK GERİLİM SEVİYELERİNDEKİ GERİLİM–GENLEŞME DAVRANIŞININ BASİT KESME KOŞULLARINDA İNCELENMESİ

Bu çalışmada, kohezyonsuz zeminlerin genleşme açısının düşük gerilme koşullarında elde edilmesi ve bu değerin maksimum içsel sürtünme açısına olan katkısı incelenmiştir. Bu amaçla, maksimum genleşme açısı, maksimum içsel sürtünme açısı ve kritik durum sürtünme açısını elde etmek amacıyla Kilyos kumu üzerinde 3 farklı test yapılmıştır. Üç eksenli testin uzun süren bir prosedür olması ve cihazın nispeten pahalı olması nedeniyle alternatif yöntemler kullanılmıştır. Ayrıca üç eksenli deneyin çok düşük gerilme seviyelerinde uygulanmasının pratik olmaması alternatif yöntemlerin kullanılmasının bir diğer sebebidir. Çok kısa sürede maksimum genleşmenin hesaplanmasını sağlayacak bir ekipman, elektronik bileşenleri ve gerekli Arduino kodu ile birlikte tasarlanmıştır. Ekipmanın temel ilkesi, numuneye eşit bir şekilde kayma birim deformasyonu uygulanması ve ilgili hacim değişiminin ölçülmesidir. Ardından, genleşme oranını hesaplamak için kayma ve hacimsel birim yer değiştirmeler arasındaki bağıntı değerlendirilmiştir. Tasarlanan mekanizma aracılığıyla, %14 ile %79 arasında değişen rölatif sıkılıklardaki kum numunelerinin maksimum genleşme değerleri, yalnızca kendi ağırlıklarından kaynaklanan gerilme altında belirlenmiştir. Ekipman, fotoğraf çekilmesine olanak sağlayacak şekilde saydam olan yan duvarlara sahiptir. Parçacık görüntülü hız ölçümü analizleri için testler sırasında çekilen fotoğraflar kullanılmıştır. PGHÖ analizlerinden elde edilen sonuçlar aracılığıyla, kayma yüzeyleri, aktif kamalar ve birim deformasyon alanları gözlenmiştir. Kayma yüzeylerinin sayısı ve yoğunluğu gözlenip, sayılarının artan rölatif sıkılık ile arttığı görülmüştür. Bunun yanında, rölatif sıkılık arttıkça aktif kamanın yatay eksen ile yaptığı açının da arttığı gözlemlenmiştir. Ayrıca, numune üzerindeki farklı noktalar için hacimsel birim deformasyon – kayma birim deformasyon grafikleri çizilerek numunenin kayma esnasındaki üniformluğu incelenmiştir. Bunun yapılması kayma lokalizasyon davranışının araştırılmasına yardımcı olur. Testlerden ve bunlarla ilişkili PGHÖ analizlerinden elde edilen sonuçlar incelenerek hacimsel birim deformasyon ile kayma birim deformasyon arasındaki ilişkinin üçüncü derece polinom ile çok uyumlu olduğu görülmüştür. Ayrıca, aynı gerilme değeri ve rölatif sıkılık kombinasyonu

için, literatürde yer alan basit bir metot kullanılarak zeminin en yüksek sürtünme açıları belirlenmiştir. Son olarak, kritik durum sürtünme açısı basitleştirilmiş bir yöntem kullanılarak elde edilmiştir. En yüksek genleşme açısı, en yüksek içsel sürtünme açısı ve kritik durum sürtünme açısı büyüklüklerinin deneysel olarak elde edilmesinden sonra, gerilim – genleşme parametreleri r, Q ve R belirlenmiştir.

TABLE OF CONTENTS

LIST OF FIGURES

LIST OF TABLES

LIST OF SYMBOLS

A_ψ	Constant value
B	Width
c	Cohesion
e	Void ratio
e_{max}	Maximum void ratio
e_{min}	Minimum void ratio
G_s	Specific gravity
g_x	x component of gravitational acceleration
g_y	y component of gravitational acceleration
g_z	z component of gravitational acceleration
H	Height of the soil
H_b	Distance between distance sensors and the base of the equipment
H_s	Distance between distance sensors and the top of the soil
I_D	Relative density
I_R	Relative density index
L	Length
p_A	Atmospheric pressure
p'	Mean principal stress
Q	Soil-type constant
r	A line fitting parameter
R	Soil-type constant
a	Angle of rotation
γ	Unit weight
ε	Strain
ε_v	Volumetric strain
$d\varepsilon_v$	Volumetric strain increment
ε_1	Principal strain
$d\varepsilon_1$	Principal strain increment

ε_q	Shar strain
$d\varepsilon_q$	Shar strain increment
σ'	Mean effective stress
$\sigma_c{}'$	Initial confining pressure
$\sigma_{mp}{}'$	Mean effective stress at peak shear strength
ψ	Dilatancy angle
ψ_p	Peak dilatancy angle
φ	Internal friction angle
φ'_p	Effective peak friction angle
φ'_c	Effective critical state friction angle
σ'_{mp}	Mean effective stress
ΔH	Change in height
Γ	Critical state material parameter
λ	Critical state material parameter

LIST OF ACRONYMS /ABBREVIATIONS

ASTM	American Society for Testing and Material
CS	Critical State
LS-T-SS	Low Stress Transparent Simple Shear
PIV	Particle Image Velocimetry

1. INTRODUCTION

Civil engineers generally deal with construction materials (concrete, steel, timber, etc.) of which properties are well defined. However, different from other civil engineering branches, geotechnical engineers do not use materials that are produced for a specific purpose, instead they work with soil and rock which are natural materials with unknown engineering properties. Although in common civil engineering materials, shear strength is governed by their molecular strength, shear failure in soils occurs when the stresses between particles are such that they slide or roll past each other since soil is a particulate material. Therefore, primary source of soil's shear strength is the interactions between the particles rather than the particles' individual strength.

Soil strength parameters are cohesion which is the ability of the particles of the same kind to pull each other by applying electrostatic force and internal friction angle which can be described as the ability of a cohesionless material to withstand shear stress. Shear strength of clean sands is governed by internal friction angle alone, these types of soils are called cohesionless. Kilyos sand is used in this study and the physical properties are taken from the literature (Cagdas and Cinicioglu, 2019).

In geotechnical literature, dilatancy was first noticed by Reynolds in 1885. It is now commonly accepted that dilatancy provides excess shear strength to soil by increasing internal friction angle. Dilatancy is the phenomenon of volume increase observed in the soil due to rearrangement of the particles when sheared. The purpose of this thesis is investigating the effect of dilatancy on friction angle for low stress conditions by specifying maximum dilatancy, peak friction angle and critical state (minimum) friction angle. For this purpose, an equipment which is made of plexiglass is designed. The equipment is a cubical simple shear equipment with transparent sidewalls. The walls on the opposite sides of the equipment which are in x – z space can rotate freely about x axis while the base and the other reciprocal two walls which are in y – z space are fixed. The main principal of the equipment is shearing the sand specimen inside while measuring and recording the rotation angle and height of the specimen continuously by using accelerometers and distance sensors. Dilatancy angle is a function of relative density of soil and effective stress state. The tests are conducted

under self-weight of the samples and only relative densities varied between the tests. As a result, all tests are conducted under low stress conditions. Meanwhile deformations and strain fields are observed by analyzing images captured during the test via an image processing software (GeoPIV-RG). GeoPIV-RG was developed by Stainer, et al. (2016).

On the other hand, peak friction angle under low stresses is measured using the method proposed by Giampa and Bradshaw (2018). They suggested that peak friction angle of a cohesionless soil can be determined by compacting it into a cylindrical steel mold and tilting until shallow slope failure is induced. As suggested by Giampa and Bradshaw (2018), this method can be used under low confining pressure levels. Moreover, a simple test suggested by Santamarina and Cho (2001) is conducted to obtain critical state (minimum) angle of friction. The soil is submerged inside a graduated cylinder, tilted and brought back gently to the vertical position to record the angle of repose.

Using the results of these tests, the relationship between peak dilation, peak friction angle and critical state friction angle is investigated.

2. LITERATURE REVIEW

The strength of sand is the main focus of this study. Since internal friction angle is the only strength parameter of cohesionless soils, studies for the purpose of finding maximum and minimum friction angles are carried out. Critical state (minimum) angle of shearing which is fundamentally a function of mineralogy and average grain shape is constant in the absence of crushing. Peak angle of shearing, on the other hand, is dependent on factors such as relative density and confining pressure. In geotechnical literature, it is a commonly accepted fact that dilatancy is influential over internal friction angle. By using simplified version of Rowe's (1962) stress-dilatancy relationship, Bolton (1986) suggested a new empirical correlation between peak friction angle and peak angle of dilation as shown in Equation 2.1:

$$\varphi'_p = \varphi'_c + r\,\psi_p \tag{2.1}$$

where,

- r is a line fitting parameter, suggested 0.8 by Bolton (1986).
- φ'_p is the peak friction angle.
- φ'_c is the critical state friction angle.
- ψ'_p is peak angle of dilation.

In this study, peak and critical state friction angles and peak angle of dilatancy are assessed by using various methods, Bolton's line fitting parameter (r) and dilation index coefficients (Q and R) are then determined for low stress conditions.

2.1. Internal Friction Angle

Internal friction angle can be described as the ability of a cohesionless material to withstand shear stress. Its definition is derived from linear failure criterion of Mohr-Coulomb

model. In the stress plane of shear stress – normal stress, the inclination with respect to normal stress axis of failure envelope provides internal friction angle.

Soil is a particulate material; hence shear failure occurs when the stresses between particles are such that they slide or roll past each other. Accordingly, soil shear strength primarily depends on interactions between the particles, not on their internal strength. Taking the fact into consideration that sand is a cohesionless soil, it is concluded that shear strength of sand is governed by internal friction angle (φ'). To determine shear strength of sand, internal friction angle needs to be obtained. The value of φ' depends on both the frictional properties of the individual particles and the interlocking between particles.

In this study, critical state friction angle (φ'_c) is determined by using Santamarina and Cho's (2001) Simplified Method while peak friction angle (φ'_p) is assessed using Giampa and Bradshaw's (2018) Tilt Method.

2.1.1. Simplified Method to Assess Critical State Friction Angle

The magnitude of critical state angle of shearing depends on particle mineralogy and angularity (Bolton 1986, Sadrekarimi and Olson 2011). It can be determined by conventional triaxial test; however, it is a slow procedure and required test equipment is relatively expensive. To overcome these disadvantages, a simple method proposed by Santamarina and Cho (2001) is used to determine critical state friction angle. The test set is normally used to obtain critical state parameters λ and Γ; however, a portion of this device which is used to assess critical state friction angle is used within the scope of this study.

In the CS test, as can be seen in Figure 2.1, the soil is poured into a graduated, 1000-ml transparent cylinder filled with water. It is tilted and brought back slowly to the vertical position. Critical state friction angle is recorded as repose angle in the middle region of the soil's surface since the angle may be different towards the wall due to adhesion effect. Since the soil is submerged, it will mimic the behavior of a loose soil, thus the resulting friction angle refers to critical state parameters.

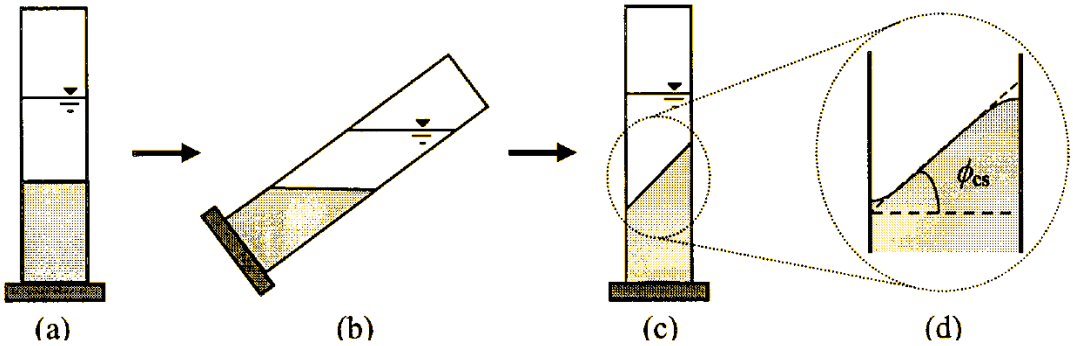

Figure 2.1. Simplified Method to Determine Critical State Friction Angle: (a) Pour the soil in a 1000-ml cylinder with water. (b) Rotate the cylinder passed 60°. (c) Slowly return the cylinder to its vertical position and measure the angle of repose. (d) The angle is measured in the middle region of the slope. (Santamarina and Cho, 2001).

The suggested methodology is fast and economical, and the results were verified by comparing them against critical state parameters obtained by conventional triaxial test. For this reason, this method is preferred to obtain critical state friction angle in this study.

2.1.2. Tilt Method to Assess Peak Friction Angle

Although triaxial tests have been conducted at low effective stress levels, the results of the tests may be unreliable since certain factors that are normally neglected such as contribution of the membrane's strength, self-weight of the specimen and piston pressure become significant at low initial confining pressures less than 10 kPa. In addition, it is a time-consuming procedure and required set of tests can be relatively expensive. Given these disadvantages of triaxial tests, Giampa and Bradshaw (2018) proposed a simple method to estimate angle of peak friction $\varphi_p^{'}$ of sand at very low confining pressures.

The proposed tilt method is based on the theory of infinite slopes, which determines the conditions under which a layer of soil will slip along a plane parallel to the ground surface. The equipment used to determine unit weight and relative density was used when performing tilt test (ASTM D4253-00, Standard Test Methods for Maximum Index Density and Unit Weight of Soils Using a Vibratory Table; ASTM D4254-00, Standard Test Methods for Minimum Index Density and Unit Weight of Soils and Calculation of Relative Density) as shown in Figure 2.2. This includes a steel mold having a volume of 2,823 cm^3, a surcharge

weight with a hoisting handle, a surcharge base plate having a thickness of 12.7 mm, a metal guide sleeve to stabilize the surcharge weight and a vibratory table with an adjustable frequency of 0 to 60 Hz. A tiltmeter is attached to the side of the steel mold to measure the tilt angle.

The following procedure was followed to estimate peak friction angle. Dry sand was poured into the specimen mold placed on the vibratory table, by using a funnel maintaining almost zero drop height to obtain a loose soil state. The excess soil was struck to both flatten the surface and make the specimen height equal to the height of the mold. To make the specimen denser, the base plate and surcharge weight were placed on the soil surface with the surcharge guide sleeve secured to the outer portion of the mold. To reach the desired relative density, the specimen was vibrated for up to eight minutes.

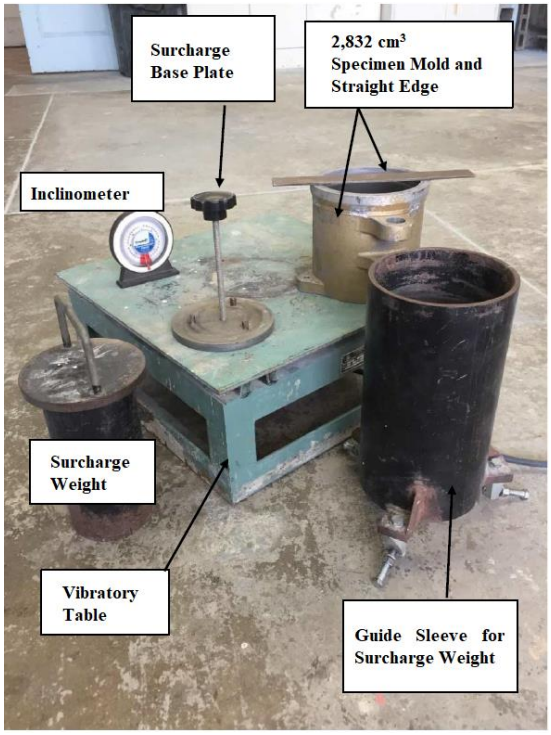

Figure 2.2. Equipment Used to Perform Proposed Tilt Method (Giampa and Bradshaw, 2018).

Special attention was paid when removing the surcharge weight, guide sleeve and base plate to have the soil surface flat and smooth as shown in Figure 2.3(a). The specimen was weighed to compute relative density by assuming that the soil near the surface is at the same relative density as the global specimen. Then the mold started to be tilted gently as

shown in Figure 2.3(b). The process of tilting was continued until a small slope failure occurred. The tilt angle at that point was recorded as the peak effective friction angle $\varphi_p^{'}$ of the sand.

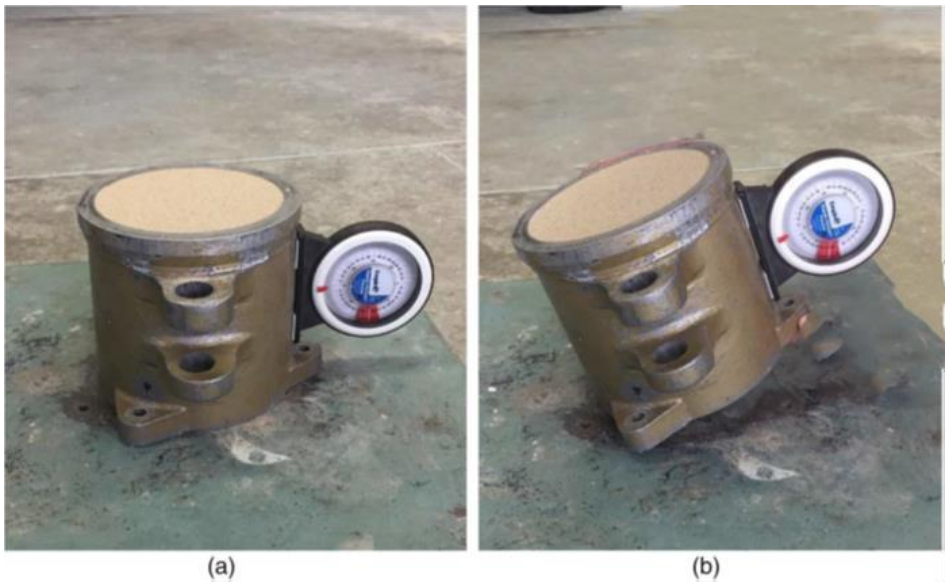

Figure 2.3. Photograph Showing (a) the Soil Surface Before Tilting and (b) the Tilted Specimen (Giampa and Bradshaw, 2018).

The summary of the results is presented in Figure 2.4 as relative density index I_D versus peak friction angle $\varphi_p^{'}$ in degrees. I_D is defined as following:

$$I_D = \frac{e_{max} - e}{e_{max} - e_{min}} \tag{2.2}$$

where,

- e_{max} is the maximum void ratio.
- e_{min} is the minimum void ratio.
- e is the current void ratio.

As can be seen in Figure 2.4, peak angle of friction increases with increasing relative density by maintaining a very good fit with a quadratic equation.

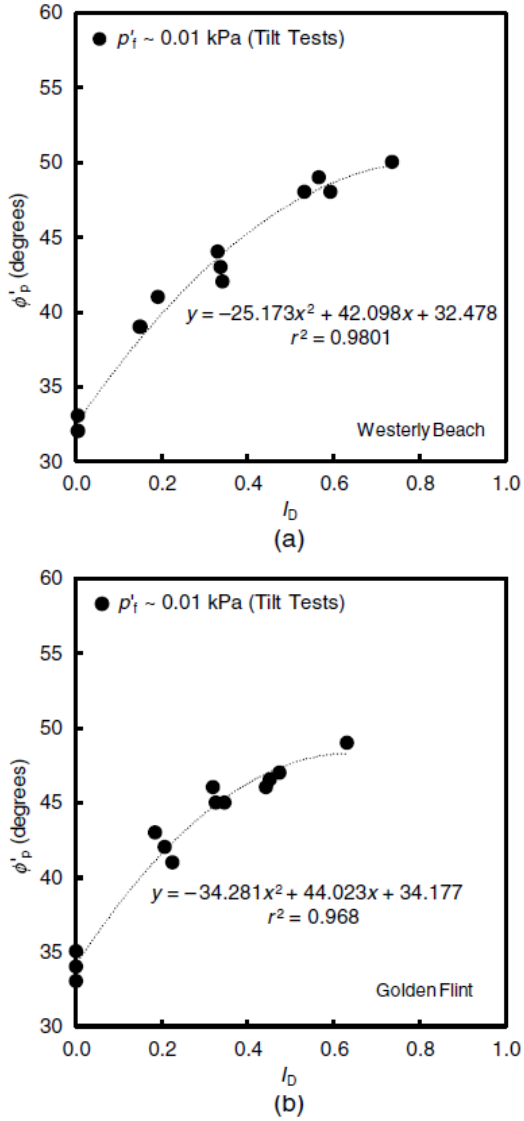

Figure 2.4. Tilt Test Results for (a) Westerly Sand and (b) Golden Flint (Giampa and Bradshaw, 2018).

Very loose soils are hypothetically contractile even at very low confining pressures and thus the critical state friction angle should be equal to the peak friction angle. To validate the suggested method, Giampa and Bradshaw (2018) compared the friction angles obtained in the tilt test at $I_D = 0\%$ were compared to the critical state friction angles obtained by Bolton (1986) and Santamarina and Cho (2001). The comparison is provided in Table 2.1.

Table 2.1. Comparison of Average Critical State Friction Angles Determined Using Three Different Methods Including (Giampa and Bradshaw, 2018).

	Critical State Friction Angle, ϕ'_c (degrees)		
Sand	Bolton (1986)	Santamarina and Cho (2001)	Tilt (This Study)
Westerly	32.3	31.6	32.4
Golden Flint	33.9	32.8	34.0

As can be seen in the table, the critical state friction angles for two different sand obtained by Giampa and Bradshaw's tilt method are almost identical the those determined by Bolton (1986) and about 1^o greater than those obtained in Santamarina and Cho's tilt method.

2.2. Dilatancy

Dilatancy is the phenomenon of volume increase observed in the soil due to rearrangement of the particles during shearing as can be seen in Figure 2.5. This occurs since the grains in a compacted state interlock and therefore do not have the freedom to move around one another. Many studies have been conducted on the phenomenon of dilatancy so far (Reynolds, 1885; Taylor, 1948; Bishop, 1950; Roscoe, Schofield, and Wroth, 1958; Rowe, 1962; Schofield and Wroth, 1968; De Josselin De Jong, 1976; Vaid and Sasitharan, 1992; Schanz and Vermeer, 1996; Li and Dafalias, 2000; Chakraborty and Salgado, 2010; Cinicioglu and Abadkon, 2015). Angle of dilation, by the definition, is the volume change during shearing, hence it can be calculated as

$$\psi = tan^{-1}\left(\frac{d\varepsilon_v}{d\varepsilon_q}\right) \tag{2.3}$$

where ψ is the angle of dilation, $d\varepsilon_v$ is volumetric strain increment and $d\varepsilon_q$ is engineering shear strain increment.

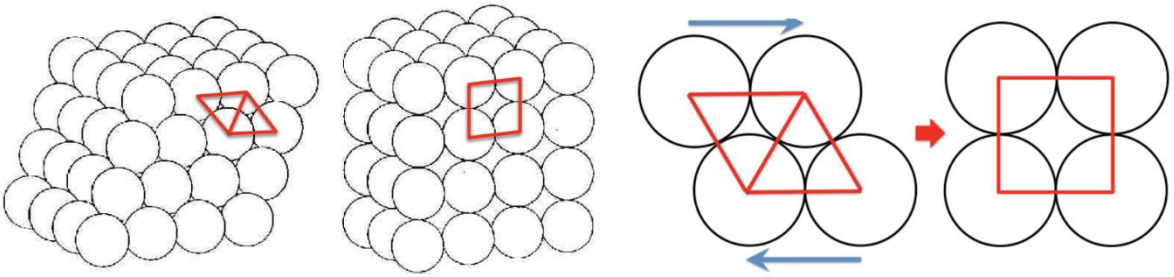

Figure 2.5. Visual Representation of Volume Expansion During Shearing (Tordesillas, Steer and Walker, 2014).

2.2.1. Bolton's Study (1986)

The main objective of Bolton's (1986) study is to analyze effects of relative density and confining pressure on peak dilatancy angle (ψ_p) and peak friction angle (φ'_p). He collated an extensive data belonging plane strain and triaxial compression tests conducted on 17 sands at different relative densities and confining stresses. Firstly, stress-strain behaviors of a dense sand under low and high stresses were observed. It can be seen in Figure 2.6 that dense sand exhibits a dilatant behavior under low stresses, while it mimics loose sand under elevated confining pressures. This is because the volume contracts due to extreme stresses, and this contraction suppresses the expansion due to dilation.

The results of plain strain and triaxial tests performed on sands with changing relative density at a constant mean effective stress level can be seen in Figure 2.7 and Figure 2.8. It can be concluded from the figures that the variation between φ'_p and φ'_c and rate of dilatancy is increasing with increasing relative density.

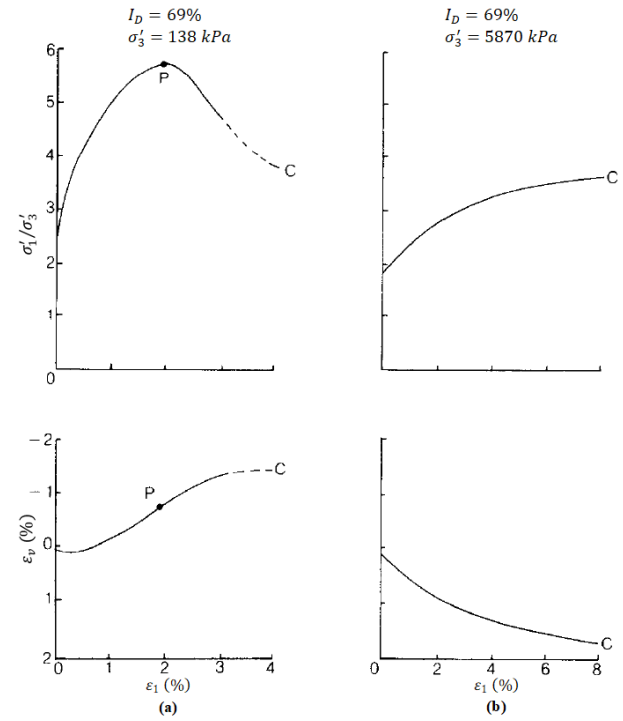

Figure 2.6. Stress-Strain Behavior of Dense Sand in Plane Compression (a) at Low Stress and (b) at High Stress (Bolton, 1986).

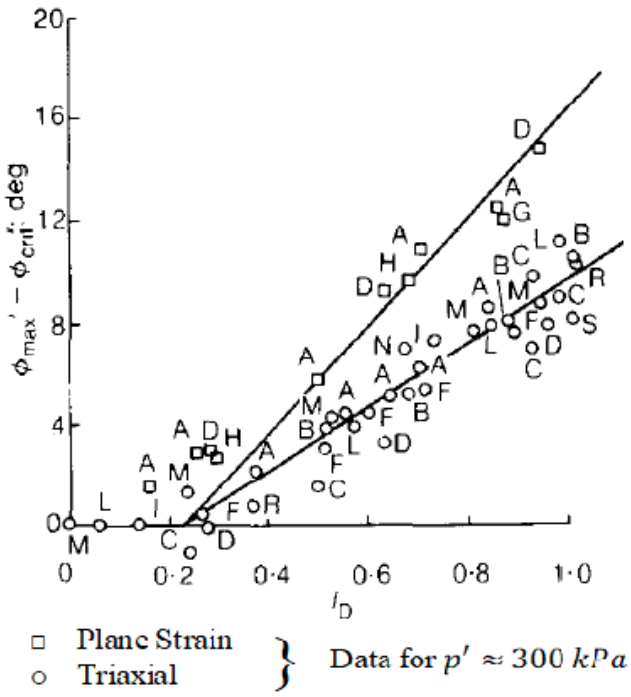

Figure 2.7. The Effect of Relative Density on the Variation Between Peak and Critical State Friction Angles (Bolton, 1986).

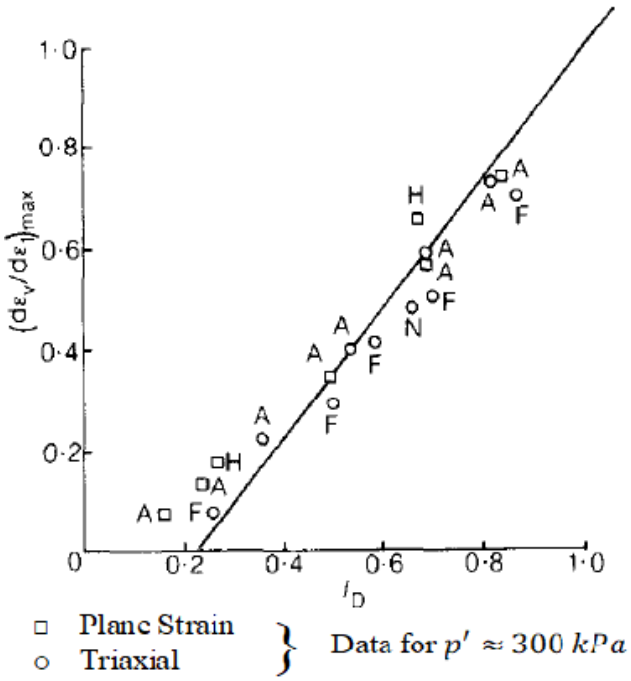

Figure 2.8. The Effect of Relative Density on the Rate of Dilatancy (Bolton, 1986).

By employing a similar approach to Rowe's stress-dilatancy theory for plane strain tests, Bolton came up with a simplified version of Rowe's relationship that correlates φ'_p and ψ_p (Equation 2.1).

By using the available published data for plain strain and triaxial compression tests, Bolton suggested new equations containing a new density index that reveals the effects of density and confining pressure.

For plain strain tests:

$$\varphi'_p - \varphi'_c = 0.8\,\psi_p = 5I_R. \tag{2.4}$$

For triaxial tests:

$$\varphi'_p - \varphi'_c = 0.8\,\psi_p = 3I_R \tag{2.5}$$

where I_R is the new relative density index, ranging from 0 to 4, suggested by Bolton as

$$I_R = I_D(Q - \ln p') - R \tag{2.6}$$

where,

- I_D is the relative density of the specimen, ranging from 0 to 1.
- p' is the mean effective stress at failure.
- Q and R are soil-type constants (proposed as $Q = 10$ and $R = 1$).

Bolton suggested the following correlation between rate of dilatancy and relative density index for both plane strain and triaxial tests. Figure 2.8 displays the applicability of Equation 2.7 in both test configurations:

$$\left(-\frac{d\varepsilon_v}{d\varepsilon_1}\right)_{max} = 0.3\, I_R \tag{2.7}$$

where,

- $\left(-\frac{d\varepsilon_v}{d\varepsilon_1}\right)_{max}$ is the rate of dilatancy.
- $d\varepsilon_v$ is the volumetric strain increment.
- $d\varepsilon_1$ is the principal strain increment.

2.2.2. Chakraborty and Salgado's Study (2010)

The main focus of Chakraborty and Salgado's (2010) research was to establish the dependence of peak angle of dilation and peak effective friction angle on relative density and confining pressure. The main difference of this study from Bolton's study is the level confining stress. Since Bolton's research did not contain data for very low confining pressure, Chakraborty and Salgado investigated whether the correlations proposed by Bolton would be applicable under low confinement or not. Their aim was to analyze the data for plain strain and triaxial compression tests to specify the effects of relative density and confining stress on dilatancy and friction angle under low confining pressures. They defined three ranges of confining pressures:

- $\sigma'_{mp} < 50\ kPa$
- $50 \leq \sigma'_{mp} \leq 100\ kPa$
- $\sigma'_{mp} > 100\ kPa$

where σ'_{mp} is the mean effective stress at peak shear strength.

Based on their relative densities, specimens were categorized as

- very loose $(0 - 15\ \%)$
- loose$(15 - 35\ \%)$
- medium $(35 - 65\ \%)$
- dense $(65 - 85\ \%)$
- very dense $(85 - 100\ \%)$

Since the available data for Toyoura sand are comprehensive and include the results of the tests conducted at low confining stresses, they were used in this study. They suggested a correlation between peak friction angle, critical state friction angle and relative density index similar to the one proposed by Bolton:

$$\varphi'_p = \varphi'_c + A_\psi\, I_R \tag{2.8}$$

where,

- A_ψ is a line fitting parameter, $A_\psi = 5$ for plain strain and $A_\psi = 3$ for triaxial conditions (Bolton, 1986).
- φ'_p is the peak friction angle.
- φ'_c is the critical state friction angle.
- I_R is the relative density index.

The variation between peak and critical state friction angle ($\varphi'_p - \varphi'_c$) versus I_D and I_R were plotted in Figure 2.9, respectively, for both plain strain and triaxial conditions. They emphasized that data points belonging to both test conditions lie approximately on the same locus which indicates a similar contribution to shear strength by dilatancy.

Based on Figure 2.9 (b), they rewrote Equation 2.8 as

$$\varphi'_p = \varphi'_c + A_\psi\, I_R. \tag{2.9}$$

with $A_\psi = 3.8$ for both plain strain and triaxial conditions. Equations provided by Bolton different for triaxial and plain strain conditions were modified to a single equation for both conditions as

$$\varphi'_p = \varphi'_c + 0.62\,\psi_p \approx \varphi'_c + 0.6\,\psi_p. \tag{2.10}$$

By combining Equation 2.6 and Equation 2.10, following equation was found.

$$\frac{\varphi'_p - \varphi'_c}{3.8} + I_D \ln\frac{100\,\sigma'_{mp}}{p_A} = I_D Q - R. \tag{2.11}$$

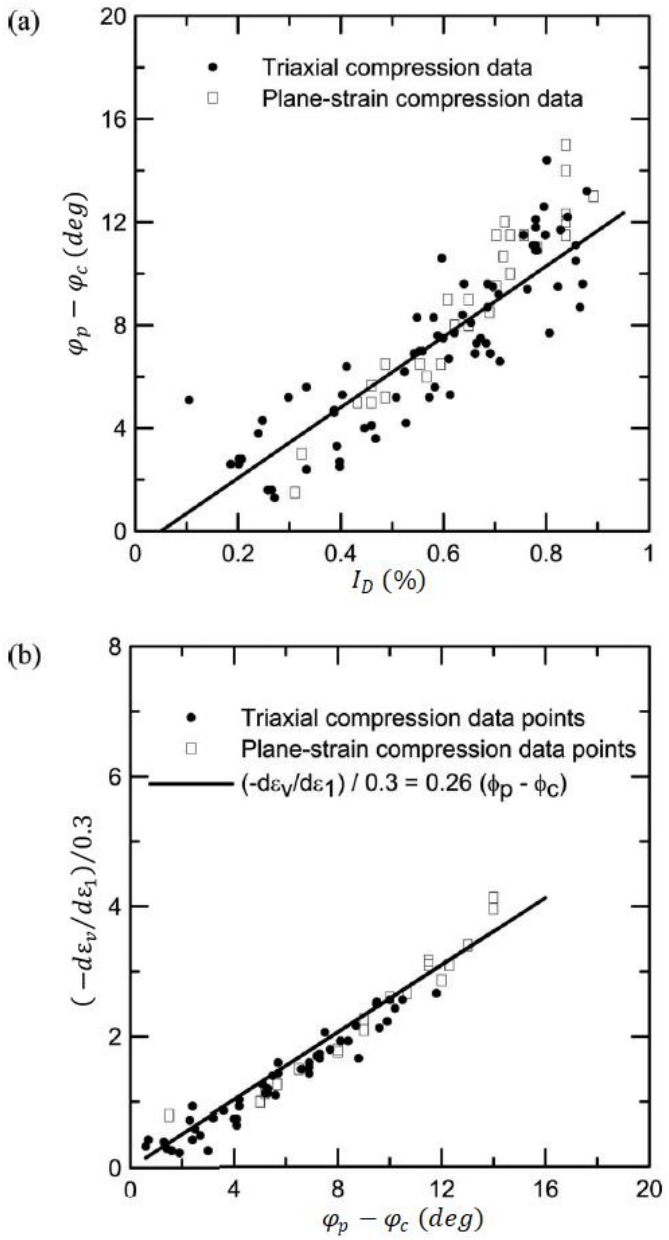

Figure 2.9. Triaxial and Plain Strain Compression Data Points for Toyoura Sand for Determining A_ψ on (a) Plot of $(\varphi'_p - \varphi'_c)$ versus I_D (b) Plot of I_R versus $(\varphi'_p - \varphi'_c)$ (Chakraborty and Salgado, 2010).

Based on the data for triaxial and plane strain tests, Chakraborty and Salgado established the plots of $I_R + I_D \ln\left(100\ \sigma'_{mp}/p_A\right) = I_D Q - R$ versus I_D corresponding to different confining levels with relative densities ranging from 30 to 90%. The Q values fall in the $7.7 - 10.0$ range in triaxial compression tests and $8.4 - 10.7$ range in plain strain tests when R is set to 1. Figure 2.10 and Figure 2.11 reveal the dependence of Q on initial

confining pressure σ_c'. They proposed simple relationships between Q and σ_c' expressing that Q increases logarithmically with increasing σ_c'.

For triaxial compression:

$$Q = 7.4 + 0.60 \ln \sigma_c'. \quad (2.12)$$

For plane strain compression:

$$Q = 7.1 + 0.75 \ln \sigma_c'. \quad (2.13)$$

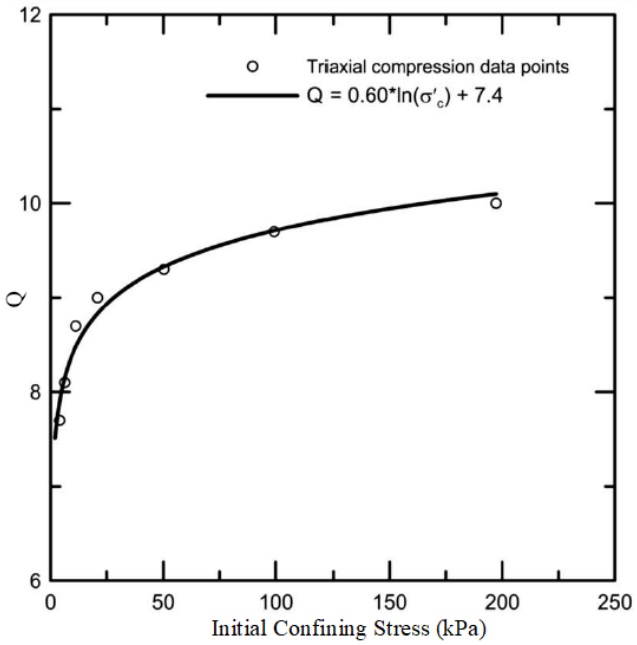

Figure 2.10. Variation of Q Values with Increasing Effective Confining Stress for Triaxial Compression Tests (Chakraborty and Salgado, 2010).

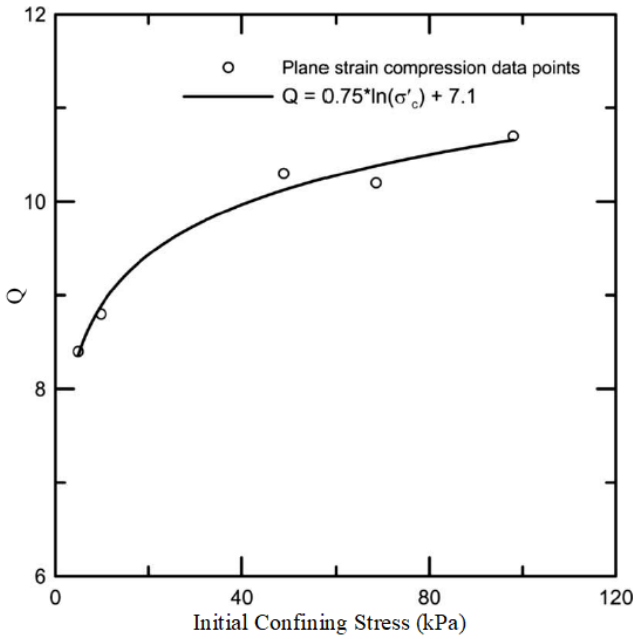

Figure 2.11. Variation of Q Values with Increasing Effective Confining Stress for Plain Strain Compression Tests (Chakraborty and Salgado, 2010).

2.3. Particle Image Velocimetry

Particle Image Velocimetry is an image-based deformation measurement technique. It was used by White, et al. (2003) before to measure soil deformation. In this research, GeoPIV-RG which is one of the MATLAB-based PIV techniques is used. GeoPIV-RG developed by Stainer, et al. (2016) is a free image analysis module for MATLAB and suitable for geotechnical applications.

A photo frame and a reference image are selected first. Extremely small subsets called ‘mesh’ are created entering mesh size and distance inputs, inside Region of Interest which is drawn as a boundary region. Deformations of the subsets are followed from the reference image, which is the first image in the frame, until the final image. Deformation and strain fields are created based on the deformations of subsets. The algorithm of the software compares the subsets in consecutive images to estimate the deformations. Strains can be computed based on deformations and the position of subsets on the reference image. This way, localization response and the evolution of shear planes and slip surfaces can be observed.

The images captured during LS-T-SS tests are used in the analyses. The deformation and evolution of strain fields during shearing are investigated. On shear and volumetric strain fields, strain concentrations can be observed. Strain matrices containing strain values of each subset for all images can also be obtained.

To be able to perform GeoPIV-RG analyses, pictures of the deformations due to the rotation of sidewalls should be taken consecutively with high resolution. The camera needs to be fixed to prevent any blur or possible change in the angle of pictures. These may result in miscalculation of deformations.

3. METHODOLOGY

Three types of test are performed in this study, with the aim of obtaining dilatancy, peak friction angle and critical state friction angle. Once they are obtained, data analysis is made in order to assess line fitting parameter (r) in Equation (2.1) and soil-type constants (Q and R) suggested by Bolton in Equation (2.6). The combination of Equations (2.1), (2.6) and (2.8) gives the following formula:

$$\frac{\psi_p . r}{A_\psi} + I_D \ln\left(\frac{100\, p'_f}{p_a}\right) = I_D Q - R \qquad (3.1)$$

where $A_\psi = 5$ under plain strain conditions (suggested by Bolton (1986)).

Moreover, PIV analyses are performed to produce strain matrices and observe evolution of strain fields of the soil during LS-T-SS tests.

3.1. LS-T-SS Test

Angle of dilation can be obtained using triaxial test, however the time it requires is very long and the set of tests is relatively expensive. Additionally, triaxial test is difficult to conduct under low – very low stress levels. To avoid these disadvantages, an alternative method to determine dilatancy was researched.

A new equipment which allows practical determination of dilatancy angle for low stress levels was designed. In the succeeding sections of this thesis, the test conducted by this equipment will be referred to as ‘Low Stress Transparent Simple Shear’ and abbreviated to ‘LS-T-SS’. One of the goals is to observe the evolution of the fields throughout the tests. This requires a transparent testing mechanism so that the sample is observable. In the design of the equipment, colorless plexiglass was preferred owing to its transparency which enables observation of the changes in soil during the test.

The equipment is 20 cm in length (L), 15 cm in width (B) and 24 cm in height (H). The reciprocal two sidewalls which are in x – z space can rotate freely about x axis while the base and the other reciprocal two sidewalls which are in y – z space are fixed. The rotating walls are connected to each other with a plexiglass bar at the top so that their rotation angles are always the same. This way, cross-sectional areas of the samples in horizontal plane remain constant. Accordingly, normal strains are zero between the sidewalls. Since sand is a granular material, it is possible that the grains of the specimen get out the equipment between the walls when rotating. To avoid this phenomenon, very thin pieces of sponge were placed along the lines of interaction as seen in Figure 3.1.

Figure 3.1. The Specimen just Before Starting the Test.

The electronic part of the equipment consists of 2 accelerometers, 3 distance sensors, 1 real time clock sensor, 1 SD card module, 1 LCD screen and 1 Arduino Uno as shown in Figure 3.2. Accelerometers are placed on the free-to-rotate sidewalls to measure rotation angle. They measure x, y and z components of the gravitational acceleration, in order for the rotation angle to be calculated. Although the walls are rotating in the same direction by the same angle, sensors are put on both walls to increase the accuracy. Distance sensors are utilized to measure the height of the soil. They are placed so that measurements are taken from the left, middle and right portions of the specimen in both x and y directions. Additionally, real time clock (rtc) sensor -which measures the passage of time as hour, minute and second- and SD card module -to record the data obtained from distance, angle and rtc sensors- are utilized. LCD screen is used to display the data coming from the sensors. All of these pieces are connected to Arduino through a specifically developed code.

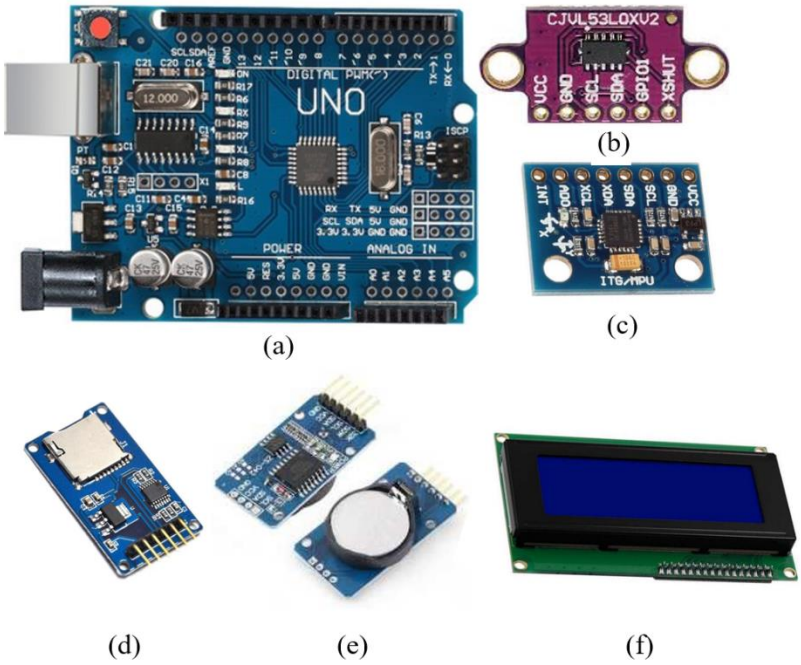

Figure 3.2. Electronic Components of LS-T-SS Equipment: a) Arduino Uno, b) Distance Sensor, c) Accelerometer, d) SD Card Module, e) RTC Module and f) LCD Screen.

The mechanical section of the equipment was designed so that the granular soil is sheared by rotating the reciprocal walls in the same direction by the same angle so that no volume change occurs. Besides, it was adjusted to prevent the soil grains from getting out through the intersection of the fix and free-to-rotate walls. The Arduino code outputs the data coming from the sensors, saves them in an SD card and displays them in an LCD screen. The data collection rate is 1 Hz (distance, components of acceleration in 3 dimensions and the time). All the sensors are mounted on the mechanical part of LS-T-SS. The equipment before and after the rotation of the sidewalls can be seen in Figure 3.4 and Figure 3.5. A sample Arduino output is shown in the Figure 3.3. The change in the volume of cohesionless soils and the evolution of strain fields when they are subjected to shear was investigated within the scope of this research.

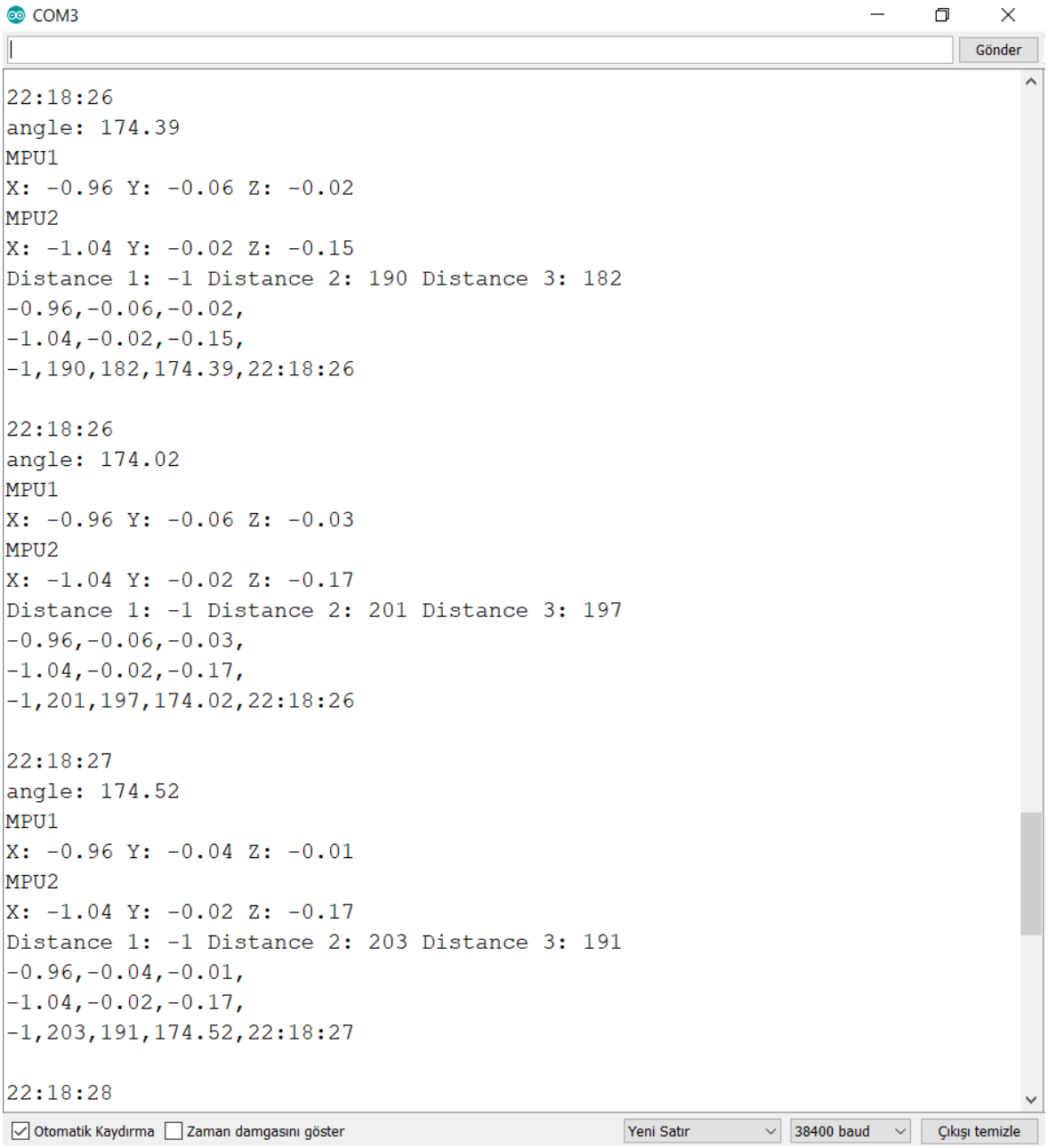

Figure 3.3. Sample Arduino Output.

3.1.1. Preparation of Samples

To perform LS-T-SS tests, following steps need to be followed. First of all, the sidewalls of the equipment, which are free to rotate, are fixed using screws to prevent them from moving before the test starts and to ensure right angle between the base and the sidewalls. The position of distance sensors is determined and the distance between the sensors and the base of the equipment are measured. The average of 3 height values is noted

as H_b. A soil sample secured in a weighing bowl is weighed using a digital balance and the mass is recorded as M. The specimen is then poured into the equipment and compacted to a level. In order to achieve a uniform compaction, the process of pouring and compacting the sand is realized in three layers. Utmost attention is paid in order for the specimen to have a flat surface. The heights at 4 corners are measured with a ruler ad the average of these 4 measurements is recorded as h. Meanwhile, a camera is prepared to capture images on which PIV analyses will be performed. All the sensors are mounted on the mechanical part of the equipment. The top bar is then loaded on both rotating sidewalls. Having the top bar on the walls ensures a constant cross section area in horizontal plane. The screws tightened before pouring the soil are removed. The soil is sheared by rotating the sidewalls very slowly. Distances between the distance sensors and the top of the soil are measured continuously during the test and recorded as H_s. The associated gravitational accelerations in x, y and z directions are measured by accelerometers. The test is finished when the angle of rotation reaches approximately 25°.

After finishing the test, the sidewalls are brought back to vertical position and the screws are tightened to keep them constant. The sensors are displaced following the removal of the top bar. The equipment is then emptied. The procedure is repeated for various relative density – pressure combinations.

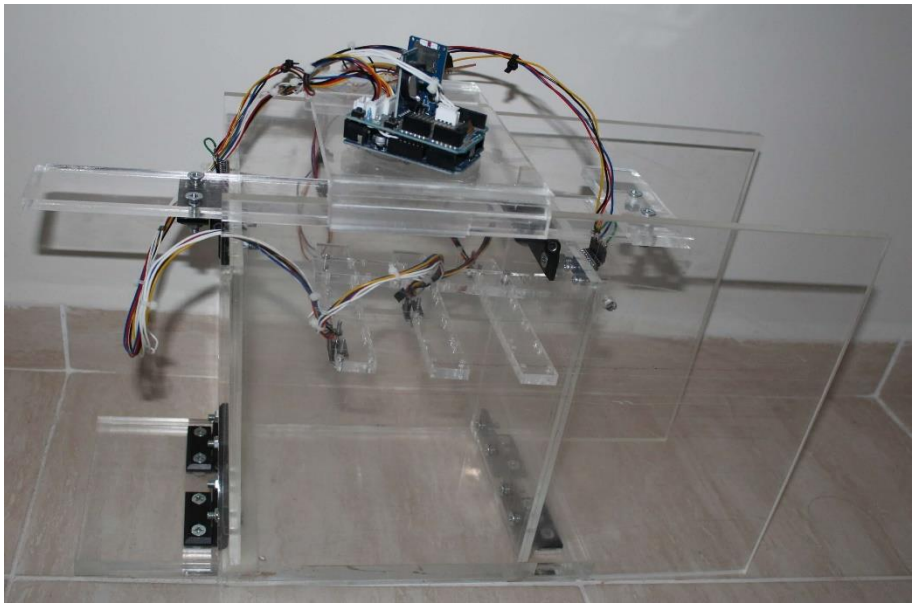

Figure 3.4. LS-T-SS Equipment Before Rotation of the Sidewalls.

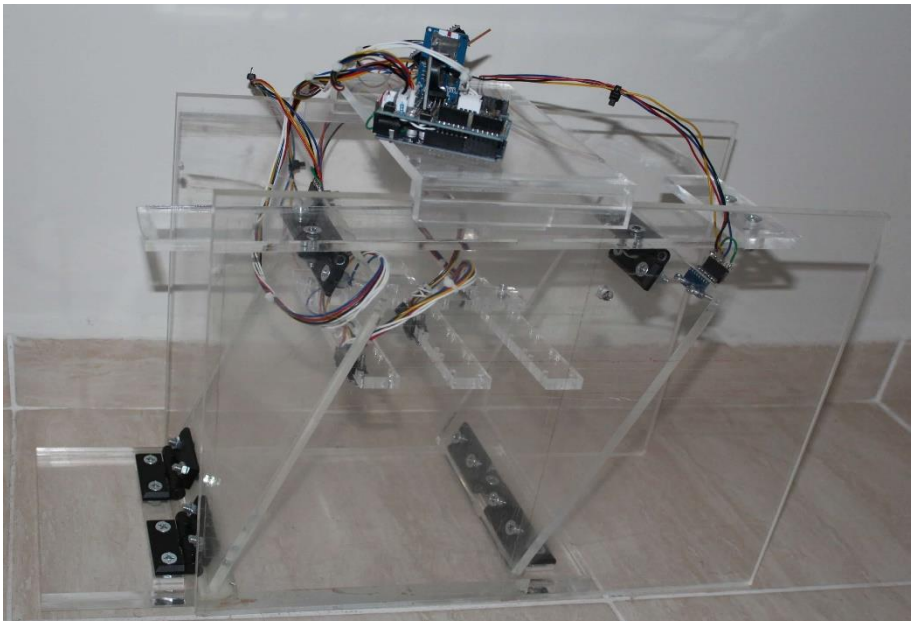

Figure 3.5. LS-T-SS Equipment After Rotation of the Sidewalls.

3.1.2. Dilatancy Determination

To be able to compute the angle of dilation, volumetric strain and shear strain need to be obtained. This requires determination of the angle of rotation and the volume of the specimen. The angle is calculated by the following formula:

$$\alpha = \cos^{-1} \frac{\sqrt{g_x^2 + g_y^2}}{\sqrt{g_x^2 + g_y^2 + g_z^2}} \tag{3.2}$$

where,

- α is the angle of rotation.
- g_x, g_y and g_z are x, y and z components of gravitational acceleration measured by accelerometers, respectively.

The devised equipment works in plain strain conditions. Thus, engineering shear strain is used in this study. The term ‘shear strain’ will refer to ‘engineering shear strain’ in the following sections of this thesis. The average of two angles is recorded and used in shear strain determination. Shear strain is calculated as

$$\varepsilon_q = tan\,\alpha \tag{3.3}$$

where ε_q is shear strain.

The height of the soil during the test (each second) is obtained by the following formula:

$$H = H_b - H_s \tag{3.4}$$

where,

- H_b is the distance between the distance sensors and the base.
- H_s is the distance between the distance sensors and the top of the soil.

The average of 3 heights is used in volumetric strain determination. Since width (B) and length (L) of the specimen are constant, volumetric strain equals to the strain in height. Volumetric strain is thus found by the equation

$$\varepsilon_v = \frac{\Delta H}{H}. \tag{3.5}$$

Rate of dilation is not constant and continuously changes during shearing. The reason why peak angle of dilation is investigated is because most of the soil properties are dependent on that value since it directly affects peak friction angle. The plot of volumetric strain versus shear strain is then constructed and dilatancy at which the ratio $d\varepsilon_v / d\varepsilon_q$ got the maximum value is determined and recorded as peak dilatancy angle.

The volume of the soil is found using the following equation:

$$V = (B)(L)(h) \tag{3.6}$$

where,

- V is the volume of the specimen.
- B, L and h are the width, length and height of the specimen, respectively.

For void ratio determination, volume of solids needs to be calculated:

$$V_s = \frac{M}{G_s \, \rho_w} \tag{3.7}$$

where,

- V_s is the volume of solids.
- M is the mass of the specimen.
- G_s is the specific gravity.
- ρ_w is the density of water.

Using the volume of the specimen (V) and the volume of the solids (V_s), the current void ratio is computed by the following equation:

$$e = \frac{V_v}{V_s} \tag{3.8a}$$

$$e = \frac{V - V_s}{V_s} \tag{3.8b}$$

where,

- e is the current void ratio.
- V_v is the volume of voids.

Using minimum and maximum void ratios, relative density is obtained under the assumption that it is the same for the entire region:

$$I_D = \frac{e_{max} - e}{e_{max} - e_{min}} \tag{3.9}$$

where,

- I_D is the relative density of the specimen.
- e_{max} is the maximum void ratio.
- e_{min} is the minimum void ratio.

Stress level is then calculated at the middle depth considering only the soil's own weight since there is no additional loading on the soil:

$$\sigma' = \frac{\gamma h}{2} \quad (3.10a)$$

$$\sigma' = \frac{(M)(g)}{V}\, x \frac{h}{2} \quad (3.10b)$$

where,

- σ' is the level of effective stress.
- g is the gravitational acceleration.

Calculated stress is the average for the sample.

3.2. Peak Friction Angle Determination

Peak friction angle is not constant for a specific soil type, instead it varies depending on certain parameters. Both confining pressure and relative density affect the angle of dilation of the soils and thereby their peak friction angles. Angle of peak friction thus needs to be assessed under changing relative density and stress conditions.

In order to establish a correlation between peak friction angle and dilatancy, they should be acquired under the same conditions. LS-T-SS test is explained in the preceding section including how to calculate stress and relative density. The tests that are conducted with the aim of obtaining peak friction angle are performed on the soil having the same parameters.

Giampa and Bradshaw (2018) suggested a simple tilt method to determine peak friction angle at low confining pressures. They utilized the equipment that is used for determination of unit weight of soils and calculation of relative density in accordance with specifications as can be seen in Figure 2.2. The results of their study showed a good match with the results in literature. A similar method is then utilized in this study which will be referred to as ‘Peak Friction Angle Test’ from this point on.

A mold which is rectangle in cross section is obtained. To be able to yield the same relative density and pressure that correspond to each LS-T-SS test, cross-section area of the mold needed to be equal to that of LS-T-SS test equipment. In this way, the height of the

specimen is assured to be same with the one in LS-T-SS test. Hence, the length and width of the mold are 20 cm and 15 cm, respectively. 2 accelerometers connected to an Arduino are mounted on two walls on the opposite sides of the mold. They are used in tilt angle determination.

As explained in the preceding section, relative density and pressure in LS-T-SS tests are calculated using the weight and the height of the soil after it is secured in the equipment. In peak friction angle tests, on the other hand, same amount of soil is compacted into the mold until the predetermined height is achieved. A particular attention is paid to flatten the surface prior to starting the test. Utmost attention is expended to prepare uniform samples and therefore global I_D for the sample represents the I_D at the top surface of the prepared specimen.

(a) (b)

Figure 3.6. Peak Friction Angle Test a) Before and b) After Tilting.

As shown in Figure 3.6, the mold with the compacted sand is tilted very slowly, until a small slope failure occurs. Meanwhile, the accelerometers measure and record x, y and z components of gravitational acceleration together the time. Tilt angle is found using Equation (3.2). The time is announced at the moment a small slope failure is observed. The associated angle is recorded as the peak friction angle.

3.3. Critical State Friction Angle Determination

Santamarina and Cho (2001) proposed a simple method to estimate critical state friction angle as shown in Figure 2.1. This method is used in this study. The soil is poured into a 1000-ml cylinder that is full of water up to a level. The system is rotated more than 60 degrees after soil grains settled completely. It is then returned slowly to the vertical position and angle of repose is recorded as critical state friction angle.

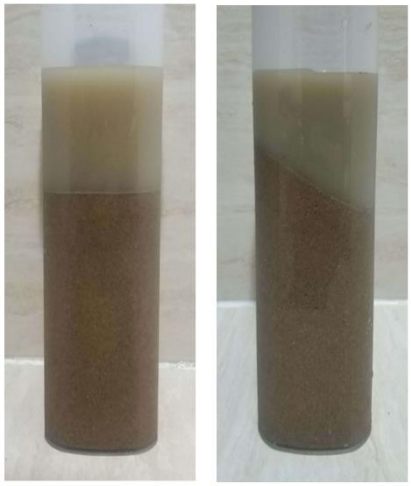

(a) (b)

Figure 3.7. Critical State Friction Angle Determination.

Unlike peak friction angle, critical state friction angle is constant and does not vary with changing conditions. However, since the amounts of water and the soil were not specified in Santamarina and Cho's study, the test is conducted a couple of times with changing amounts of water and soil. In this way, not only the effects of the quantities were examined but also the accuracy tried to be increased.

Once critical state friction angle tests are completed together with dilatancy and peak friction angle tests; peak dilatancy angle (ψ_p), peak angle of friction (φ'_p) and critical state friction angle (φ'_c) have been obtained. φ'_p is then plotted against ψ_p with φ'_c intercept on the vertical axis and line fitting parameter (r) could be determined through Equation (2.1). With the line fitting parameter obtained, the left side of Equation (3.1) could be plotted against relative density. The slope of that plot is then recorded as Q and the intercept as R.

3.4. Particle Image Velocimetry Analysis

Image-based deformation measurement is performed to study the changes in the specimen when sheared. GeoPIV-RG which is a MATLAB module is utilized for that purpose. Images are taken during the tests that are conducted by the LS-T-SS equipment.

A photo frame and a reference image are selected first. Very small subsets called ‘mesh’ are created by entering the inputs of size of the meshes and the distance between them as 50 pixels for both. Borders of Region of Interest which is the area in which the deformations will be estimated are then drawn. Examining the changes in the position of the subsets, the software produced displacement and strain values between each image for all subsets along RoI. Both volumetric and shear strain distributions are then plotted at 20% increments in the number of images to reveal the changes in the specimen. Shear planes and active slip band are observed and correlated with relative density of the soil on both shear strain and volumetric strain fields as shown in Figure 3.8 and Figure 3.9.

For the points at which maximum and minimum shear strains occurred, shear and volumetric strain values corresponding to each image are then extracted. Moreover, average of the strain values for all subsets are calculated. In this wise, shear strain versus volumetric strain plots for minimum and maximum strain points and the average are plotted to reveal the action at extreme points and RoI.

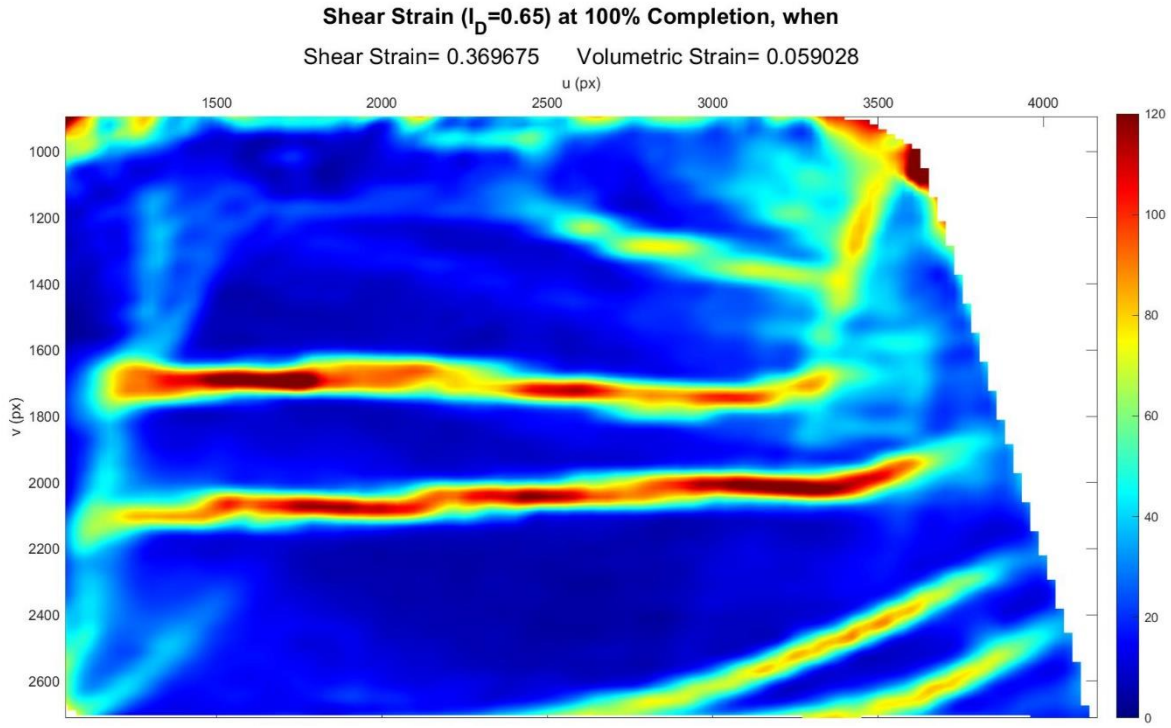

Figure 3.8. Sample Shear Strain Field at the End of the Analysis.

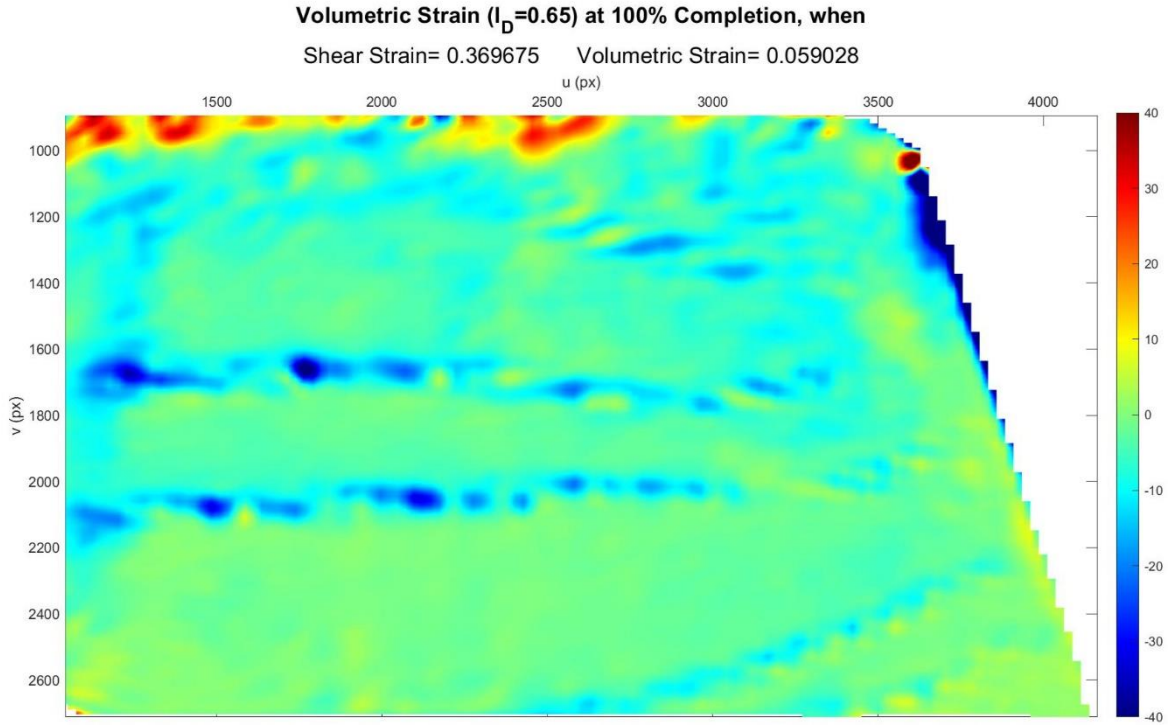

Figure 3.9. Sample Volumetric Strain Field at the End of the Analysis.

4. RESULTS AND DISCUSSION

4.1. LS-T-SS Test

As mentioned in Methodology section, dilatancy was determined making use of an alternative equipment which was created within the scope of this study. Kilyos sand was poured into the equipment and sheared very slowly by rotating the sidewalls, meanwhile the height of the specimen and the rotation angle were recorded to calculate volumetric strain and shear strain using the Equations (3.3) and (3.5), respectively. A sample test will be explained from beginning to end in order to explain the procedure of the test in detail. The results of all tests are provided in Appendix B. LS-T-SS test device with the specimen before and after the test can be seen in the following figure.

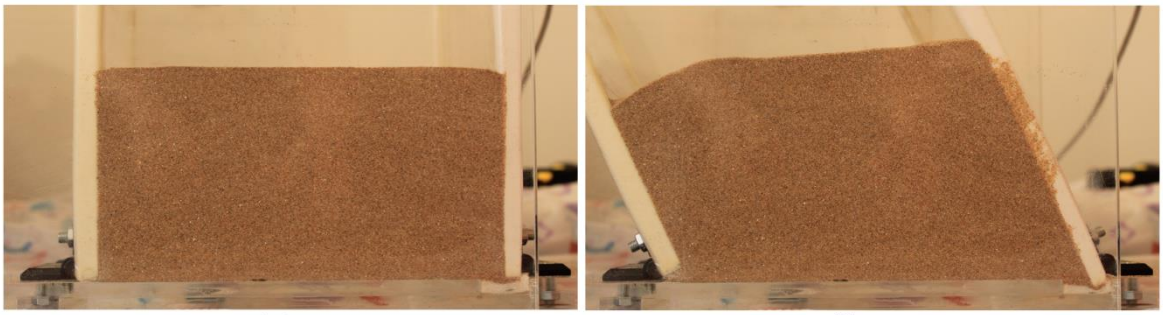

(a) (b)

Figure 4.1. LS-T-SS Test Device a) Before and b) After the Test.

To be able to observe the behavior of the soil, volumetric strain is plotted with respect to shear strain as can be seen in Figure 4.2.

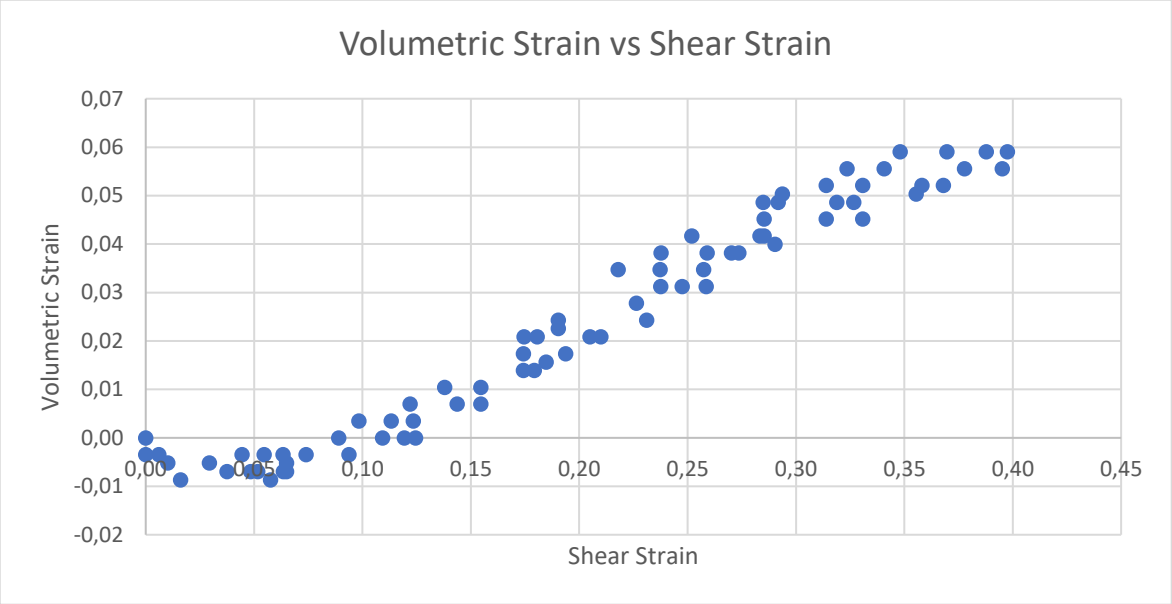

Figure 4.2. Sample Shear Strain vs Volumetric Strain Diagram.

In shear strain versus volumetric strain diagrams of dense soils, a contraction occurs in advance to expansion of the soil. This is because the soil gets even denser before it starts dilating. Therefore, volumetric strain drops to negative values first, then it starts ascending on the positive side. This behavior can be observed in all LS-T-SS tests as shown in Figure 4.2.

4.1.1. Computation of Dilatancy

Dilatancy is linked, through Equation (2.3), to the derivative of equation of the curve constructed by combining the datapoints in Figure 4.2. Trendline was thus added to the graph and it was deducted that 3rd degree polynomial shows a perfect match with test results.

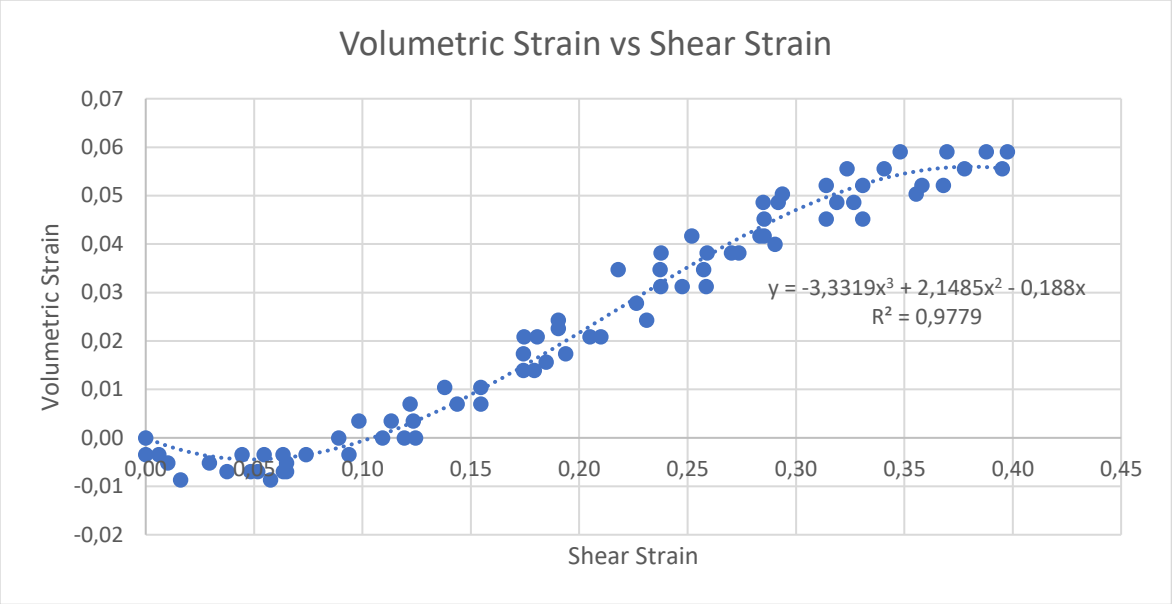

Figure 4.3. Trendline Equation with Origin Intercept.

As shown in Figure 4.3, the equation of the volumetric strain with origin intercept is found as

$$\varepsilon_v = a(\varepsilon_q)^3 + b(\varepsilon_q)^2 + c(\varepsilon_q) + d \tag{4.1}$$

yielding $R^2 = 0.9776$; where,

- $a = -3.3319$
- $b = 2.1485$
- $c = -0.1880$
- $d = 0$

The coefficient of determination, R^2, of a data set is a measure of how well the data fits the regression line which describes the interrelation of a dependent variable with one or more independent variables. Its value varies between 0% and 100%. The higher the coefficient, the higher percentage of points the line passes through when the data points and line are plotted. In this test, the coefficient of determination is 0.9776 which is an indication of a good agreement of the datapoints with the trendline.

Peak angle of dilation occurs at the point where $d\varepsilon_v/d\varepsilon_q$ gets its maximum value. Taking the derivative of Equation (4.1), the following equation was obtained:

$$\frac{d\varepsilon_v}{d\varepsilon_q} = 3a(\varepsilon_q)^2 + 2b(\varepsilon_q) + c. \tag{4.2}$$

Equation (2.3) was altered to calculate peak dilatancy as shown below:

$$\psi_p = tan^{-1}\left(\frac{d\varepsilon_v}{d\varepsilon_q}\right)_{max}. \tag{4.3}$$

The maximum value of an equation can be found by equating its first order derivative to zero. For finding the point at which $d\varepsilon_v/d\varepsilon_q$ gets its maximum value, Equation (4.2) was differentiated one more time and equated to zero:

$$\frac{d^2\varepsilon_v}{d\varepsilon_q{}^2} = 6a(\varepsilon_q) + 2b = 0. \tag{4.4}$$

$\left(d\varepsilon_v/d\varepsilon_q\right)_{max}$ was then determined substituting the shear strain value that makes $\frac{d^2\varepsilon_v}{d\varepsilon_q{}^2}$ zero in Equation (4.2). Peak angle of dilation is finally calculated using Equation (4.3). The steps of dilatancy determination are given below for the sample test:

$$\varepsilon_v = -3.3319(\varepsilon_q)^3 + 2.1485(\varepsilon_q)^2 - 0.1880(\varepsilon_q), \tag{4.5a}$$

$$\frac{d\varepsilon_v}{d\varepsilon_q} = -9.9958(\varepsilon_q)^2 + 4.297(\varepsilon_q) - 0.1880, \tag{4.5b}$$

$$\frac{d^2\varepsilon_v}{d\varepsilon_q{}^2} = -19.9917(\varepsilon_q) + 4.2970, \tag{4.5c}$$

$$\frac{d^2\varepsilon_v}{d\varepsilon_q{}^2} = -19.9917(\varepsilon_q) + 4.2970 = 0, \tag{4.5d}$$

$$\varepsilon_q = 0.2150, \tag{4.5e}$$

$$\left(\frac{d\varepsilon_v}{d\varepsilon_q}\right)_{max} = -9.9958(0.2150)^2 + 4.297(0.2150) - 0.1880, \quad (4.5f)$$

$$\left(\frac{d\varepsilon_v}{d\varepsilon_q}\right)_{max} = 0.2738, \quad (4.5g)$$

$$\psi_p = tan^{-1}(0.2738), \quad (4.5h)$$

$$\psi_p = 15.3°. \quad (4.5i)$$

4.1.2. LS-T-SS Test Results

In all tests repeated for relative density values ranging from 14% to 79%, dilatancy angles were computed by following the steps provided in Equation (4.5). Based on the results obtained from all tests, peak dilatancy angle is plotted against relative density as shown in Figure 4.4.

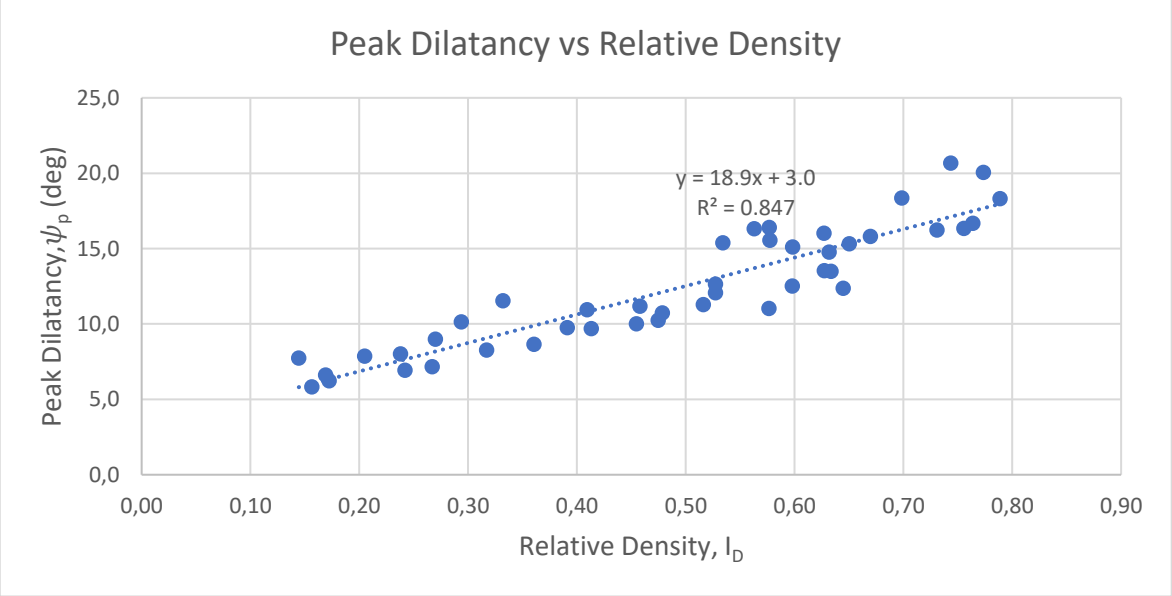

Figure 4.4. Peak Dilatancy Angle versus Relative Density.

Although angle of dilation depends not only on relative density of the soil but also on mean effective stress level, it showed a very good match as shown in Figure 4.4. The reason behind this is the tests being conducted under very low confining pressures. The dependence of peak dilatancy on relative density is found as the following:

$$\psi_p = 18.9\, I_D + 3.0°. \tag{4.6}$$

Theoretically, peak angle of dilation is zero when relative density is zero. To set the contribution of dilatancy on peak friction angle to zero for the soils with zero relative density, the same plot is established with origin intercept.

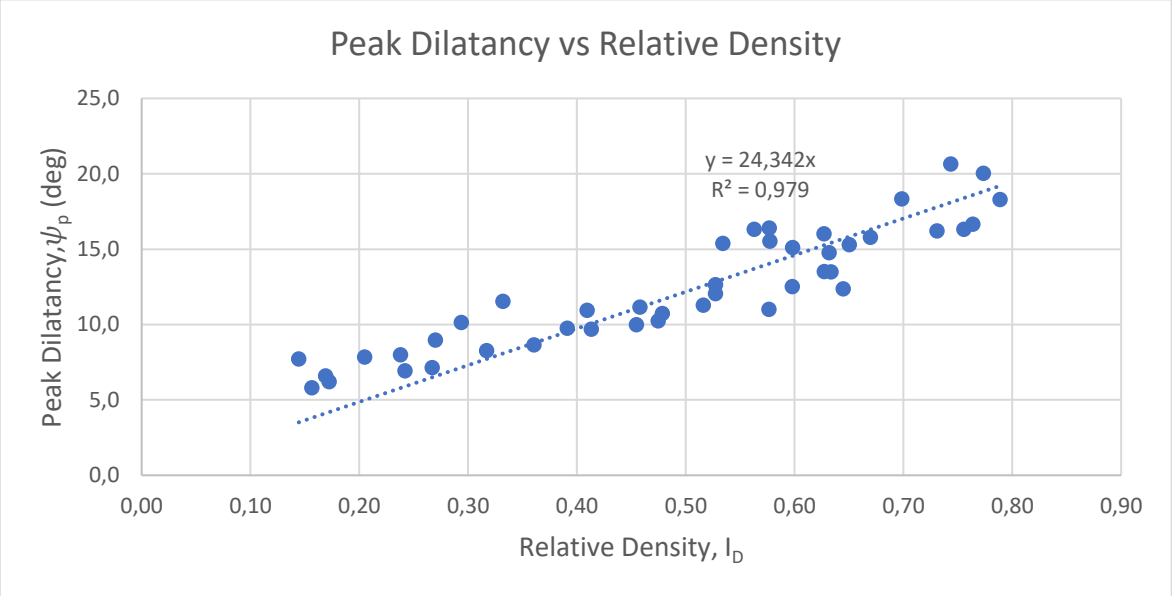

Figure 4.5. Peak Dilatancy Angle versus Relative Density with Origin Intercept.

With origin intercept, the correlation was found as following:

$$\psi_p = 24.3\, I_D. \tag{4.7}$$

Datapoints in Figure 4.5 at low relative density values fall above the line of best fit. A new equation to satisfy all relative density intervals is thus researched. It was noticed that a nonlinear equation fits better than linear equation.

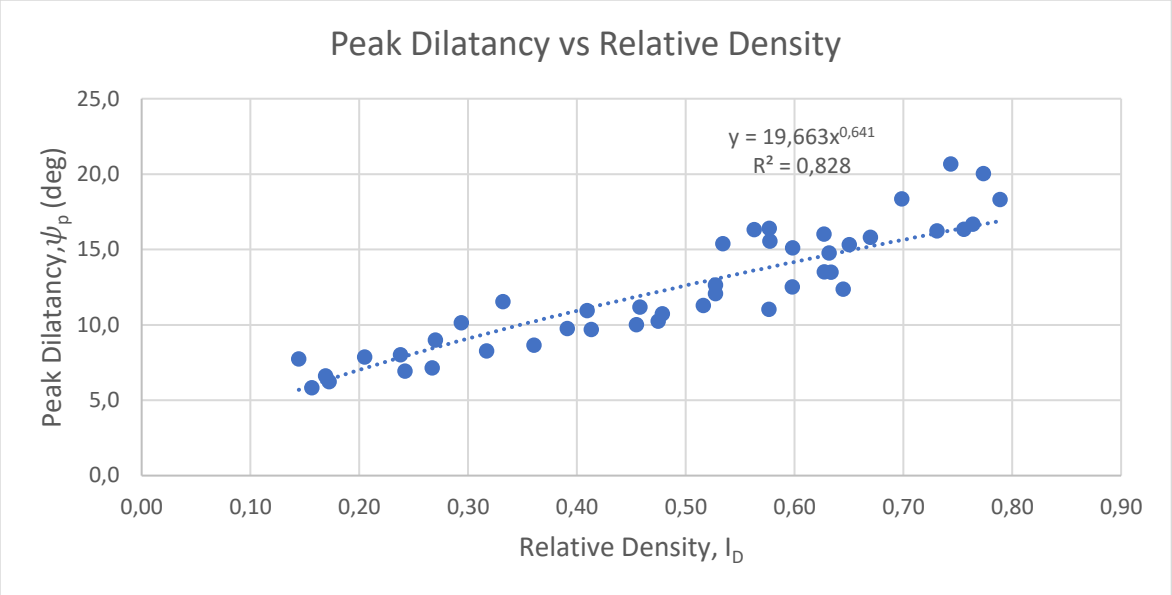

Figure 4.6. Peak Dilatancy Angle versus Relative Density with Nonlinear Equation.

The equation is found as following:

$$\psi_p = 19.7\, I_D{}^{0.64}. \tag{4.8}$$

The angle of dilation is adjusted to zero when relative density is zero.

4.2. Particle Image Velocimetry Analysis

For particle image velocimetry analysis, GeoPIV-RG which is a MATLAB module is used in this study. Analyses were performed on the images captured during LS-T-SS tests. Once the analysis for a test is completed, shear and volumetric strain fields are plotted periodically to reveal the changes in the soil progressively. This way, localization response and the evolution of shear planes and slip surfaces can be observed.

4.2.1. Strain Fields

Shear and volumetric strain fields of a sample test, the results of which were provided in 'LS-T-SS Test Results' can be seen in the following figures. When LS-T-SS tests were being conducted, utmost attention was paid to rotate the sidewalls at a constant rate and the pictures were captured at constant frequency. Hence, the analysis results are presented in 5

steps with 20% increments in the numbers of images, considering it represents the percentage of completion of the tests.

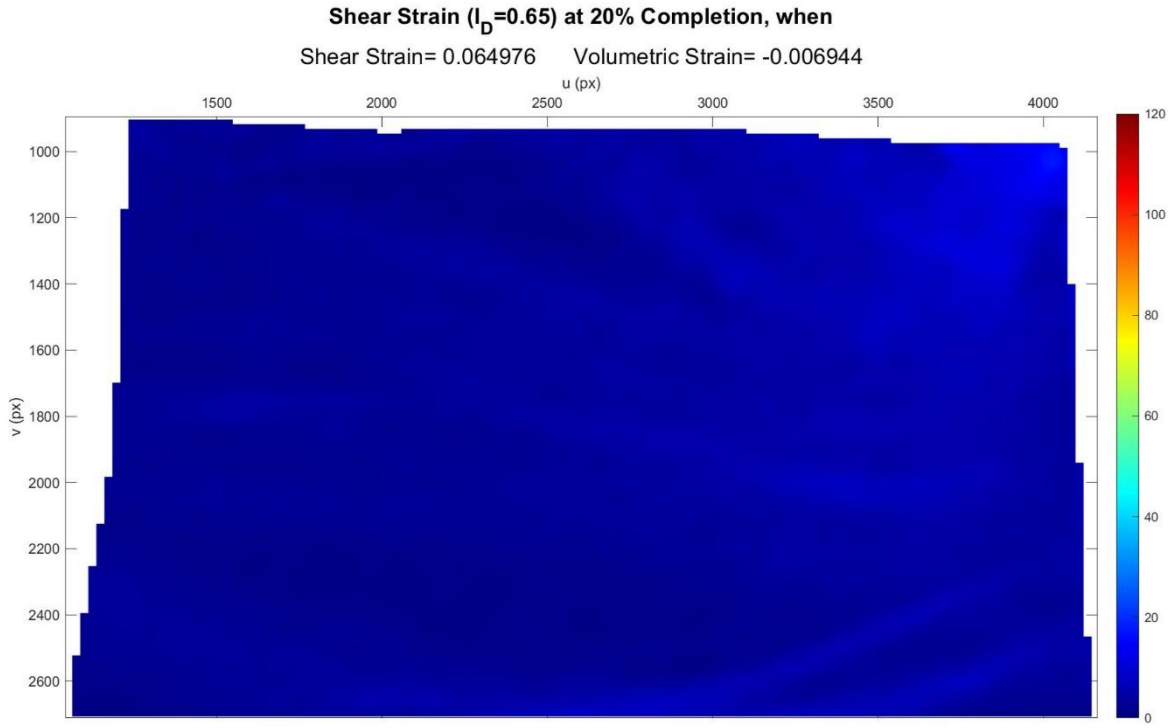

Figure 4.7. Shear Strain Field at 20% Completion ($I_D = 0.65$ & $\sigma' = 0.96\ kPa$).

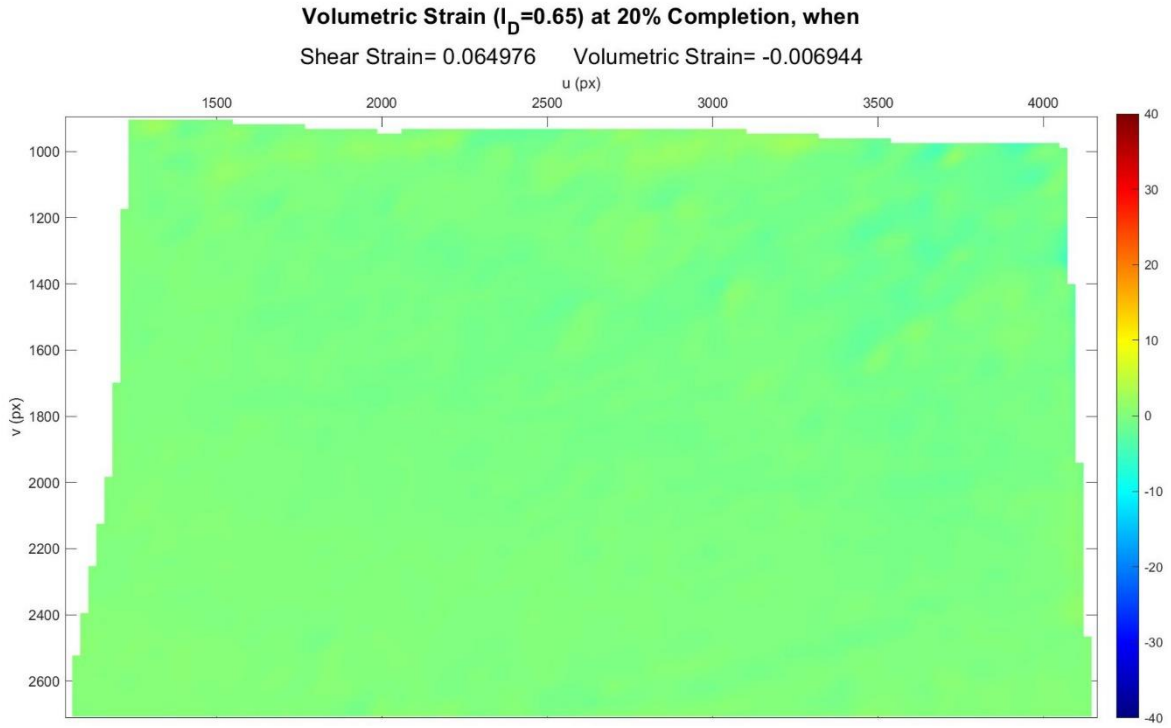

Figure 4.8. Volumetric Strain Field at 20% Completion ($I_D = 0.65$ & $\sigma' = 0.96kPa$).

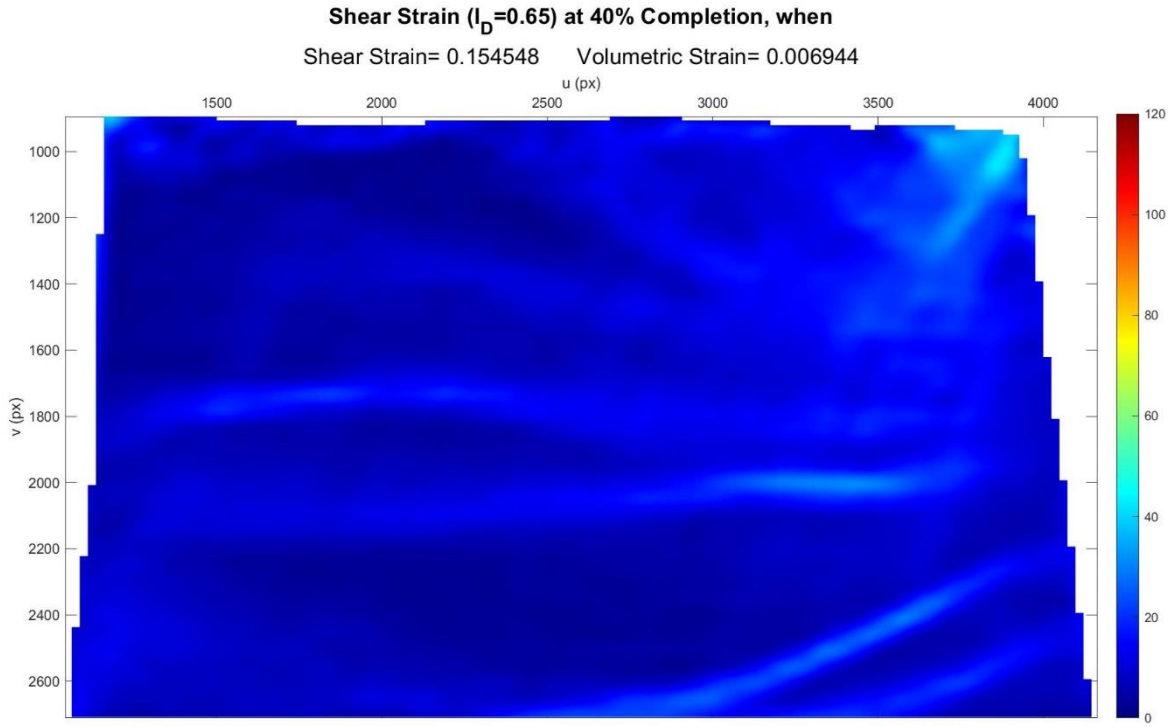

Figure 4.9. Shear Strain Field at 40% Completion ($I_D = 0.65$ & $\sigma' = 0.96\ kPa$).

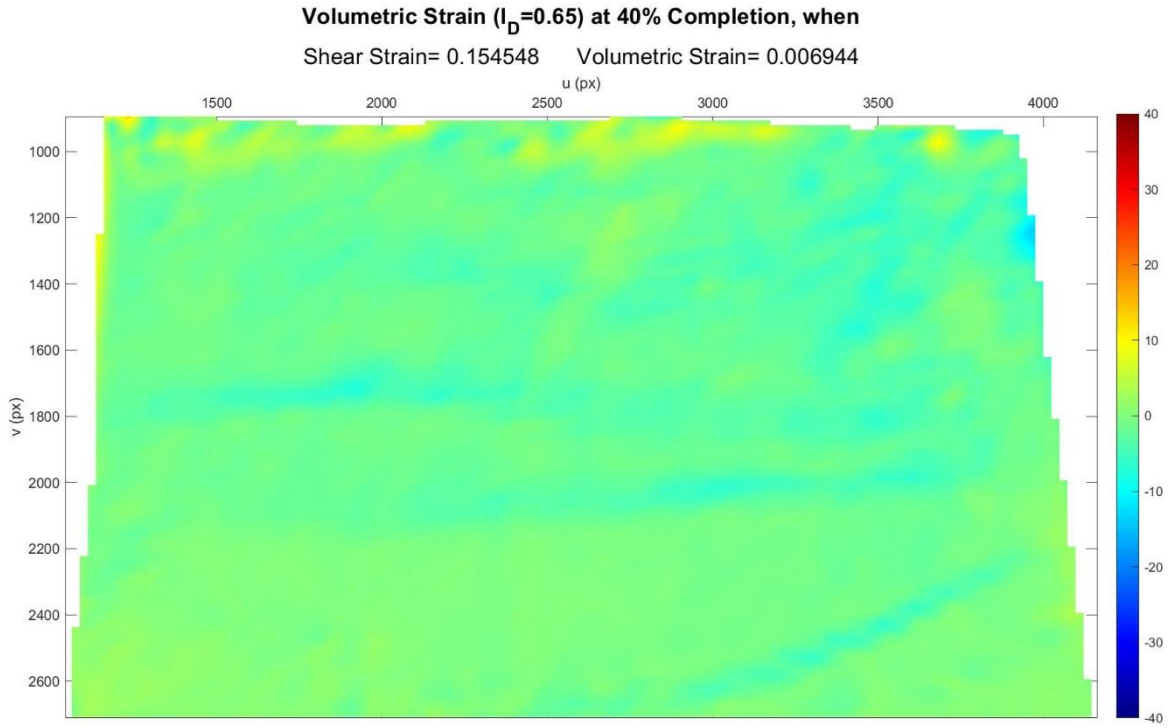

Figure 4.10. Volumetric Strain Field at 40% Completion ($I_D = 0.65$ & $\sigma' = 0.96kPa$).

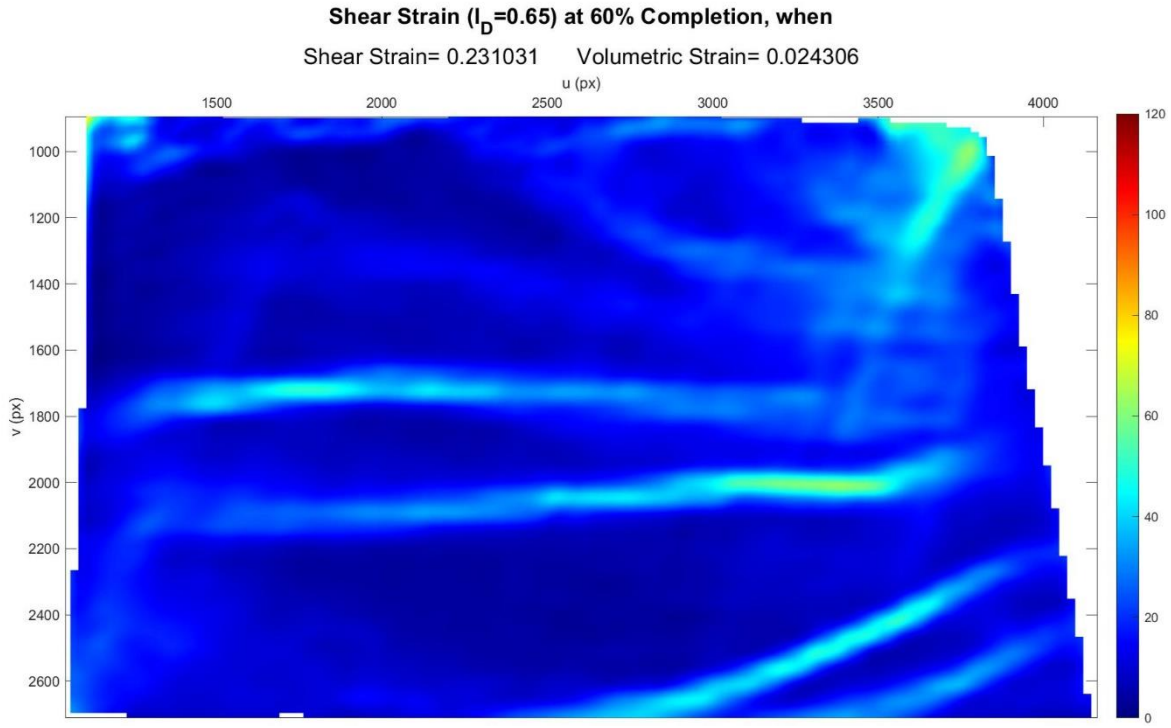

Figure 4.11. Shear Strain Field at 60% Completion ($I_D = 0.65$ & $\sigma' = 0.96\ kPa$).

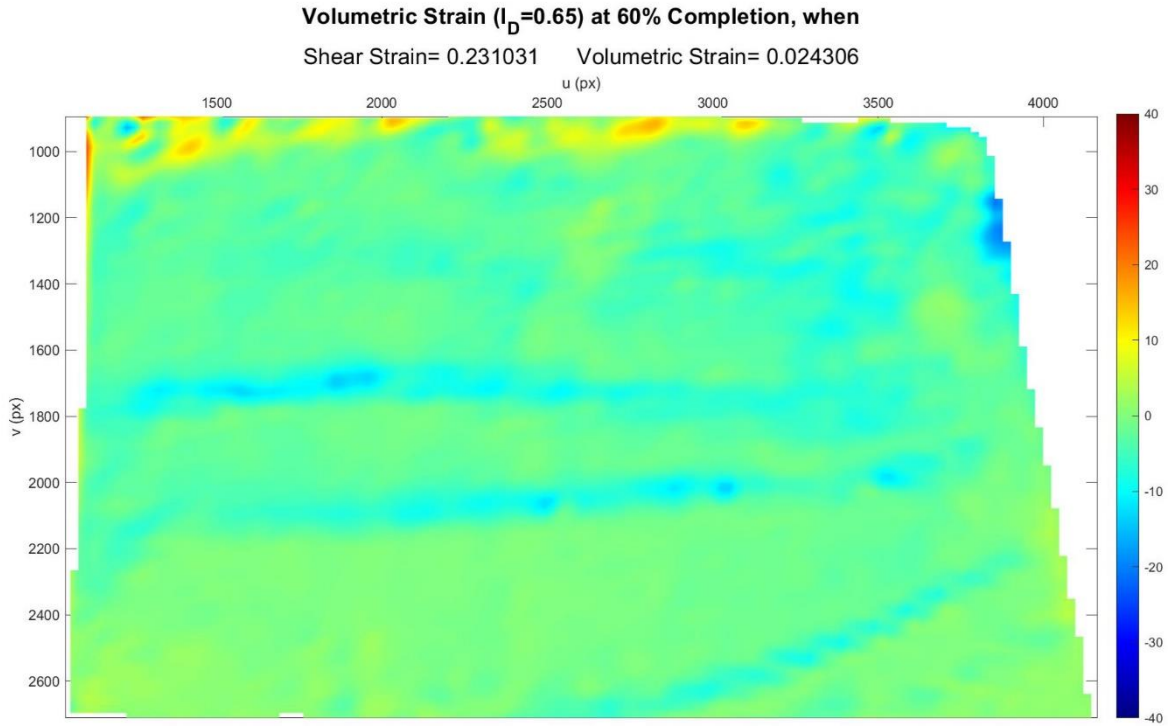

Figure 4.12. Volumetric Strain Field at 60% Completion ($I_D = 0.65$ & $\sigma' = 0.96kPa$).

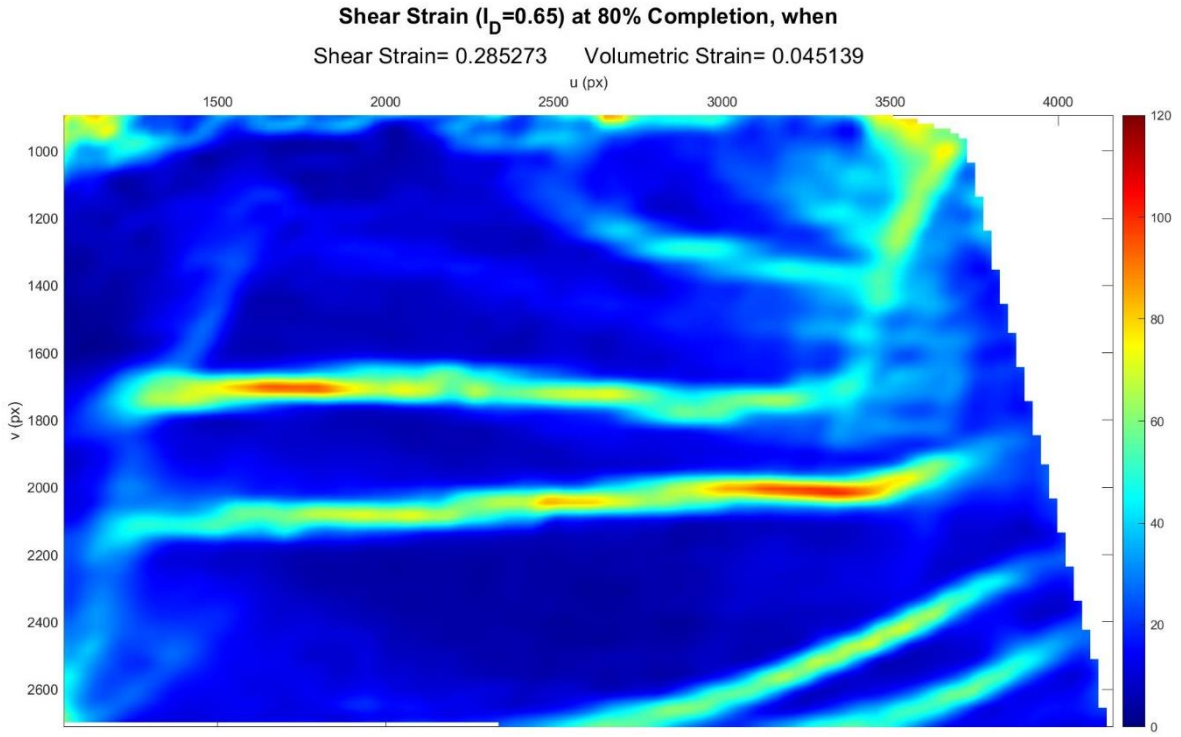

Figure 4.13. Shear Strain Field at 80% Completion ($I_D = 0.65$ & $\sigma' = 0.96\ kPa$).

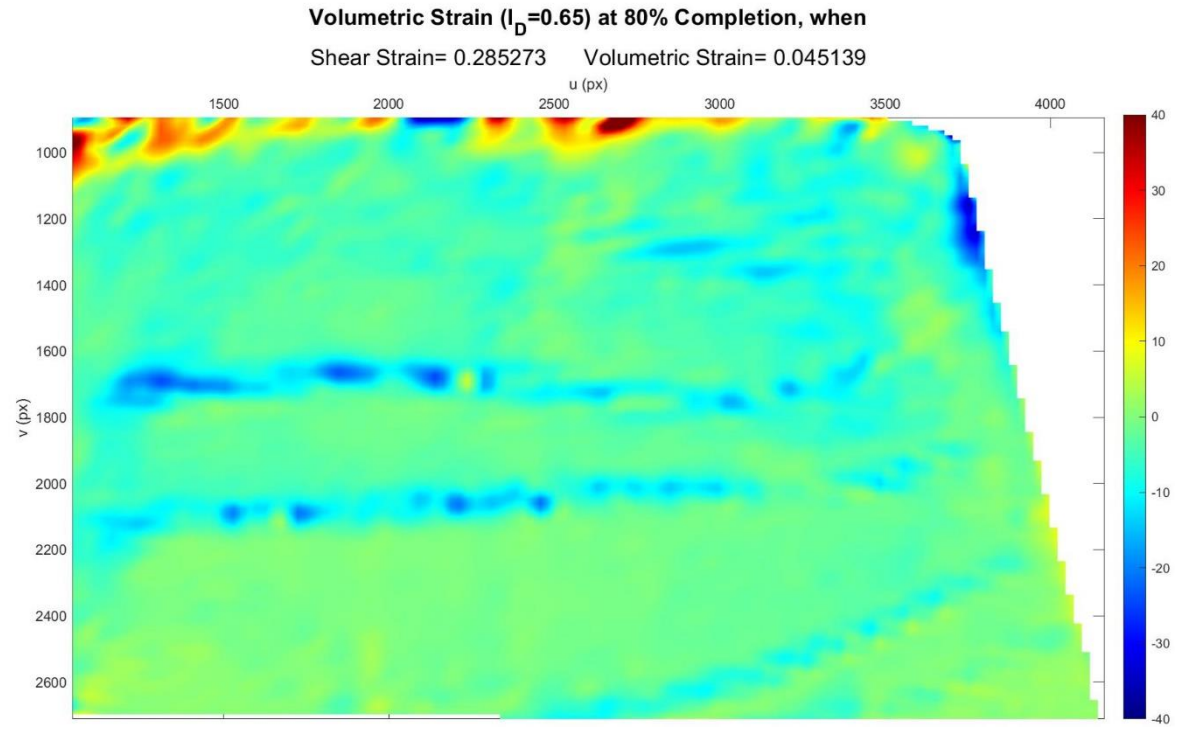

Figure 4.14. Volumetric Strain Field at 80% Completion ($I_D = 0.65$ & $\sigma' = 0.96kPa$).

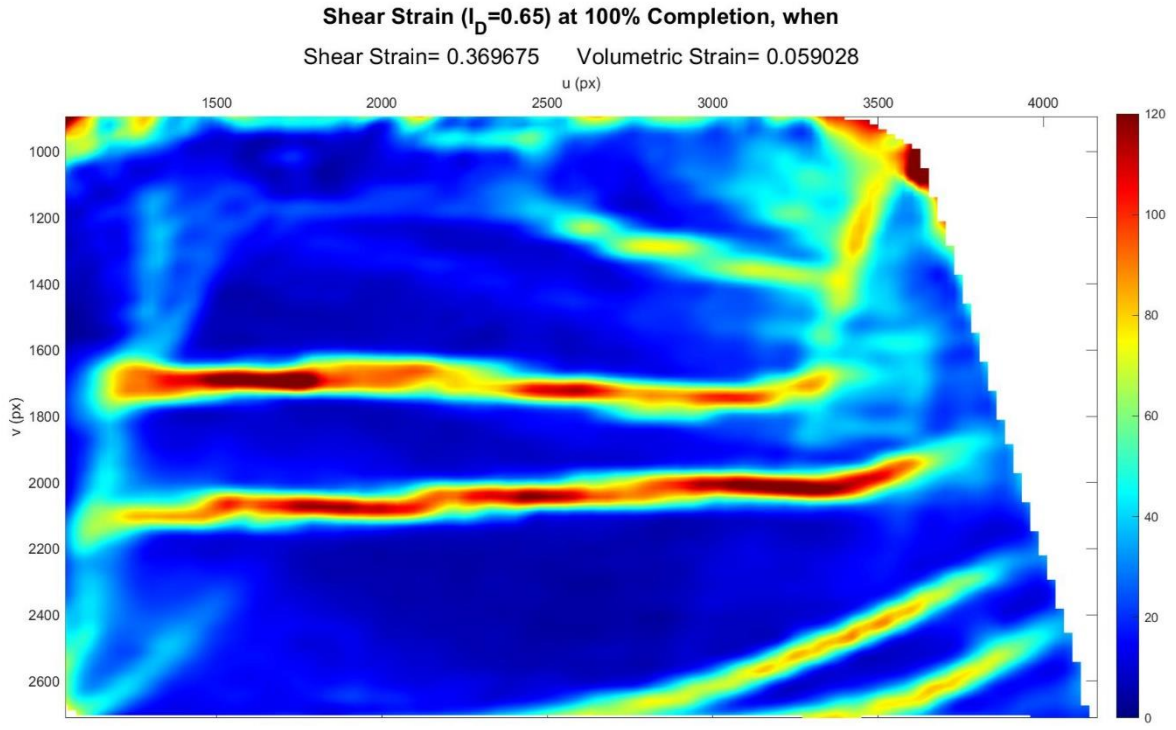

Figure 4.15. Shear Strain Field at 100% Completion ($I_D = 0.65$ & $\sigma' = 0.96\ kPa$).

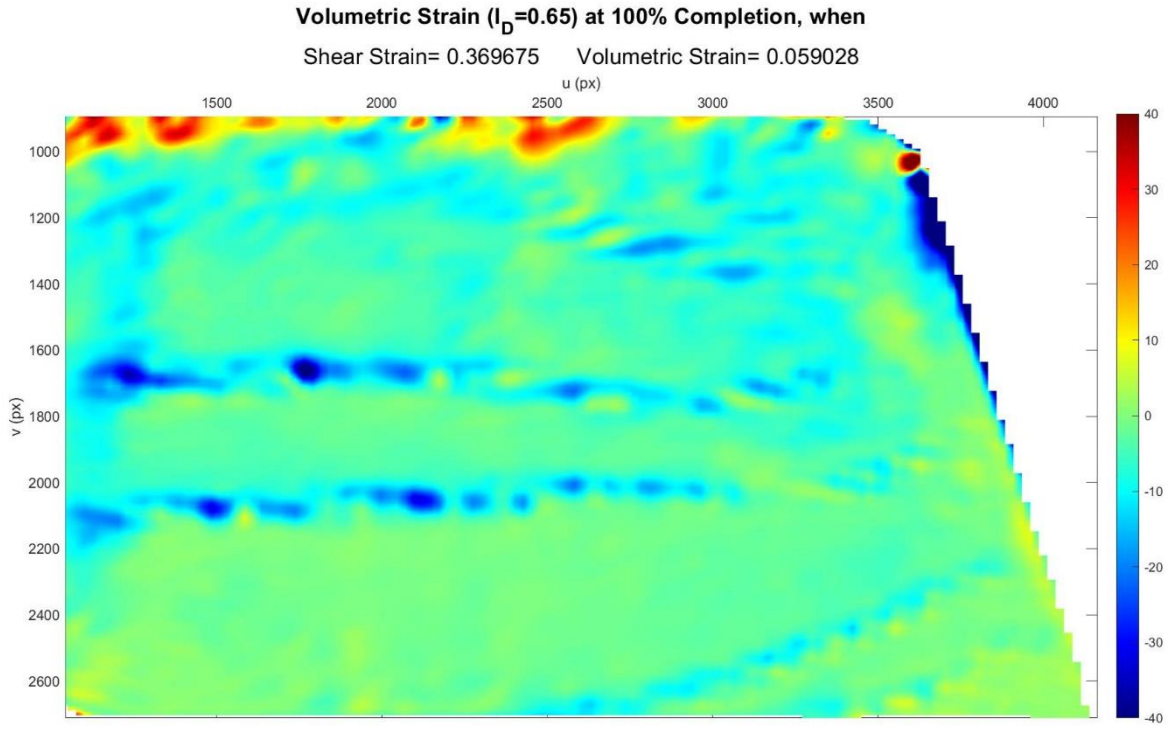

Figure 4.16. Volumetric Strain Field at 100% Completion ($I_D = 0.65$ & $\sigma' = 0.96kPa$).

Taking the analysis results into consideration, lower and upper limits on the color bar were set as 0 and 120 on shear strain field, -40 and 40 on volumetric strain field, respectively. These values are in percentage since GeoPIV-RG produces strain fields in this format i.e., upper limit for shear strain is 1.2 while lower and upper limits for volumetric strain field are -0.4 and 0.4, respectively. Horizontal and vertical position coordinates on the image are given in image space (pixels). Shear strain and volumetric strain values in the titles of strain fields are the strain values corresponding to the relevant step of the analysis and were taken from LS-T-SS test results.

Prior to starting the analysis, Region of Interest (RoI) on which the analysis will be executed was constructed as a bounding rectangle. While the sidewalls of the equipment were rotated to the left during the analysis, soil grains moved with them. Some of the soil grains that remain on the left side thus left RoI. Hence, these subsets were excluded from RoI. In the beginning of the analysis, a gap can be observed on the left side of the strain fields due to exclusion of these subsets. Towards the end of the analysis, due to the movement of soil grains together with the walls, a void started appearing on the right side of RoI while the one on the left side was disappearing as can be seen from Figure 4.7 until Figure 4.16. Not only the soil grains on the left side but also the ones lying on the surface were excluded from RoI since they moved beyond the upper bound of RoI owing to the expansion developed due to shearing.

4.2.2. Effects of Relative Density and Height of the Soil on Shear and Slip Planes

Two evident parallel planes called shear planes on which shear strains are concentrated can easily be seen in Figure 4.15 and Figure 4.16. By examining the strain fields obtained from all analyses that are provided in Appendix, number of shear planes in a field was noticed to be increasing with increasing relative density. The thickness of these planes and the values of shear strain (intensity) on the planes are greater at higher relative densities, as well. Additionally, it was detected that they are affected by the height of the sample as well. For samples with greater heights, not only the number of shear bands but also their thicknesses and shear strain values on these bands are higher. Consequently, the rate of the total area of shear bands to the area of specimen is greater at higher relative densities.

Volumetric strain fields exhibit similar concentration planes that coincide with shear planes. The number, thickness and intensity of the planes are directly proportional to those in shear strain fields. However, both expansion and contraction can be observed on the same shear plane. Since this study focuses on dilatant behavior, the results associated with the subsets at which dilation occurred were provided for the maximum-sheared point (the point with maximum shear strain).

Active slip surfaces occurred due to movement of the soil can be observed in Figure 4.15 starting from the bottom left of the field since the sidewalls rotated to the left. The angle between the slip band and vertical axis was observed to be decreasing with increasing relative density. This is because an increment in relative density results in increase in angle of dilation thereby peak friction angle.

4.2.3. Strain Matrices

Strain matrices containing strain values for every mesh of all images are extracted to observe shear strain behavior with respect to volumetric strain for extreme points and average of RoI. It was observed in Figure 4.15 that minimum shear occurs on the regions just around the shear planes. The mesh that lies on one of the shear planes and has the greatest shear strain value is detected together with the one that is just around the shear plane and has the smallest shear strain value. Figure 4.17 presents shear and volumetric strain values for the subset having maximum shear strain. Particle image velocimetry analysis was conducted on 92 images, volumetric – shear strain combination between each image can be seen in Figure 4.17.

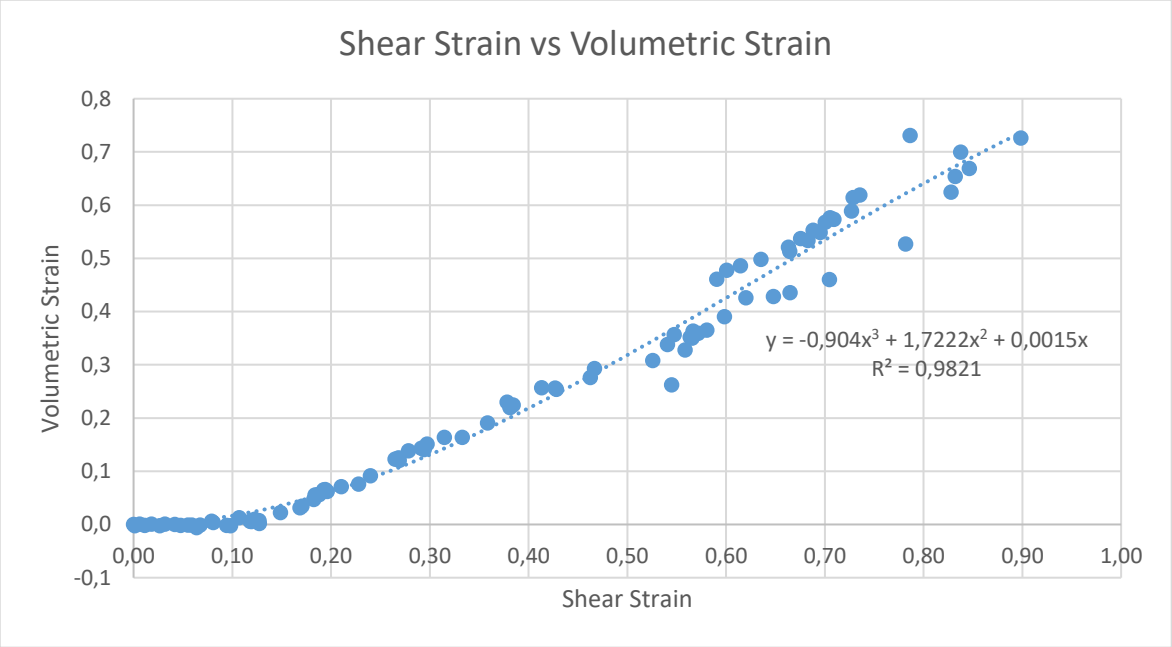

Figure 4.17. Shear Strain versus Volumetric Strain for a Point on Shear Plane (Mesh with Maximum Shear Strain).

As shown in Figure 4.17, shear strain values reach about 90%, while the maximum volumetric strain is approximately 80%. Just like the LS-T-SS test results, the datapoints displayed a perfect match with 3rd order polynomial with $R^2 = 0.9821$. Using the 3rd degree equation of the trendline as explained in Equation (4.5), dilatancy was calculated as 47.6 degrees. The same procedure was followed for the subset at which minimum shear strain occurs.

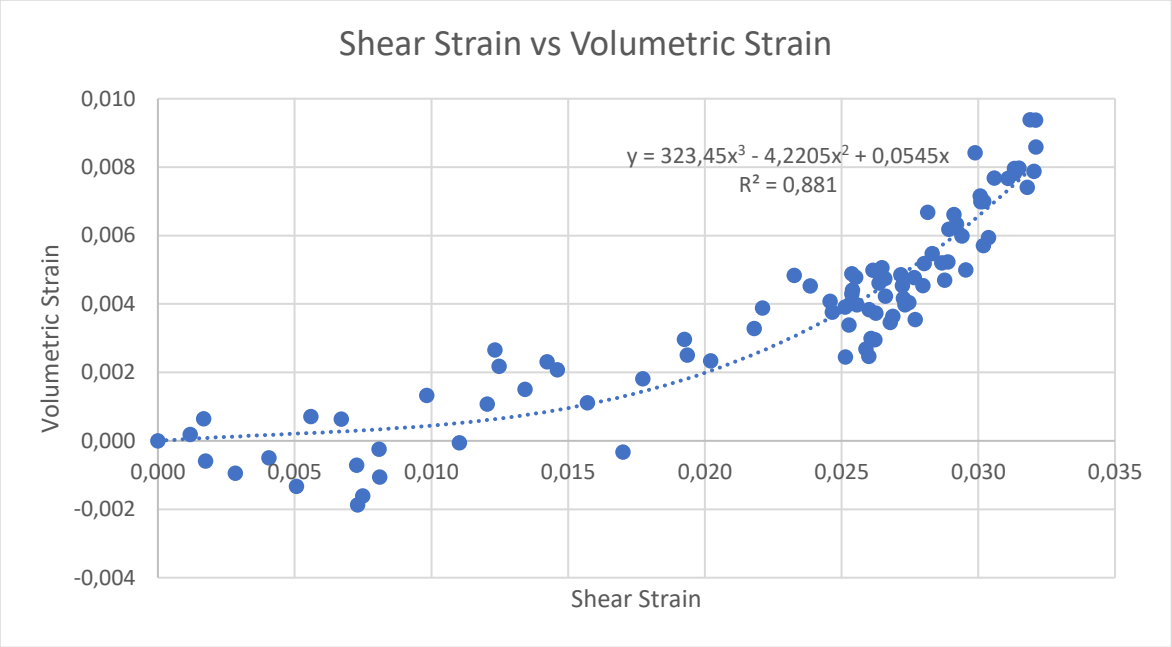

Figure 4.18. Shear Strain versus Volumetric Strain for a Point Just Around Shear Plane (Mesh with Minimum Shear Strain).

Coefficient of determination is generally low for the subset that exhibits minimum shear strain since the fluctuations in the datapoints of minimum-sheared mesh (the mesh with minimum shear strain) is relatively significant. Using Equation (4.5), dilatancy was computed as 2.1 degrees. For inspecting the entire RoI, average strain values of all subsets were evaluated, and the behavior is shown in Figure 4.19.

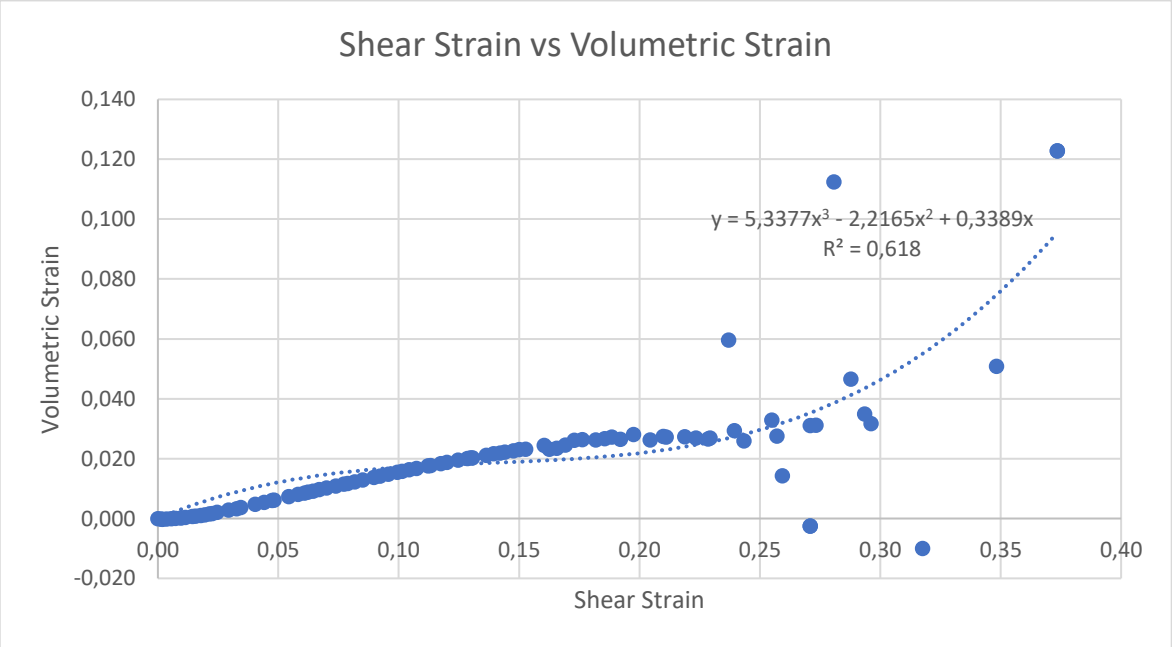

Figure 4.19. Average Shear Strain versus Volumetric Strain of All Subsets.

It is evident from Figure 4.19 that there occur fluctuations at higher shear strain values. This does not develop in most of the analyses. Volumetric – shear strain diagrams in Figure 4.3 and Figure 4.19 are slightly similar to each other. Shear strain values in both diagrams expands up to approximately 0.4 whereas volumetric strain values in the two diagrams are considerably different from each other even though the fluctuations at higher shear strains were ignored.

4.2.4. Comparison of LS-T-SS Test and PIV Analysis

As mentioned previously, some soil grains were excluded from RoI and the average does not include them. Thus, for the entire region, the result provided in LS-T-SS Test Results part is more reliable than the average obtained as a result of GeoPIV-RG analysis.

Figure 4.17, Figure 4.18 and Figure 4.19 represent the extreme points and the average of the entire region. By comparing them, it can be deducted that the point on one of the shear planes got extremely high strain values while the one just around the shear plane was much more stable so that the maximum shear strain was practically 3% of that of the maximum-sheared subset and 10% of that of the average.

Dilatancy values of the maximum and minimum-sheared subsets were listed in Table 4.1 together with those obtained through LS-T-SS tests.

Table 4.1. Sample Dilatancy Values Obtained from LS-T-SS Test and PIV Analysis.

Parameter	Value
ψ_{peak} (LS-T-SS Test)	15.3°
ψ_{max} (PIV)	47.6°
ψ_{min} (PIV)	2.1°

It can be seen in Figure 4.17 that the soil in maximum-sheared subset exhibits almost 80% expansion in the volume. Taking this much dilation into consideration, the dilatancy angle of 47.6° is very high as expected.

Dense soils exhibit dilatant behavior unless the level of stress applied on the soil is not high enough to depress the expansion. In this study, the stress on the specimen was the pressure exerted by the soil itself, without any additional loading on the soil. Hence, expansion could be monitored both in LS-T-SS test and particle image velocimetry analysis. However, the data assembled from PIV analyses did not display expected contraction prior to expansion of the soil. LS-T-SS tests, on the other hand, revealed the decrease in the volume of the soil before the increase. Angles of dilation taken from LS-T-SS tests and PIV analyses are presented in Table 4.2.

Table 4.2. Dilatancy Values Obtained from LS-T-SS Tests and PIV Analyses.

Peak Dilatancy, ψ_p	Maximum Dilatancy, ψ_{max}	Minimum Dilatancy, ψ_{min}	Average Dilatancy, ψ_{ave}	Peak Dilatancy, ψ_p	Maximum Dilatancy, ψ_{max}	Minimum Dilatancy, ψ_{min}	Average Dilatancy, ψ_{ave}
5.8	36.7	0.1	5.8	11.0	35.7	-0.1	0.2
6.2	37.3	-0.2	5.7	11.2	41.9	-0.3	10.6
6.6	30.2	0.6	-1.3	11.3	40.7	0.2	1.6
6.9	36.2	0.3	7.7	11.5	39.1	0.3	24.1
7.2	27.9	0.3	7.2	12.1	36.4	-2.3	-48.4
7.7	36.6	-0.2	2.1	12.5	46.7	0.3	5.3
7.9	27.7	0.4	-1.1	12.6	38.4	0.5	4.6
8.0	31.5	-1.5	9.6	14.8	57.2	1.2	0.8
8.3	46.4	-1.0	-3.1	15.3	47.6	2.1	1.8
8.7	33.1	0.7	-1.0	15.4	41.6	-5.8	-8.8
9.0	35.8	-2.1	-1.0	15.5	39.5	-2.0	53.2
9.7	42.5	1.6	-2.6	15.8	37.3	0.5	-1.8
9.8	47.3	4.2	7.4	16.0	44.1	0.3	3.6
10.0	43.6	0.3	-6.4	16.2	40.3	0.1	4.0
10.1	39.7	0.4	7.1	16.4	35.2	3.1	11.0
10.3	38.6	1.8	18.3	18.3	53.9	0.1	1.0
10.7	40.3	0.5	38.9	18.4	49.9	-0.5	5.3
11.0	43.0	-0.9	2.5	20.7	46.0	3.9	-3.3

4.3. Peak Friction Angle Determination

Peak friction angle tests were performed on Kilyos sand under relative density and stress conditions computed while LS-T-SS tests were being conducted. After the soil was compacted into the mold to reach the desired relative density and height (thereby stress)

conditions, the mold started to be tilted until a small slope failure occurs. The angle measured by an accelerometer was then recorded as peak friction angle.

In Giampa and Bradshaw's method, the mold was completely filled. Since the level of stress computed in LS-T-SS tests tried to be obtained in this study, the mold was filled up to a predetermined level. In order to investigate if this application produces any error, some of the tests were conducted with the mold completely filled with sand. The results obtained in both conditions were noticed to be the same. Hence, the sample was poured into the mold so that the stress requirement is satisfied.

The results will be plotted in the following sections, following to determination of critical state friction angle.

4.4. Critical State Friction Angle Determination

Using the method suggested by Santamarina and Cho (2001), critical state friction angle was assessed. Despite the fact that it is not dependent on parameters as relative density or pressure, the test was repeated 5 times to increase the accuracy. The cylinder was tilted until passed 60° and brought back to vertical position very slowly. The angle of repose was measured by a protractor and recorded as critical state friction angle.

The results and critical state friction angle determination are provided Table 4.3.

Table 4.3. Critical State Friction Angle Test Results.

Test Number	Critical State Friction Angle, φ_c' (deg)
1	33.2
2	33.5
3	33.4
4	33.3
5	33.5
Average	33.38 ≅ 33.4

As shown in Table 4.3, critical state friction angle for Kilyos sand was assessed as $\varphi_c' = 33.4°$. After conducting the tests with various amounts of water, it was deducted that the amount of water does not influence critical state angle of friction.

4.5. Determination of Soil Constants

Once peak angle of dilation, peak and critical state friction angles were achieved, φ_p' was plotted against ψ_p.

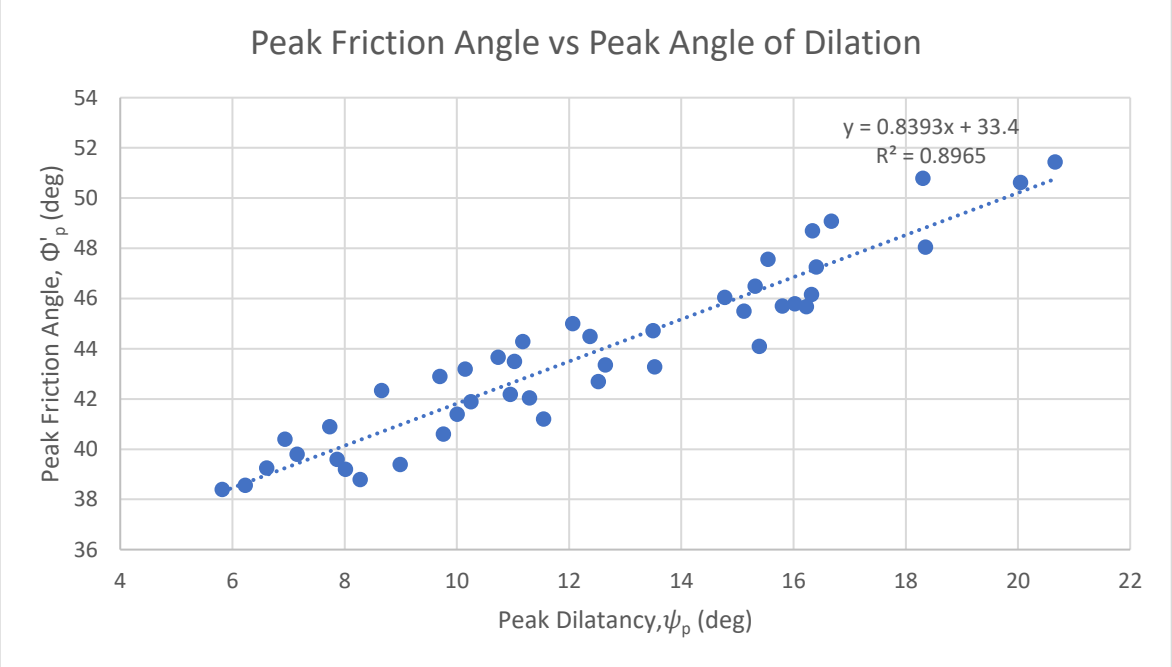

Figure 4.20. Peak Angle of Friction Against Peak Dilatancy Angle.

By adjusting y-intercept as critical state friction angle, the following equation was obtained:

$$\varphi'_p = 0.8393\,\psi_p + 33.4. \quad (4.9)$$

It is noticed that the same datapoints yield the same equation with no intercept. It is hence concluded that the critical state friction angle assessed by CS test is equal to the critical state friction angle obtained by plotting peak angle of friction against peak angle of dilation. Considering that the line fitting parameter is the slope of the graph in Figure 4.20, it is found

as $r = 0.8393 \cong 0.84$ through Equation (4.9). The left side of Equation (3.1) is then plotted against relative density.

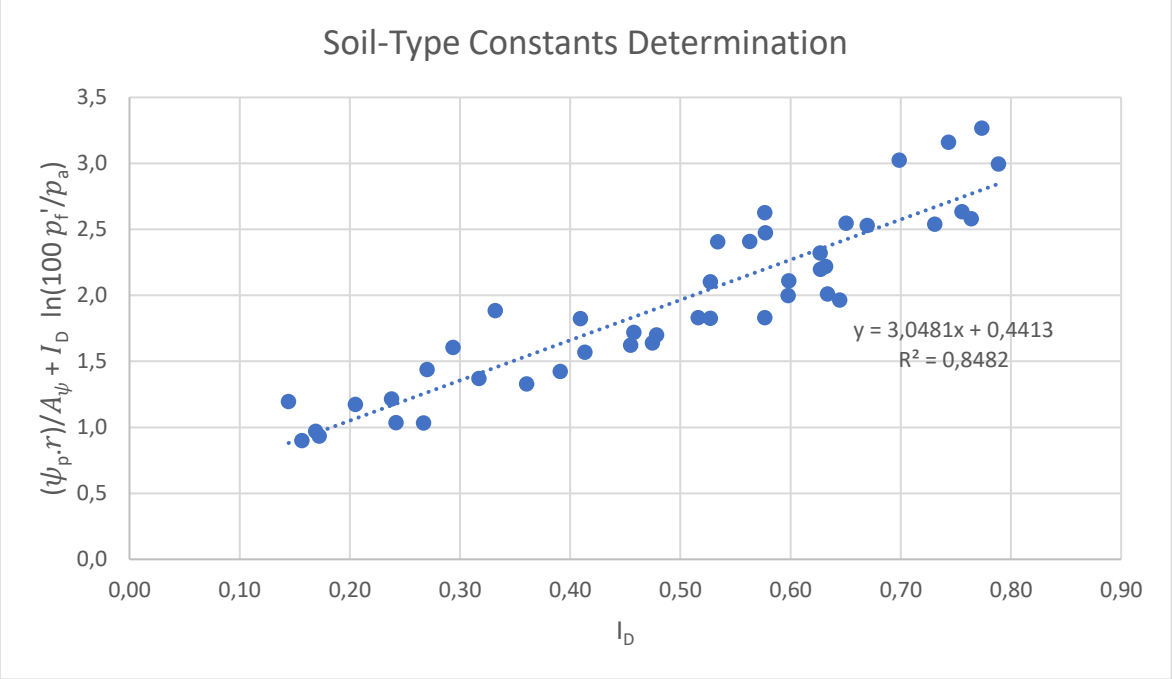

Figure 4.21. Soil-Type Constants (Q and R) Determination.

The equation of linear trendline is found as following:

$$\frac{\psi_p.r}{A_\psi} + I_D \ln\left(\frac{100\ p_f'}{p_a}\right) = 3.0481\ I_D - (-0.4413). \qquad (4.10)$$

Bolton's dilation index coefficients Q and R defined in Equation (2.6) are recorded as the slope and negative of y-intercept of the graph in Figure 4.21, respectively. Following table presents the constants obtained from all tests that were performed within the scope of this thesis. Through Equation (4.10), the index coefficients are determined $Q = 3.0488 \cong 3.05$ and $R = -0.4415 \cong -0.44$.

The same graph is plotted with y-intercept of –1 to determine the value of Q when R=1.

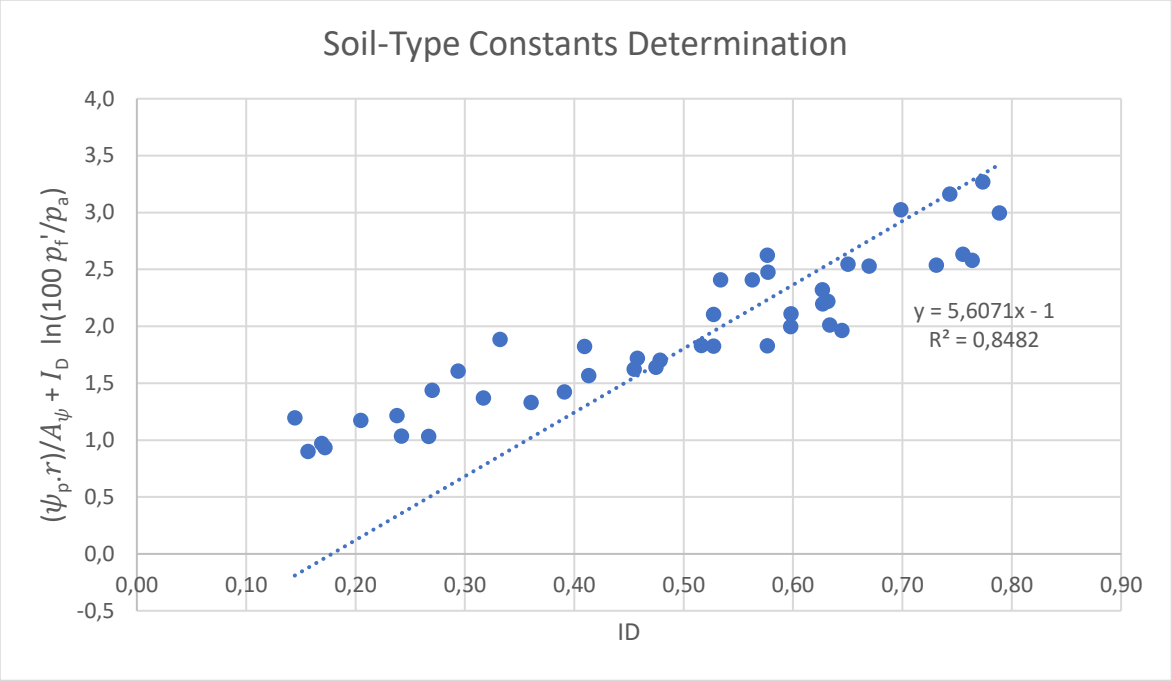

Figure 4.22. Soil-Type Constant (Q) Determination with R=1.

As shown in Figure 4.22, the value of Q is obtained as 5.61 when R is set to 1. The constants r, Q and R are presented in Table 4.4.

Table 4.4. r, Q and R Values of Kilyos Sand under Plain Strain Conditions.

Coefficient	Value	Value (R=1)
r	0.84	0.84
Q	3.05	5.61
R	-0.44	1

5. CONCLUSIONS

The goals of this study are threefold:

- Investigating the validity of Bolton (1986) stress – dilatancy equations for very low stress levels.
- Examining the mechanism of strain concentration in simple shear conditions
- Evaluating the possibility of using practical and simple tests to obtain the constants of stress – dilatancy equations of Bolton (1986).

It is very difficult to conduct triaxial tests under low confining pressure levels. Alternative practical methods were thus used in this study. Accordingly, 3 different types of tests were performed on Kilyos sand under very low stress levels, first of which was done with the aim of finding peak angle of dilation. An equipment made of transparent plexiglass was designed together with the electronic component. Distance sensors, accelerometers, rtc sensor, SD card module and LCD screen were connected to an Arduino with proper wiring. Moreover, the necessary code for Arduino was developed. 44 tests were conducted using the equipment with relative densities ranging from 14% to 79% and confining pressures resulted solely from self-weight of the soil. The sidewalls of the equipment were rotated to one side by the same amount so that no change in specimen's cross-section area in horizontal plane occurs throughout the tests. As the sidewalls were rotated, both the angle and the specimen's height were being gathered progressively. At the end of each test, by plotting volumetric strain against shear strain, it was discovered that volumetric strain – shear strain behavior of the soil can be represented very well with a 3rd degree polynomial. Using first and second order derivatives of the equation, the value of dilatancy was then calculated at the point with maximum slope and recorded as peak dilatancy angle. Images were captured during the tests to investigate the deformations and strain concentrations in the sample, continuously.

The second type of the tests was the test done with the aim of obtaining peak friction angle. A rectangular mold having the dimensions 15 cm by 20 cm was used in the tests. The sand was tested under the same relative density and pressure conditions with those in LS-T-SS tests in order to correlate peak dilatancy and peak friction angle. After the specimen was

compacted into the mold, it was tilted until a small slope failure was observed. The angle at that point was recorded as peak friction angle.

The third and the final test was a simple method to estimate critical state friction angle. In this method, the soil was poured into a graduated cylinder with water until 1000 ml and then started to be tilted. After it passed 60 degrees, it was rotated to its original vertical position slowly. The angle of repose in the middle region was recorded as critical state friction angle since the angle near the walls may be different due to effect of friction. Critical state friction angle was assessed as $\varphi_c = 33.4°$.

After all tests were realized, φ'_p was plotted against ψ_p. It was noticed that the y-intercept of the plot is equal to the critical state friction angle obtained by CS test. This is an implication of the results obtained from LS-T-SS, peak friction angle and CS tests being accurate.

Line fitting parameter (r) which is the slope of the line of best fit was then obtained as 0.84. It was suggested as 0.8 by Bolton (1986) for all soil types. With (r) determined, the left side of Equation (3.1) was plotted against relative density. Dilation index coefficients were then determined as $Q = 3.05$ and $R = -0.44$. Additionally, it was determined that $Q = 5.61$ when $R = 1$. These coefficients were suggested as $Q = 10$ and $R = 1$ by Bolton (1986) for all soil types.

Chakraborty and Salgado (2010) investigated stress – dilatancy coefficients at low effective stress levels on Toyoura Sand. Under plain strain conditions, the minimum mean effective confining pressure exerted on the specimen is 15.7 kPa. As shown in Equation (2.13), Q is found as 7.1 when the stress is equated to zero.

The results of the tests conducted in this study showed a good agreement with the suggestion of Bolton when the line fitting parameter (r) is considered. Dilation index coefficients (Q) and (R), on the other hand, are remarkably different from those suggested by Bolton and Chakraborty and Salgado. In this study, the stress level is always less than $1\ kPa$. The difference between stress – dilatancy coefficients obtained in this study and

Bolton's and Chakraborty and Salgado's studies is resulted from the difference between stress levels.

It was concluded that, by comparison of the results, dilation index coefficients obtained at very low-stress levels are considerably different from those Bolton and Chakraborty and Salgado proposed for the samples at elevated pressures.

Shear and volumetric strain fields, which reveal the deformations and evolution of shear planes and active slip surfaces, were produced via PIV analyses. The number, intensity and the thickness of shear planes were noticed to be increasing not only with increasing relative density but also with increasing height of the sample. Consequently, it was concluded that the ratio of total thickness of shear bands to total area increases with increasing relative density. Moreover, one active slip band was seen at the bottom left of RoI since the sidewalls rotated to the left. The angle the slip band makes with vertical axis was detected to be decreasing with increasing relative density of the soil. Volumetric strain fields exhibited similar concentration planes at the exact same location, as shown in Appendix C. However, both positive and negative volumetric strains could be seen on the same plane, unlike shear strain fields. Hence, although shear strain values concentrate on shear planes, volumetric strain evidently does not have a pattern. Shear strain fields also revealed that minimum shear strain occurs just around the shear planes.

Strain matrices containing shear and volumetric strains of all subsets for all images were created and volumetric strain was plotted against shear strain for the subsets at which maximum and minimum shear strain occurred. Just like the results obtained from LS-T-SS tests, the datapoints of maximum-sheared subsets were observed to show a perfect match with 3rd degree polynomial, having coefficients of determination greater than 95%. Having the results of both LS-T-SS tests and PIV analyses displayed very good match, it was deducted that shear strain versus volumetric strain graph behaves as 3rd degree polynomial. Moreover, dilatancy values at the points with maximum shear strain increase proportionally with peak dilatancy angles obtained in LS-T-SS tests.

Recommendations

- LS-T-SS tests can be done under the same relative density and confining pressure conditions with various rates of rotation in order to see the dependence of dilatancy on the speed of the shearing.
- The LS-T-SS device can be supported by addition of a motor so that it is rotated automatically. In this way, the tests can be made in strain-controlled mode.
- The scope of the research can be expanded by the tests conducted on different types of sands to verify the equipment.
- GeoPIV-RG analyses can be performed on the soils with the same relative density and different heights to reveal the effect of height on shear planes.
- GeoPIV-RG analyses can be performed on the soils having the same height and different stress levels to reveal the effect of stress on shear planes.
- Active slip planes can be clearly seen in strain fields obtained from PIV analyses. A study concentrated on the angle of these bands can be made to establish a dependence between slip surface angle and angle of dilation, thereby peak friction angle.
- Influence of sample size on strain localization and number and orientation of intense shearing can be investigated.
- Tests can be repeated at elevated stress conditions to understand the influence of stress on response.

REFERENCES

ASTM D4253-00, 2000, "Standard Test Methods for Maximum Index Density and Unit Weight of Soils Using a Vibratory Table", *ASTM International, West Conshohocken, PA.*

ASTM D4254-00, 2000, "Standard Test Methods for Minimum Index Density and Unit Weight of Soils and Calculation of Relative Density", *ASTM International, West Conshohocken, PA.*

Bolton, M. D., 1986, "The Strength and Dilatancy of Sands", *Geotechnique,* Vol. 36, No. 1, pp. 65-78.

Cagdas, A. and O. Cinicioglu, 2019, "Kohezyonsuz Zeminlerin Tane Dağılım ve Şekil Özelliklerinin Aktif Göçme Yüzeyi Geometrisine Etkileri", *Teknik Dergi*.

Chakraborty, T. and R. Salgado, 2010, "Dilatancy and Shear Strength of Sand at Low Confining Pressures", *Journal of Geotechnical and Geoenvironmental Engineering*, pp. 527-532.

Cinicioglu, O. and A. Abadkon, 2015, "Dilatancy and Friction Angles Based on In Situ Soil Conditions", Journal of Geotechnical and Geoenvironmental Engineering, Vol. 141, No. 4, pp. 601-4019.

De Josselin De Jong, G., 1976, "Rowe's Stress-Dilatancy Relation Based on Friction", Geotechnique, Vol. 26, No. 3, pp. 527-534.

Giampa, J. and A. Bradshaw, 2018, "A Simple Method for Assessing the Peak Friction Angle of Sand at Very Low Confining Pressures", *Geotechnical Testing Journal*, Vol. 41, No. 4, pp. 639-647.

Li, X. and Y. Dafalias, 2000, “Dilatancy for Cohesionless Soils”, *Geotechnique*, Vol. 50, No. 4, pp. 449-460.

Reynolds, O., 1885, “LVII. On the Dilatancy of Media Composed of Rigid Particles in Contact. With Experimental Illustrations”, *Philosophical Magazine*, Series 5.

Rowe, P. W., 1962, “The Stress-Dilatancy Relation for Static Equilibrium of an Assembly of Particles in Contact”, *Proceedings of the Royal Society A: Mathematical, Physical and Engineering Sciences*.

Sadrekarimi, A. and S. M. Olson, 2011, “Critical State Friction Angle of Sands”, *Geotechnique*, Vol. 61, No. 9, pp. 771-783.

Santamarina, J. and G. Cho, 2001, “Determination of Critical State Parameters in Sandy Soils - Simple Procedure”, Geotechnical Testing Journal, Vol. 24, No. 2, pp. 185-192.

Schanz, T. and P. Vermeer, 1996, “Angles of Friction and Dilatancy of Sand”, *Geotechnique*, Vol. 46, No. 1, pp. 145-151.

Stainer, S., J. Blaber, W. Take and D. White, 2016, “Improved Image-Based Deformation Measurement for Geotechnical Applications”, *Canadian Geotechnical Journal*, Vol. 53, No. 5, pp. 727-739.

Tordesillas, A., C. Steer and D. Walker, 2014, “Force chain and contact cycle evolution in a dense granular material under shallow penetration”, *Nonlinear Processes in Geophysics*, Vol. 21, No. 2, pp. 505-519

Taylor, D.W., 1948, “Fundamentals of Soil Mechanics", *John Wiley and Sons Inc.*, New York.

Vaid, Y. P. and S. Sasitharan, 1992, “The strength and dilatancy of sand”, *Canadian Geotechnical Journal*, Vol. 29, No. 3, pp. 522-526.

White, D. J., W. A. Take, and M. D. Bolton, 2003, “Soil Deformation Measurement Using Particle Image Velocimetry (PIV) and Photogrammetry", *Geotechnique*, Vol. 53, No. 7, pp. 619-631

APPENDIX A: ARDUINO CODE DEVELOPED FOR DILATANCY DETERMINATION

```
////////////////////////////////////////////////////////////////////////
//                                                                    //
// This code is written to compute the dilatancy angle of             //
// cohesionless soils by using a new method                           //
//                                                                    //
////////////////////////////////////////////////////////////////////////

#include <Wire.h>
#include <DS3231.h>
#include <SPI.h>
#include <SD.h>
#include <VL53L0X.h>

DS3231  rtc(SDA, SCL);
VL53L0X sensor1,sensor2,sensor3;// define objects for sensors

#define TCAADDR 0x70
const int MPUADDR = 0x69;

typedef struct {
    float X, Y, Z;
}Vector;

typedef struct {
    int sensor1, sensor2, sensor3;
}Distance;

Vector K;
Vector gForceVector;
Vector gForceVector1;
Vector gForceVector2;
Vector gForceVectorAverage;
Vector tempVector;

Distance distance, distanceData;
```

```
long accelX, accelY, accelZ;
float gForceX, gForceY, gForceZ;
float angle;

String time;
String dataString1 = "";
String dataString2 = "";
String dataString3 = "";
const int chipSelect = 10;

Vector GetMpuValue(const int MPUADDR);
Vector avaregeVectors(Vector vectorA,Vector vectorB);
float dotProduct(Vector vectorA,Vector vectorB);
float magnitude(Vector vector);

void setup() {
  // put your setup code here, to run once:
 rtc.begin();
 sensorInit();
 Serial.begin(38400);

  // see if the card is present and can be initialized:
  if (!SD.begin(chipSelect)) {
    Serial.println("Card failed, or not present");
    // don't do anything more:
    return;
  }
  Serial.println("card initialized.");
  Wire.begin();

  K.X=1;
  K.Y=0;
  K.Z=0;

  Serial.println("init done");

}

void loop() {
 time = rtc.getTimeStr(); // get current time
```

```
// Get acceleration sensor values
tcaselect(0);
gForceVector1 = GetMpuValue(MPUADDR);
tcaselect(1);
gForceVector2 = GetMpuValue(MPUADDR);

//calculate angle
gForceVector = avaregeVectors(gForceVector1,gForceVector2);
angle =
degrees(acos(dotProduct(gForceVector,K)/magnitude(gForceVector)));

distanceData = getDistance();//read distance sensor values

Serial.println();
Serial.println(time);

Serial.print("angle: ");
Serial.println(angle);

Serial.println("MPU1");
Serial.print("X: ");
Serial.print(gForceVector1.X);
Serial.print(" Y: ");
Serial.print(gForceVector1.Y);
Serial.print(" Z: ");
Serial.print(gForceVector1.Z);
Serial.println();

Serial.println("MPU2");
Serial.print("X: ");
Serial.print(gForceVector2.X);
Serial.print(" Y: ");
Serial.print(gForceVector2.Y);
Serial.print(" Z: ");
Serial.print(gForceVector2.Z);
Serial.println();

Serial.print("Distance 1: ");
Serial.print(distanceData.sensor1);
```

```
 Serial.print(" Distance 2: ");
 Serial.print(distanceData.sensor2);
 Serial.print(" Distance 3: ");
 Serial.print(distanceData.sensor3);
 Serial.println();


  // append sesnsor values to stirng:
  dataString1 =
String(gForceVector1.X)+","+String(gForceVector1.Y)+","+String(gForceVect
or1.Z)+",";
  dataString2 =
String(gForceVector2.X)+","+String(gForceVector2.Y)+","+String(gForceVect
or2.Z)+",";
  dataString3 =
String(distanceData.sensor1)+","+String(distanceData.sensor2)+","+String(
distanceData.sensor3)+","
  +String(angle)+","+time;

  // write collected data to SD card
  File dataFile = SD.open("datalog.txt", FILE_WRITE);
  // if the file is available, write to it:
  if (dataFile) {
    dataFile.print(dataString1);
    dataFile.print(dataString2);
    dataFile.println(dataString3);
    dataFile.close();
    Serial.println(dataString1);
    Serial.println(dataString2);
    Serial.println(dataString3);
    delay(10);
  }
  // if the file isn't open, pop up an error:
  else {
    Serial.println("error opening datalog.txt");
  }
  delay(100);
}
void tcaselect(uint8_t i) {
  if (i > 7) return;
```

```
  Wire.beginTransmission(TCAADDR);
  Wire.write(1 << i);
  Wire.endTransmission();
}
Vector avaregeVectors(Vector vectorA,Vector vectorB){
  tempVector.X = (vectorA.X+vectorB.X)/2;
  tempVector.Y = (vectorA.Y+vectorB.Y)/2;
  tempVector.Z = (vectorA.Z+vectorB.Z)/2;
  return tempVector;
}
void mpuInit(const int MPUADDR){
  Wire.begin();
  Wire.beginTransmission(MPUADDR);
  Wire.write(0x6B);
  Wire.write(0b00000000);
  Wire.endTransmission();
  Wire.beginTransmission(MPUADDR);
  Wire.write(0x1C);
  Wire.write(0b00000000);
  Wire.endTransmission();
}
Vector GetMpuValue(const int MPUADDR){
  Wire.beginTransmission(MPUADDR);
  Wire.write(0x3B);
  Wire.endTransmission();
  Wire.requestFrom(MPUADDR,6);
  while(Wire.available() < 6);
  accelX = Wire.read()<<8|Wire.read();
  accelY = Wire.read()<<8|Wire.read();
  accelZ = Wire.read()<<8|Wire.read();
  gForceX = accelX / 16384.0;
  gForceY = accelY / 16384.0;
  gForceZ = accelZ / 16384.0;
  gForceVector.X = gForceX;
  gForceVector.Y = gForceY;
  gForceVector.Z = gForceZ;
  delay(10);
  return gForceVector;
}
```

```
float dotProduct(Vector vectorA,Vector vectorB){
 return vectorA.X*vectorB.X+vectorA.Y*vectorB.Y+vectorA.Z*vectorB.Z;
}
float magnitude(Vector vector){
 return sqrt(sq(vector.X)+sq(vector.Y)+sq(vector.Z));
}
Distance getDistance(){
  distance.sensor1 = sensor1.readRangeSingleMillimeters();// get distance
for sensor 1
  distance.sensor2 = sensor2.readRangeSingleMillimeters();// get distance
for sensor 2
  distance.sensor3 = sensor3.readRangeSingleMillimeters();// get distance
for sensor 3
  return distance;
}
void sensorInit(){

  pinMode(5, OUTPUT);
  pinMode(6, OUTPUT);
  pinMode(7, OUTPUT);
  digitalWrite(5, LOW);
  digitalWrite(6, LOW);
  digitalWrite(7, LOW);

  Wire.begin();

  //SENSOR
  digitalWrite(5, HIGH);
  sensor1.init(true);
  sensor1.setAddress(0x30);
  Serial.println("set address 0x30 for first sensor");
  delay(10);

  digitalWrite(6, HIGH);
  sensor2.init(true);
  sensor2.setAddress(0x31);
  Serial.println("set address 0x31 for second sensor");
  delay(10);

  digitalWrite(7, HIGH);
```

```
  sensor3.init(true);
  sensor3.setAddress(0x32);
  Serial.println("set address 0x32 for third sensor");
  delay(10);

  sensor1.setTimeout(500);
  sensor2.setTimeout(500);
  sensor3.setTimeout(500);

  tcaselect(0);
  mpuInit(MPUADDR);
  tcaselect(1);
  mpuInit(MPUADDR);
}
```

APPENDIX B: VOLUMETRIC STRAIN VS SHEAR STRAIN DIAGRAMS OBTAINED FROM LS-T-SS TESTS

Volumetric strain against shear strain diagram for all LS-T-SS tests are presented in the following figures.

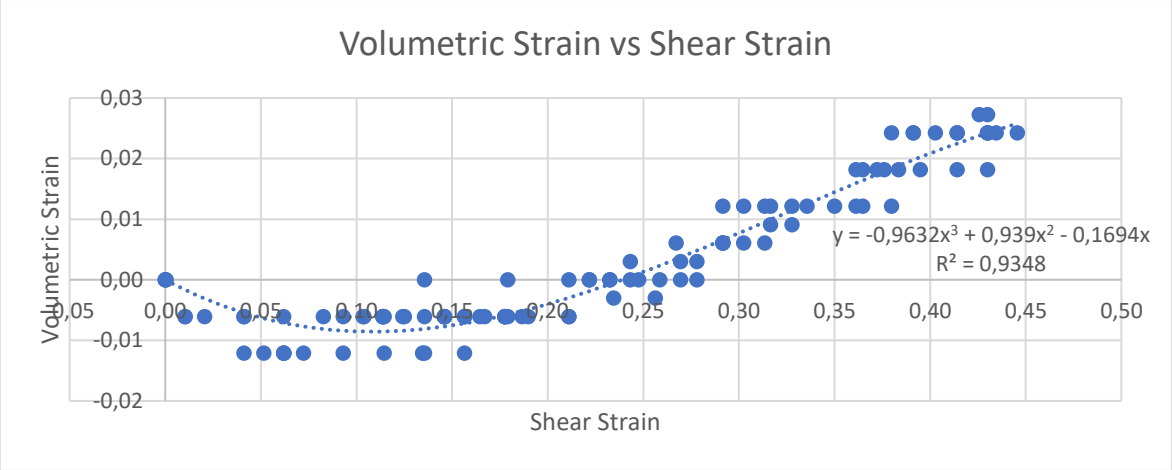

Figure B.1. Volumetric Strain vs Shear Strain Diagram ($I_D = 0.14$ & $\sigma' = 0.49\ kPa$).

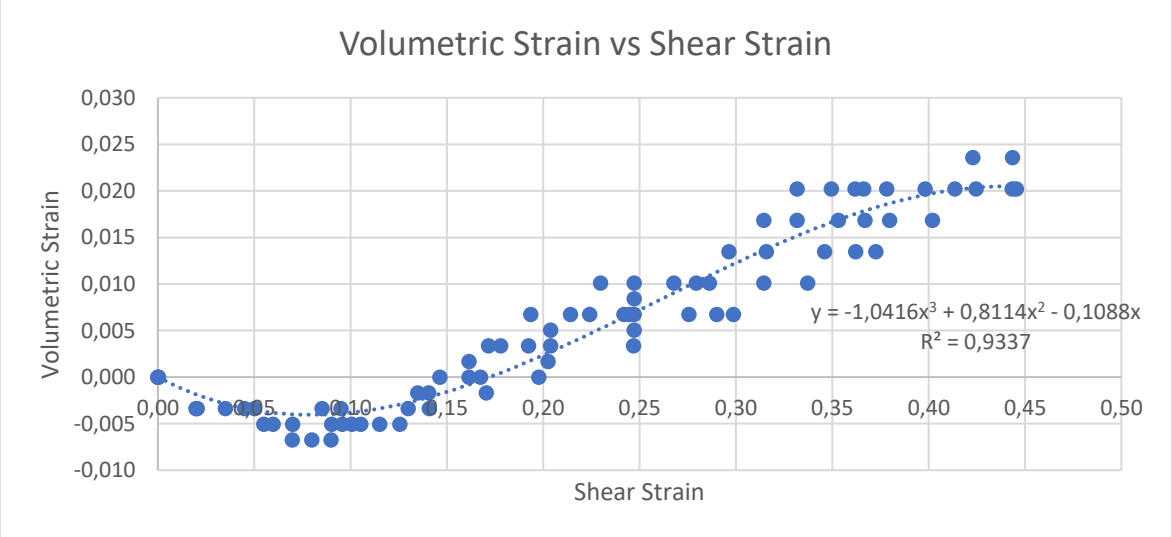

Figure B.2. Volumetric Strain vs Shear Strain Diagram ($I_D = 0.16$ & $\sigma' = 0.61\ kPa$).

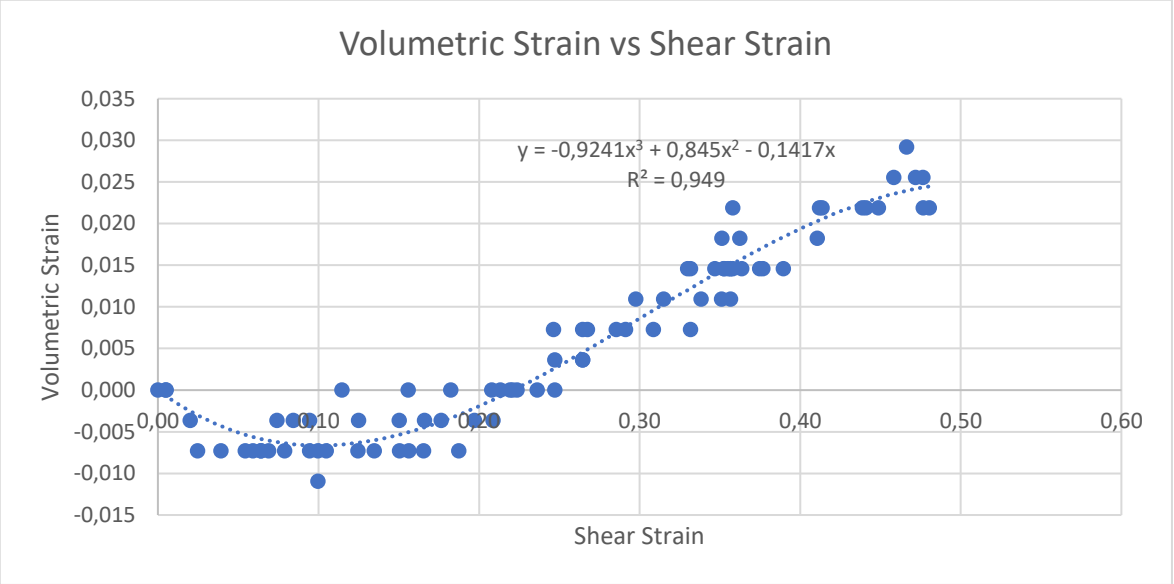

Figure B.3. Volumetric Strain vs Shear Strain Diagram ($I_D = 0.17$ & $\sigma' = 0.44\ kPa$).

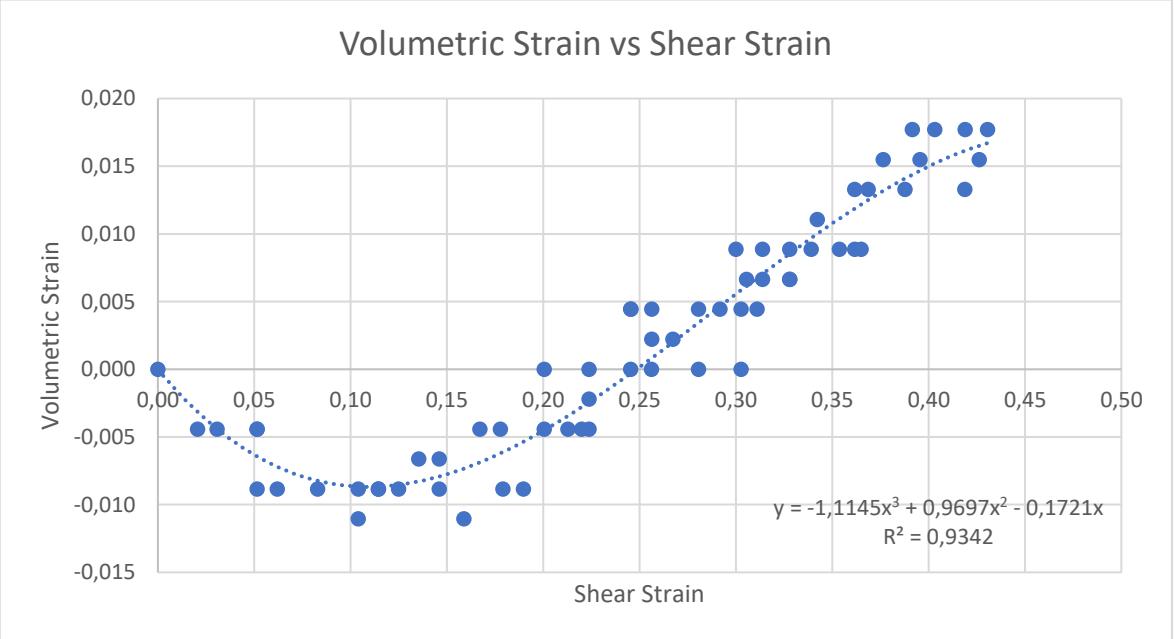

Figure B.4. Volumetric Strain vs Shear Strain Diagram ($I_D = 0.17$ & $\sigma' = 0.52\ kPa$).

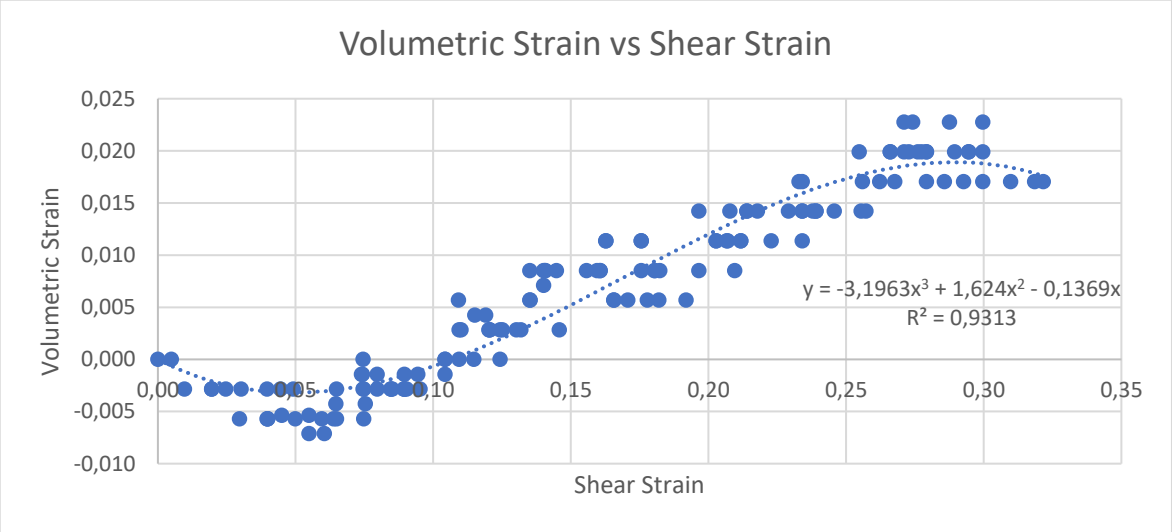

Figure B.5. Volumetric Strain vs Shear Strain Diagram ($I_D = 0.20$ & $\sigma' = 0.49\ kPa$).

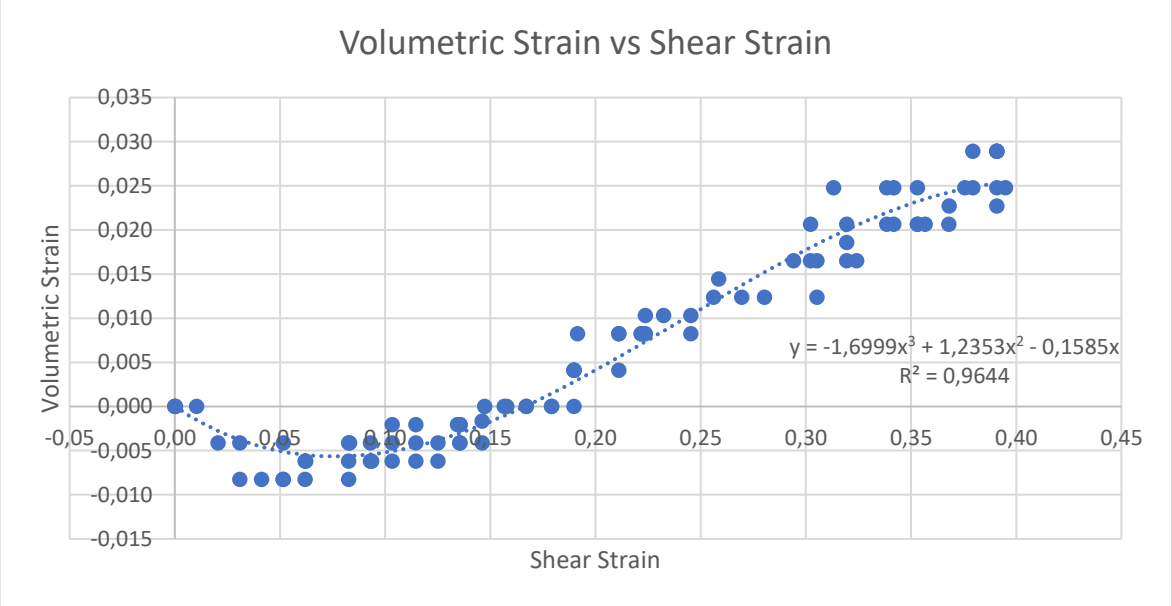

Figure B.6. Volumetric Strain vs Shear Strain Diagram ($I_D = 0.24$ & $\sigma' = 0.58\ kPa$).

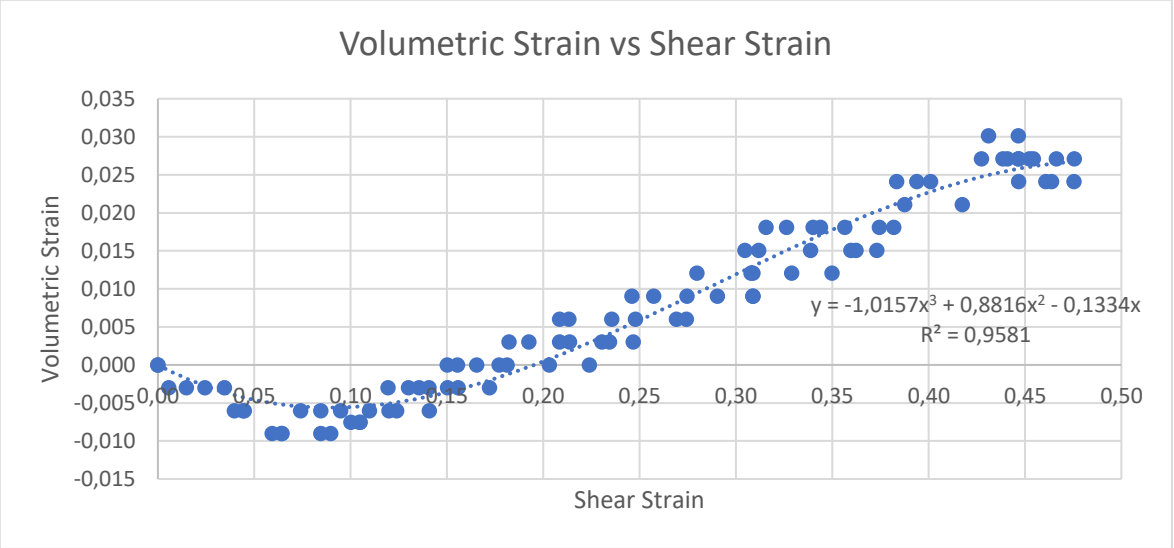

Figure B.7. Volumetric Strain vs Shear Strain Diagram ($I_D = 0.24$ & $\sigma' = 0.59\ kPa$).

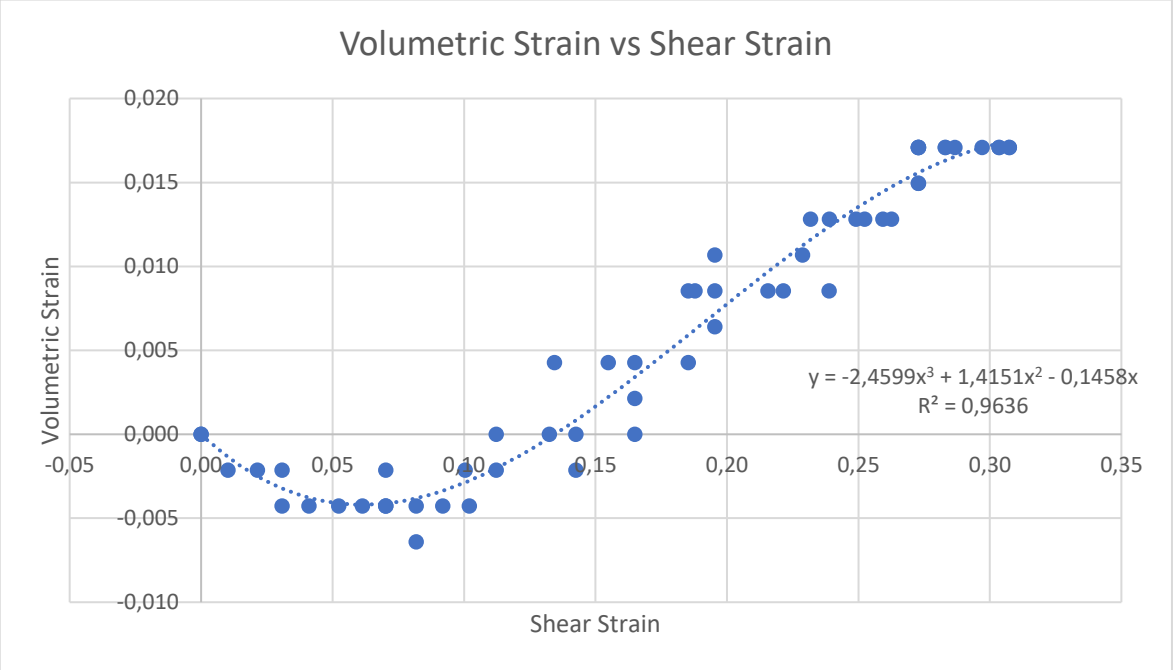

Figure B.8. Volumetric Strain vs Shear Strain Diagram ($I_D = 0.27$ & $\sigma' = 0.53\ kPa$).

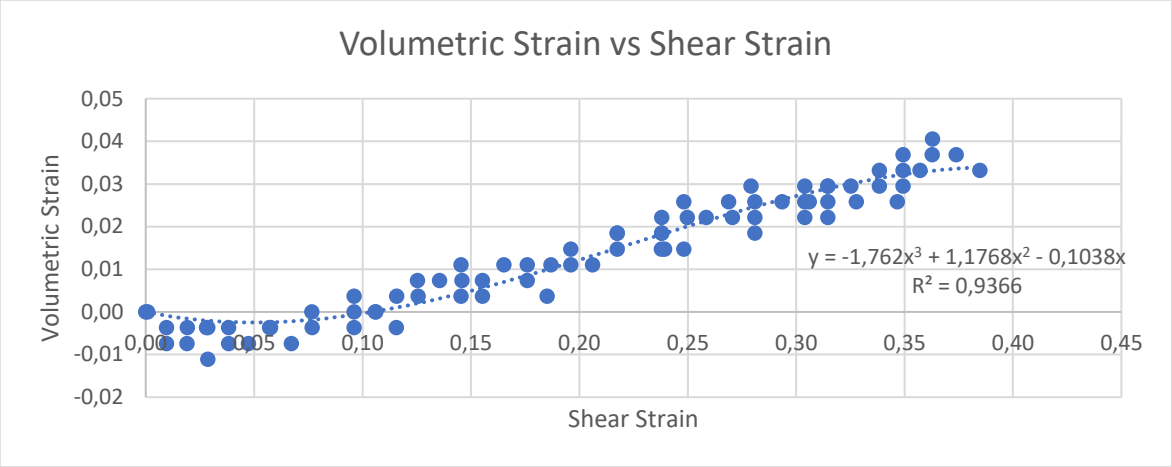

Figure B.9. Volumetric Strain vs Shear Strain Diagram ($I_D = 0.27$ & $\sigma' = 0.77\ kPa$).

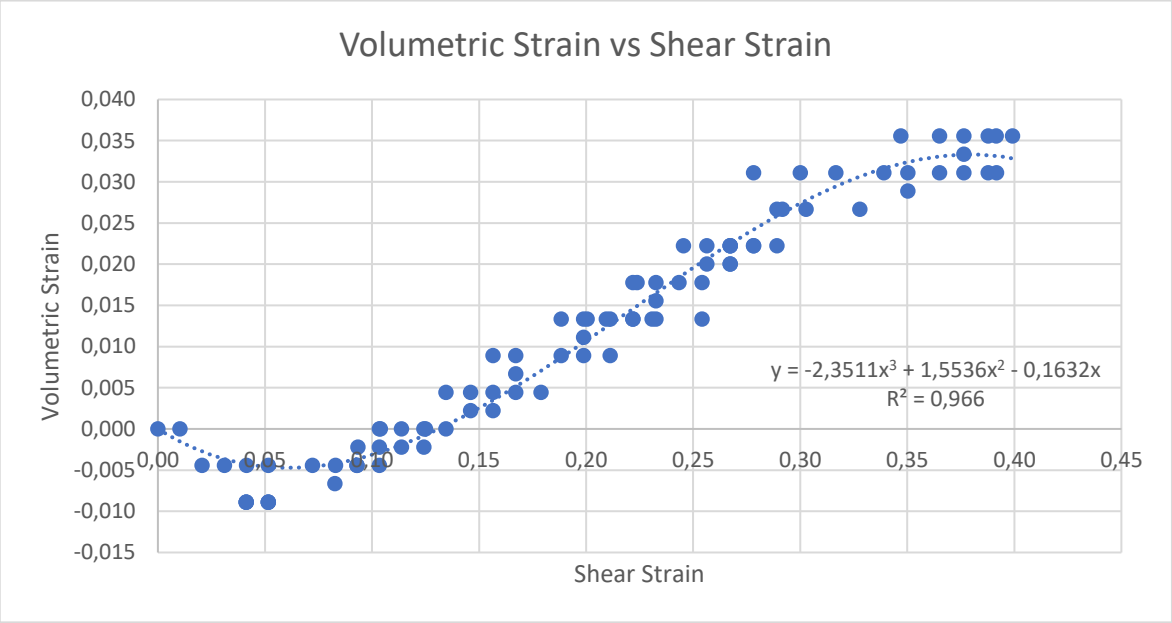

Figure B.10. Volumetric Strain vs Shear Strain Diagram ($I_D = 0.29$ & $\sigma' = 0.72\ kPa$).

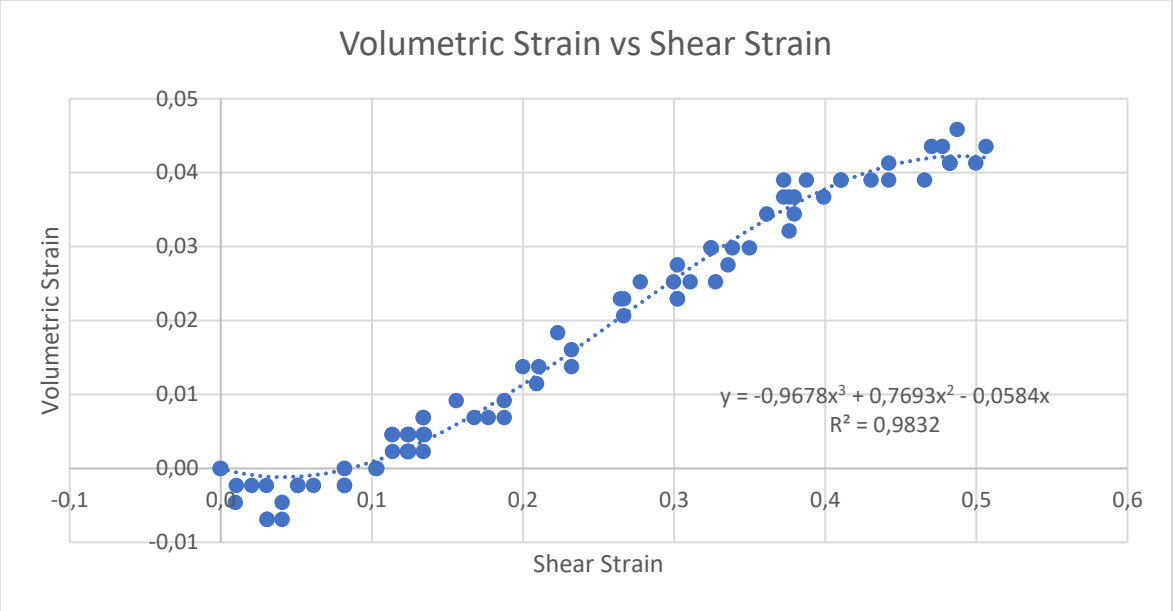

Figure B.11. Volumetric Strain vs Shear Strain Diagram ($I_D = 0.32$ & $\sigma' = 0.94\ kPa$).

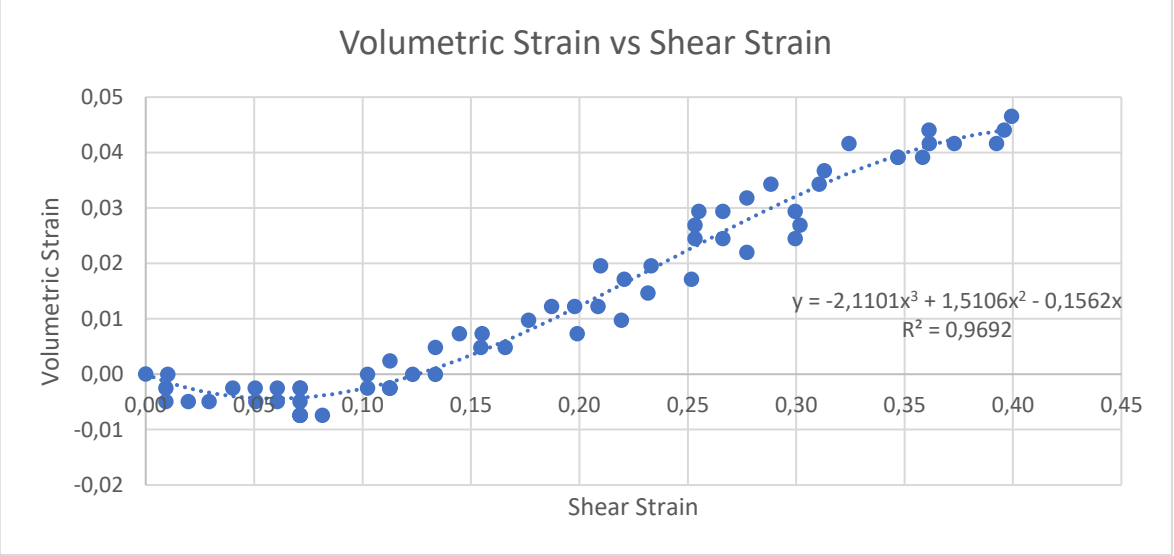

Figure B.12. Volumetric Strain vs Shear Strain Diagram ($I_D = 0.33$ & $\sigma' = 0.85\ kPa$).

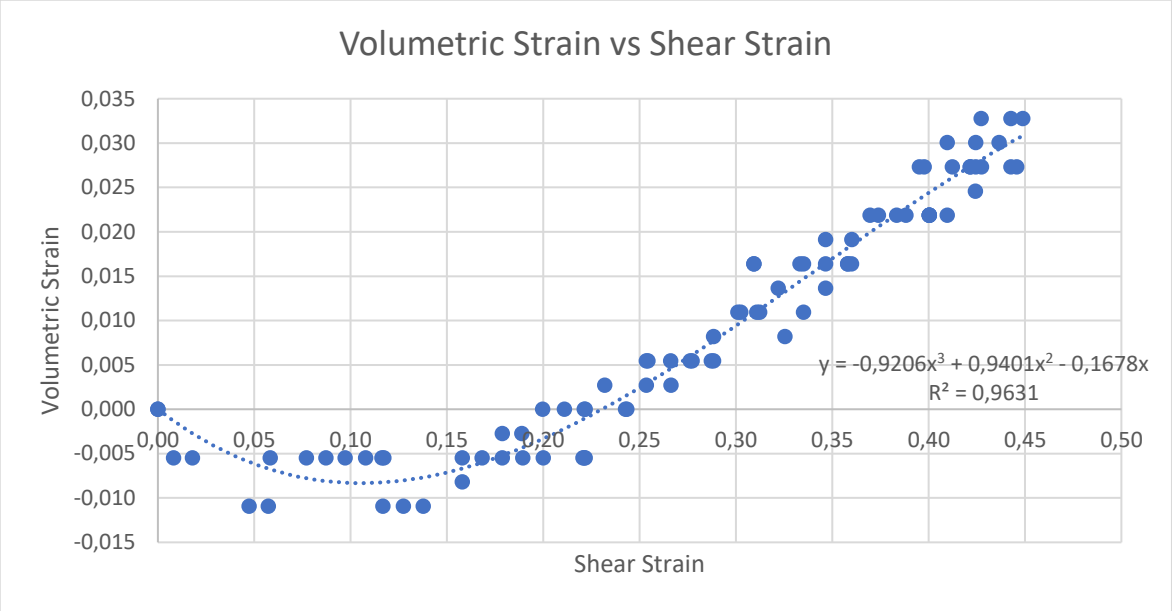

Figure B.13. Volumetric Strain vs Shear Strain Diagram ($I_D = 0.36$ & $\sigma' = 0.71\ kPa$).

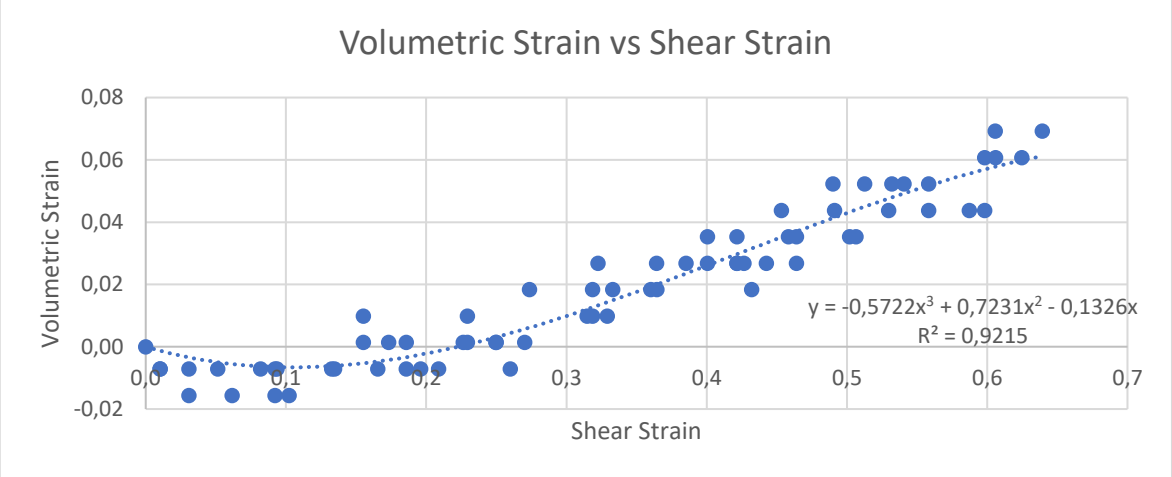

Figure B.14. Volumetric Strain vs Shear Strain Diagram ($I_D = 0.39$ & $\sigma' = 0.58\ kPa$).

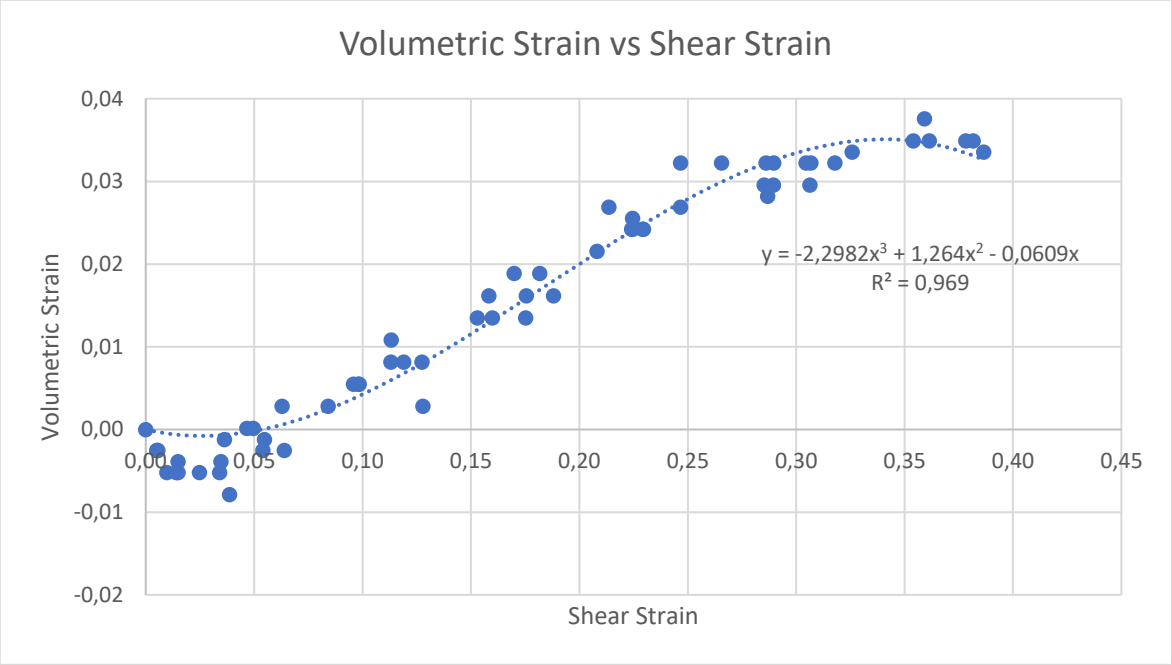

Figure B.15. Volumetric Strain vs Shear Strain Diagram ($I_D = 0.41$ & $\sigma' = 0.87\ kPa$).

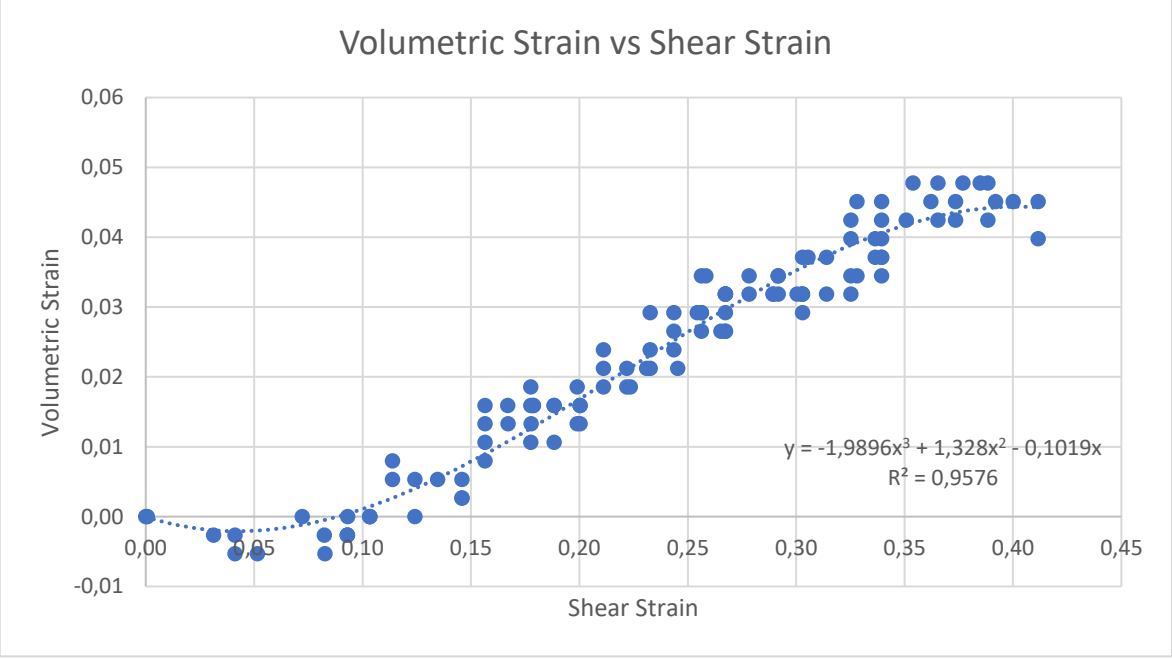

Figure B.16. Volumetric Strain vs Shear Strain Diagram ($I_D = 0.41$ & $\sigma' = 0.96\ kPa$).

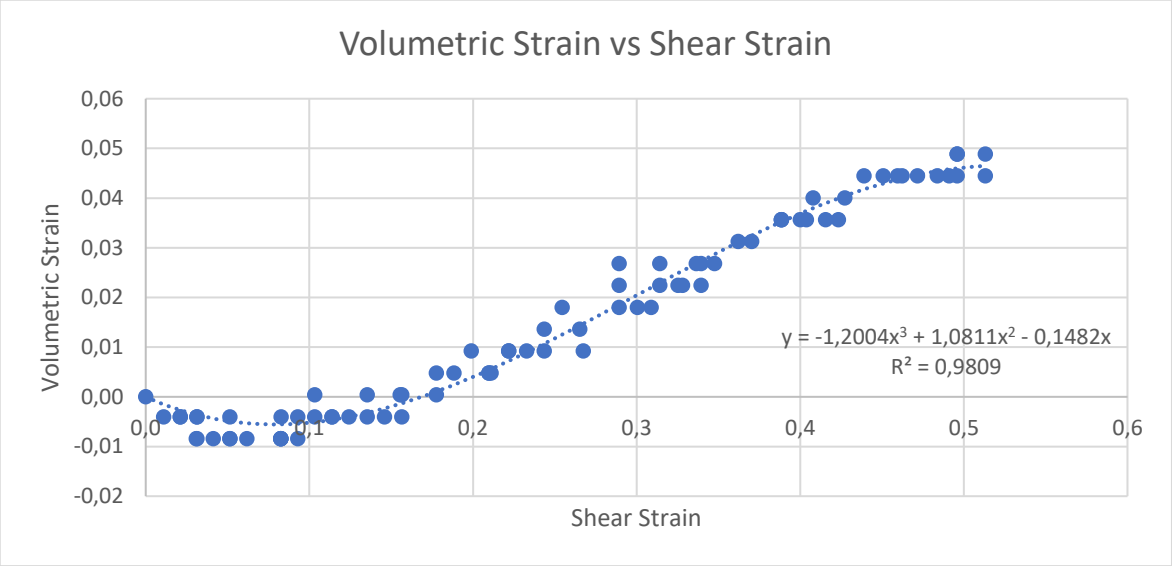

Figure B.17. Volumetric Strain vs Shear Strain Diagram ($I_D = 0.45$ & $\sigma' = 0.88\ kPa$).

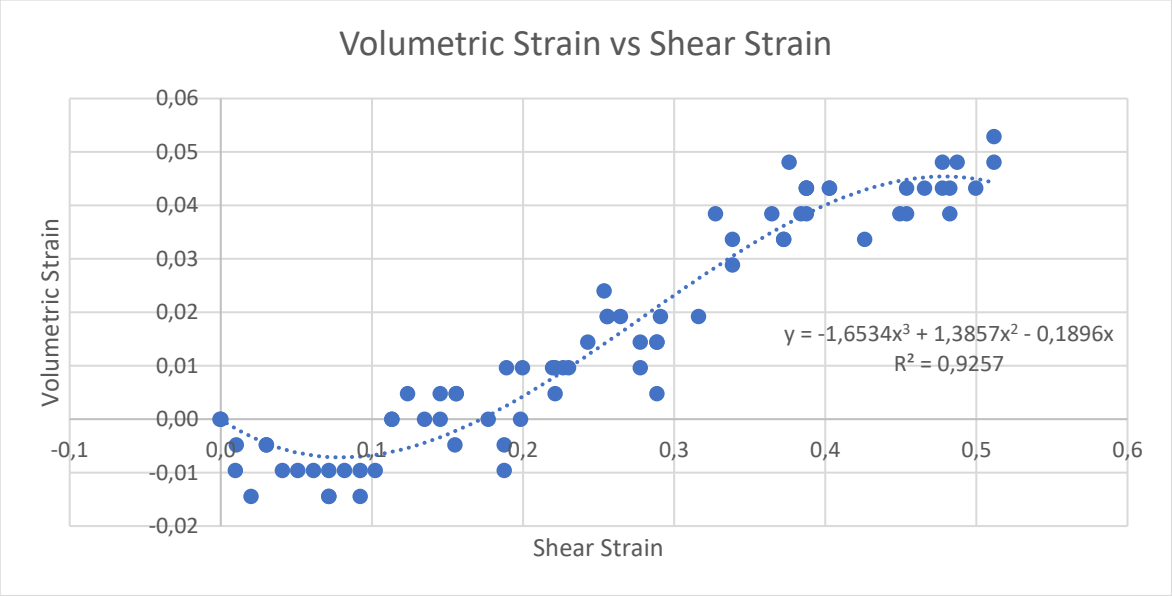

Figure B.18. Volumetric Strain vs Shear Strain Diagram ($I_D = 0.46$ & $\sigma' = 0.71\ kPa$).

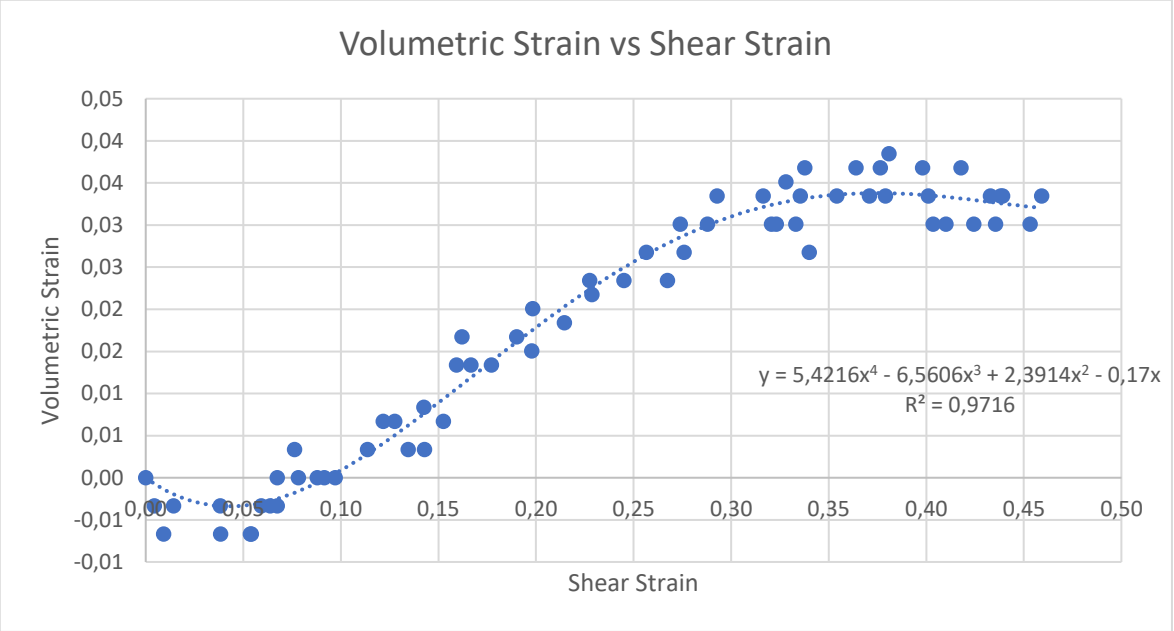

Figure B.19. Volumetric Strain vs Shear Strain Diagram ($I_D = 0.47$ & $\sigma' = 0.84\ kPa$).

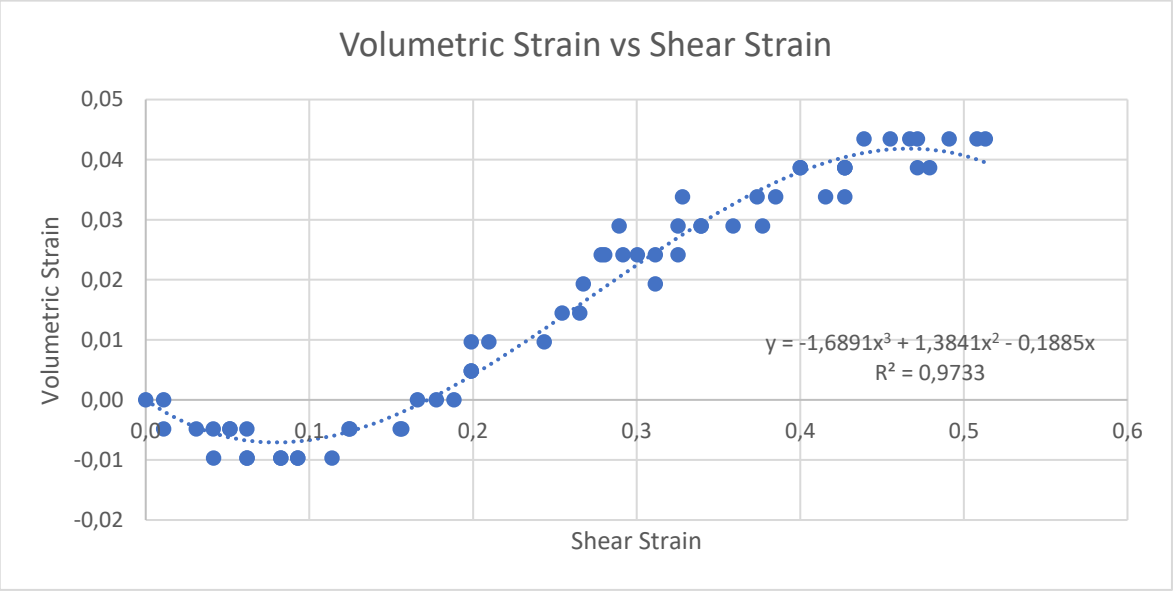

Figure B.20. Volumetric Strain vs Shear Strain Diagram ($I_D = 0.48$ & $\sigma' = 0.81\ kPa$).

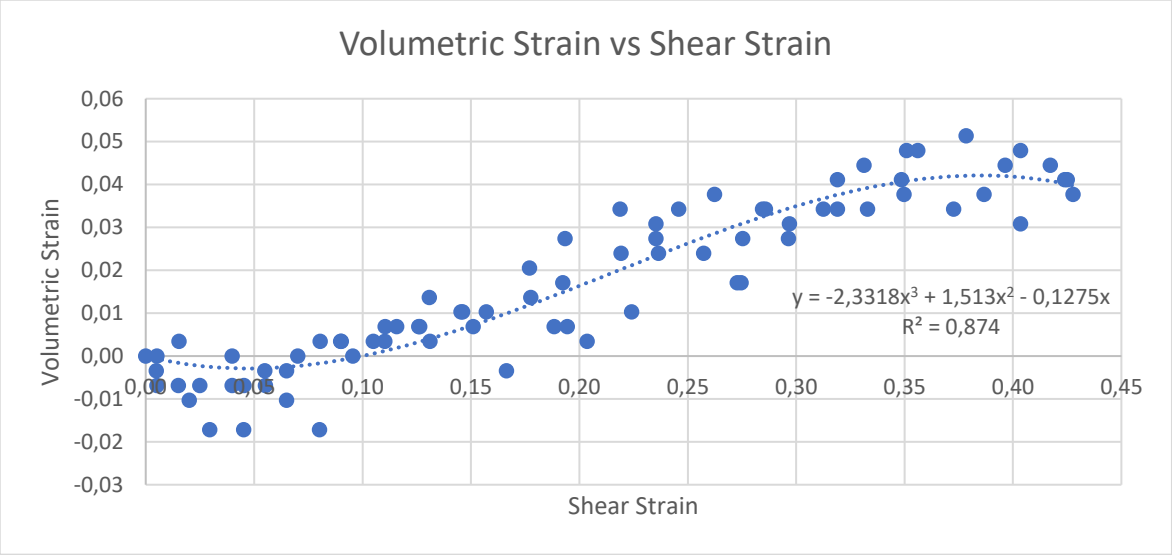

Figure B.21. Volumetric Strain vs Shear Strain Diagram ($I_D = 0.52$ & $\sigma' = 0.88\ kPa$).

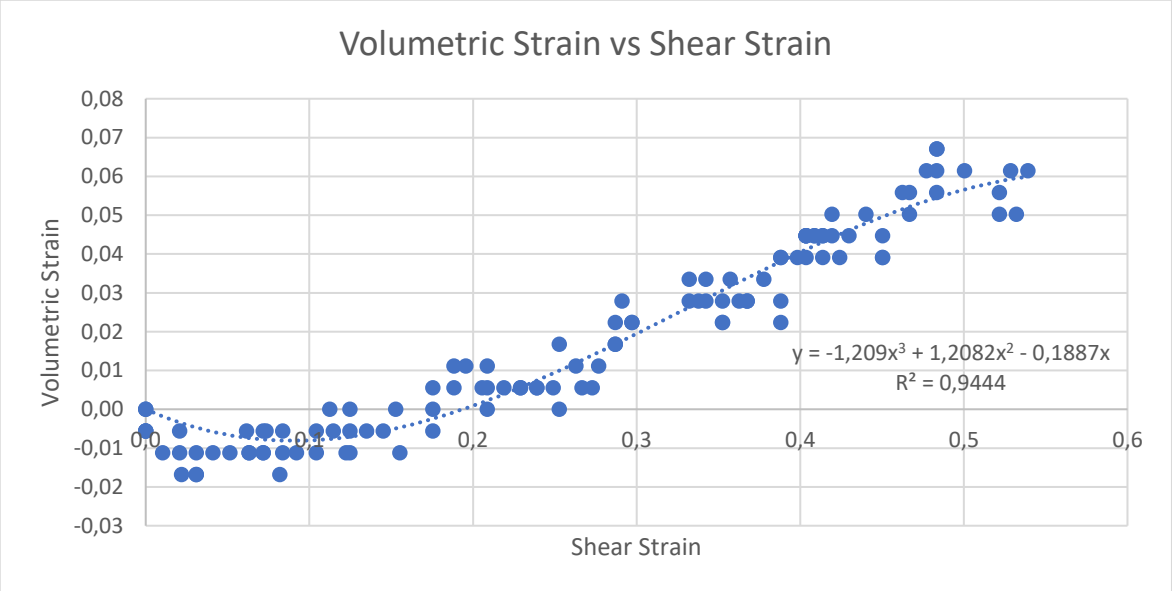

Figure B.22. Volumetric Strain vs Shear Strain Diagram ($I_D = 0.53$ & $\sigma' = 0.69\ kPa$).

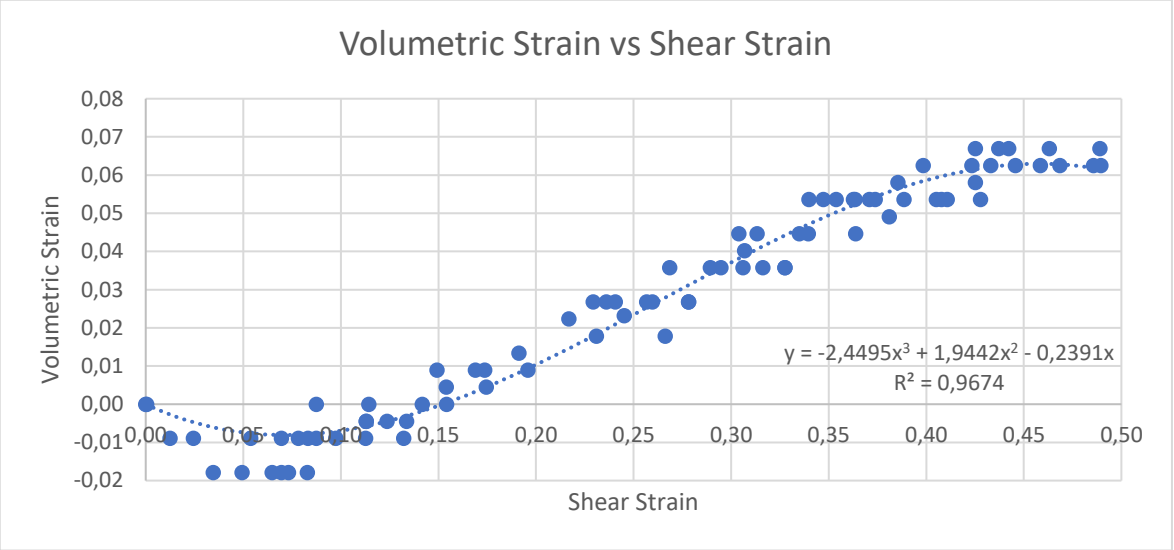

Figure B.23. Volumetric Strain vs Shear Strain Diagram ($I_D = 0.53$ & $\sigma' = 0.72\ kPa$).

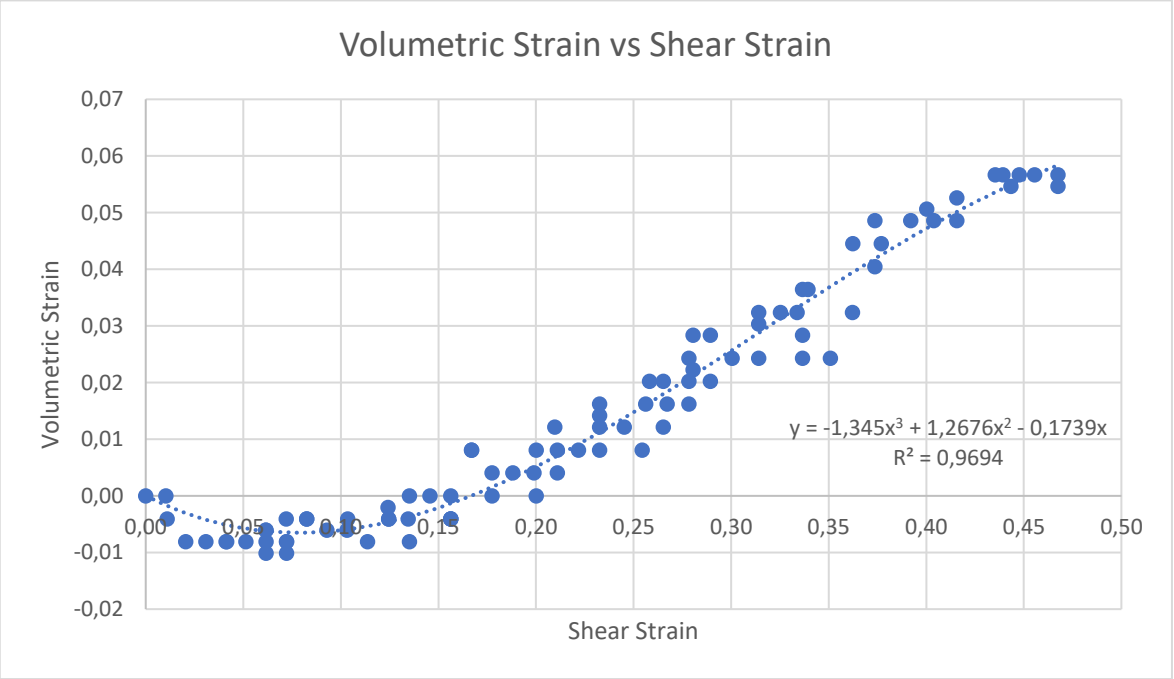

Figure B.24. Volumetric Strain vs Shear Strain Diagram ($I_D = 0.53$ & $\sigma' = 0.96\ kPa$).

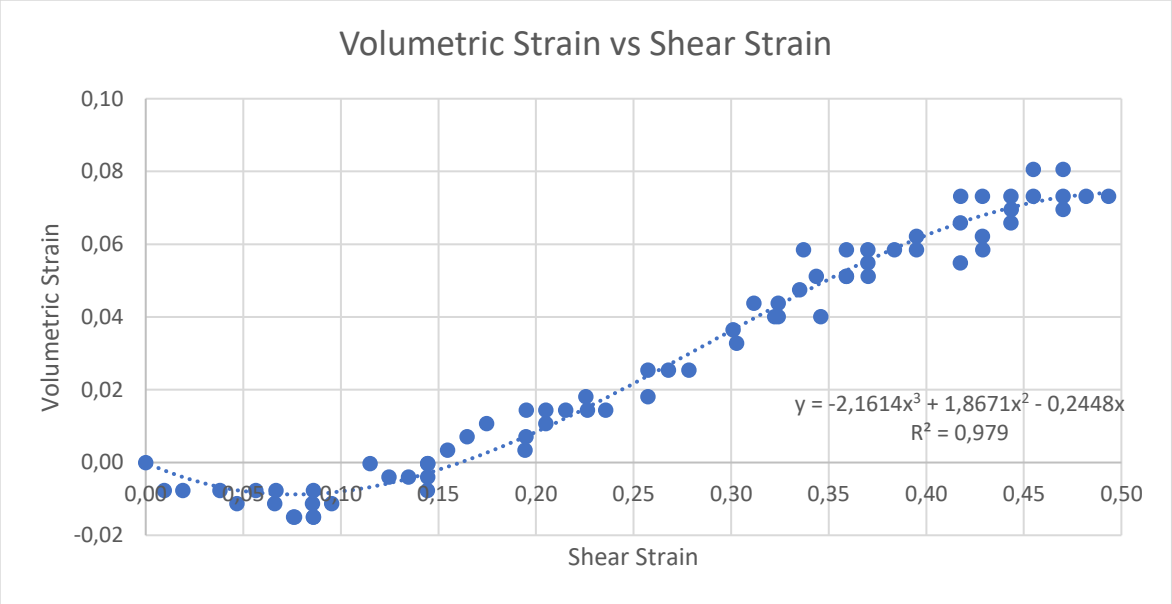

Figure B.25. Volumetric Strain vs Shear Strain Diagram ($I_D = 0.56$ & $\sigma' = 0.56\ kPa$).

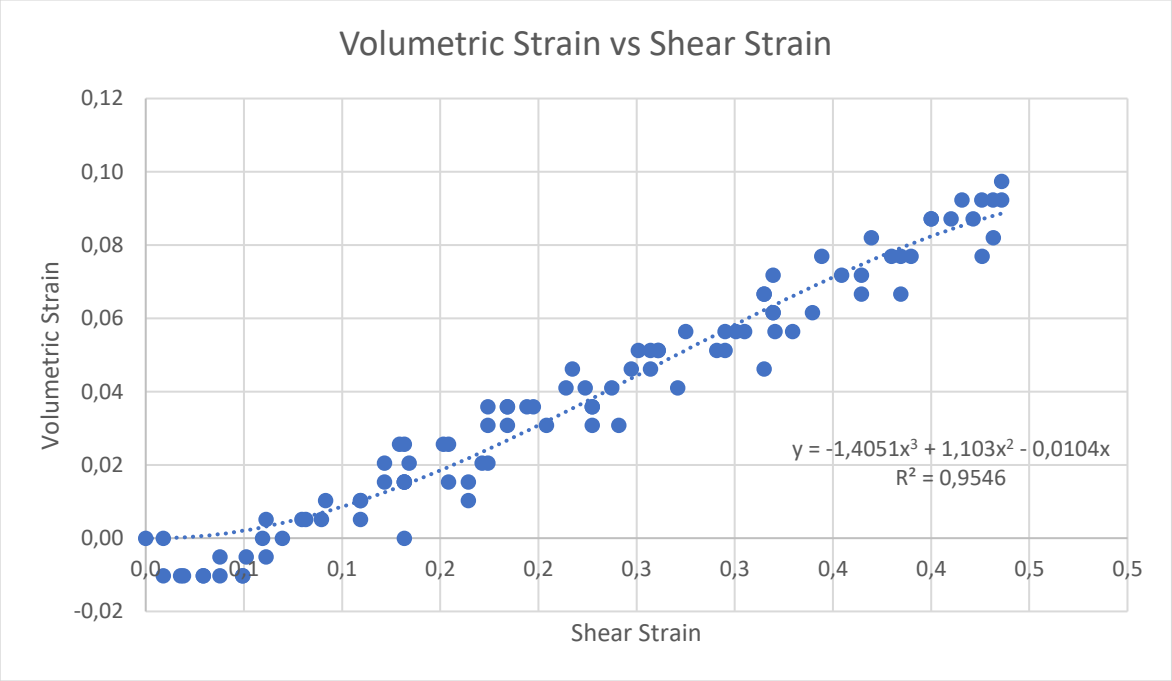

Figure B.26. Volumetric Strain vs Shear Strain Diagram ($I_D = 0.58$ & $\sigma' = 0.79\ kPa$).

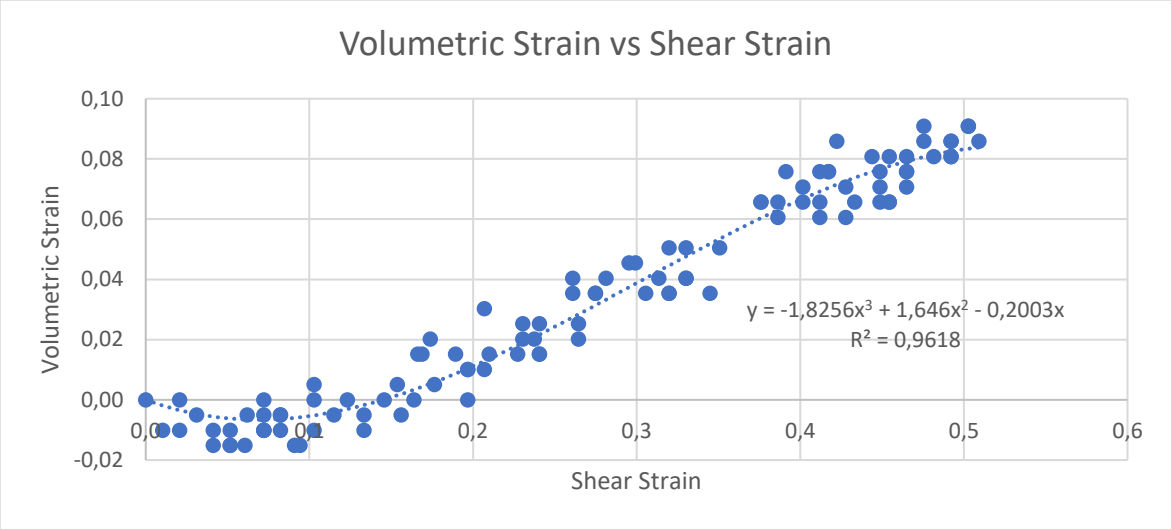

Figure B.27. Volumetric Strain vs Shear Strain Diagram ($I_D = 0.58$ & $\sigma' = 0.80\ kPa$).

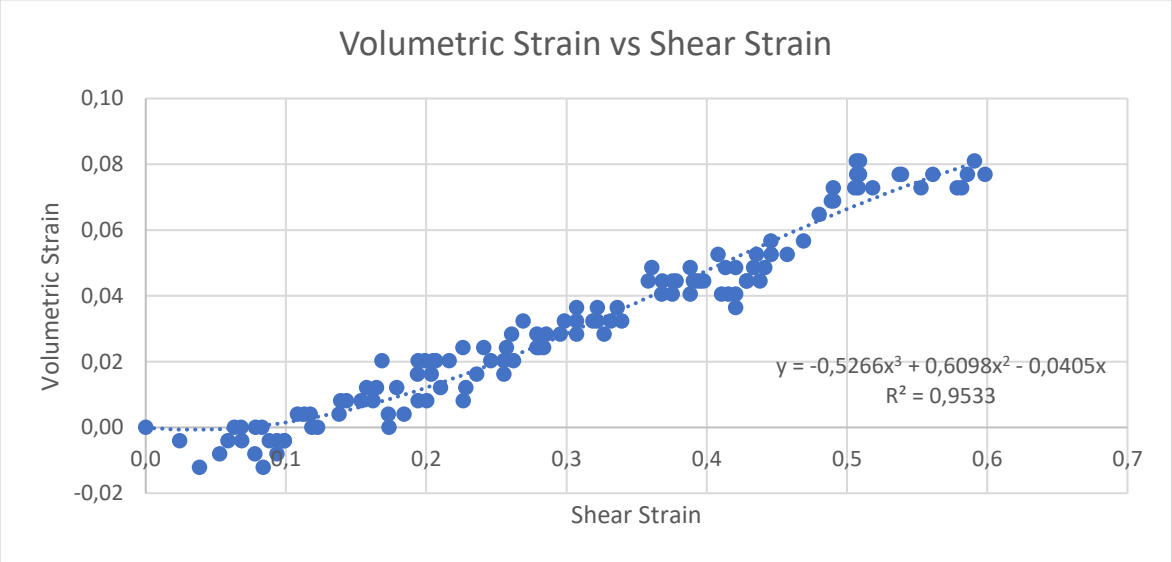

Figure B.28. Volumetric Strain vs Shear Strain Diagram ($I_D = 0.58$ & $\sigma' = 0.96\ kPa$).

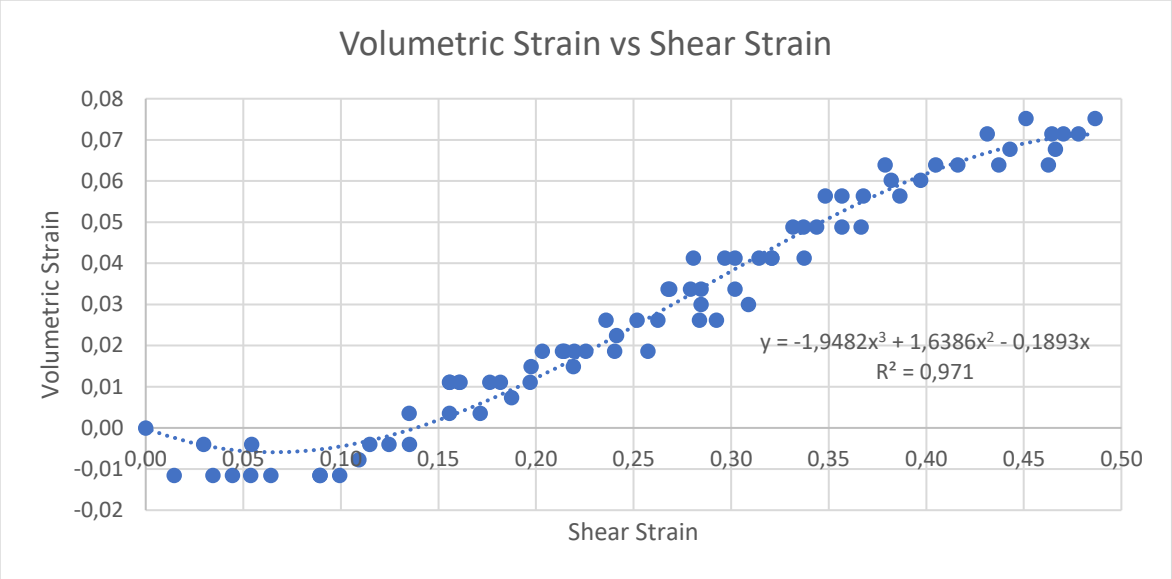

Figure B.29. Volumetric Strain vs Shear Strain Diagram ($I_D = 0.60$ & $\sigma' = 0.49\ kPa$).

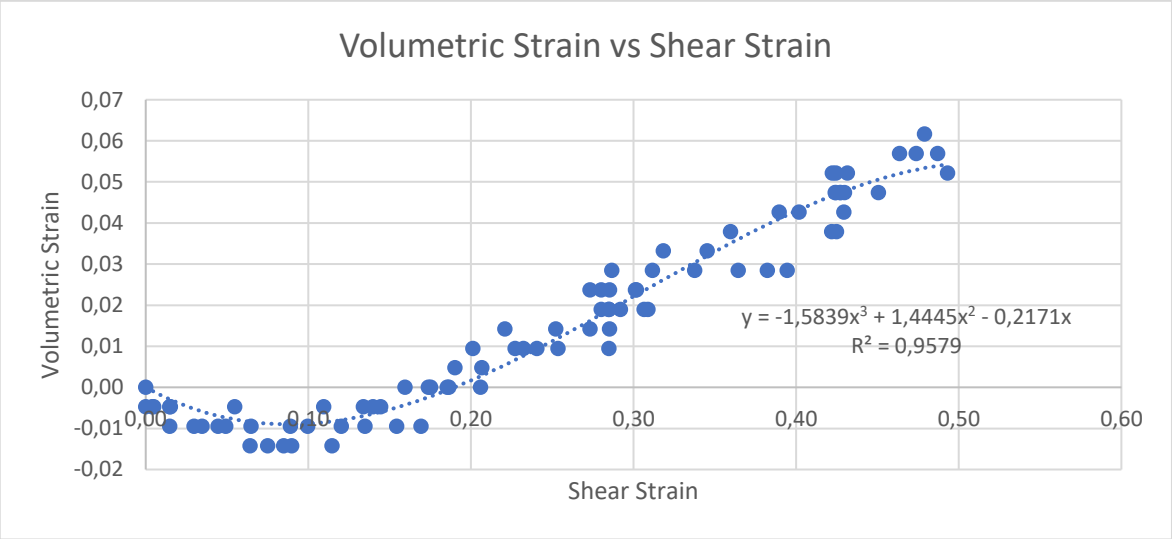

Figure B.30. Volumetric Strain vs Shear Strain Diagram ($I_D = 0.60$ & $\sigma' = 0.84\ kPa$).

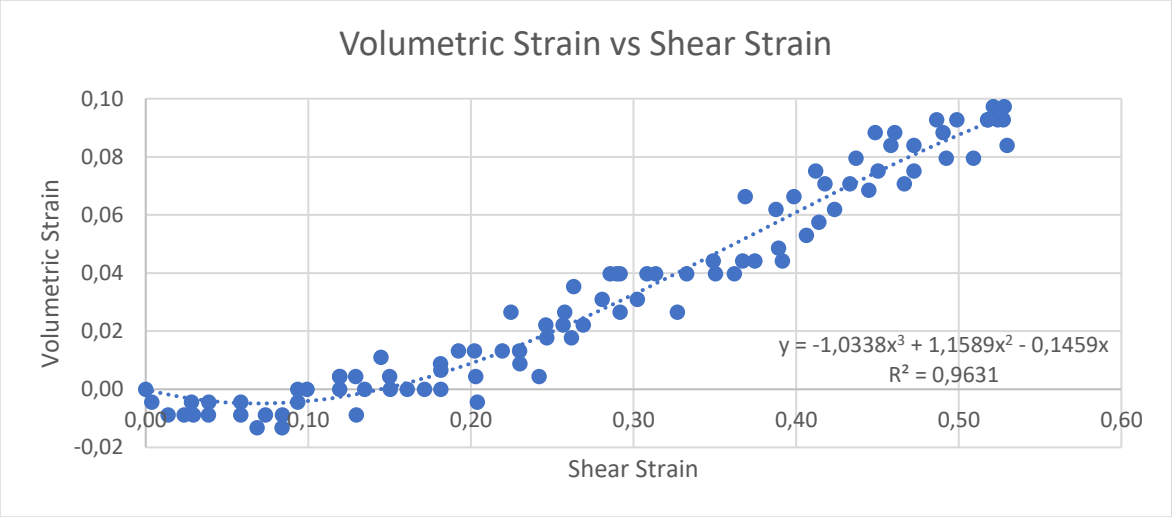

Figure B.31. Volumetric Strain vs Shear Strain Diagram ($I_D = 0.63$ & $\sigma' = 0.56kPa$).

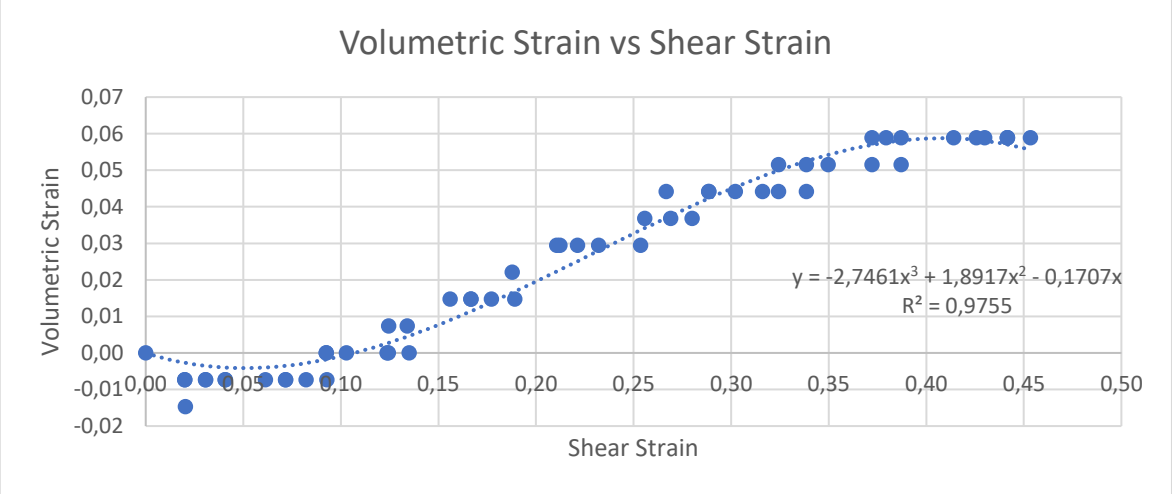

Figure B.32. Volumetric Strain vs Shear Strain Diagram ($I_D = 0.63$ & $\sigma' = 0.66\ kPa$).

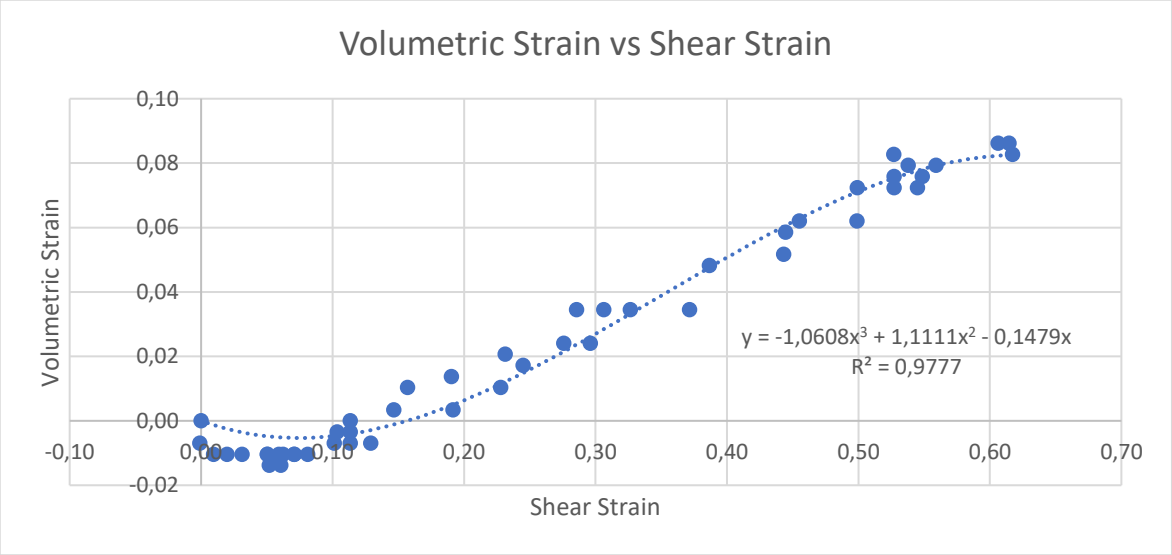

Figure B.33. Volumetric Strain vs Shear Strain Diagram ($I_D = 0.63$ & $\sigma' = 0.67\ kPa$).

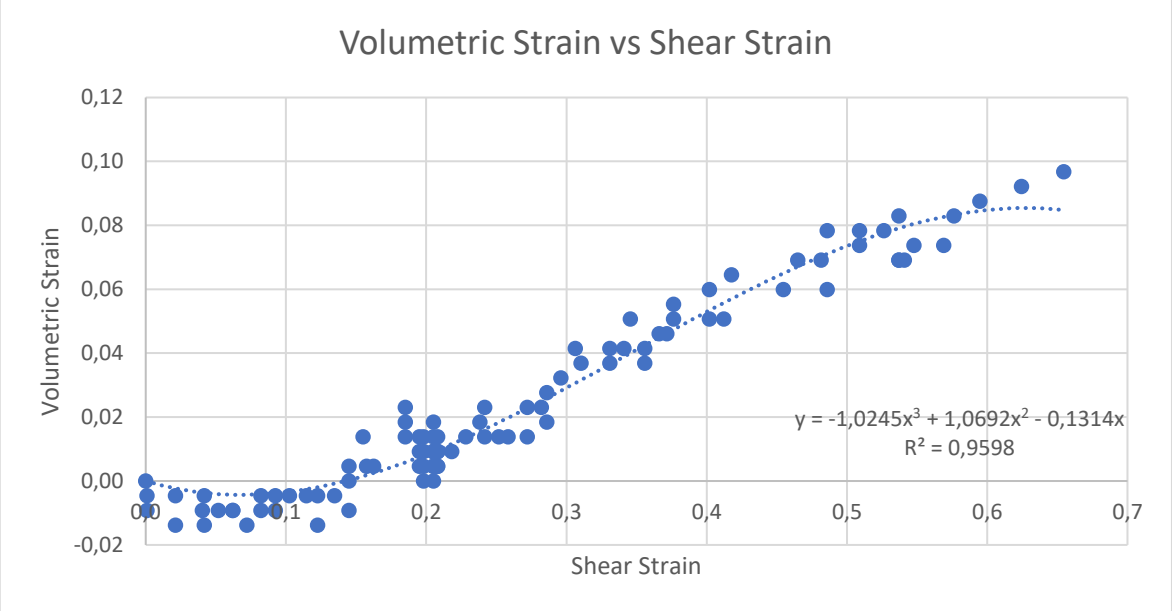

Figure B.34. Volumetric Strain vs Shear Strain Diagram ($I_D = 0.63$ & $\sigma' = 0.89\ kPa$).

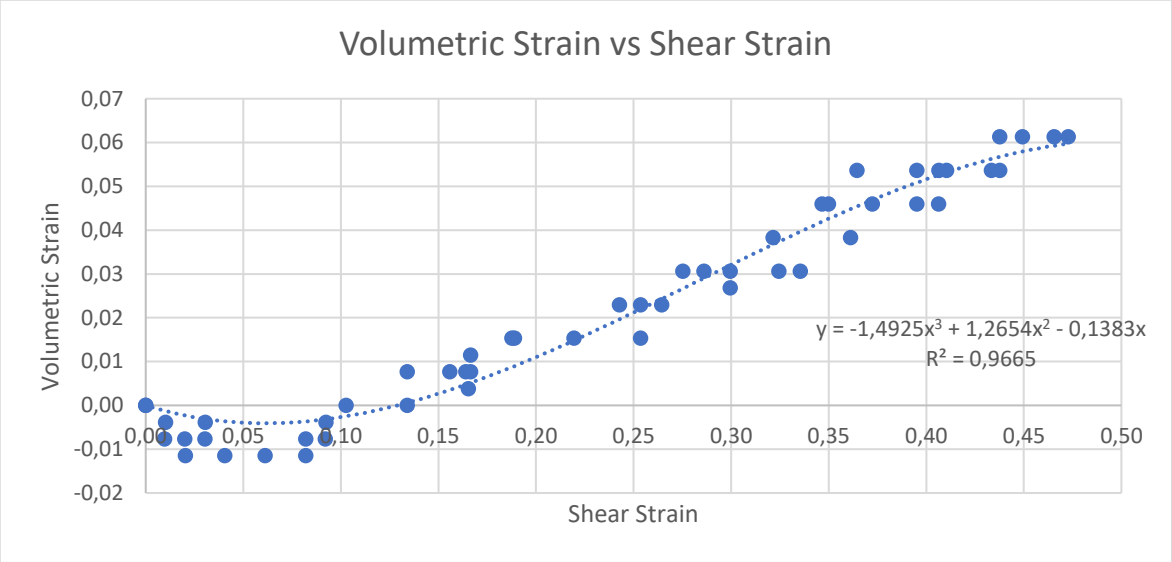

Figure B.35. Volumetric Strain vs Shear Strain Diagram ($I_D = 0.64$ & $\sigma' = 0.84\ kPa$).

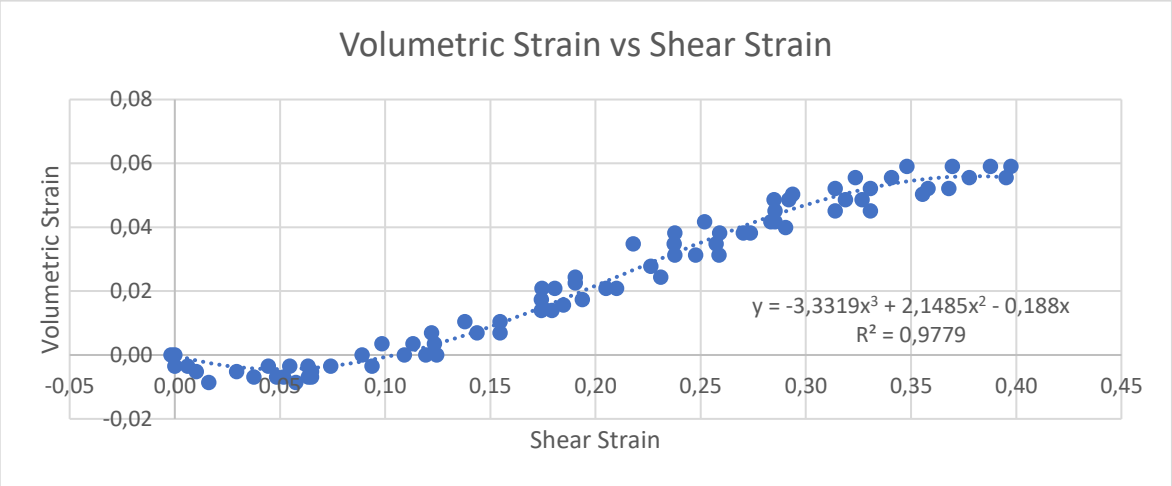

Figure B.36. Volumetric Strain vs Shear Strain Diagram ($I_D = 0.65$ & $\sigma' = 0.96\ kPa$).

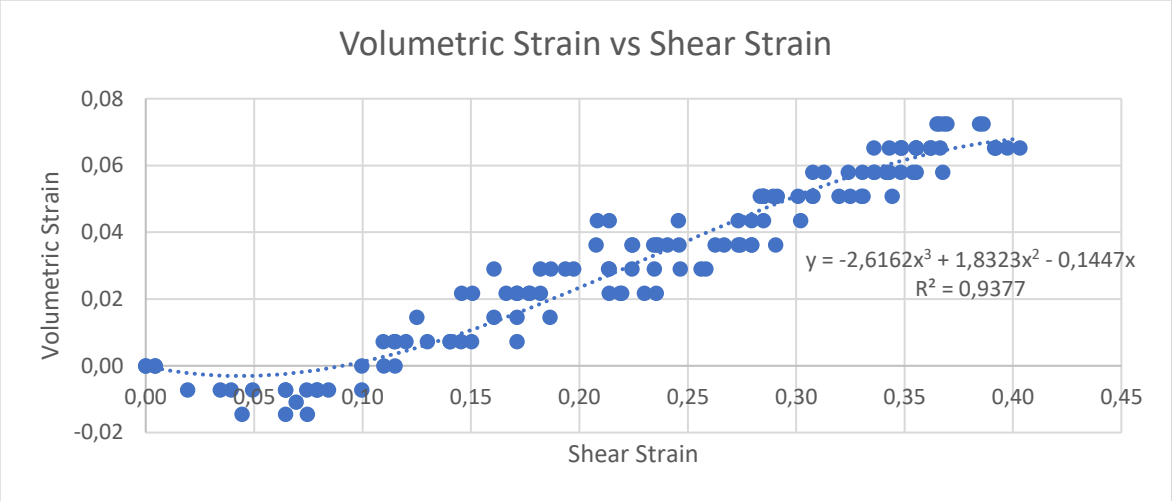

Figure B.37. Volumetric Strain vs Shear Strain Diagram ($I_D = 0.67$ & $\sigma' = 0.83\ kPa$).

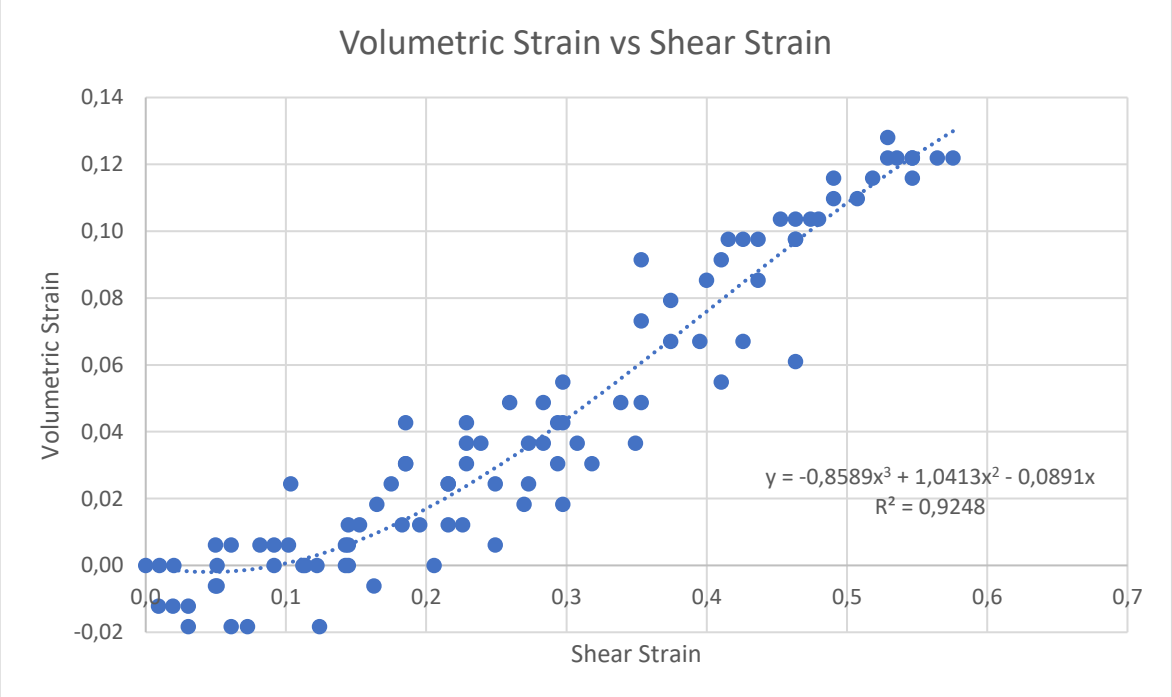

Figure B.38. Volumetric Strain vs Shear Strain Diagram ($I_D = 0.70$ & $\sigma' = 0.92\ kPa$).

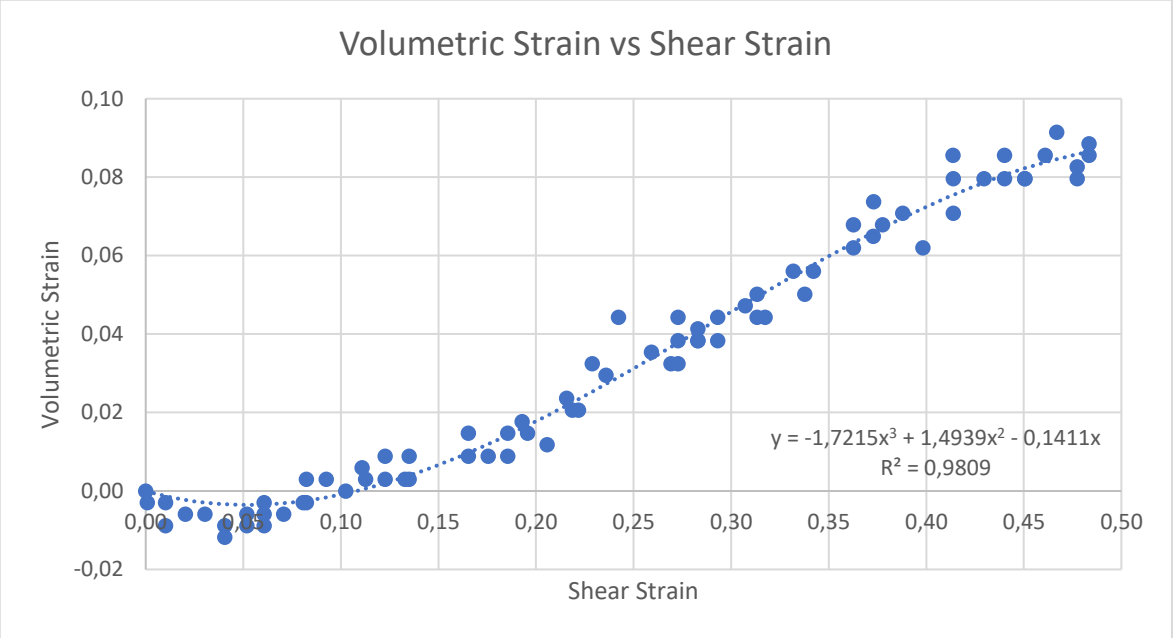

Figure B.39. Volumetric Strain vs Shear Strain Diagram ($I_D = 0.73$ & $\sigma' = 0.78\ kPa$).

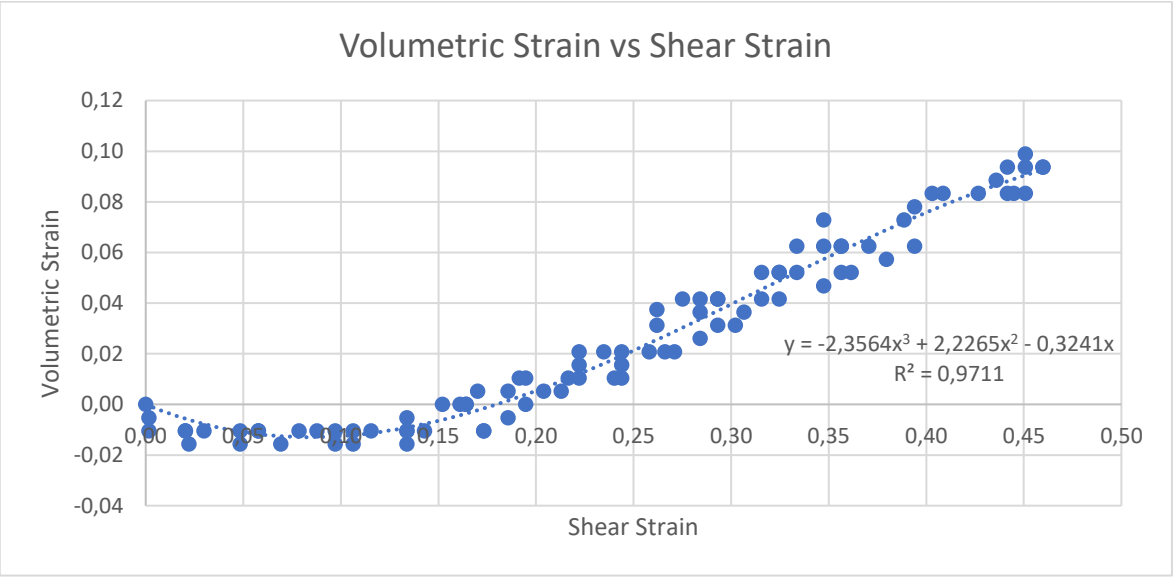

Figure B.40. Volumetric Strain vs Shear Strain Diagram ($I_D = 0.74$ & $\sigma' = 0.66\ kPa$).

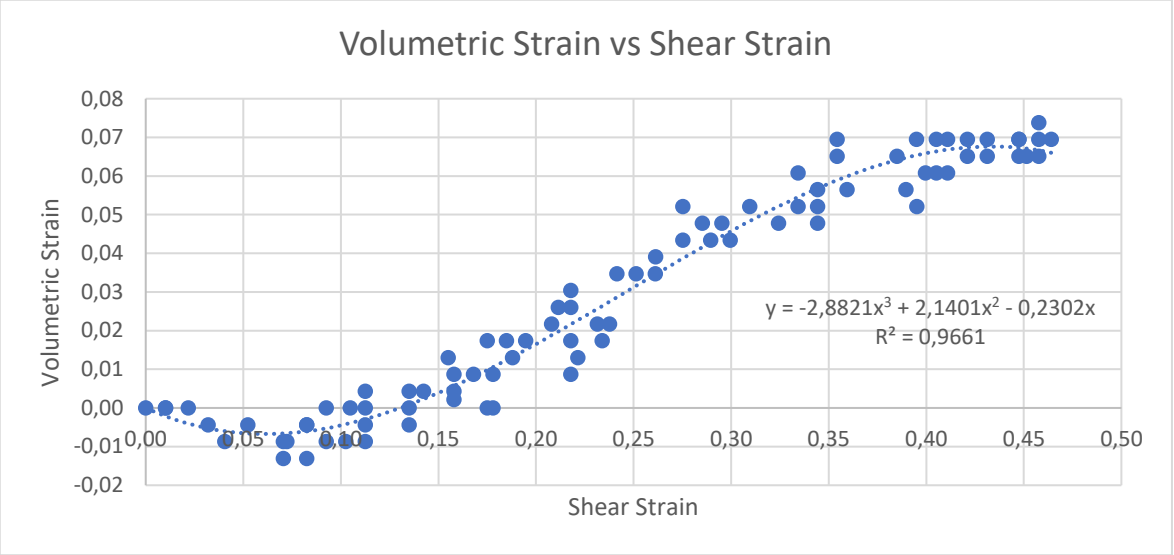

Figure B.41. Volumetric Strain vs Shear Strain Diagram ($I_D = 0.76$ & $\sigma' = 0.75\ kPa$).

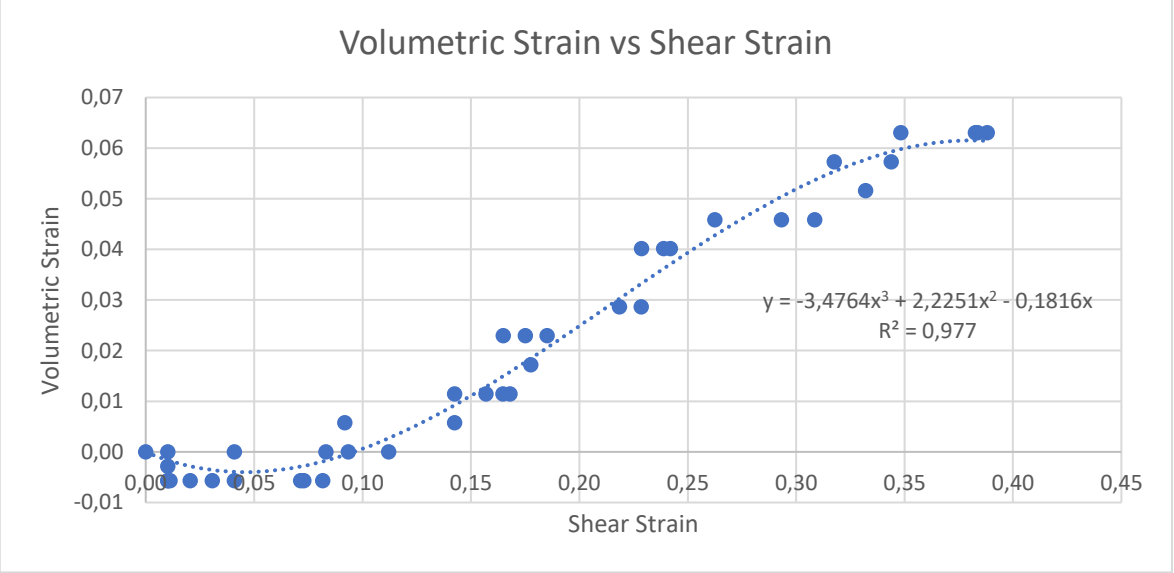

Figure B.42. Volumetric Strain vs Shear Strain Diagram ($I_D = 0.76$ & $\sigma' = 0.87\ kPa$).

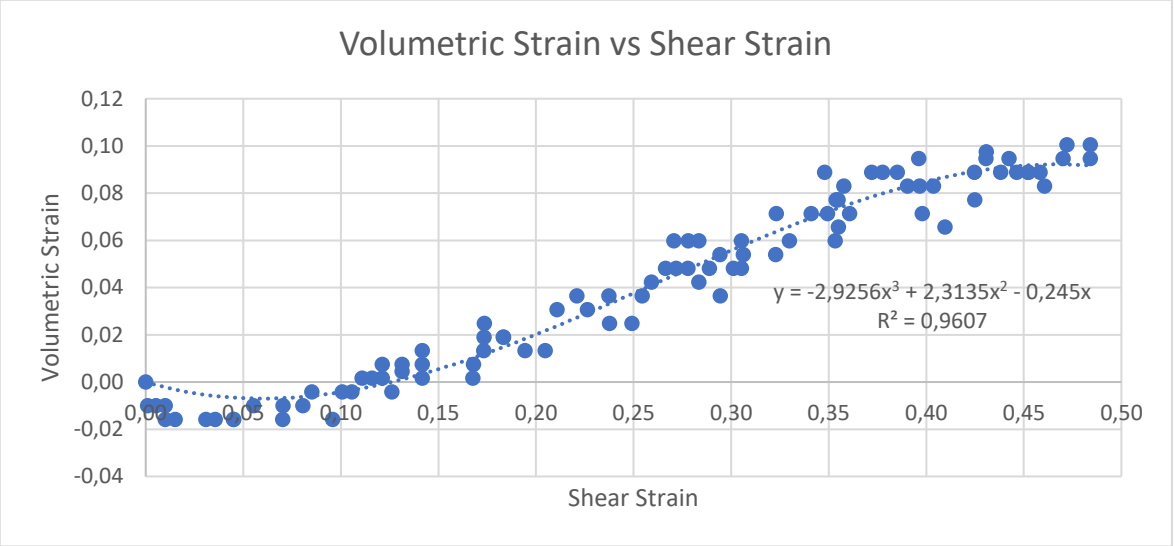

Figure B.43. Volumetric Strain vs Shear Strain Diagram ($I_D = 0.77$ & $\sigma' = 0.88\ kPa$).

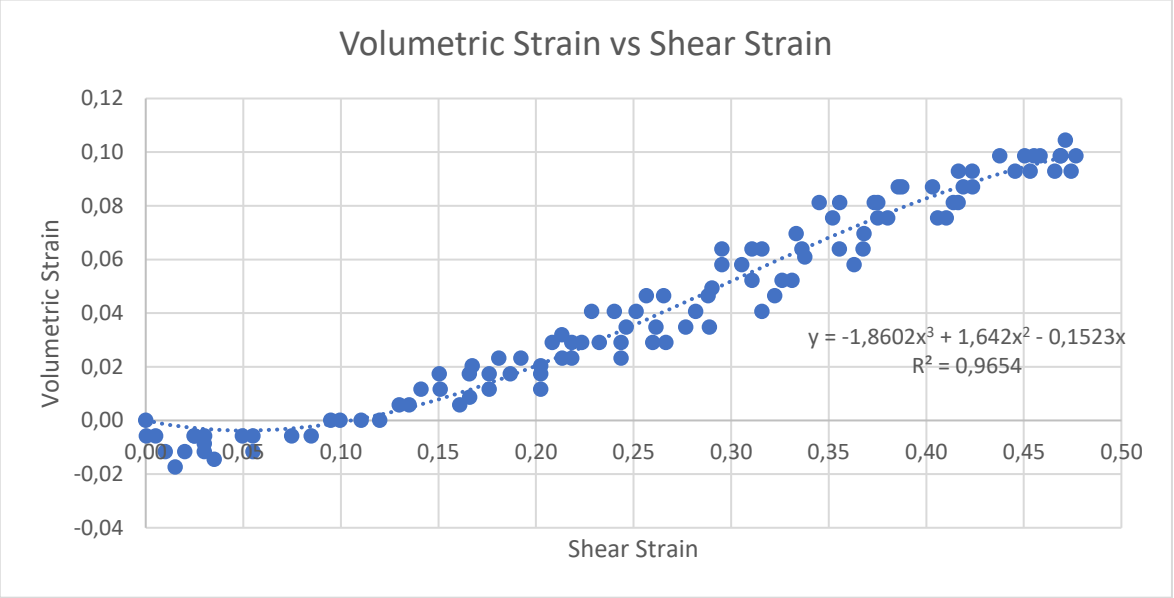

Figure B.44. Volumetric Strain vs Shear Strain Diagram ($I_D = 0.79$ & $\sigma' = 0.91\ kPa$).

APPENDIX C: SHEAR STRAIN FIELDS OBTAINED VIA GEOPIV-RG ANALYSES

Shear strain fields of all PIV analyses with 20% increments are shown in the following in the following figures.

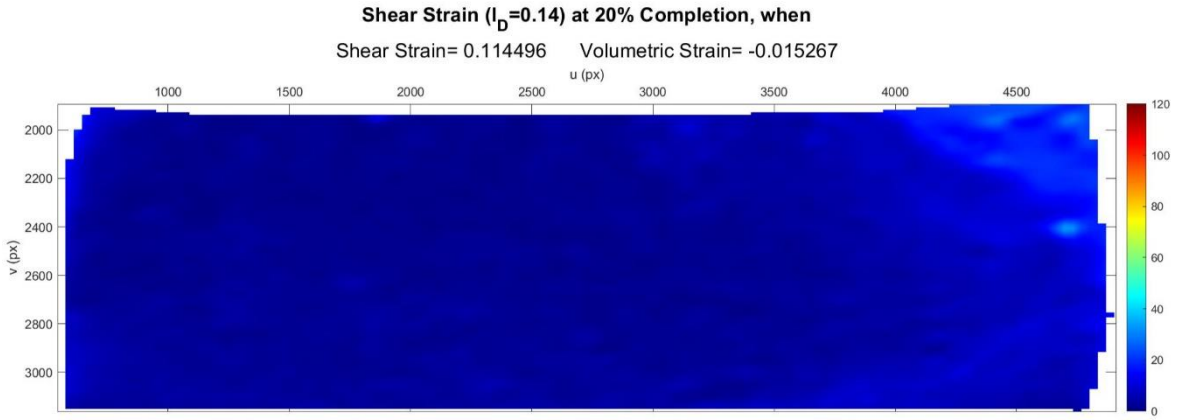

Figure C.1. Shear Strain Field at 20% Completion ($I_D = 0.14$ & $\sigma' = 0.49\ kPa$).

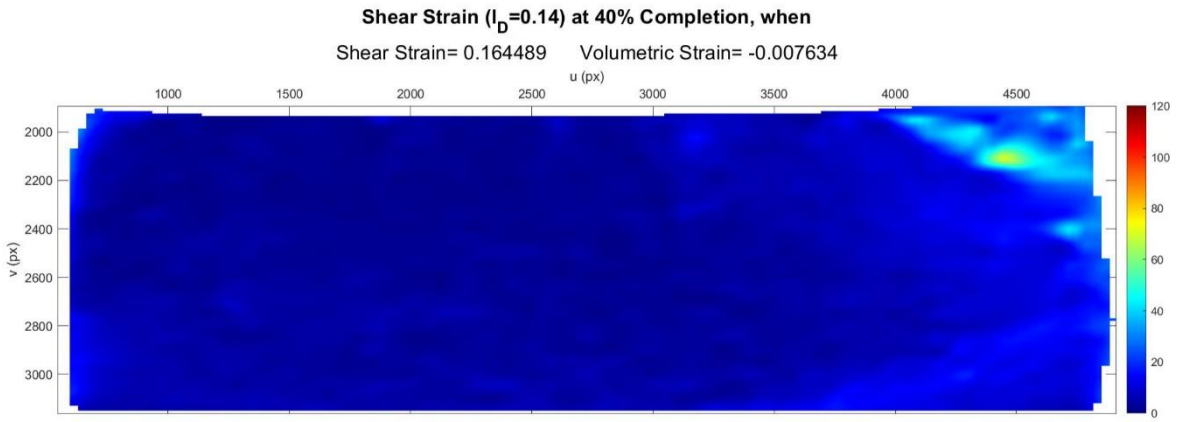

Figure C.2. Shear Strain Field at 40% Completion ($I_D = 0.14$ & $\sigma' = 0.49\ kPa$).

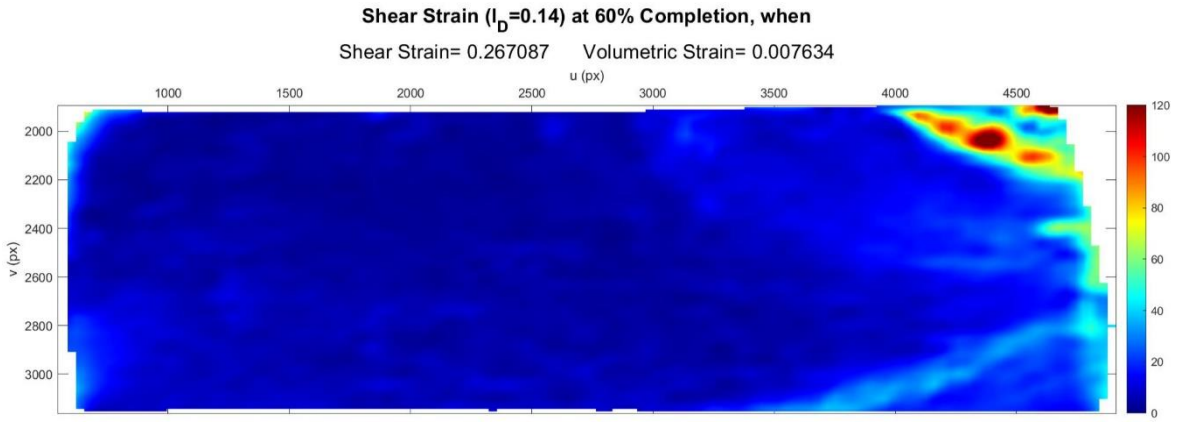

Figure C.3. Shear Strain Field at 60% Completion ($I_D = 0.14$ & $\sigma' = 0.49\ kPa$).

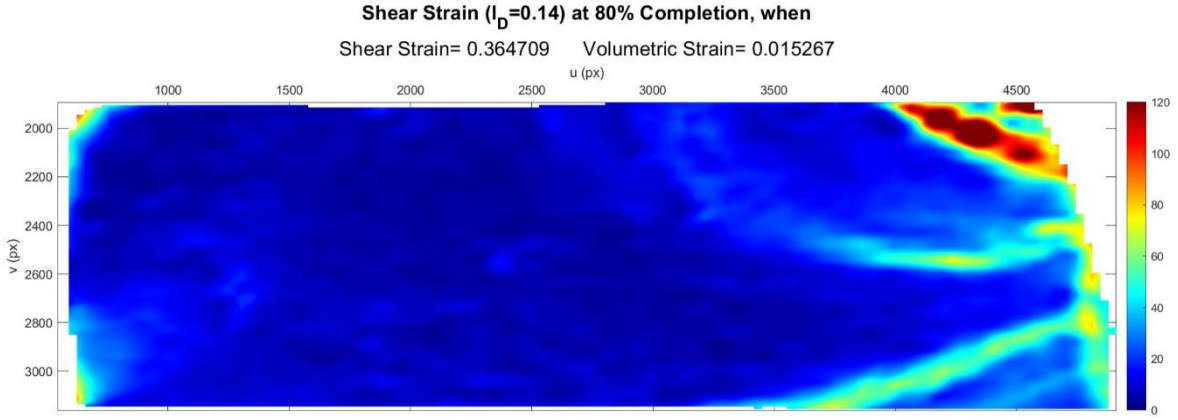

Figure C.4. Shear Strain Field at 80% Completion ($I_D = 0.14$ & $\sigma' = 0.49\ kPa$).

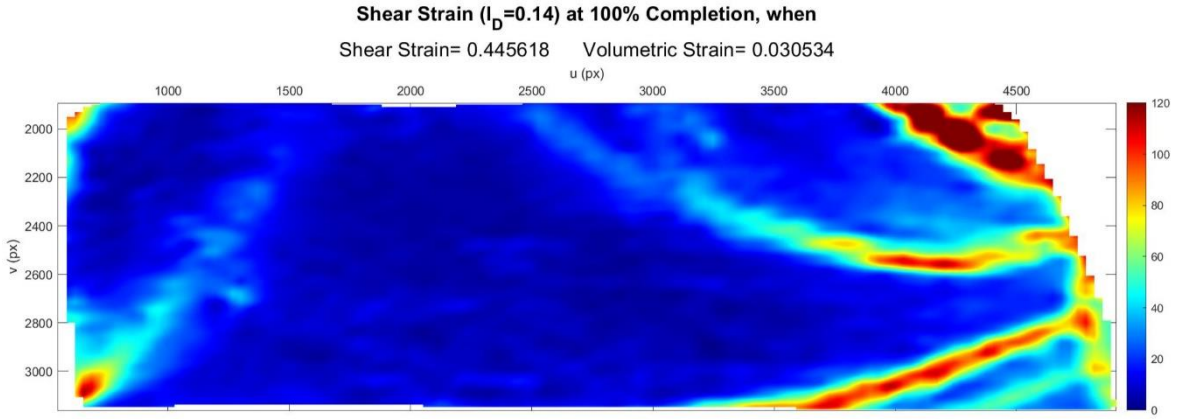

Figure C.5. Shear Strain Field at 100% Completion ($I_D = 0.14$ & $\sigma' = 0.49\ kPa$).

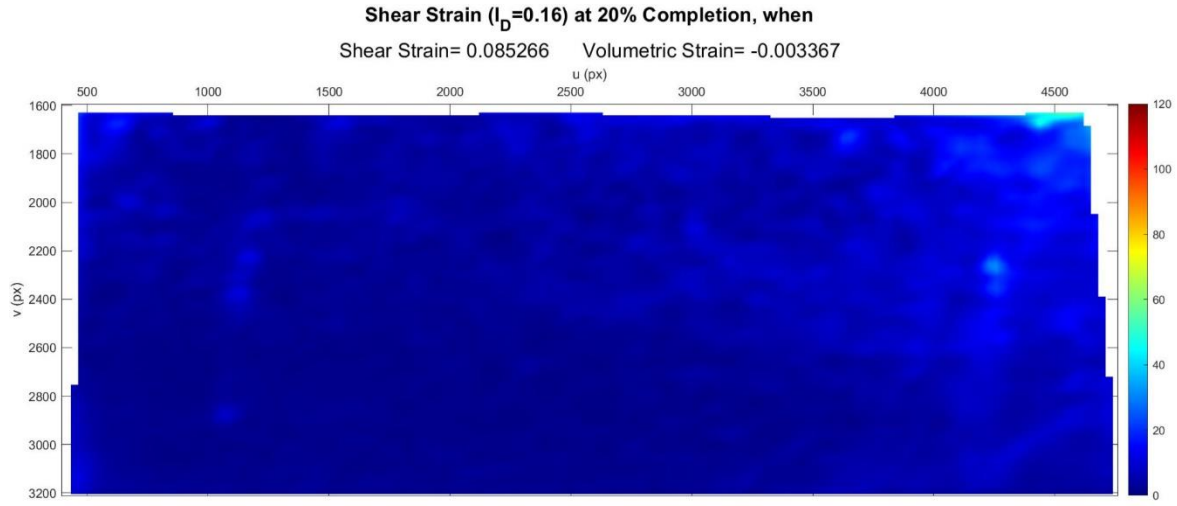

Figure C.6. Shear Strain Field at 20% Completion ($I_D = 0.16$ & $\sigma' = 0.61\ kPa$).

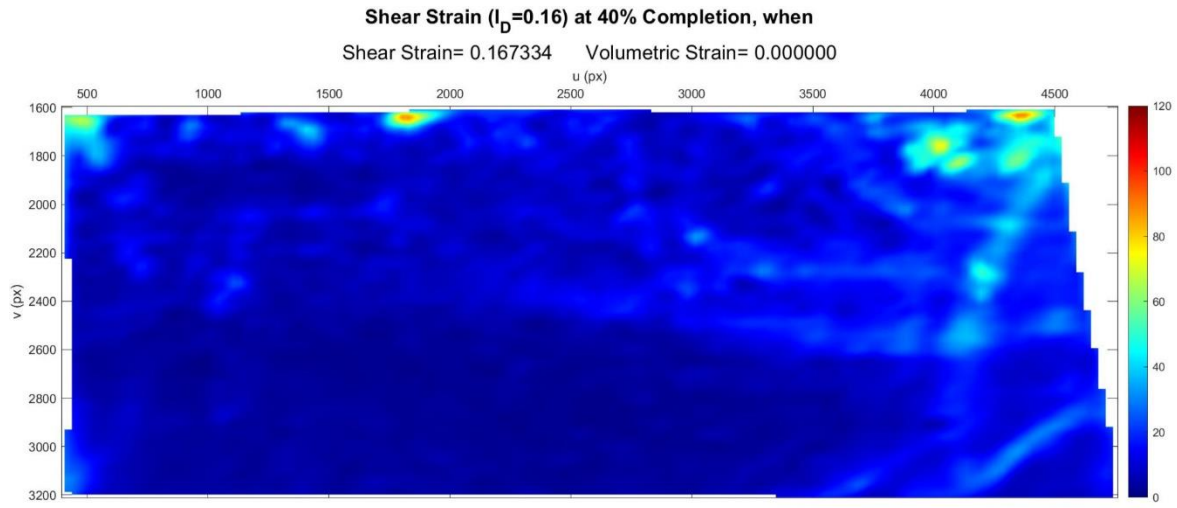

Figure C.7. Shear Strain Field at 40% Completion ($I_D = 0.16$ & $\sigma' = 0.61\ kPa$).

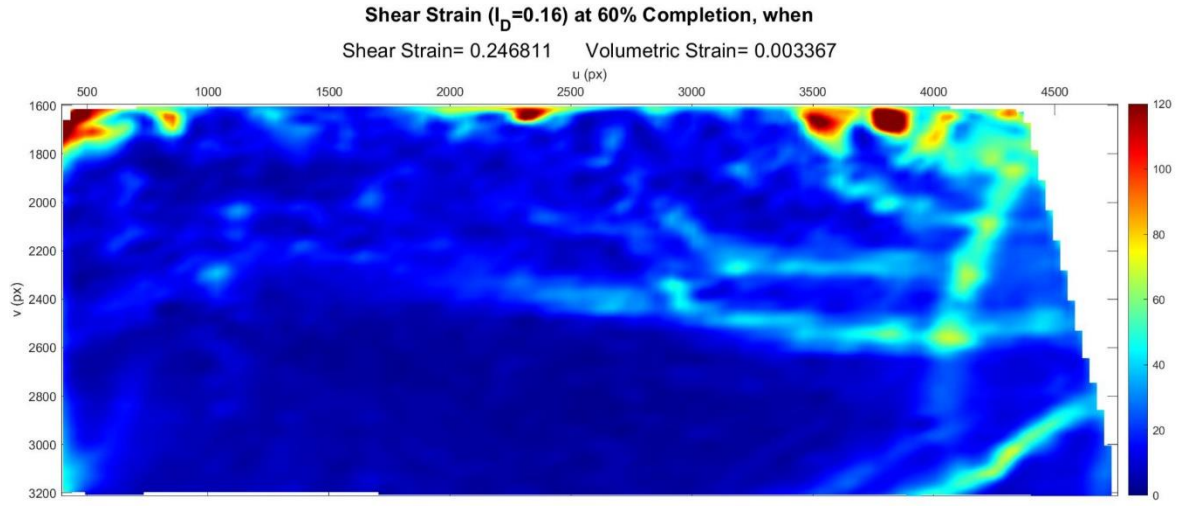

Figure C.8. Shear Strain Field at 60% Completion ($I_D = 0.16$ & $\sigma' = 0.61\ kPa$).

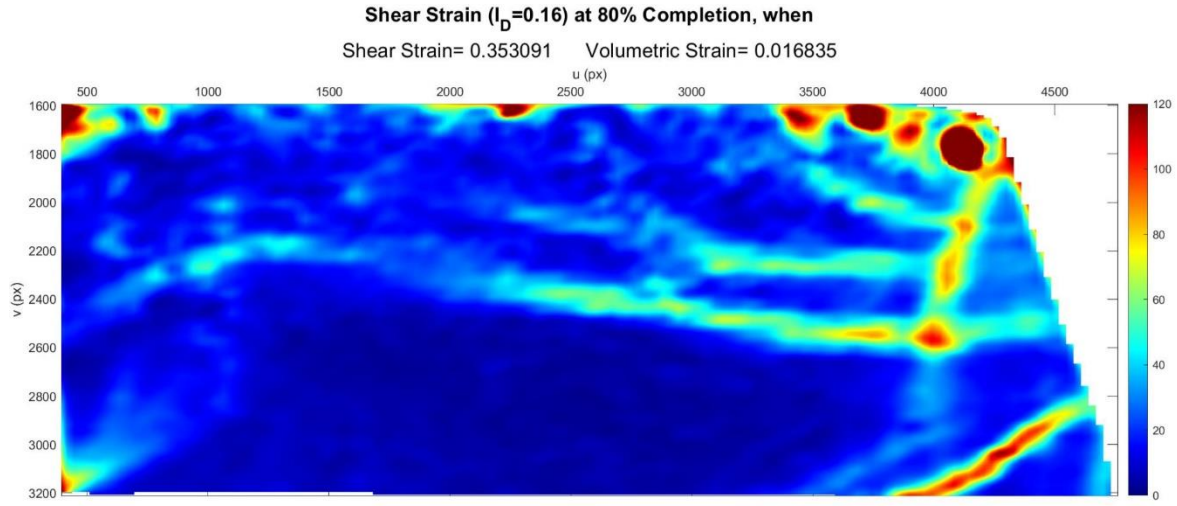

Figure C.9. Shear Strain Field at 80% Completion ($I_D = 0.16$ & $\sigma' = 0.61\ kPa$).

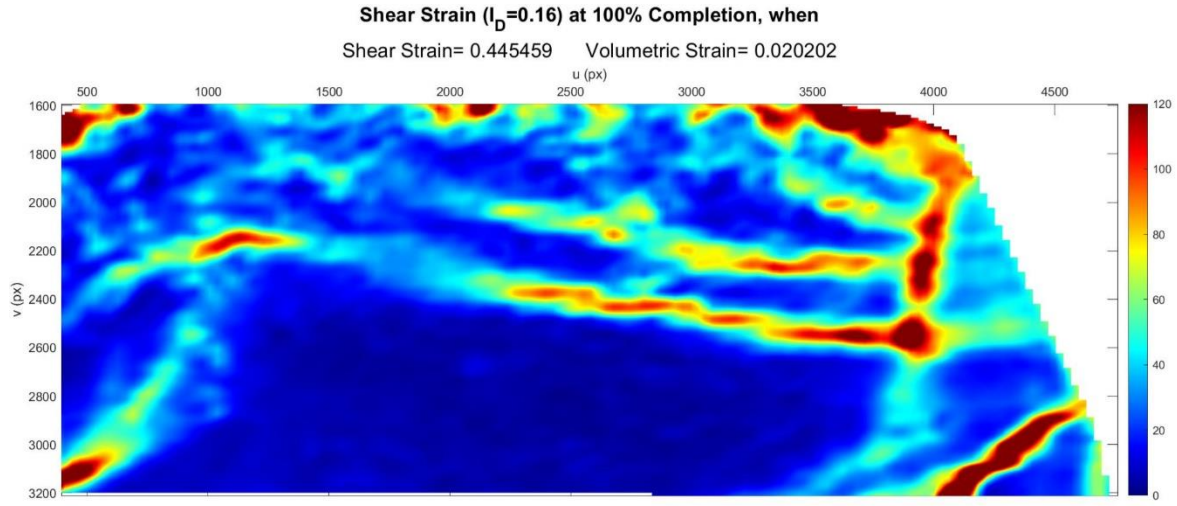

Figure C.10. Shear Strain Field at 100% Completion ($I_D = 0.16$ & $\sigma' = 0.61\ kPa$).

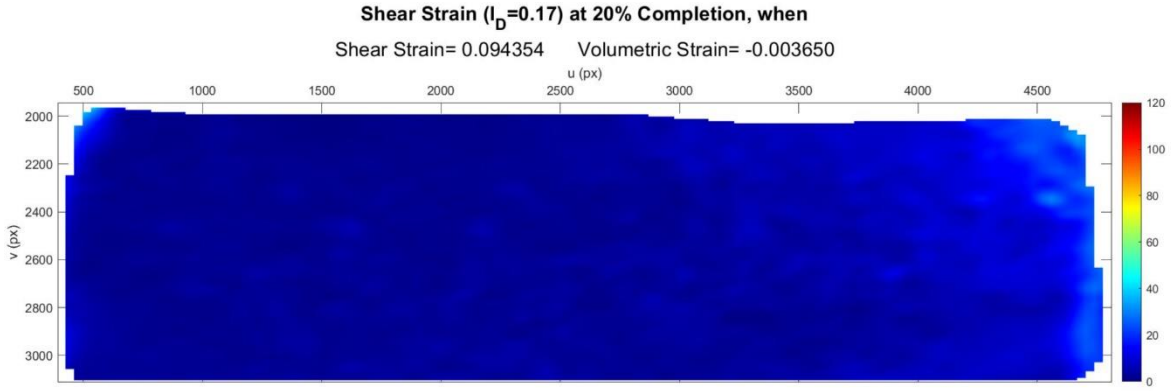

Figure C.11. Shear Strain Field at 20% Completion ($I_D = 0.17$ & $\sigma' = 0.44\ kPa$).

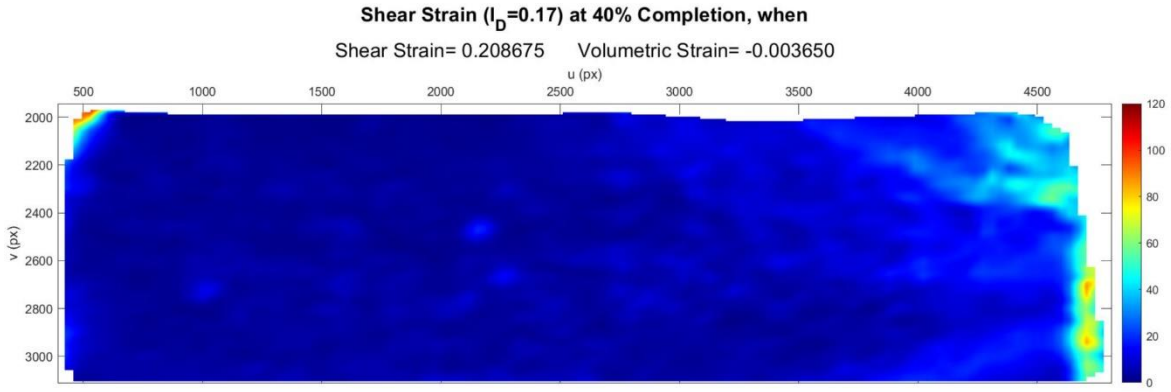

Figure C.12. Shear Strain Field at 40% Completion ($I_D = 0.17$ & $\sigma' = 0.44\ kPa$).

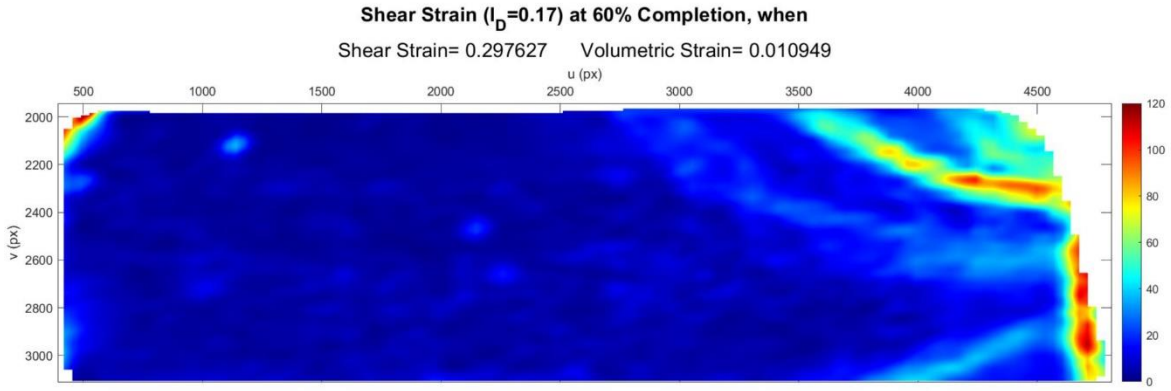

Figure C.13. Shear Strain Field at 60% Completion ($I_D = 0.17$ & $\sigma' = 0.44\ kPa$).

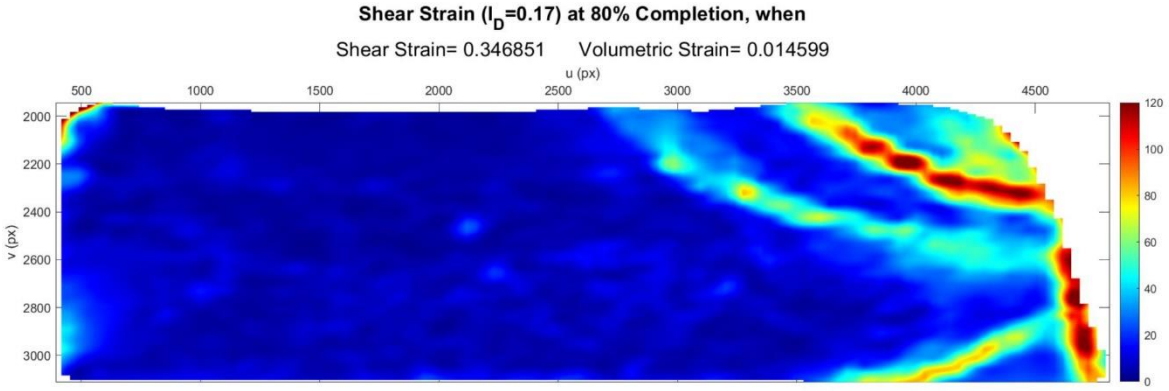

Figure C.14. Shear Strain Field at 80% Completion ($I_D = 0.17$ & $\sigma' = 0.44\ kPa$).

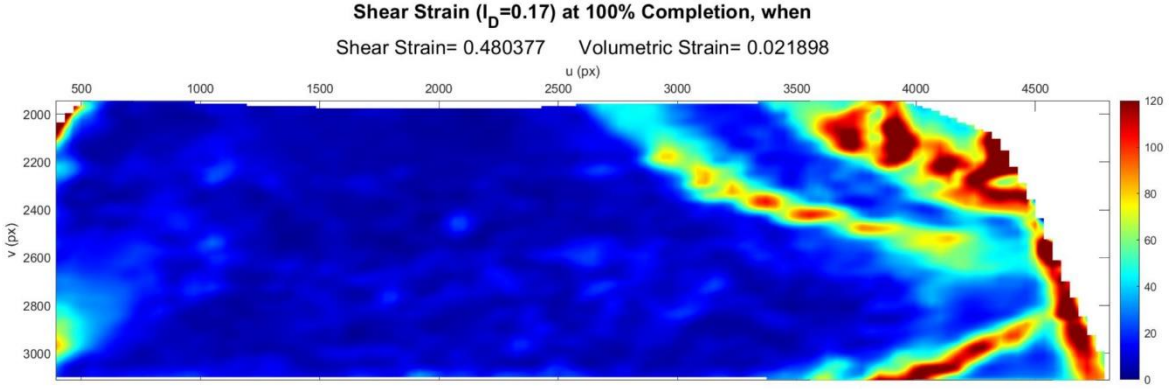

Figure C.15. Shear Strain Field at 100% Completion ($I_D = 0.17$ & $\sigma' = 0.44\ kPa$).

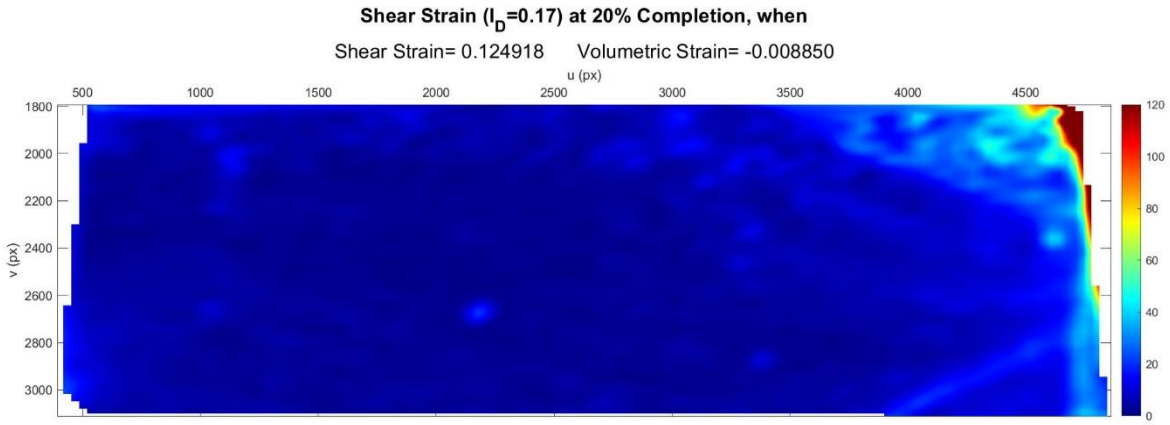

Figure C.16. Shear Strain Field at 20% Completion ($I_D = 0.17$ & $\sigma' = 0.52\ kPa$).

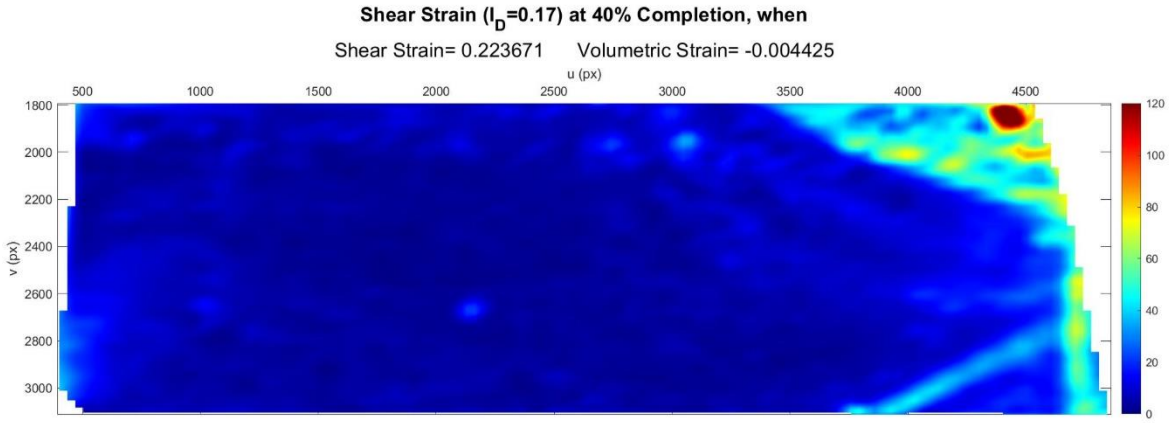

Figure C.17. Shear Strain Field at 40% Completion ($I_D = 0.17$ & $\sigma' = 0.52\ kPa$).

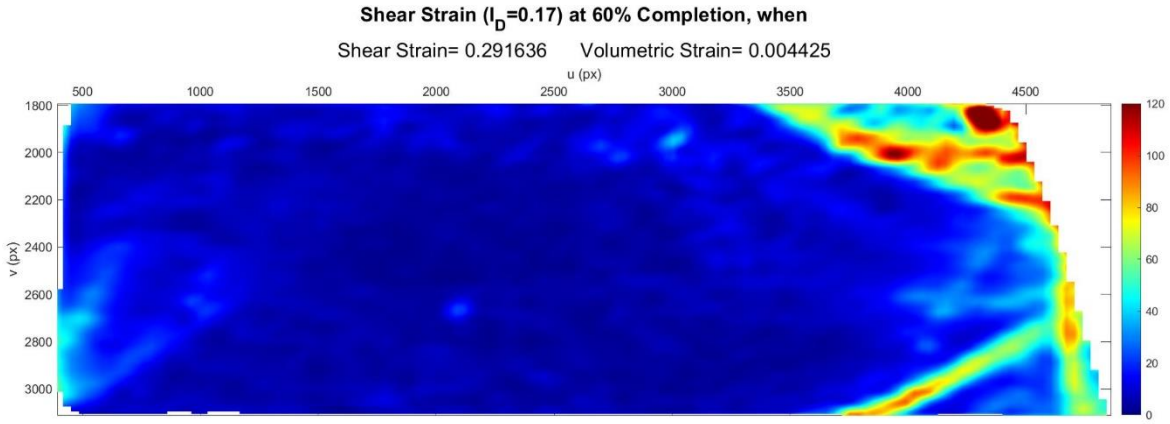

Figure C.18. Shear Strain Field at 60% Completion ($I_D = 0.17$ & $\sigma' = 0.52\ kPa$).

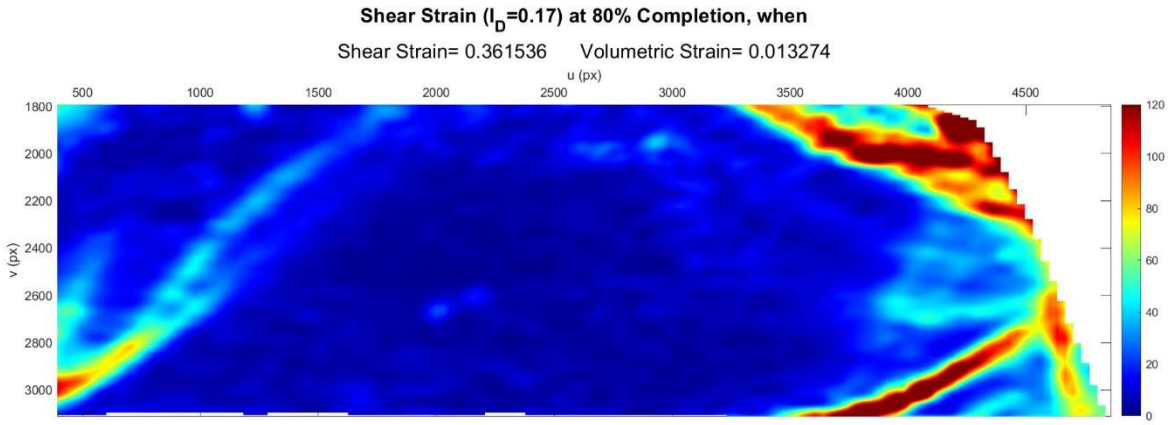

Figure C.19. Shear Strain Field at 80% Completion ($I_D = 0.17$ & $\sigma' = 0.52\ kPa$).

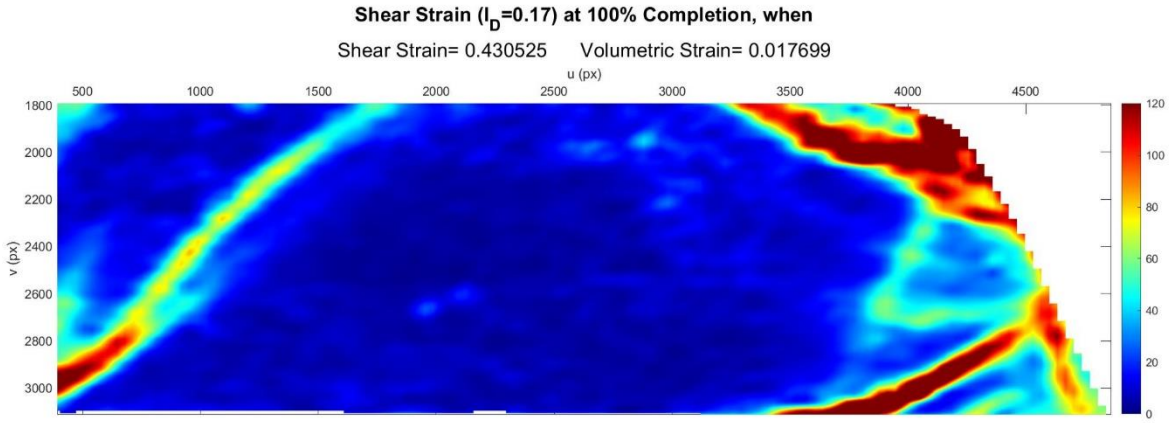

Figure C.20. Shear Strain Field at 100% Completion ($I_D = 0.17$ & $\sigma' = 0.52\ kPa$).

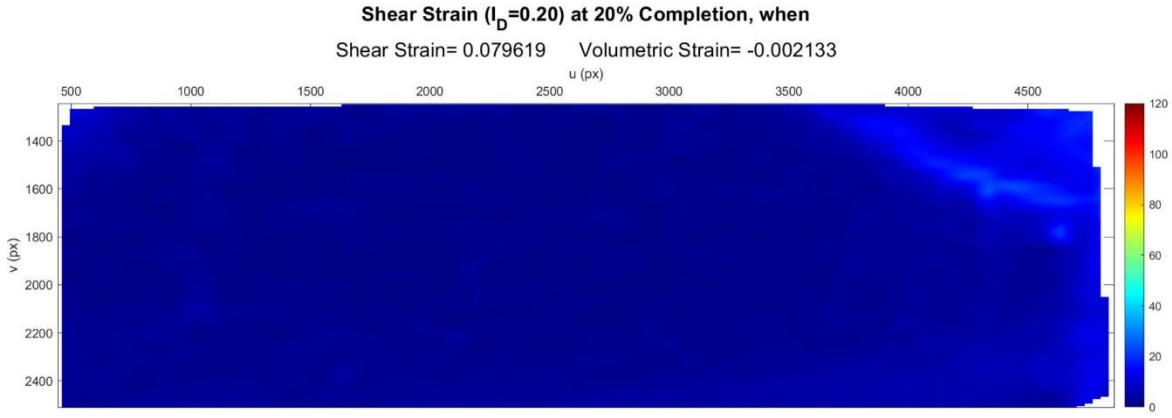

Figure C.21. Shear Strain Field at 20% Completion ($I_D = 0.20$ & $\sigma' = 0.49\ kPa$).

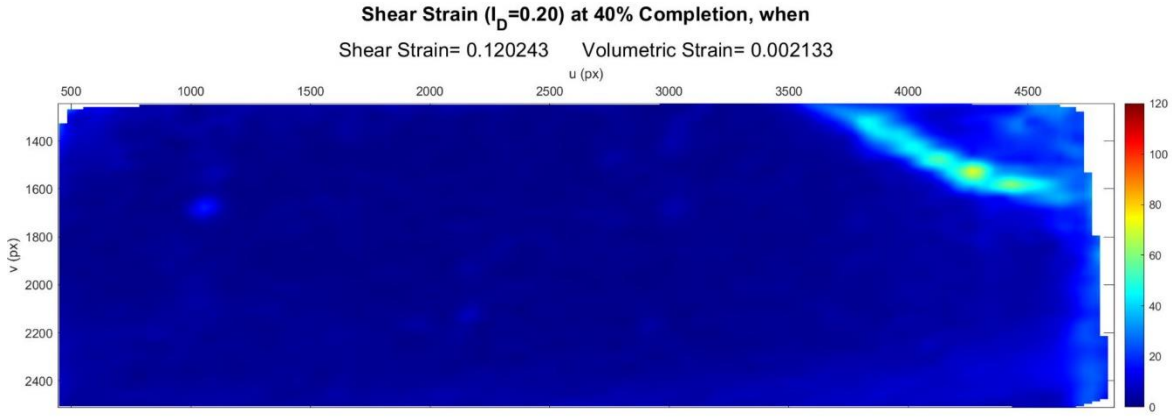

Figure C.22. Shear Strain Field at 40% Completion ($I_D = 0.20$ & $\sigma' = 0.49\ kPa$).

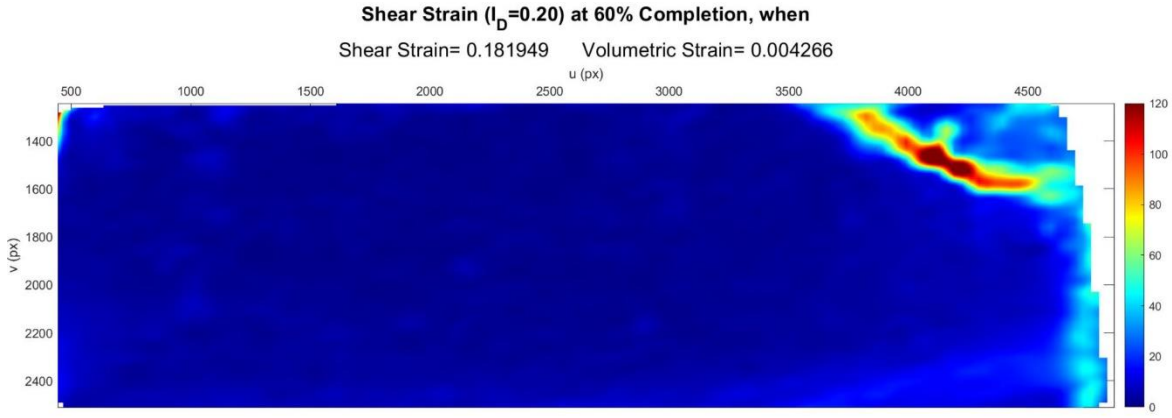

Figure C.23. Shear Strain Field at 60% Completion ($I_D = 0.20$ & $\sigma' = 0.49\ kPa$).

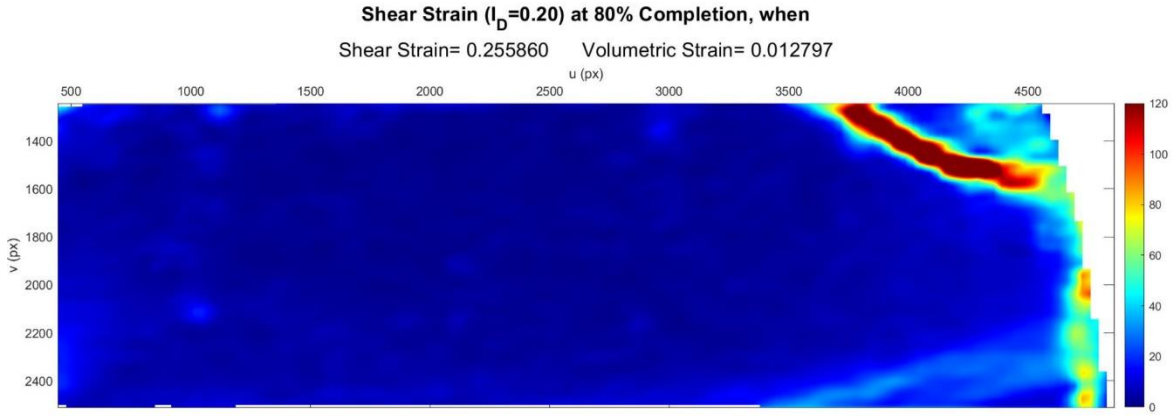

Figure C.24. Shear Strain Field at 80% Completion ($I_D = 0.20 \ \& \ \sigma' = 0.49 \ kPa$).

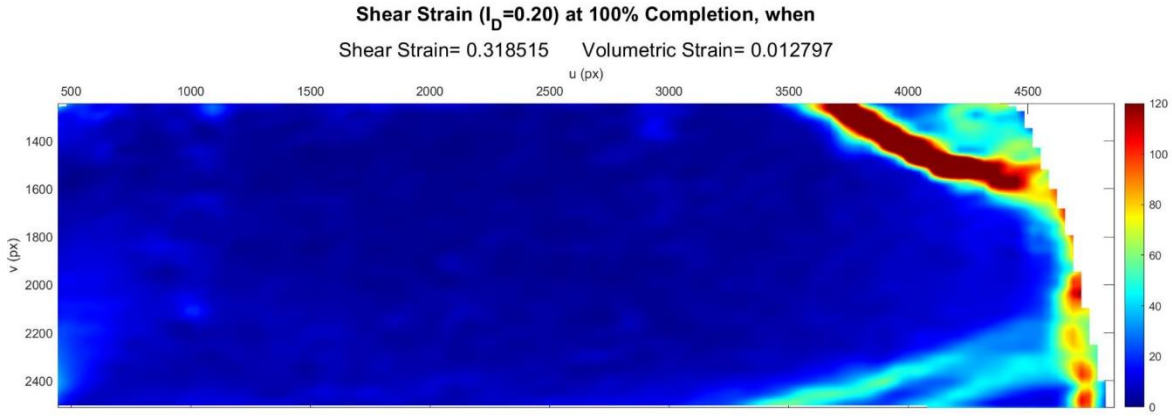

Figure C.25. Shear Strain Field at 100% Completion ($I_D = 0.20 \ \& \ \sigma' = 0.49 \ kPa$).

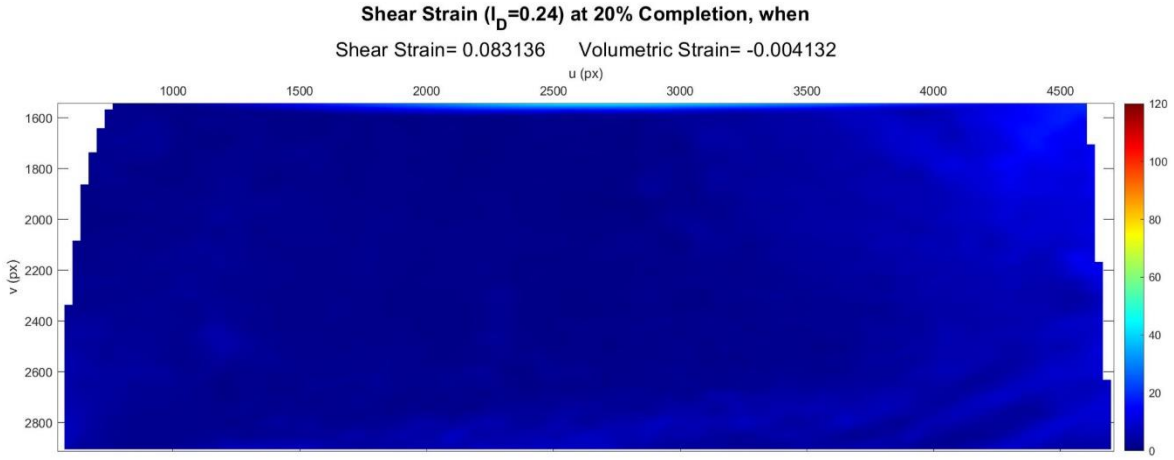

Figure C.26. Shear Strain Field at 20% Completion ($I_D = 0.24$ & $\sigma' = 0.58\,kPa$).

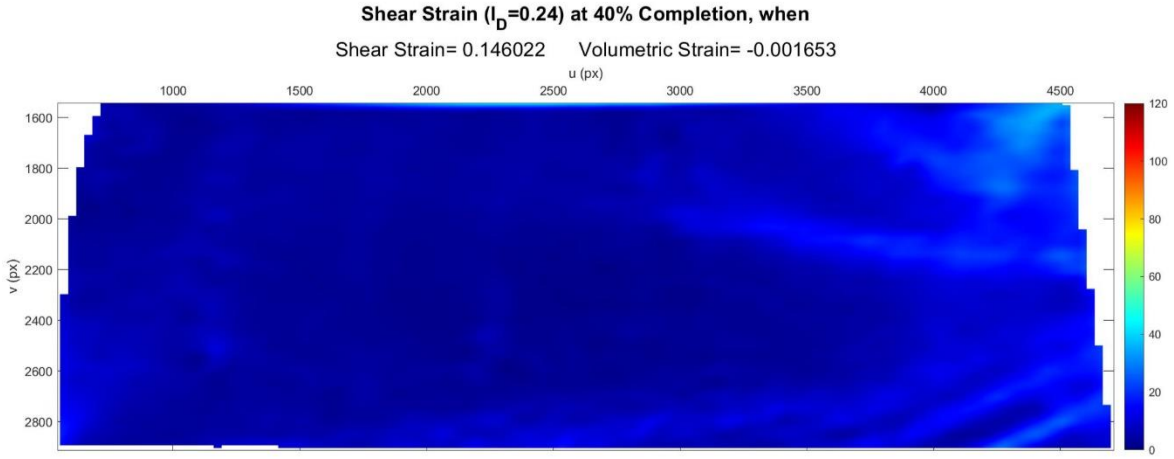

Figure C.27. Shear Strain Field at 40% Completion ($I_D = 0.24$ & $\sigma' = 0.58\,kPa$).

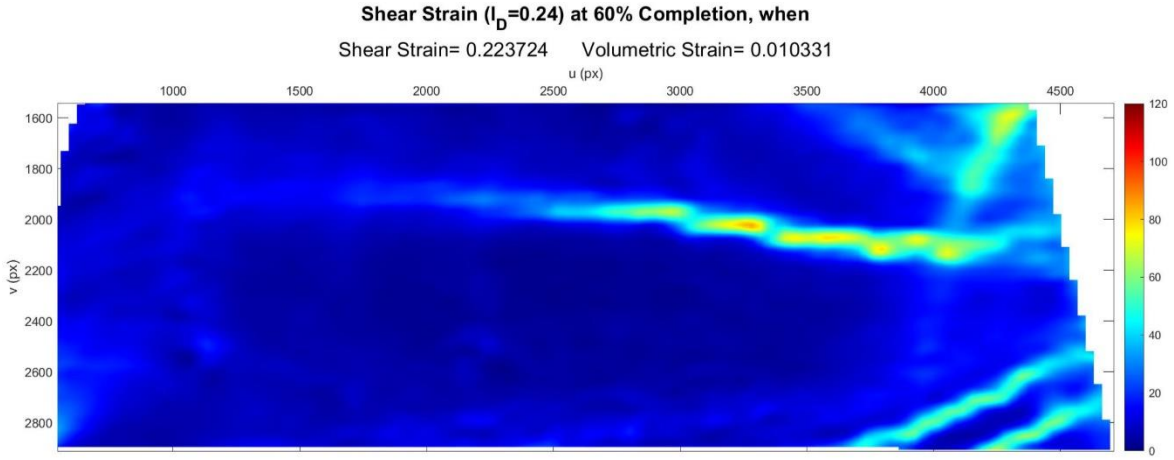

Figure C.28. Shear Strain Field at 60% Completion ($I_D = 0.24$ & $\sigma' = 0.58\,kPa$).

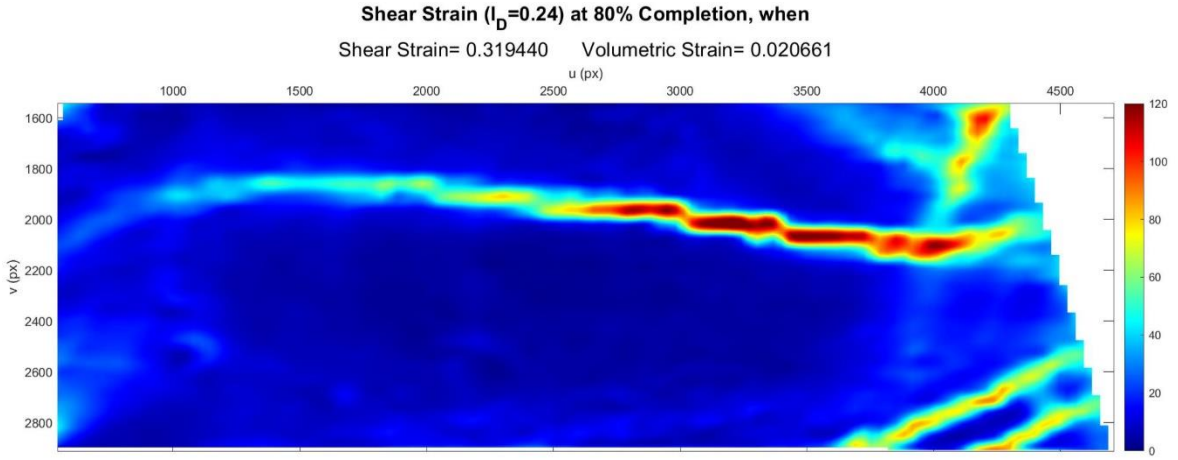

Figure C.29. Shear Strain Field at 80% Completion ($I_D = 0.24$ & $\sigma' = 0.58\ kPa$).

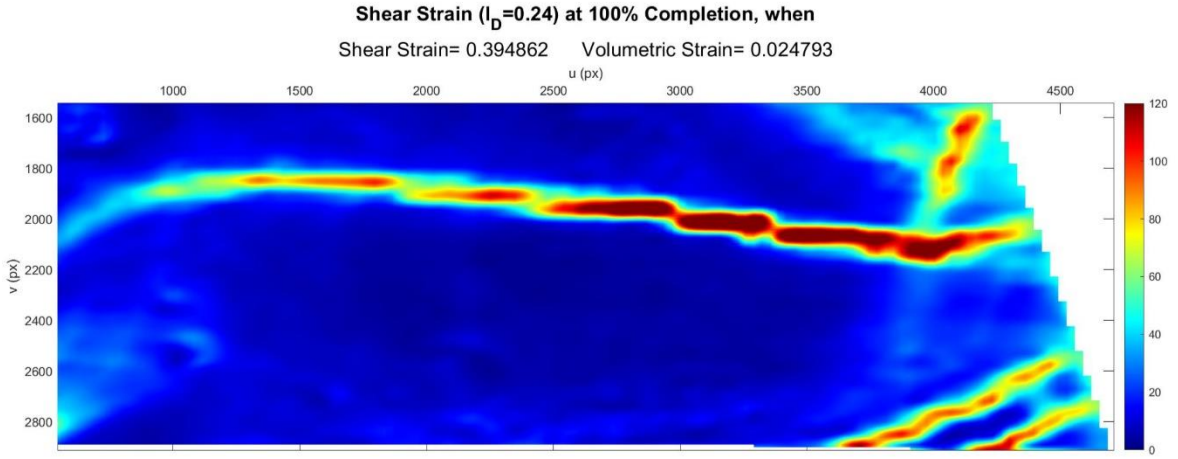

Figure C.30. Shear Strain Field at 100% Completion ($I_D = 0.24$ & $\sigma' = 0.58\ kPa$).

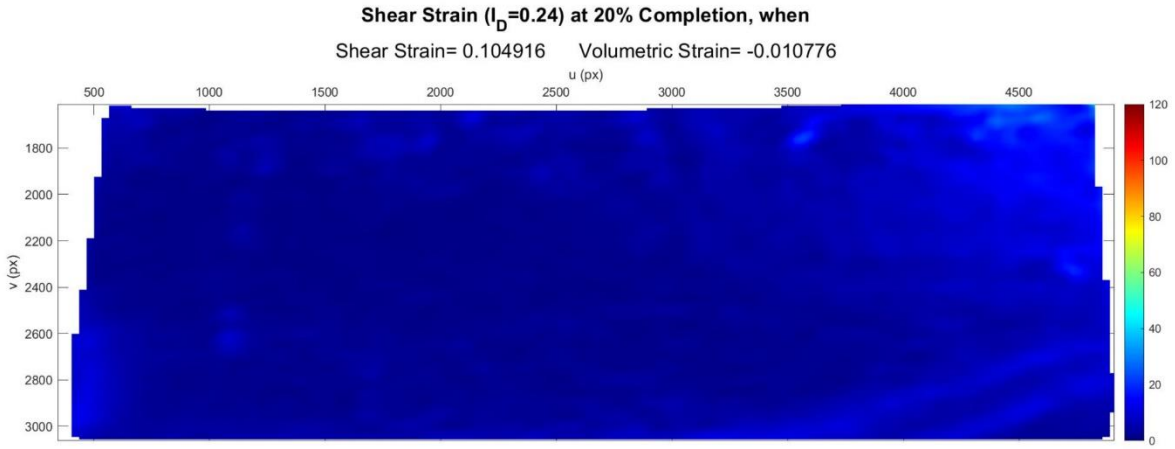

Figure C.31. Shear Strain Field at 20% Completion ($I_D = 0.24$ & $\sigma' = 0.59\ kPa$).

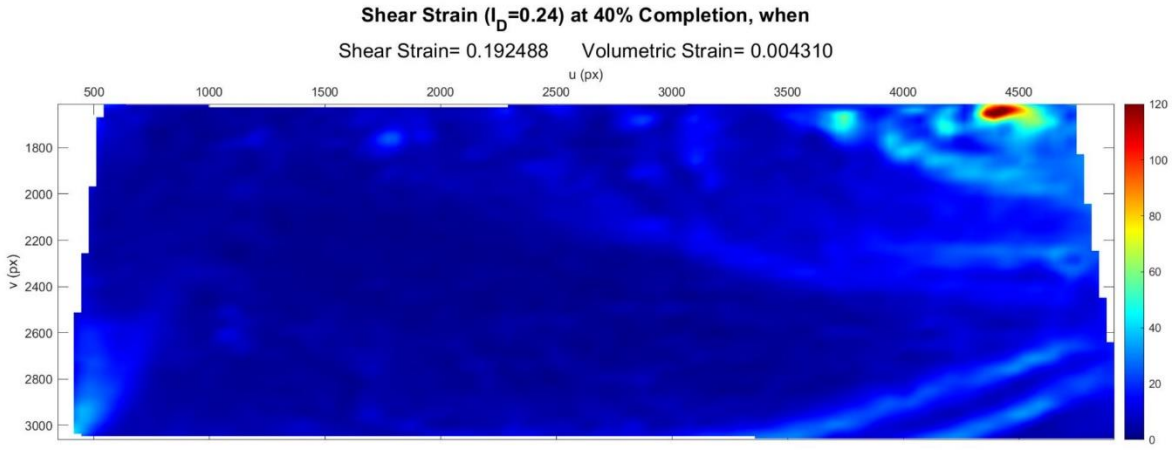

Figure C.32. Shear Strain Field at 40% Completion ($I_D = 0.24$ & $\sigma' = 0.59\ kPa$).

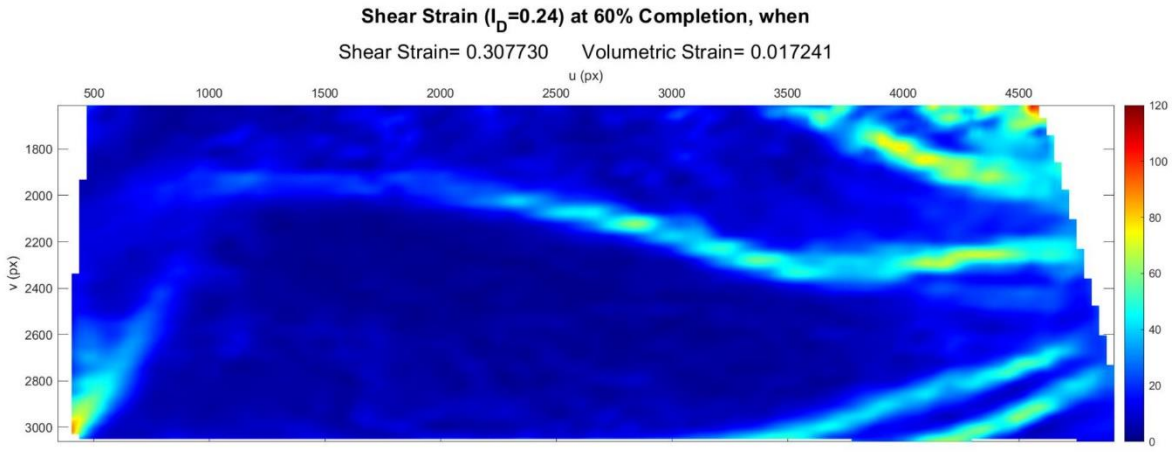

Figure C.33. Shear Strain Field at 60% Completion ($I_D = 0.24$ & $\sigma' = 0.59\ kPa$).

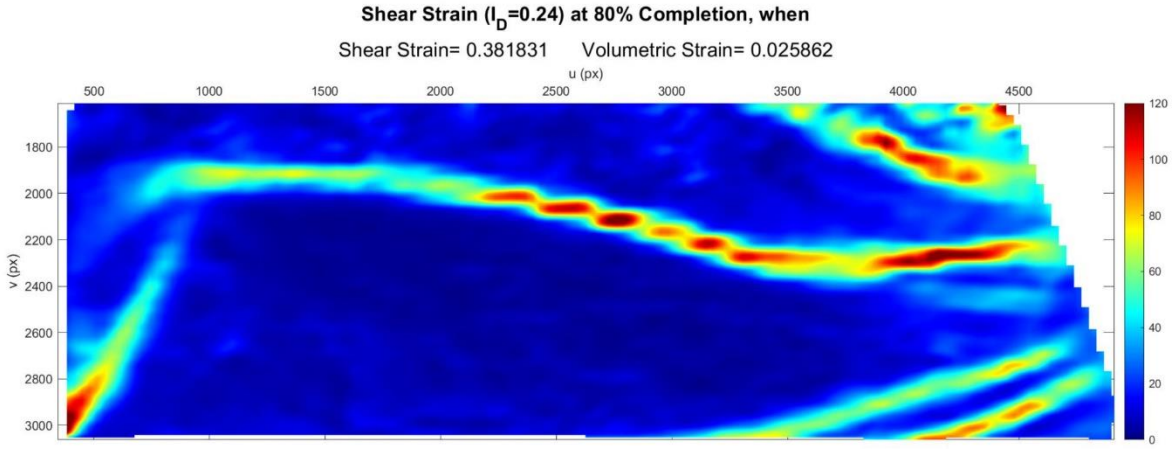

Figure C.34. Shear Strain Field at 80% Completion ($I_D = 0.24$ & $\sigma' = 0.59\ kPa$).

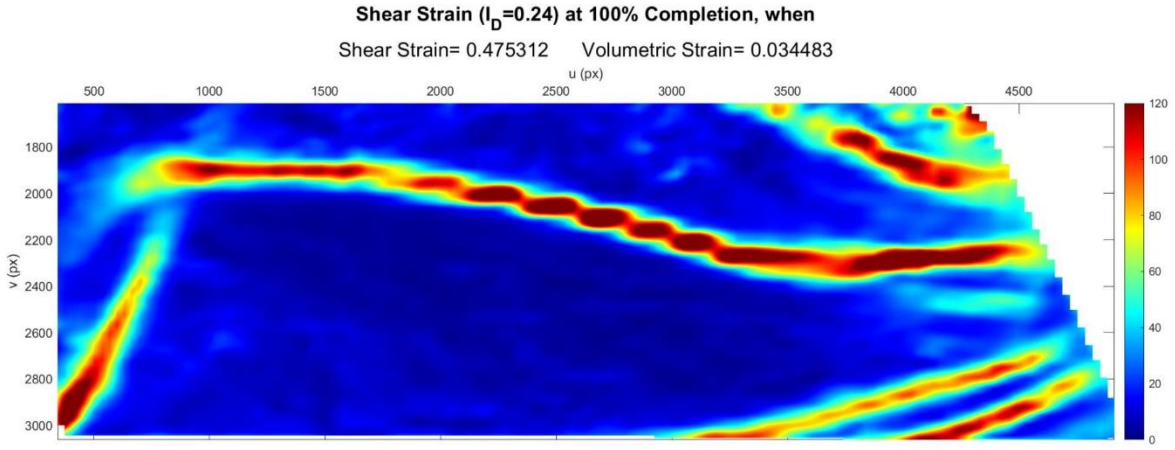

Figure C.35. Shear Strain Field at 100% Completion ($I_D = 0.24$ & $\sigma' = 0.59\ kPa$).

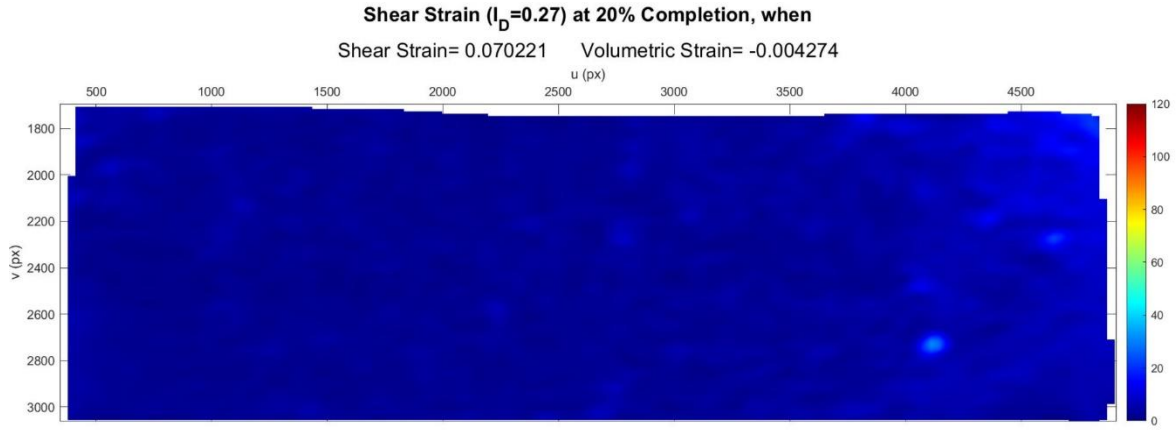

Figure C.36. Shear Strain Field at 20% Completion ($I_D = 0.27$ & $\sigma' = 0.53\ kPa$).

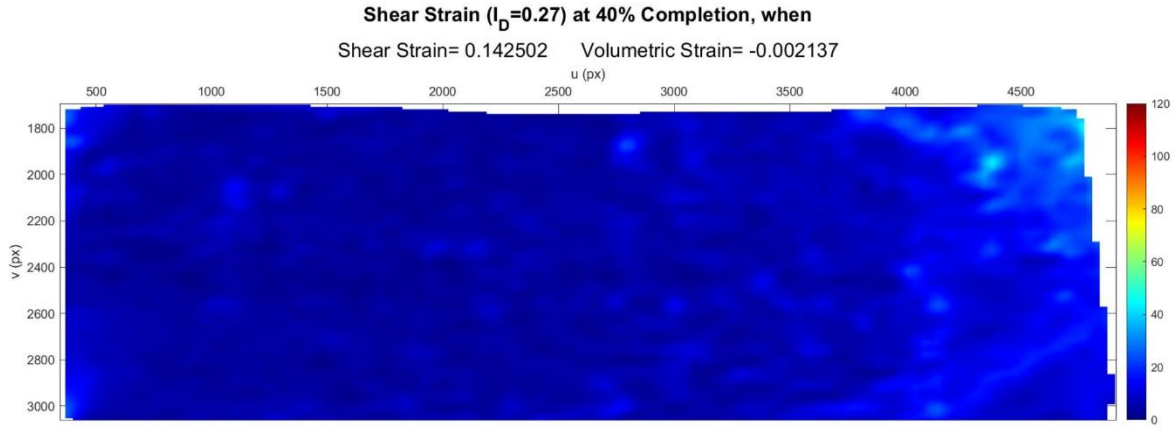

Figure C.37. Shear Strain Field at 40% Completion ($I_D = 0.27$ & $\sigma' = 0.53\ kPa$).

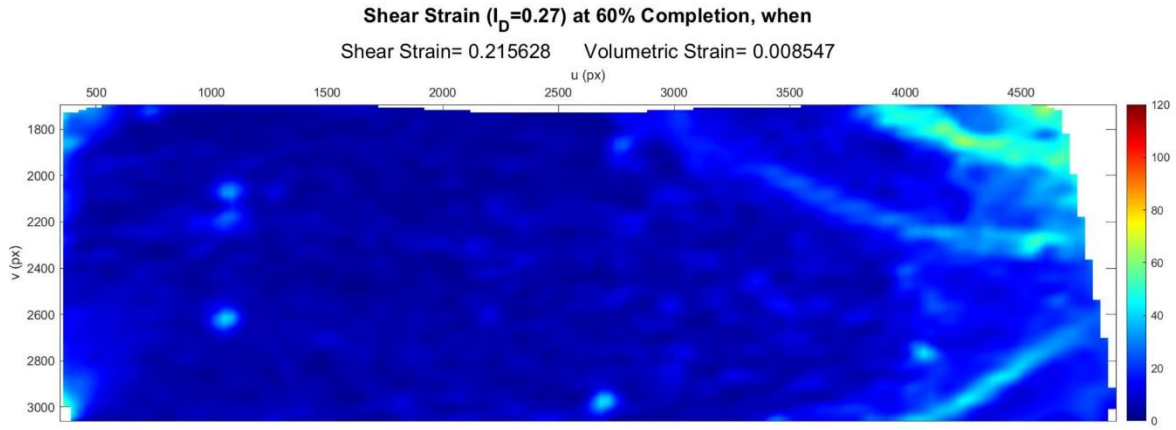

Figure C.38. Shear Strain Field at 60% Completion ($I_D = 0.27$ & $\sigma' = 0.53\ kPa$).

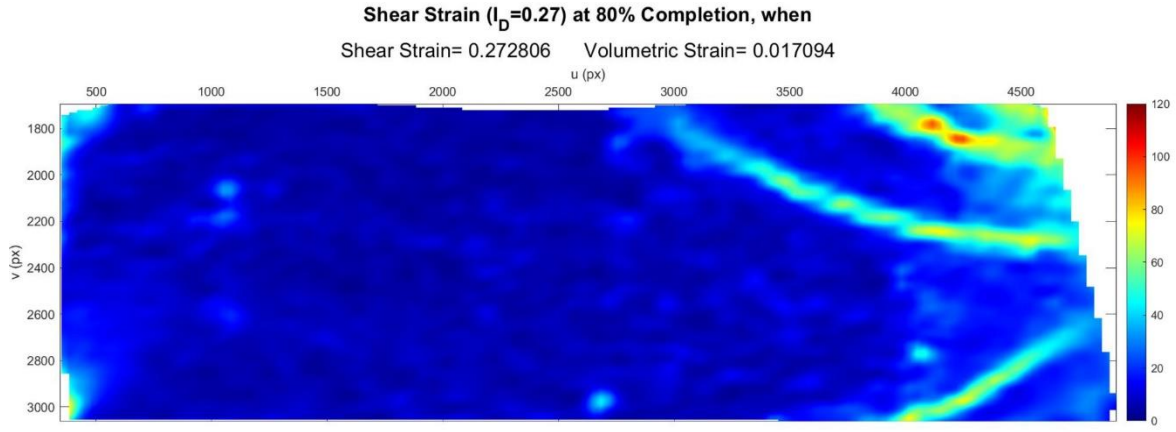

Figure C.39. Shear Strain Field at 80% Completion ($I_D = 0.27$ & $\sigma' = 0.53\ kPa$).

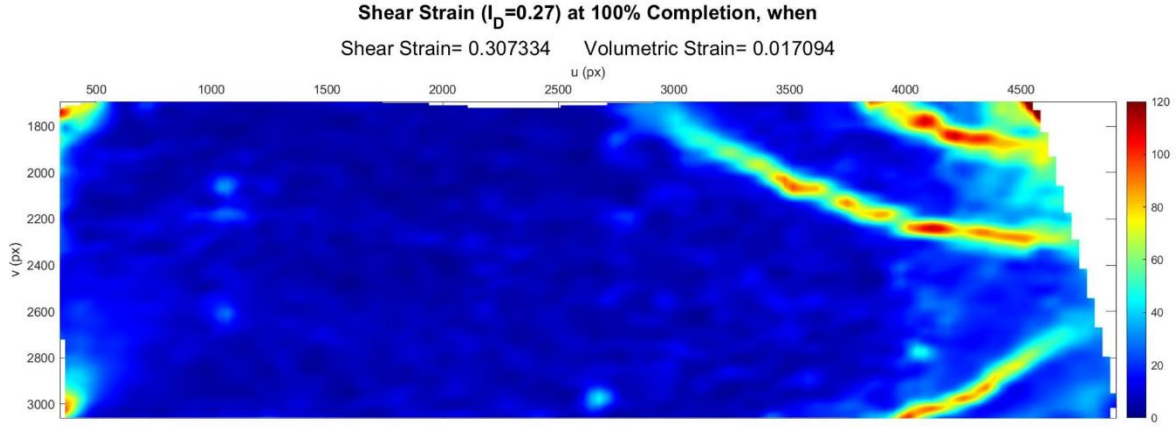

Figure C.40. Shear Strain Field at 100% Completion ($I_D = 0.27$ & $\sigma' = 0.53\ kPa$).

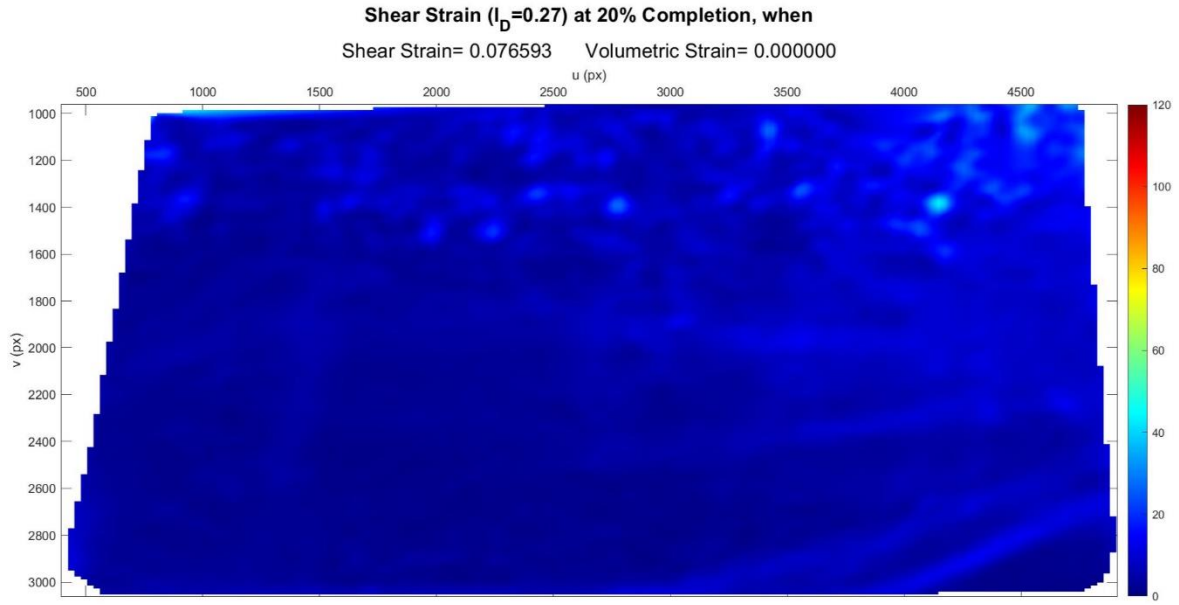

Figure C.41. Shear Strain Field at 20% Completion ($I_D = 0.27$ & $\sigma' = 0.77\ kPa$).

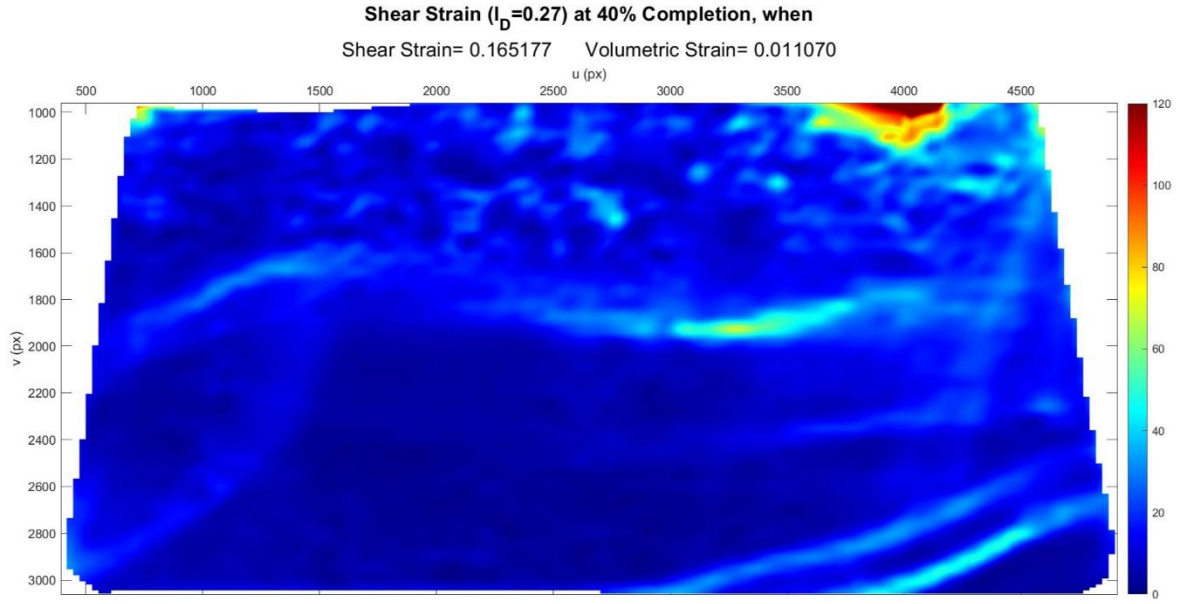

Figure C.42. Shear Strain Field at 40% Completion ($I_D = 0.27$ & $\sigma' = 0.77\ kPa$).

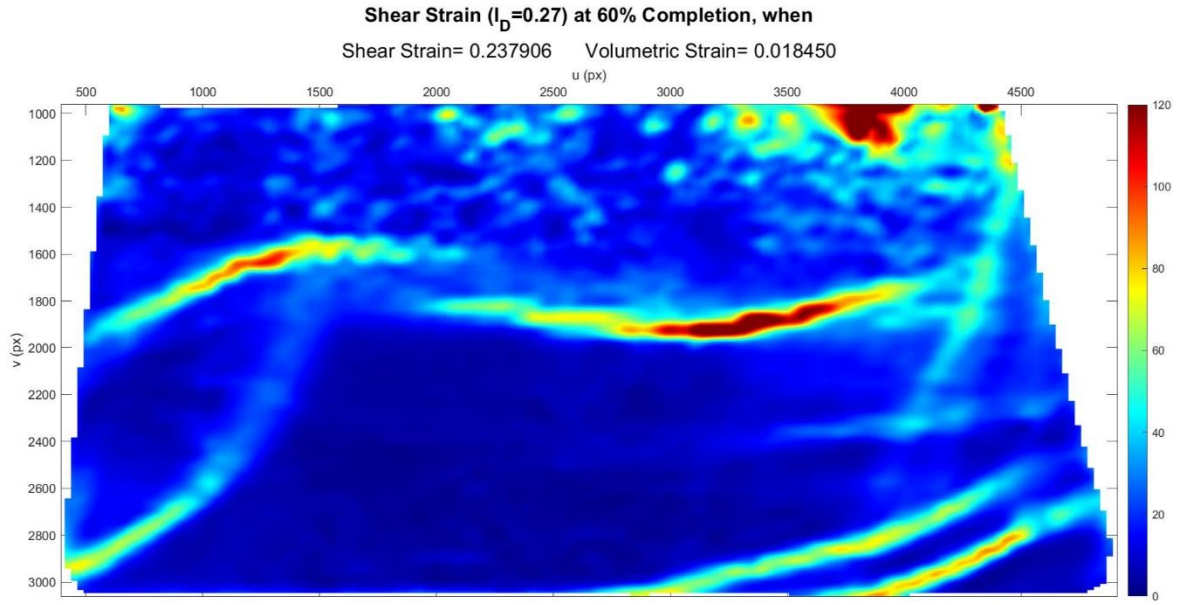

Figure C.43. Shear Strain Field at 60% Completion ($I_D = 0.27$ & $\sigma' = 0.77\ kPa$).

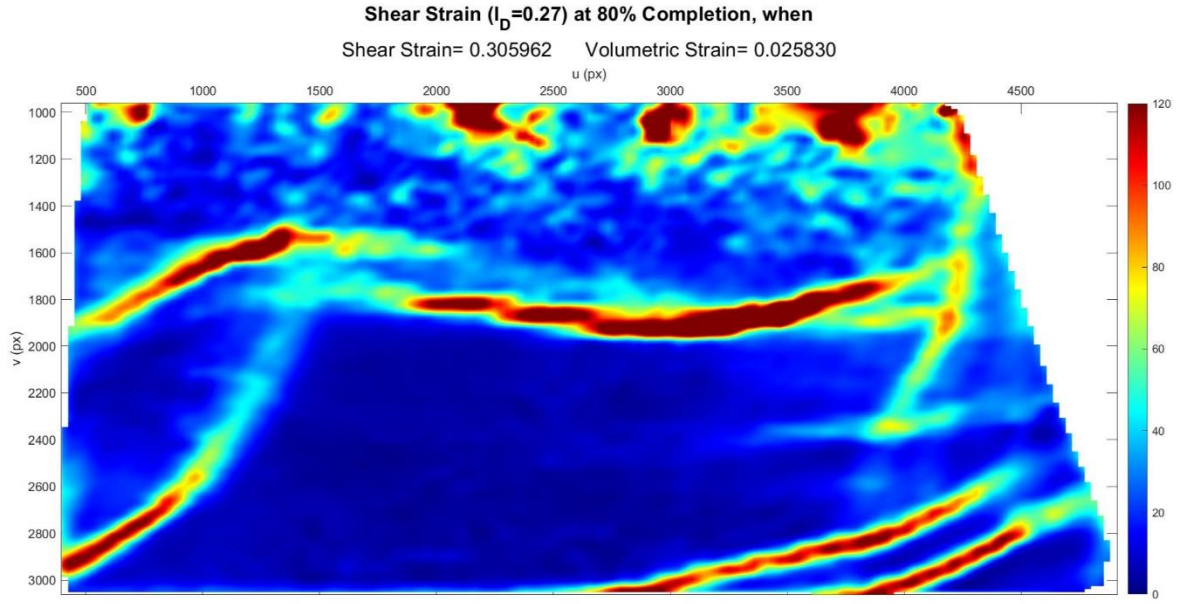

Figure C.44. Shear Strain Field at 80% Completion ($I_D = 0.27$ & $\sigma' = 0.77\ kPa$).

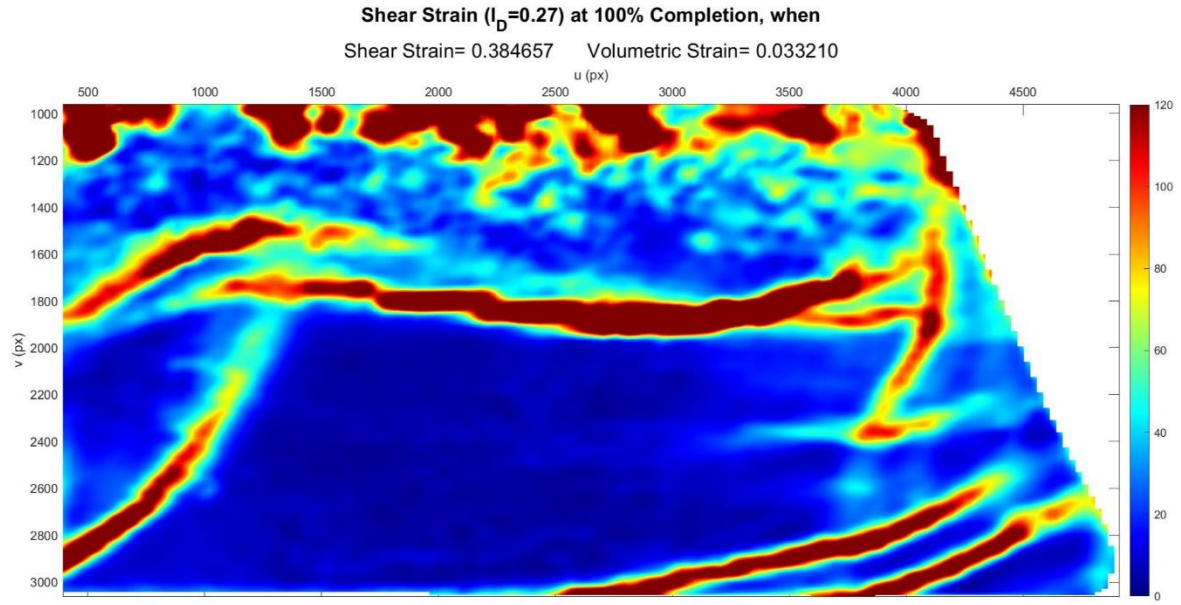

Figure C.45. Shear Strain Field at 100% Completion ($I_D = 0.27$ & $\sigma' = 0.77\ kPa$).

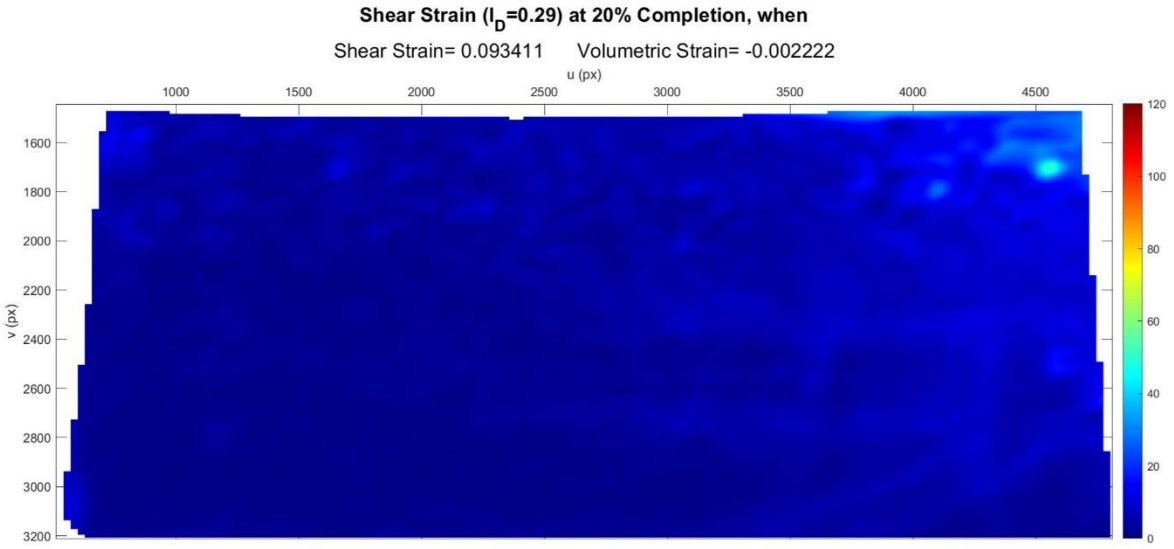

Figure C.46. Shear Strain Field at 20% Completion ($I_D = 0.29$ & $\sigma' = 0.72\ kPa$).

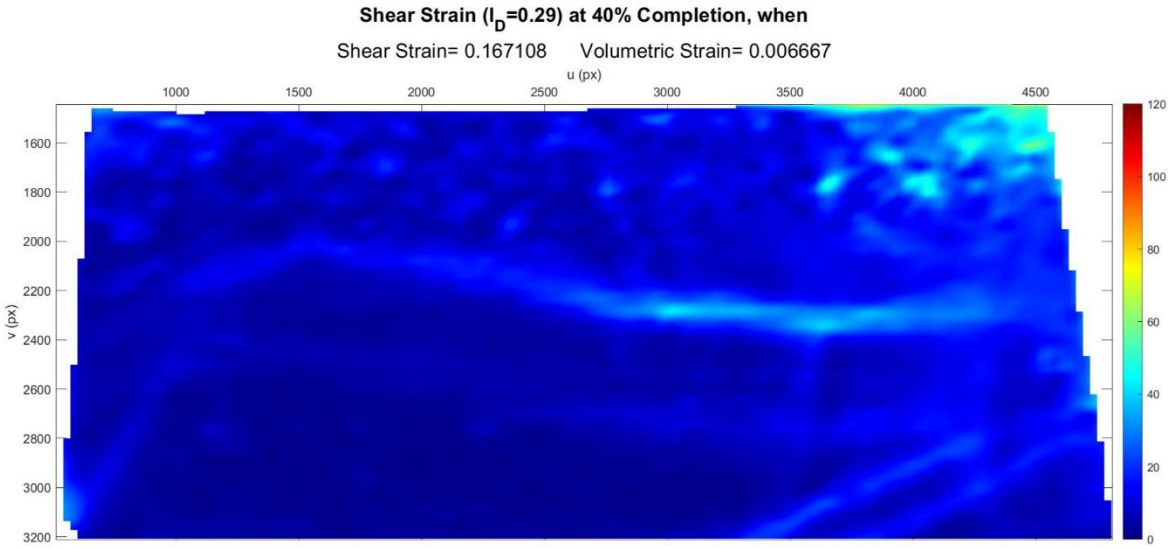

Figure C.47. Shear Strain Field at 40% Completion ($I_D = 0.29$ & $\sigma' = 0.72\ kPa$).

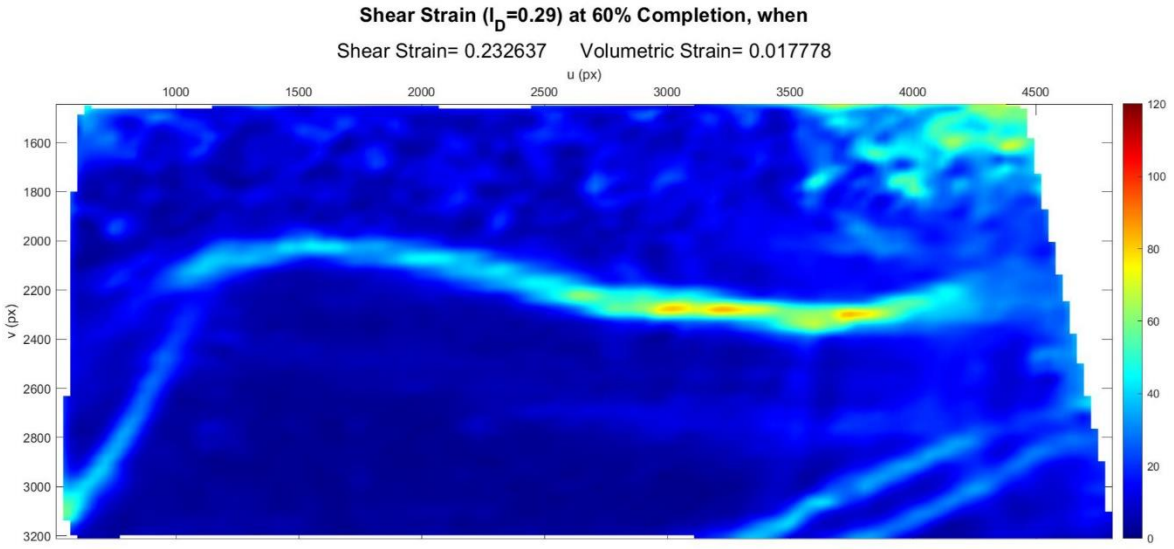

Figure C.48. Shear Strain Field at 60% Completion ($I_D = 0.29$ & $\sigma' = 0.72\ kPa$).

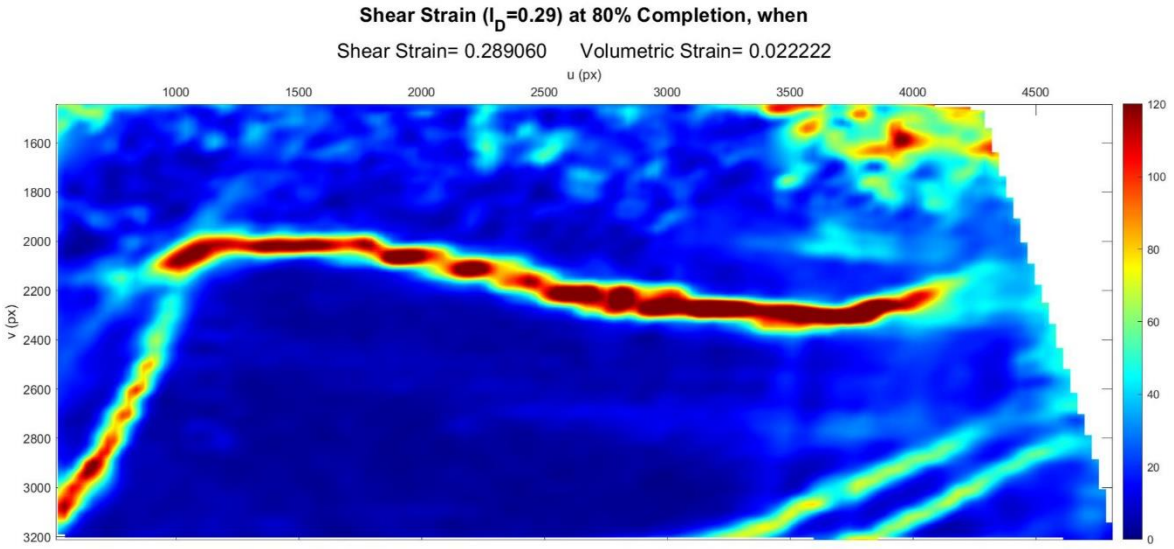

Figure C.49. Shear Strain Field at 80% Completion ($I_D = 0.29$ & $\sigma' = 0.72\ kPa$).

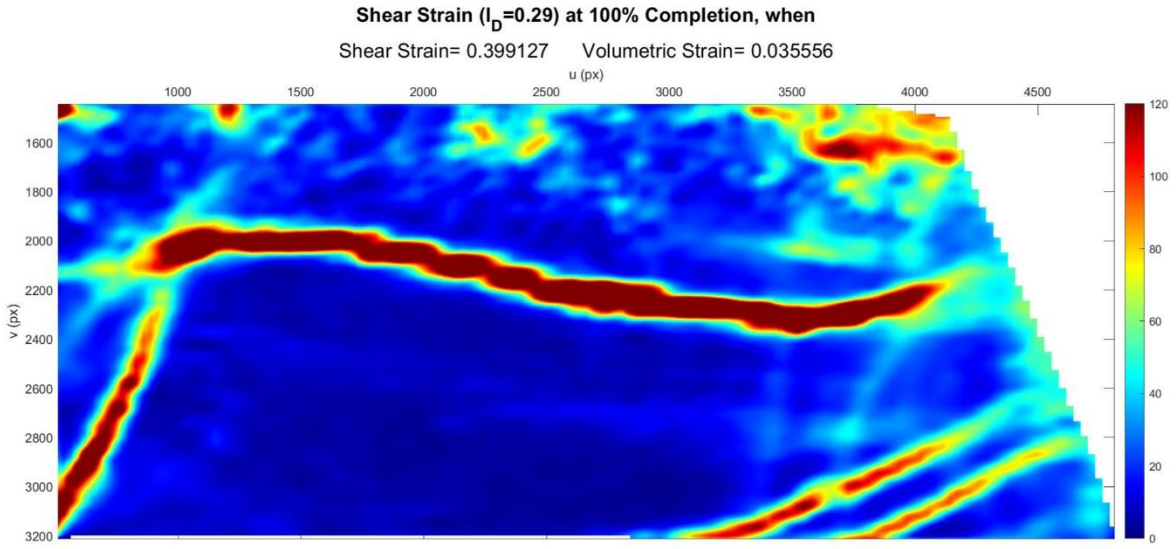

Figure C.50. Shear Strain Field at 100% Completion ($I_D = 0.29$ & $\sigma' = 0.72\ kPa$).

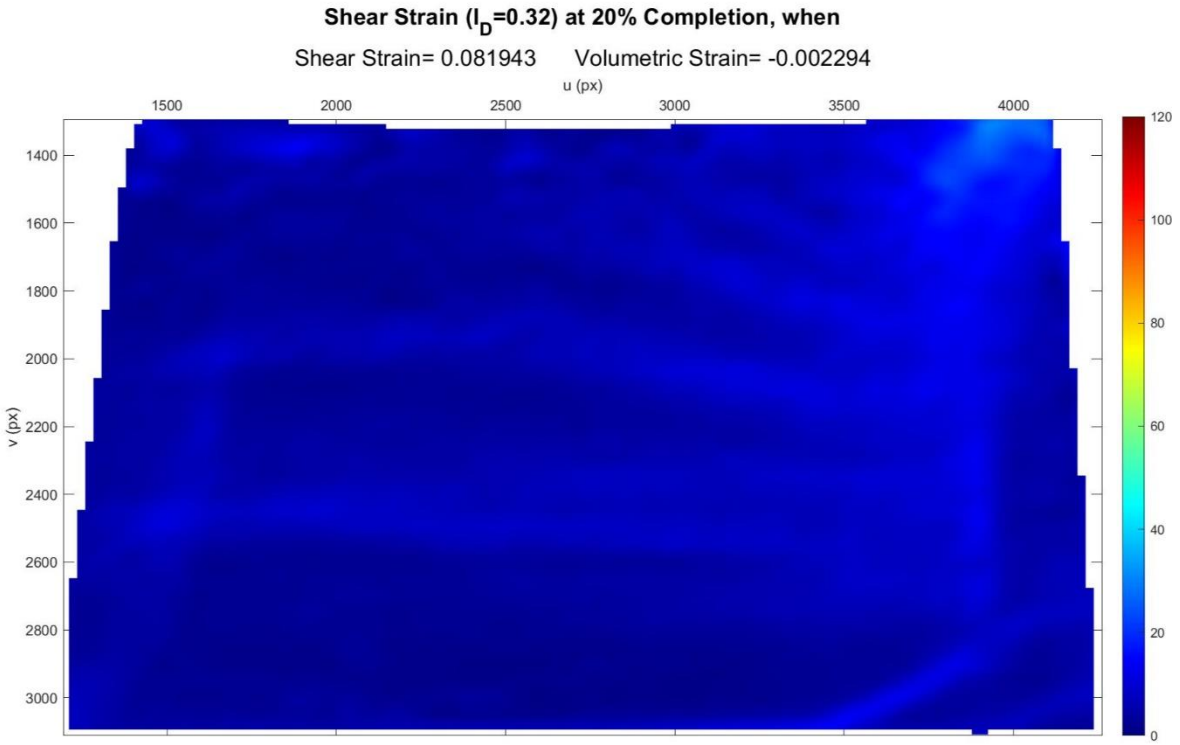

Figure C.51. Shear Strain Field at 20% Completion ($I_D = 0.32$ & $\sigma' = 0.94\ kPa$).

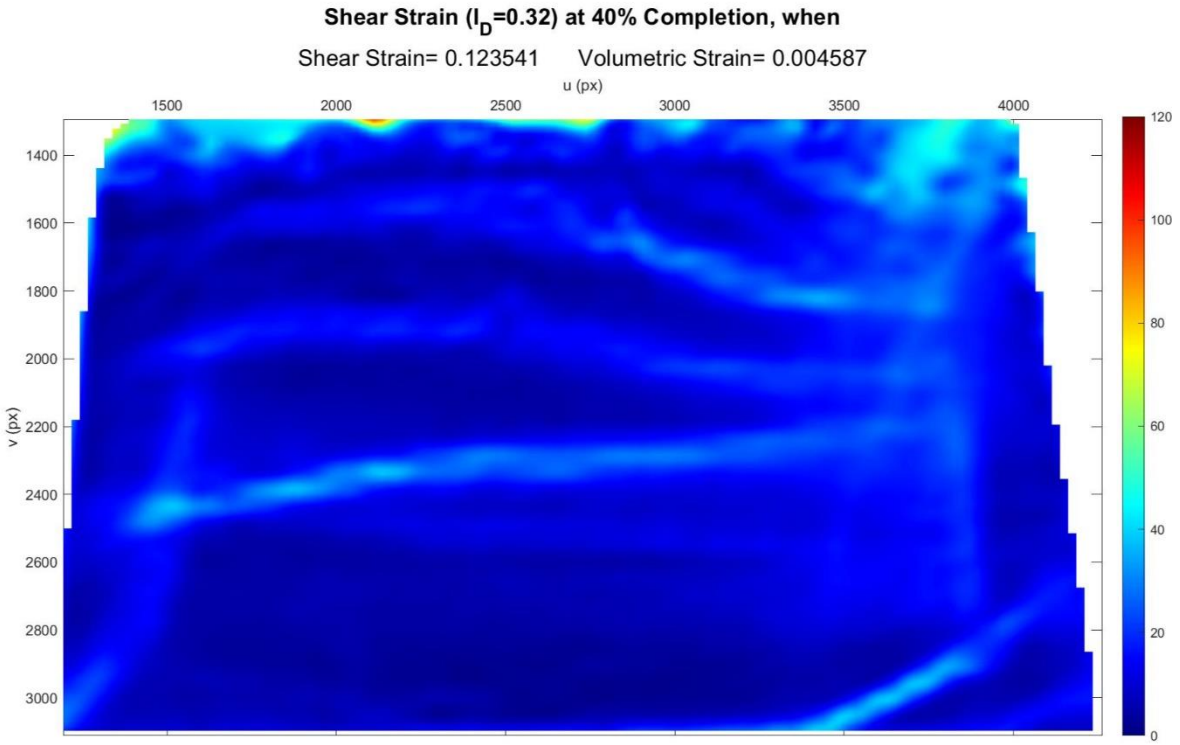

Figure C.52. Shear Strain Field at 40% Completion ($I_D = 0.32$ & $\sigma' = 0.94\ kPa$).

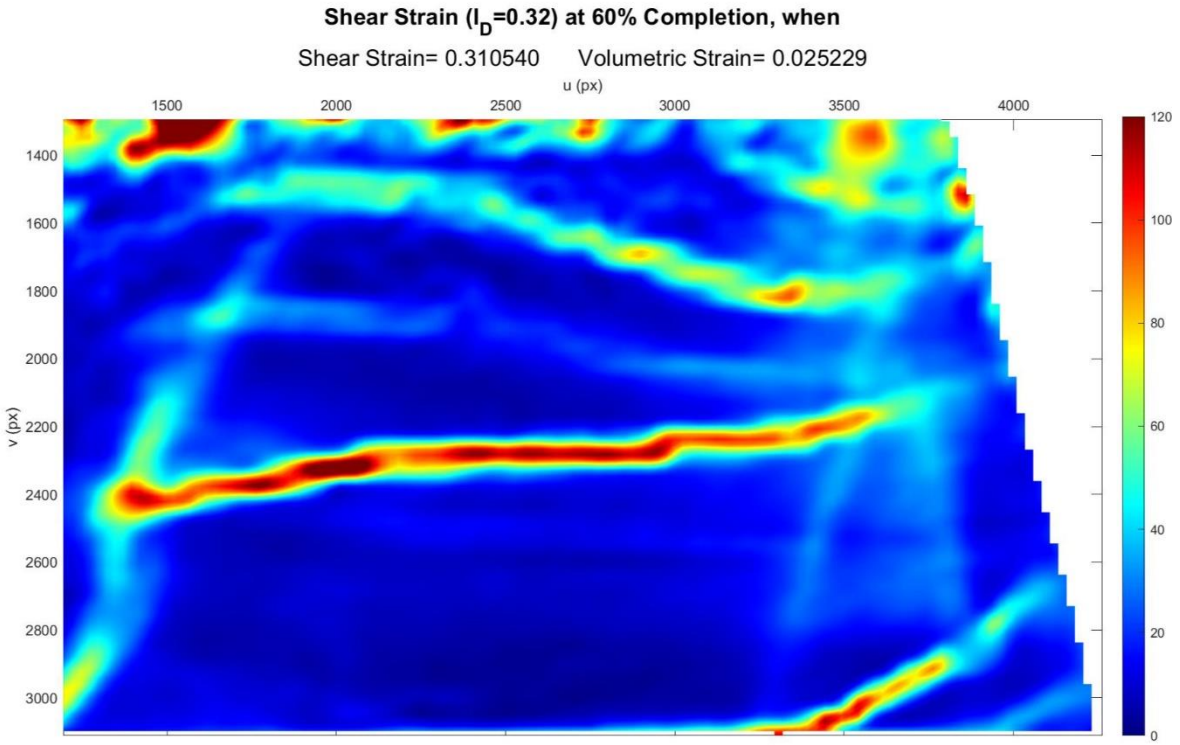

Figure C.53. Shear Strain Field at 60% Completion ($I_D = 0.32$ & $\sigma' = 0.94\ kPa$).

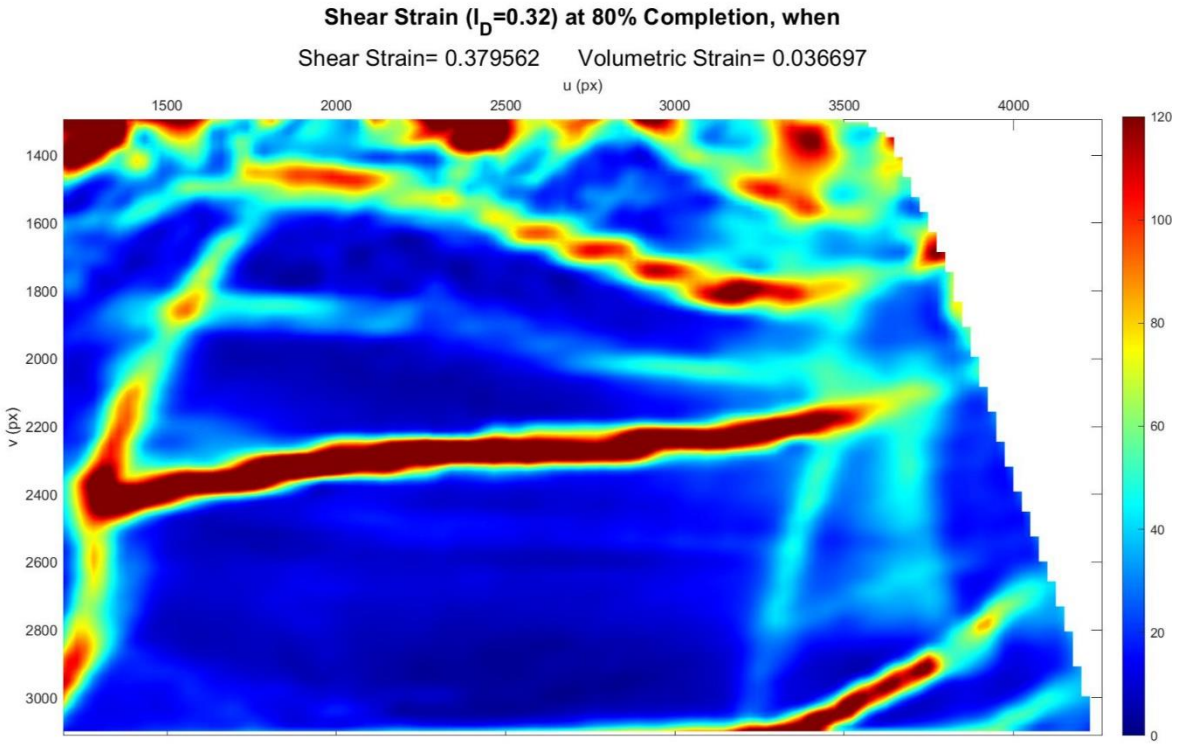

Figure C.54. Shear Strain Field at 80% Completion ($I_D = 0.32$ & $\sigma' = 0.94\ kPa$).

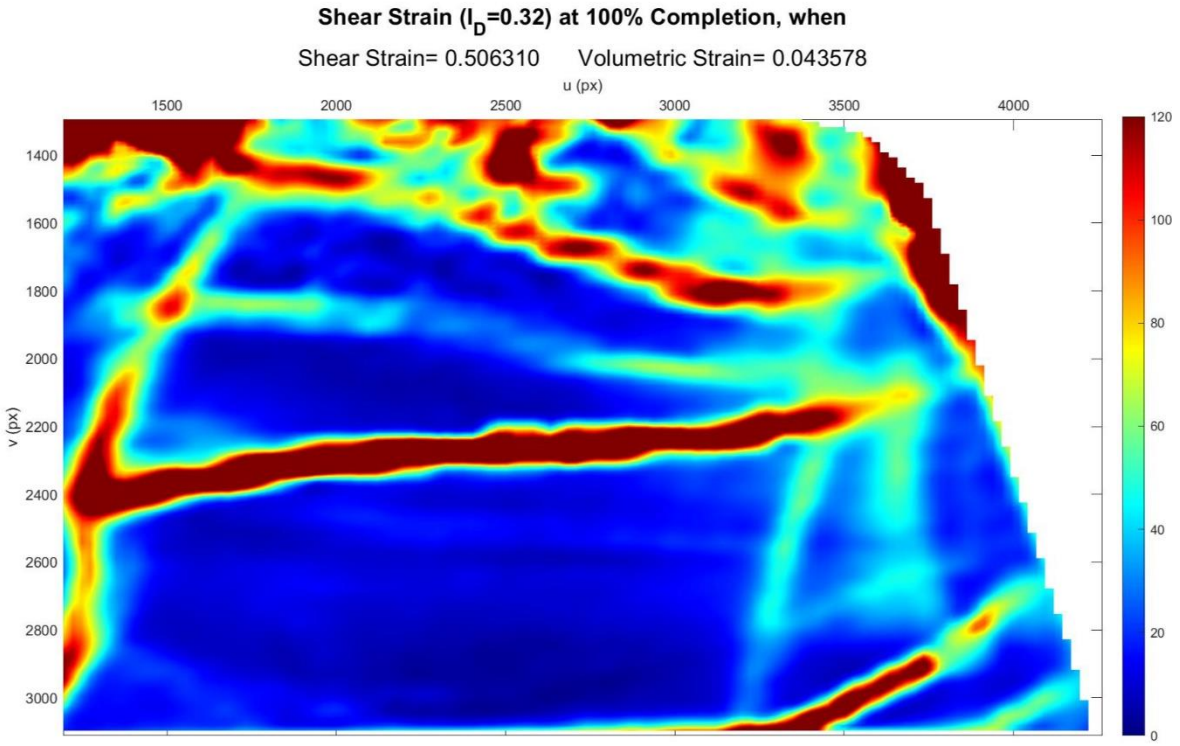

Figure C.55. Shear Strain Field at 100% Completion ($I_D = 0.32$ & $\sigma' = 0.94\ kPa$).

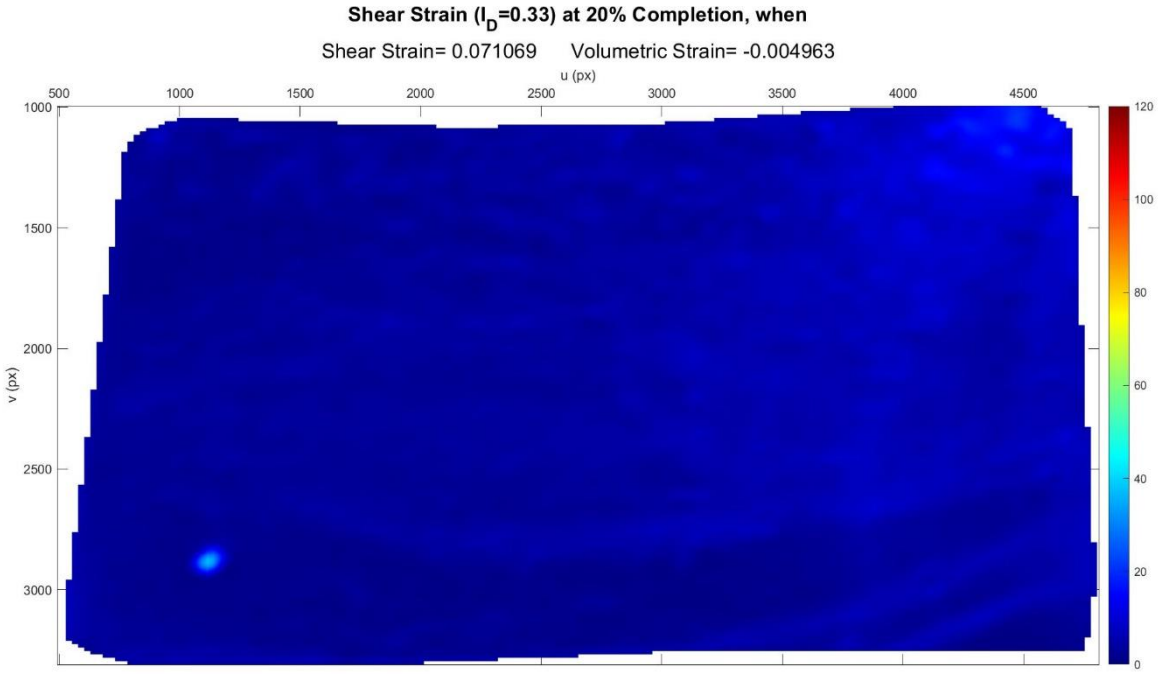

Figure C.56. Shear Strain Field at 20% Completion ($I_D = 0.33$ & $\sigma' = 0.85\ kPa$).

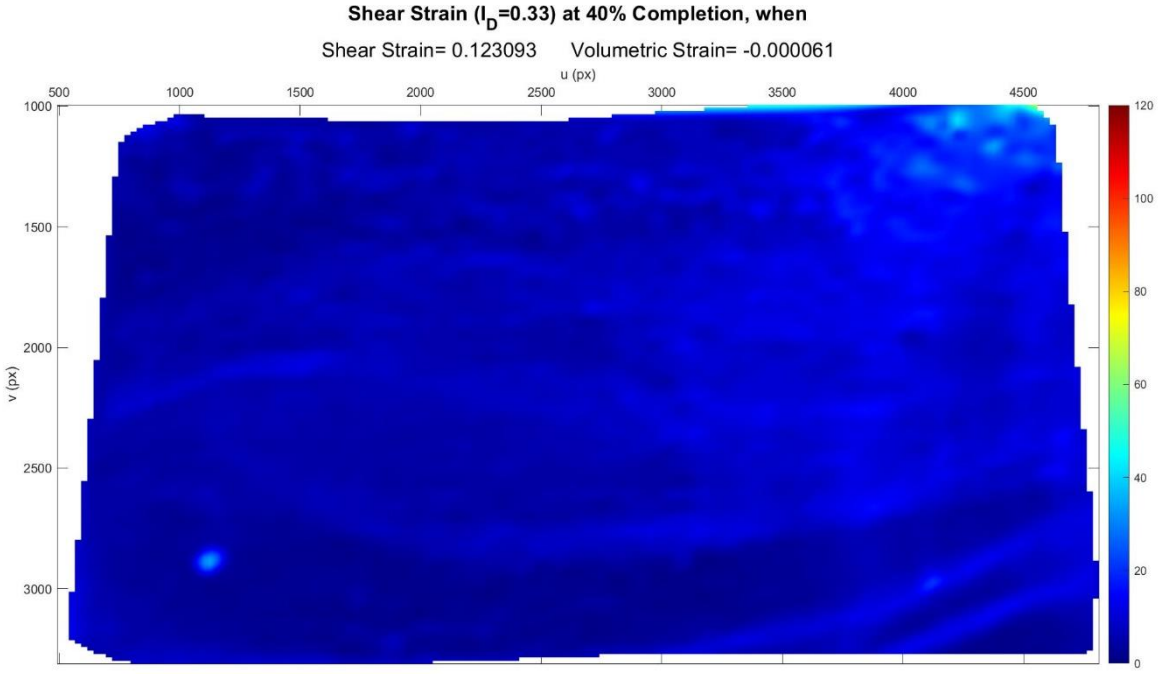

Figure C.57. Shear Strain Field at 40% Completion ($I_D = 0.33$ & $\sigma' = 0.85\ kPa$).

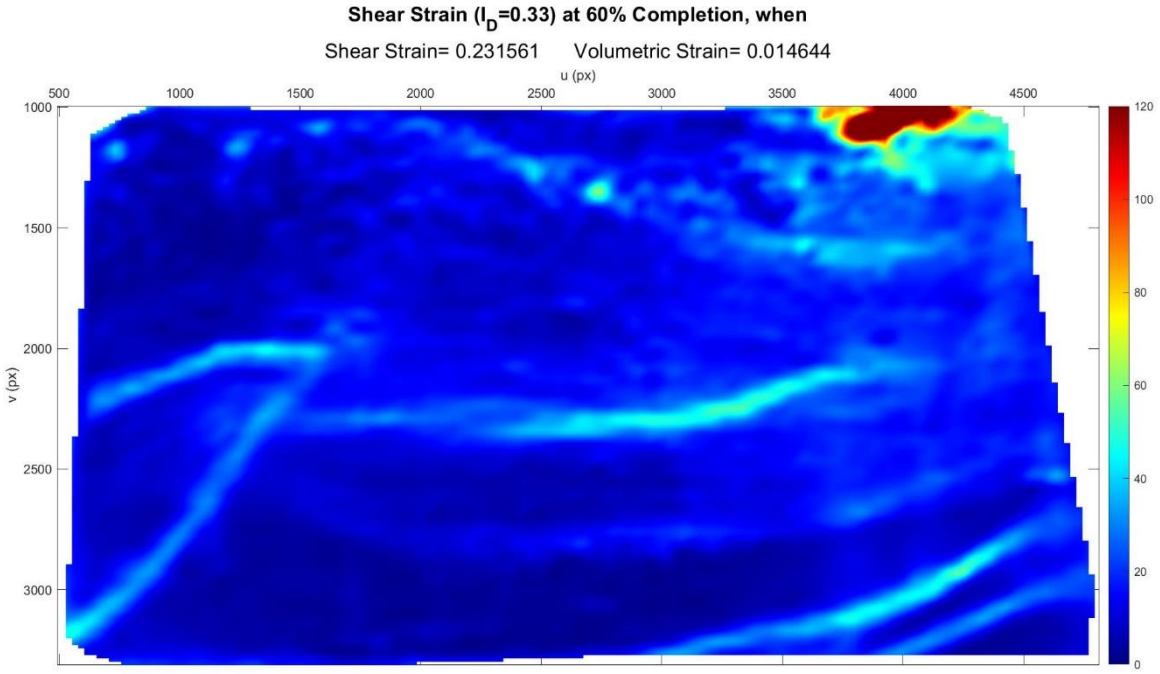

Figure C.58. Shear Strain Field at 60% Completion ($I_D = 0.33$ & $\sigma' = 0.85\ kPa$).

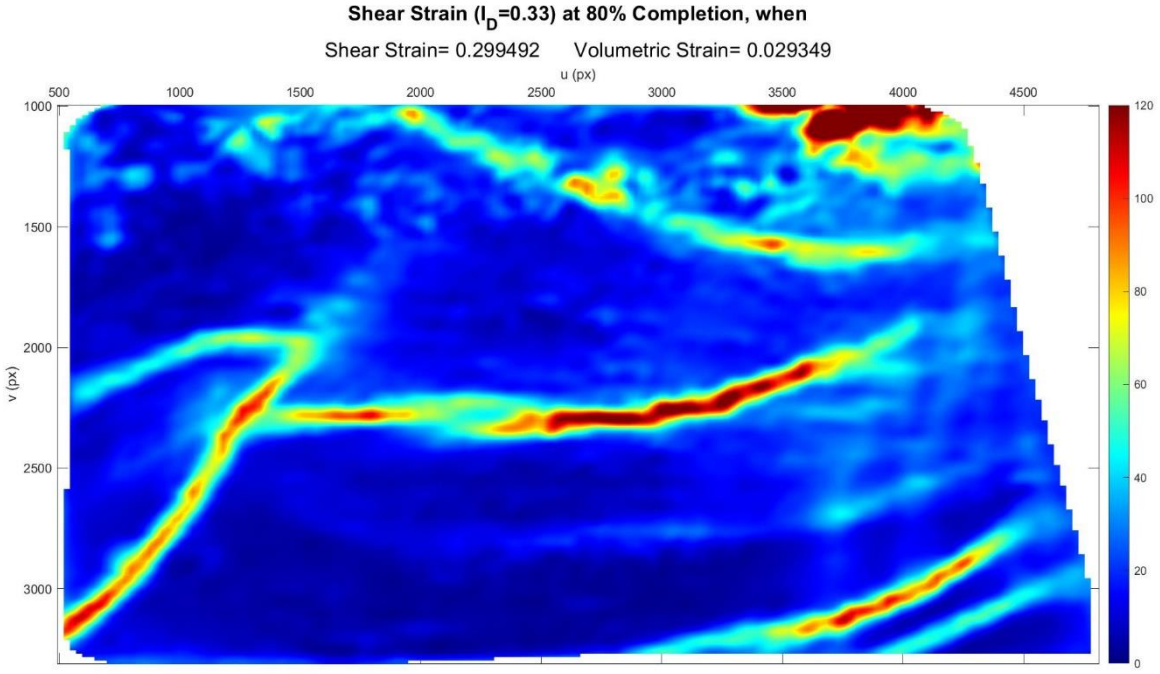

Figure C.59. Shear Strain Field at 80% Completion ($I_D = 0.33$ & $\sigma' = 0.85\ kPa$).

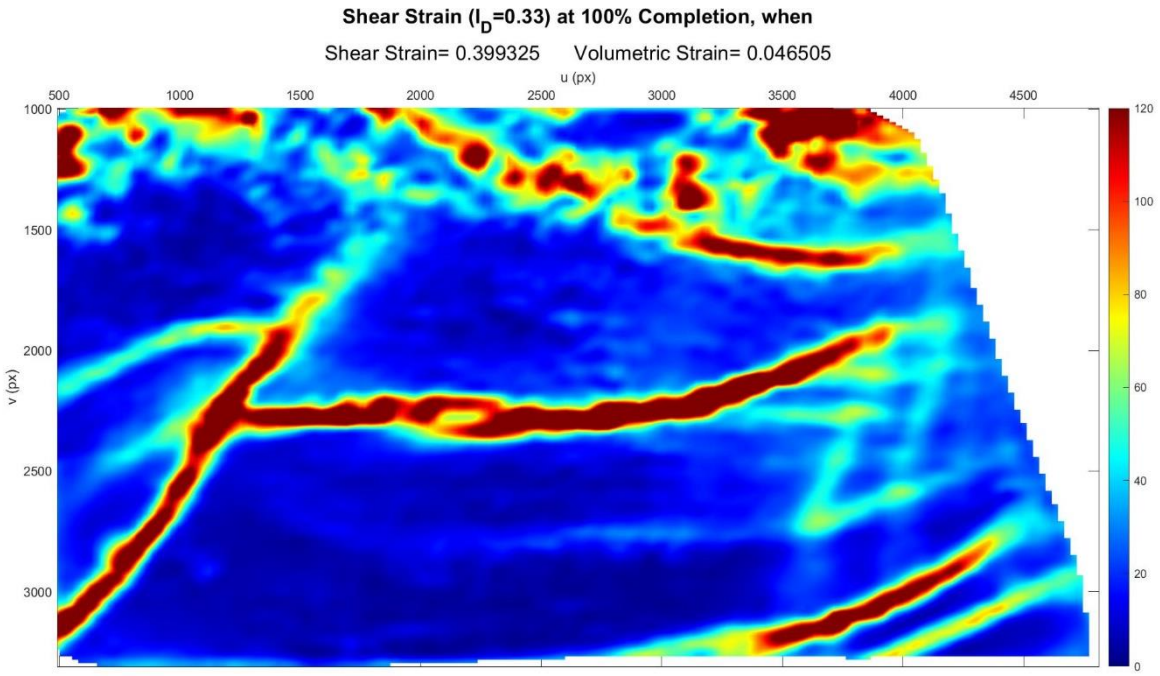

Figure C.60. Shear Strain Field at 100% Completion ($I_D = 0.33$ & $\sigma' = 0.85\ kPa$).

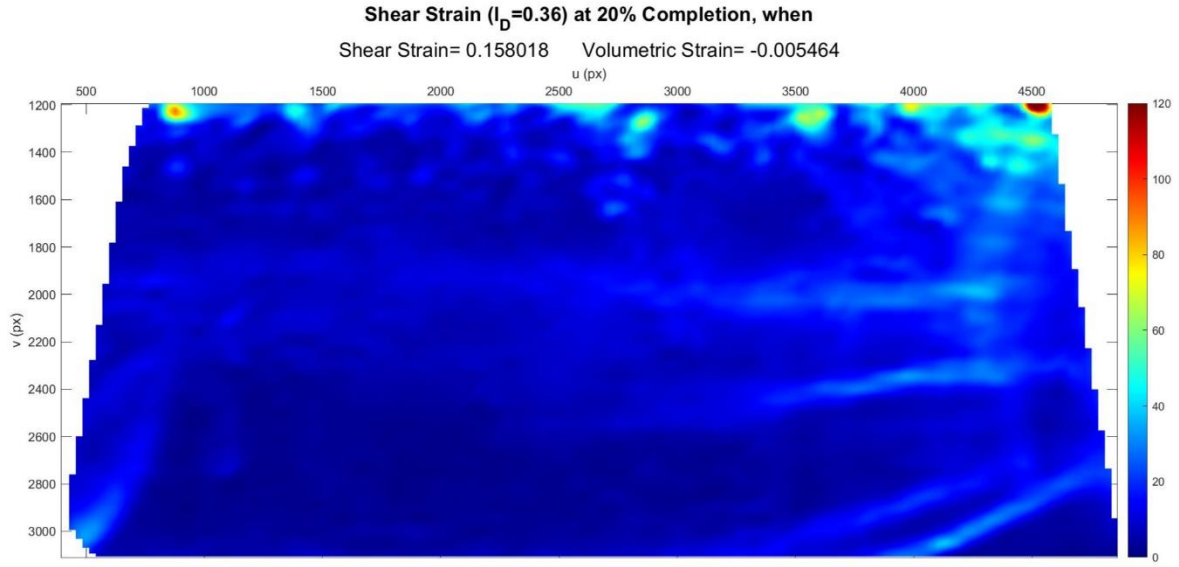

Figure C.61. Shear Strain Field at 20% Completion ($I_D = 0.36$ & $\sigma' = 0.71\ kPa$).

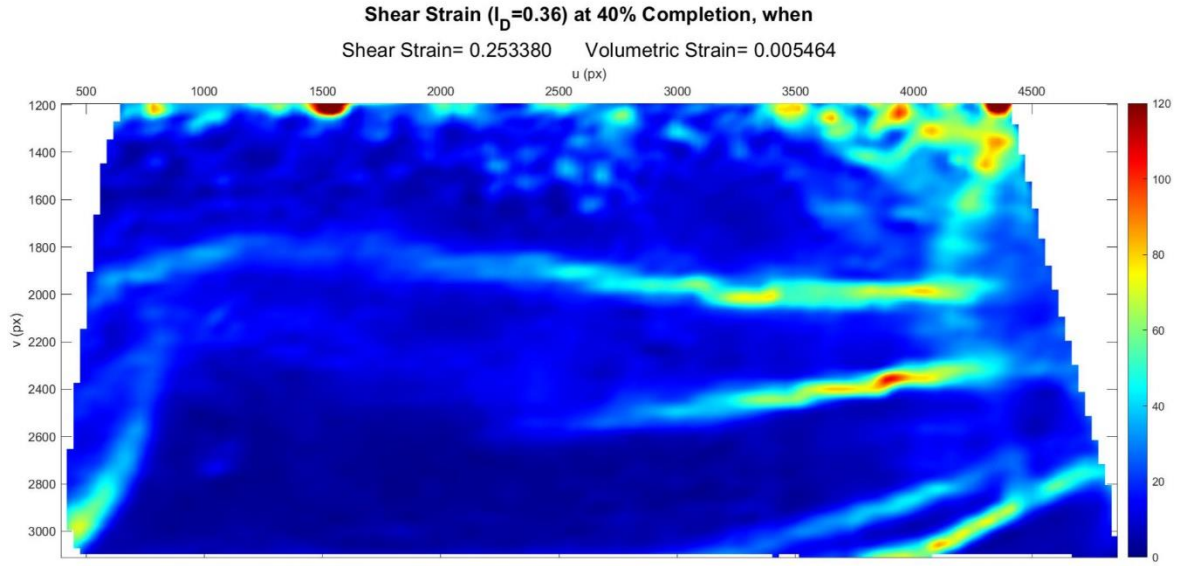

Figure C.62. Shear Strain Field at 40% Completion ($I_D = 0.36$ & $\sigma' = 0.71\ kPa$).

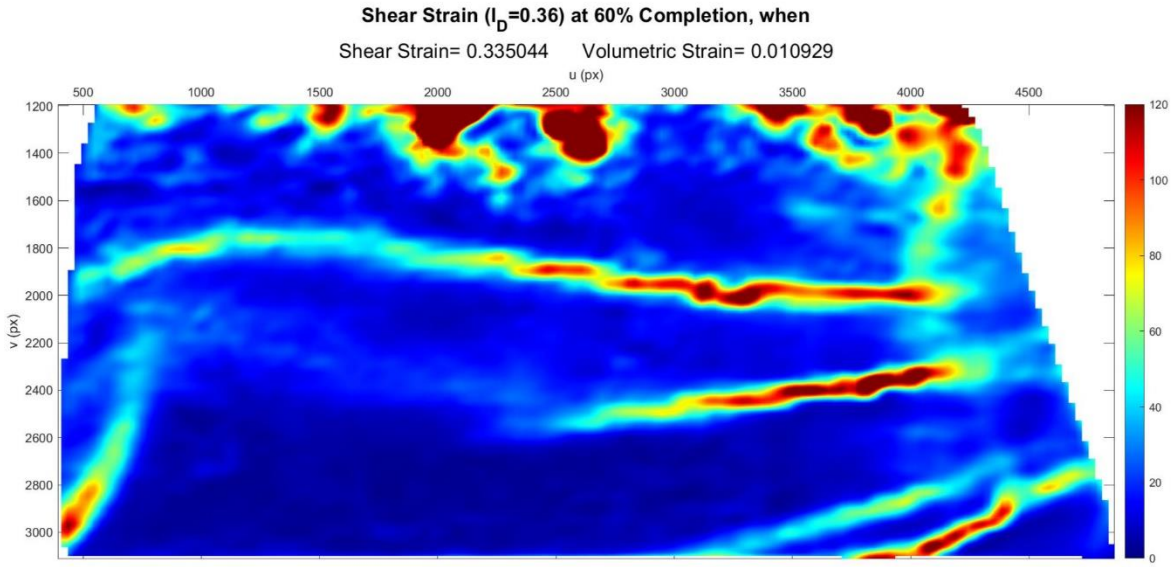

Figure C.63. Shear Strain Field at 60% Completion ($I_D = 0.36$ & $\sigma' = 0.71\ kPa$).

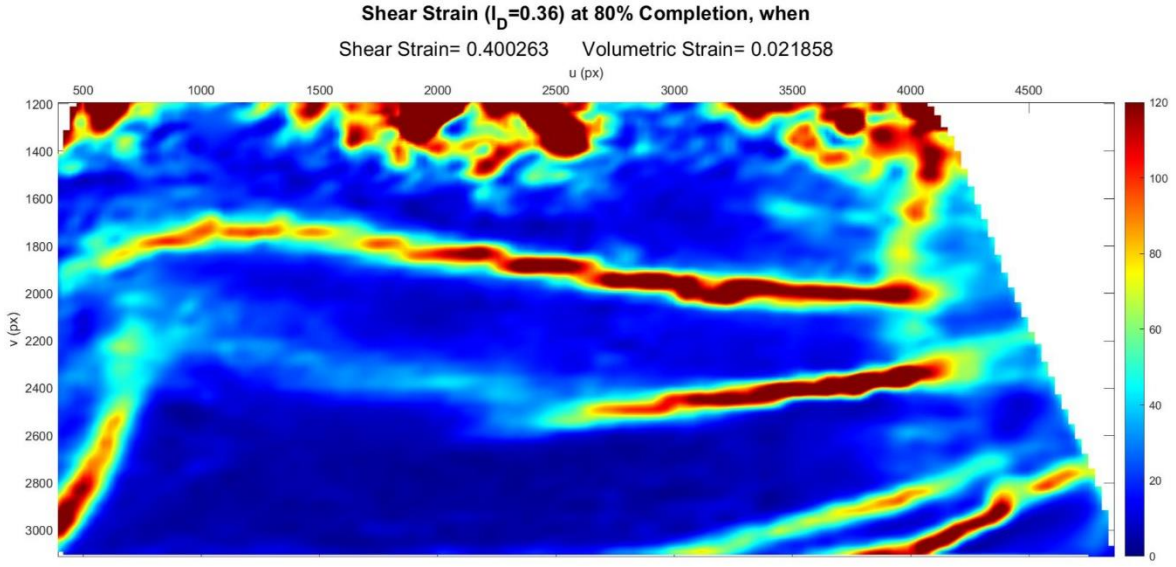

Figure C.64. Shear Strain Field at 80% Completion ($I_D = 0.36$ & $\sigma' = 0.71\ kPa$).

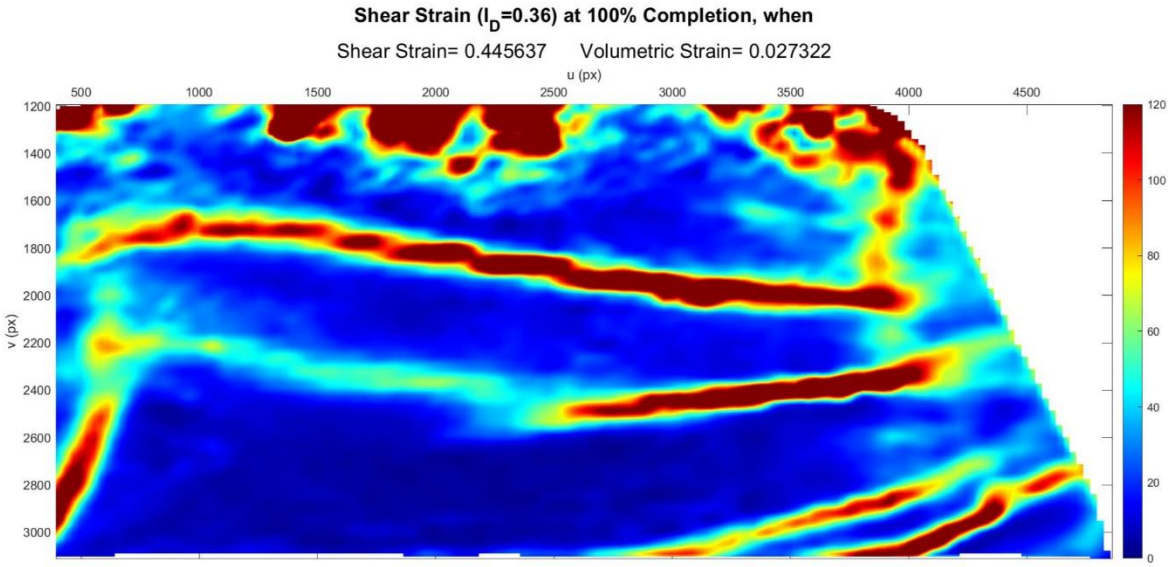

Figure C.65. Shear Strain Field at 100% Completion ($I_D = 0.36$ & $\sigma' = 0.71\ kPa$).

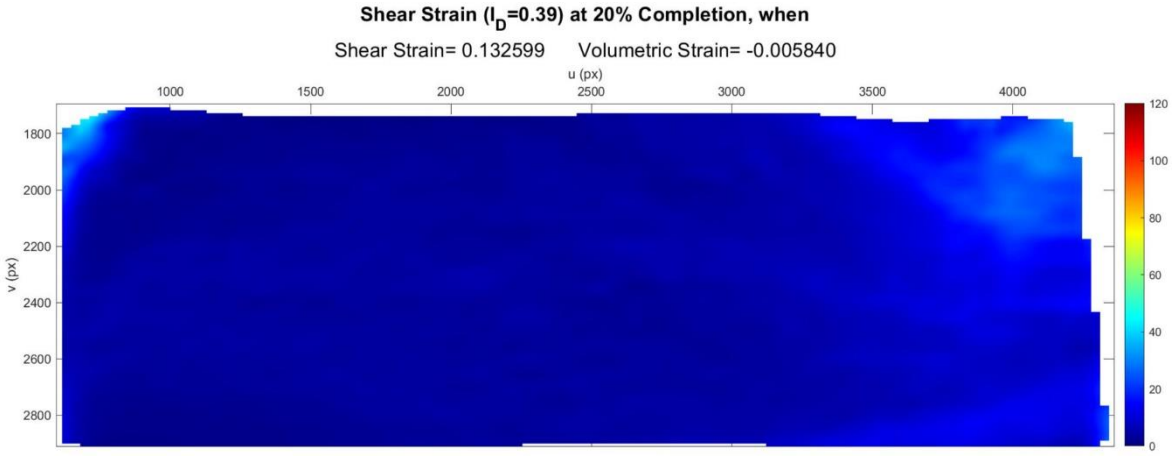

Figure C.66. Shear Strain Field at 20% Completion ($I_D = 0.39$ & $\sigma' = 0.58\,kPa$).

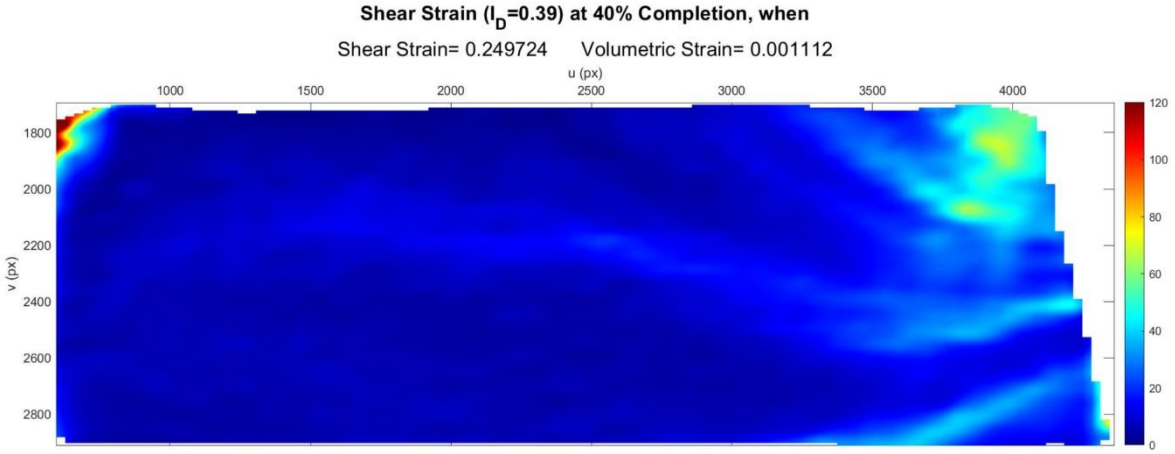

Figure C.67. Shear Strain Field at 40% Completion ($I_D = 0.39$ & $\sigma' = 0.58\,kPa$).

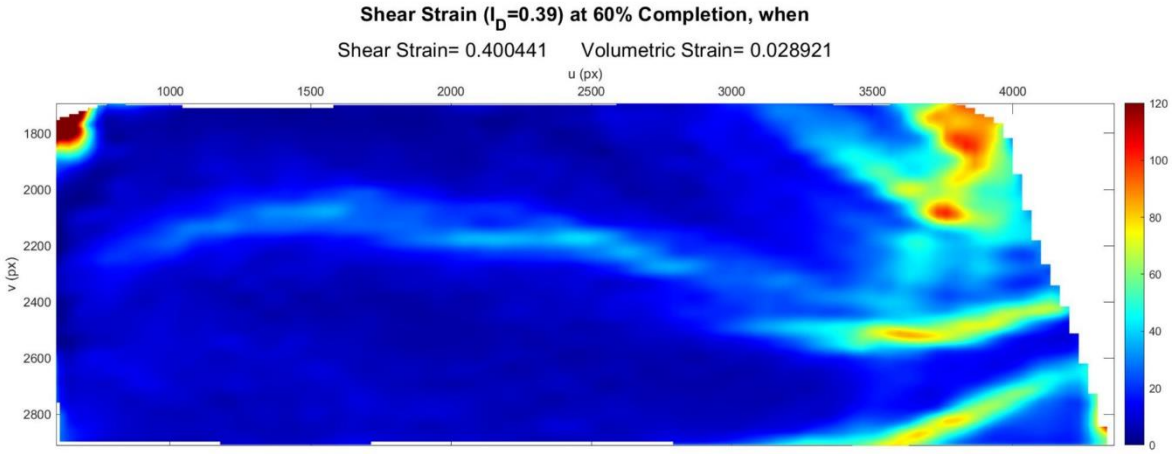

Figure C.68. Shear Strain Field at 60% Completion ($I_D = 0.39$ & $\sigma' = 0.58\,kPa$).

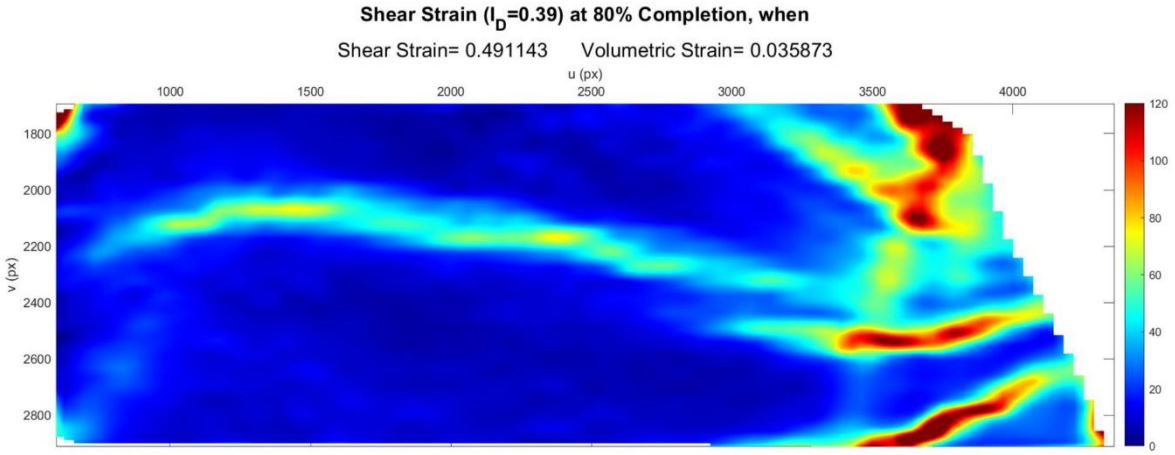

Figure C.69. Shear Strain Field at 80% Completion ($I_D = 0.39$ & $\sigma' = 0.58\,kPa$).

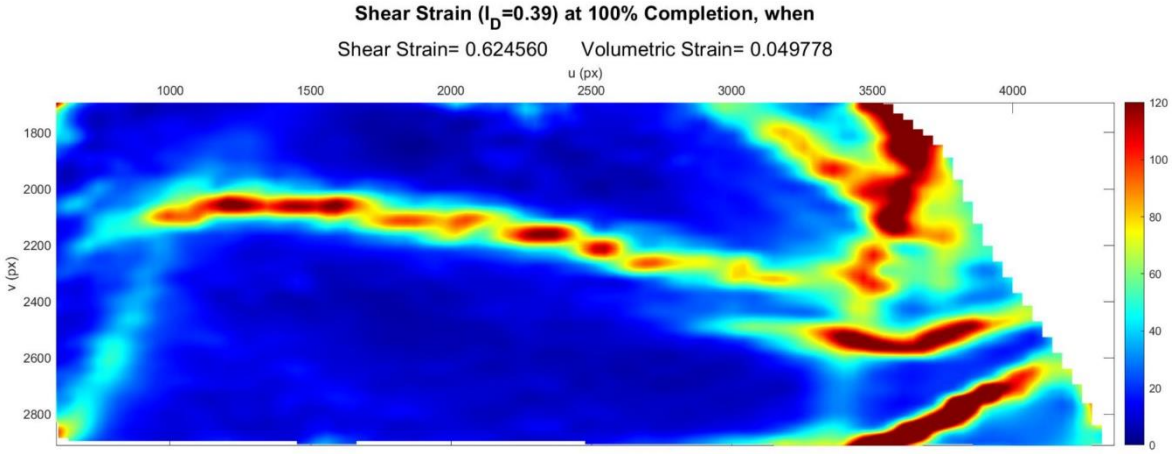

Figure C.70. Shear Strain Field at 100% Completion ($I_D = 0.39$ & $\sigma' = 0.58\,kPa$).

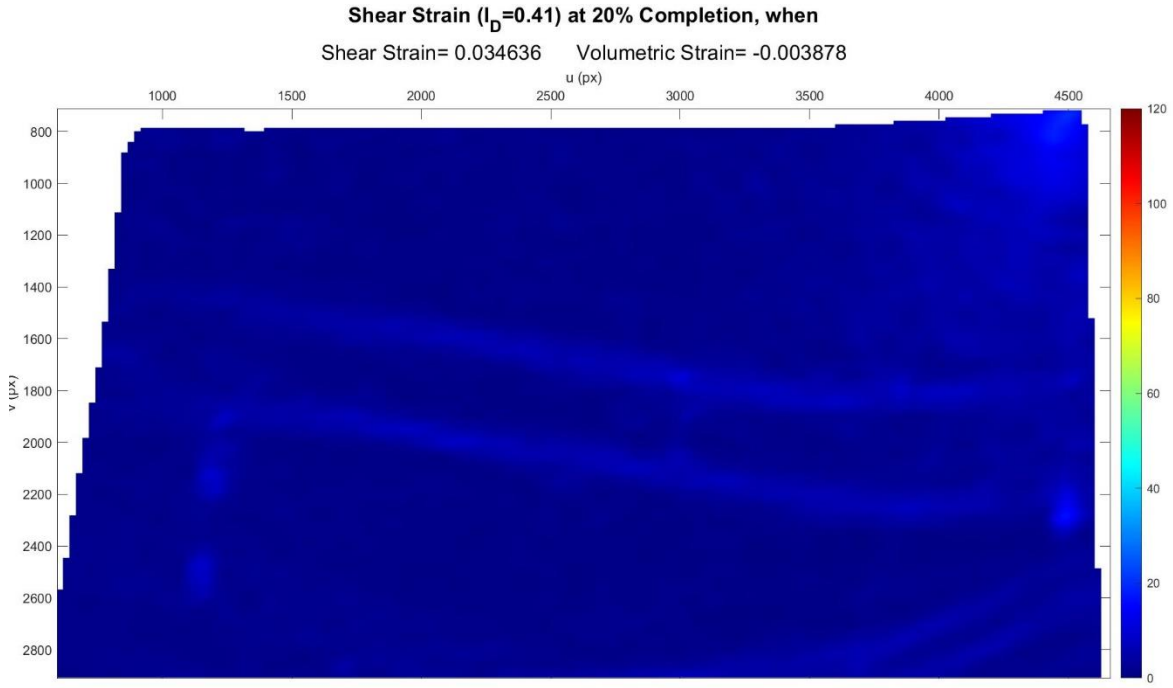

Figure C.71. Shear Strain Field at 20% Completion ($I_D = 0.41$ & $\sigma' = 0.87\ kPa$).

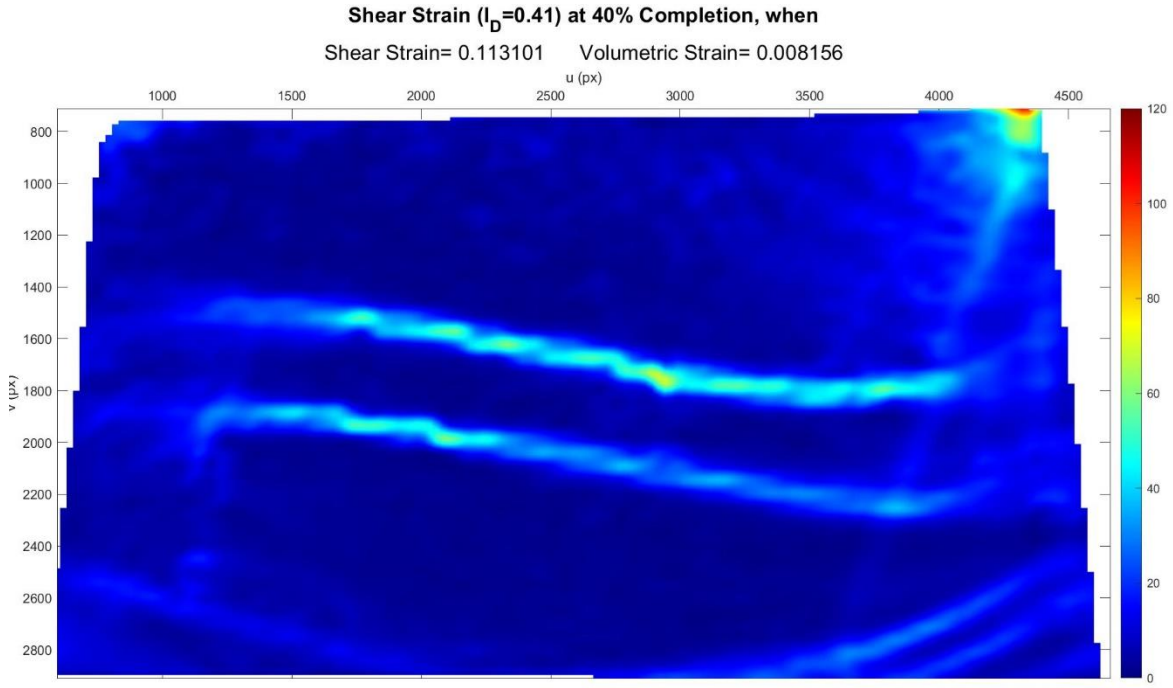

Figure C.72. Shear Strain Field at 40% Completion ($I_D = 0.41$ & $\sigma' = 0.87\ kPa$).

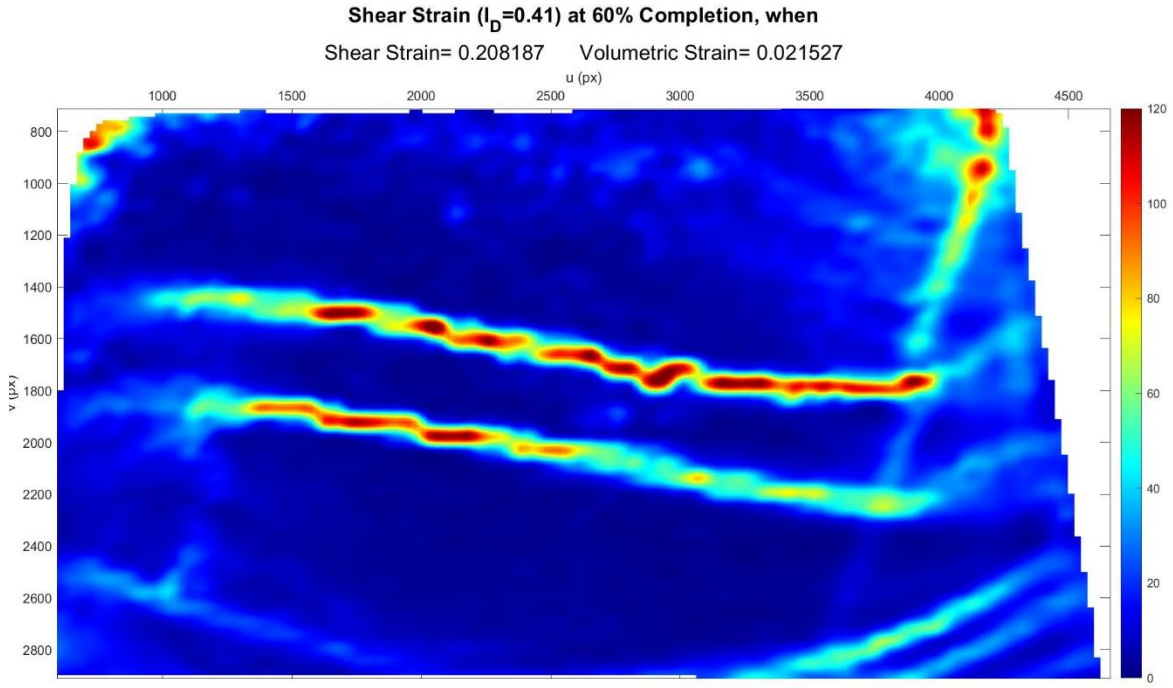

Figure C.73. Shear Strain Field at 60% Completion ($I_D = 0.41$ & $\sigma' = 0.87\ kPa$).

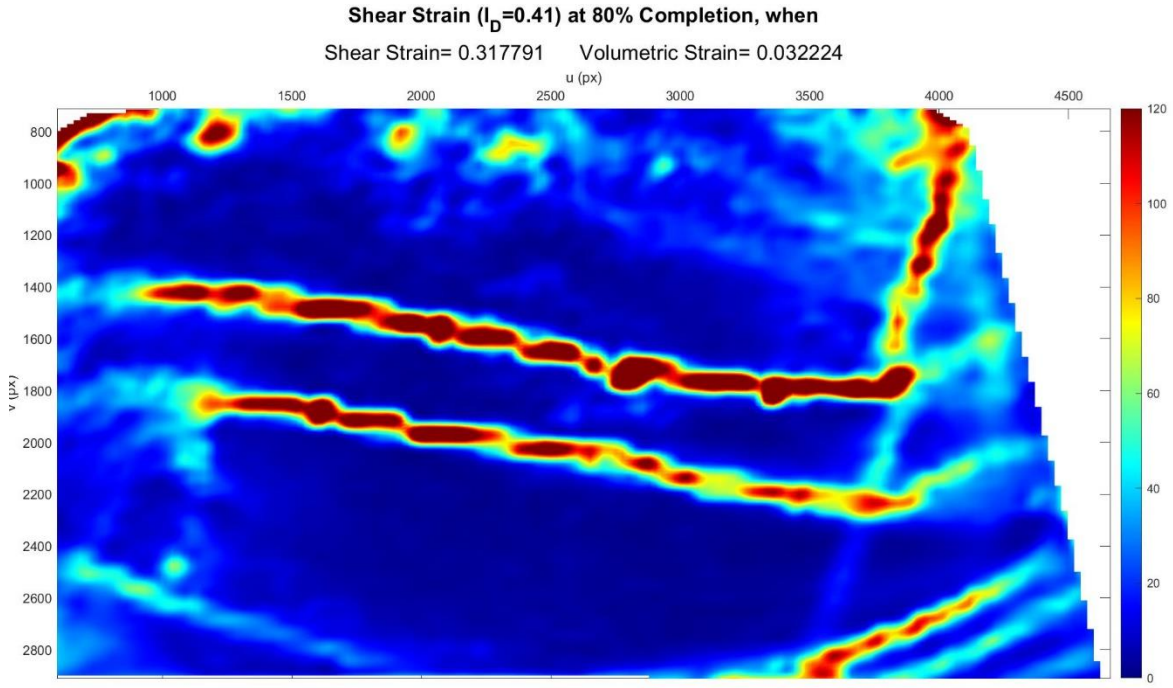

Figure C.74. Shear Strain Field at 80% Completion ($I_D = 0.41$ & $\sigma' = 0.87\ kPa$).

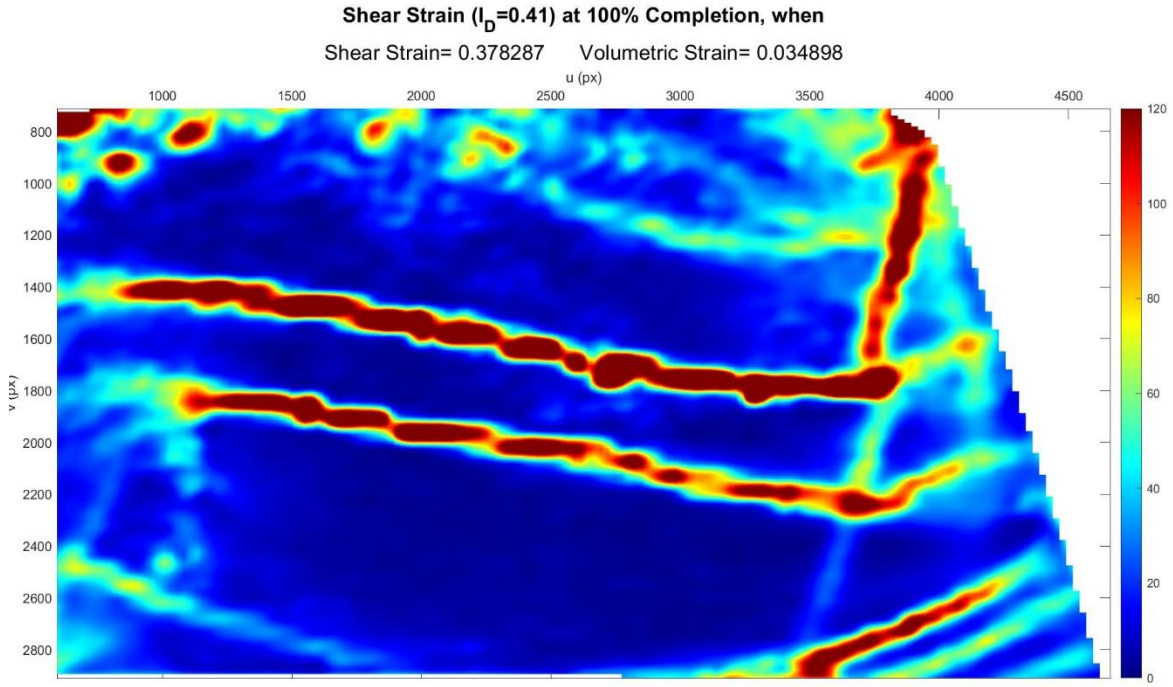

Figure C.75. Shear Strain Field at 100% Completion ($I_D = 0.41$ & $\sigma' = 0.87\ kPa$).

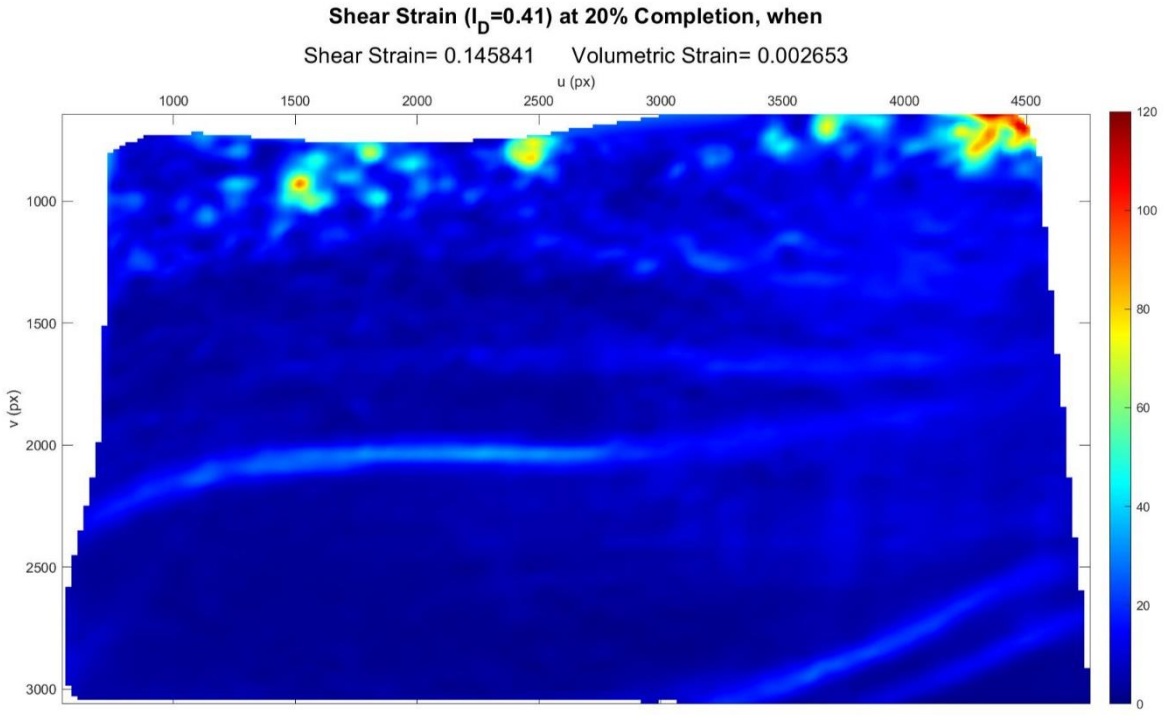

Figure C.76. Shear Strain Field at 20% Completion ($I_D = 0.41$ & $\sigma' = 0.96\ kPa$).

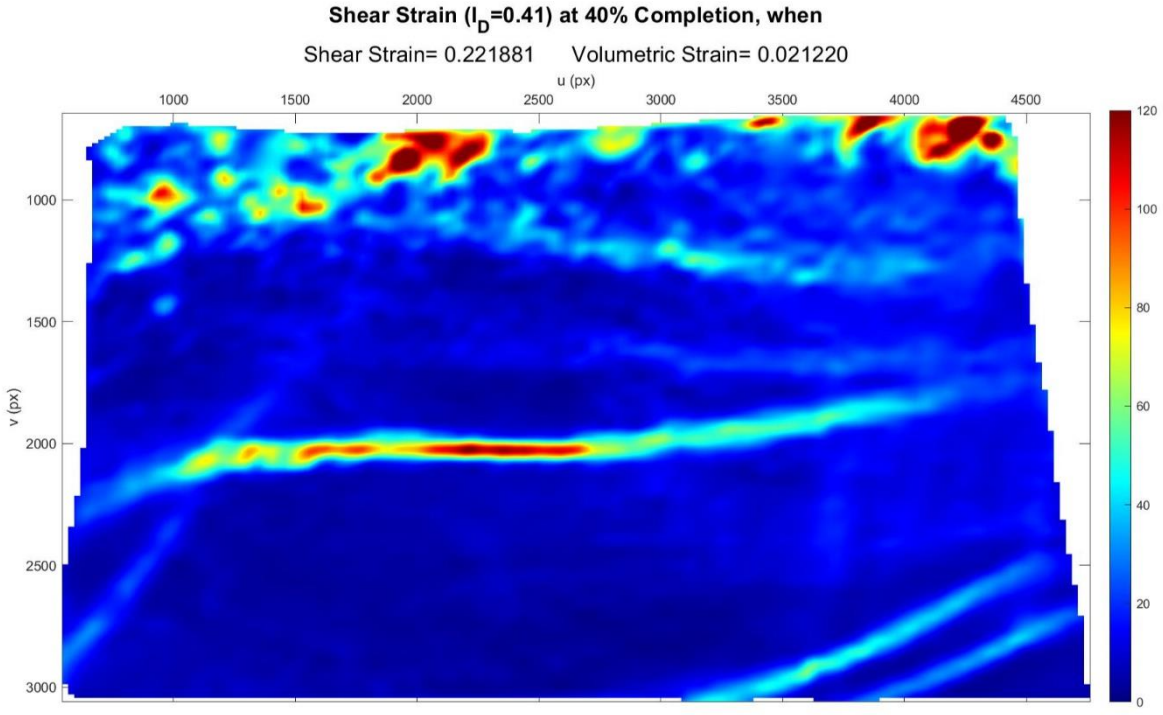

Figure C.77. Shear Strain Field at 40% Completion ($I_D = 0.41$ & $\sigma' = 0.96\ kPa$).

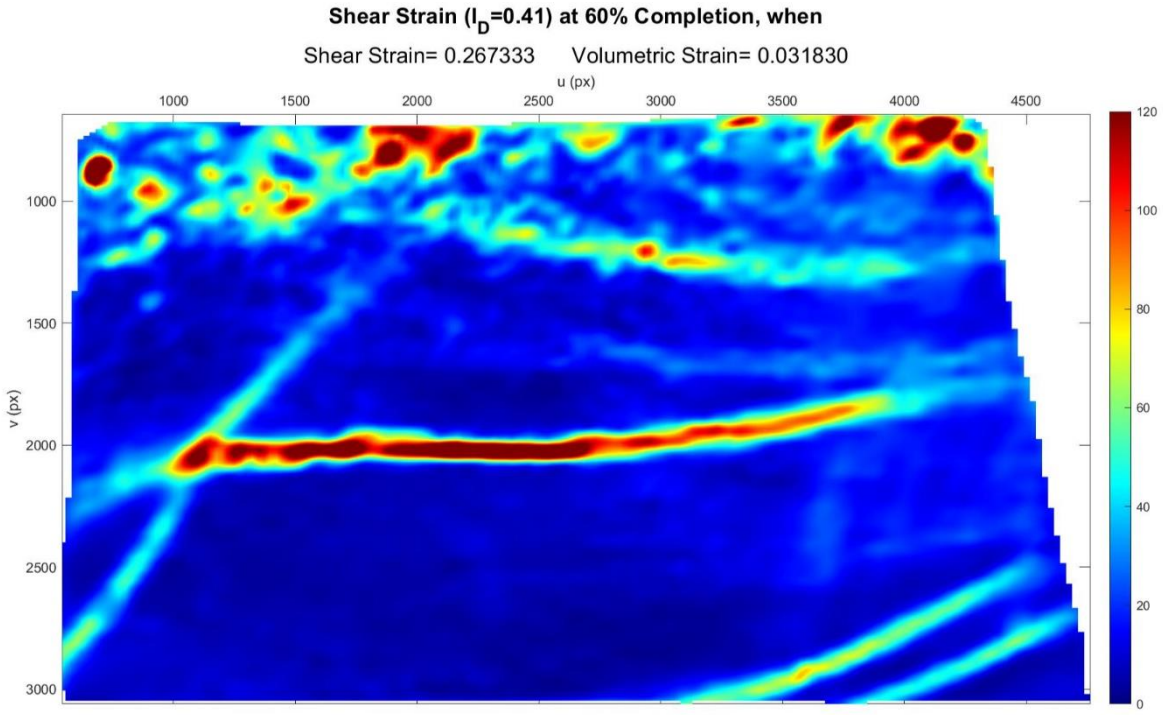

Figure C.78. Shear Strain Field at 60% Completion ($I_D = 0.41$ & $\sigma' = 0.96\ kPa$).

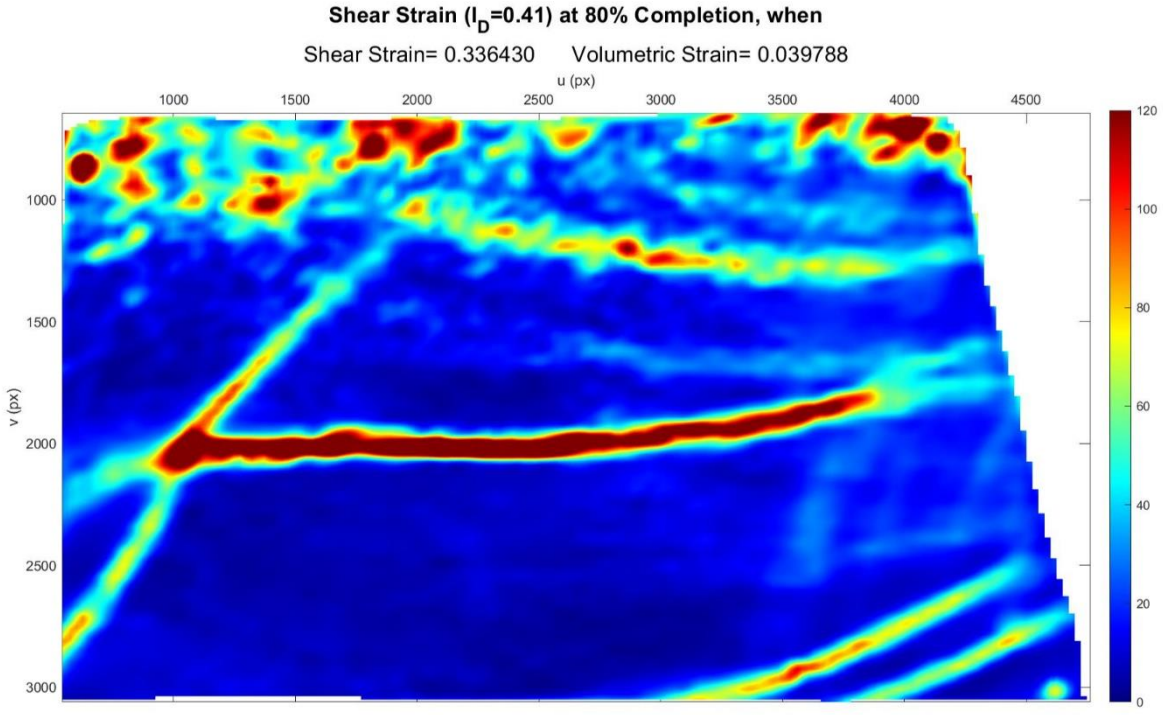

Figure C.79. Shear Strain Field at 80% Completion ($I_D = 0.41$ & $\sigma' = 0.96\ kPa$).

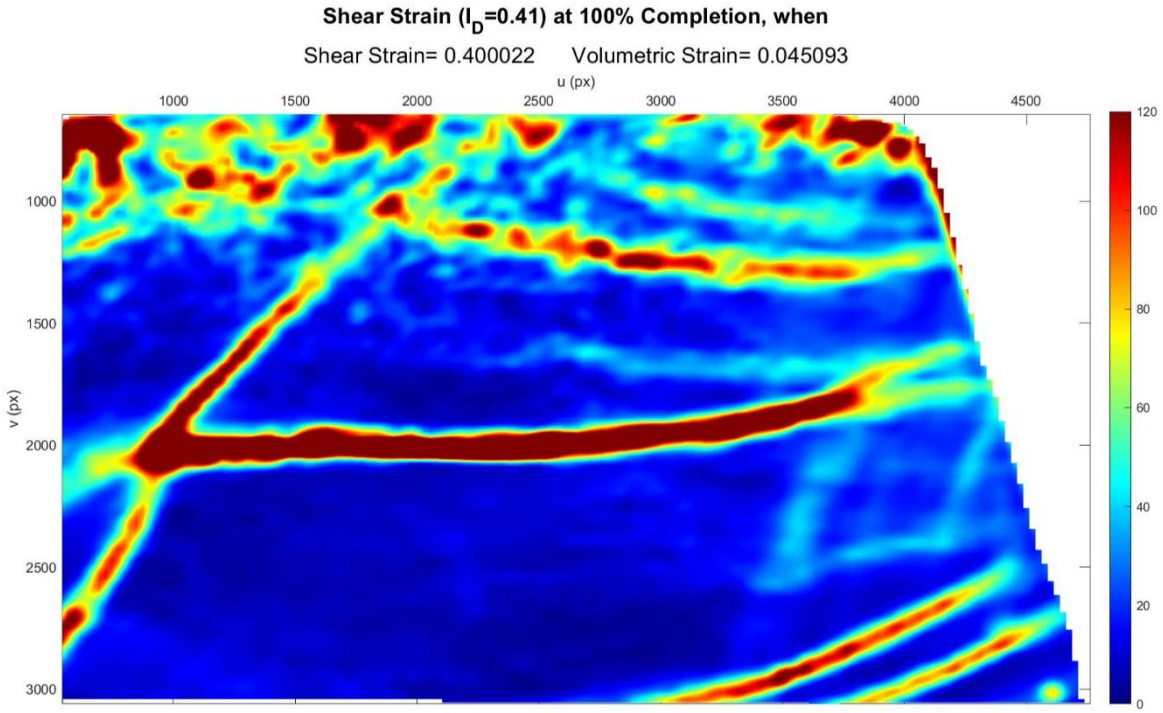

Figure C.80. Shear Strain Field at 100% Completion ($I_D = 0.41$ & $\sigma' = 0.96\ kPa$).

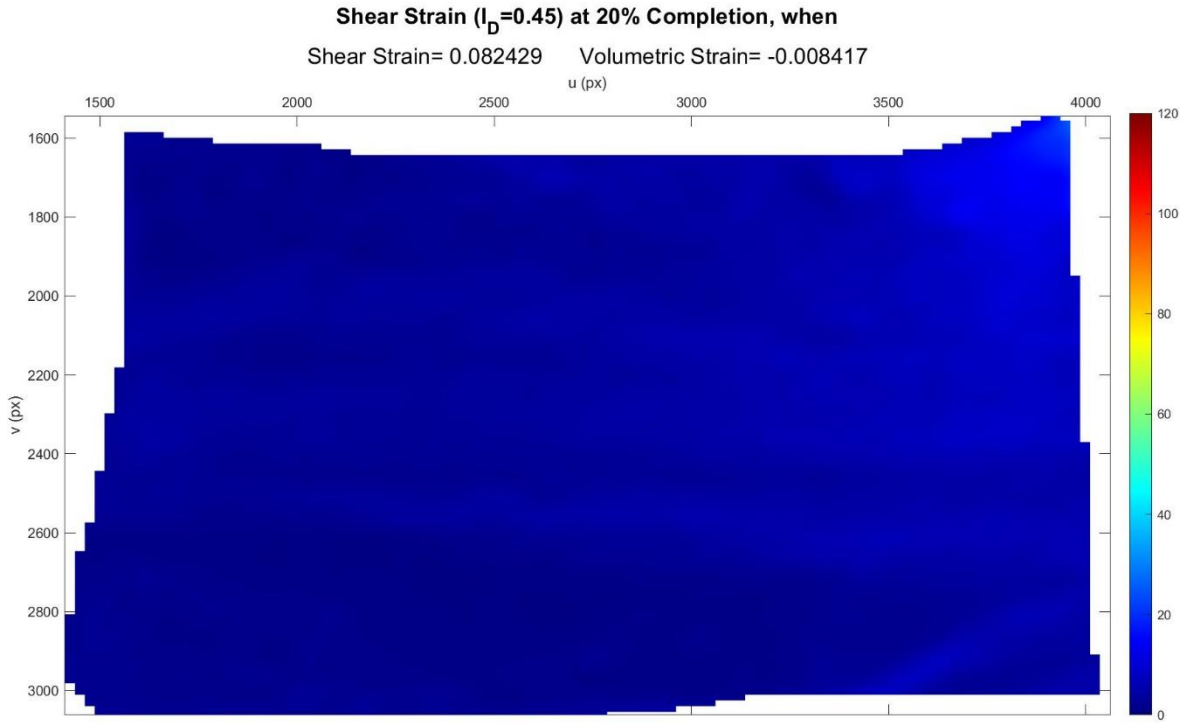

Figure C.81. Shear Strain Field at 20% Completion ($I_D = 0.45$ & $\sigma' = 0.88\,kPa$).

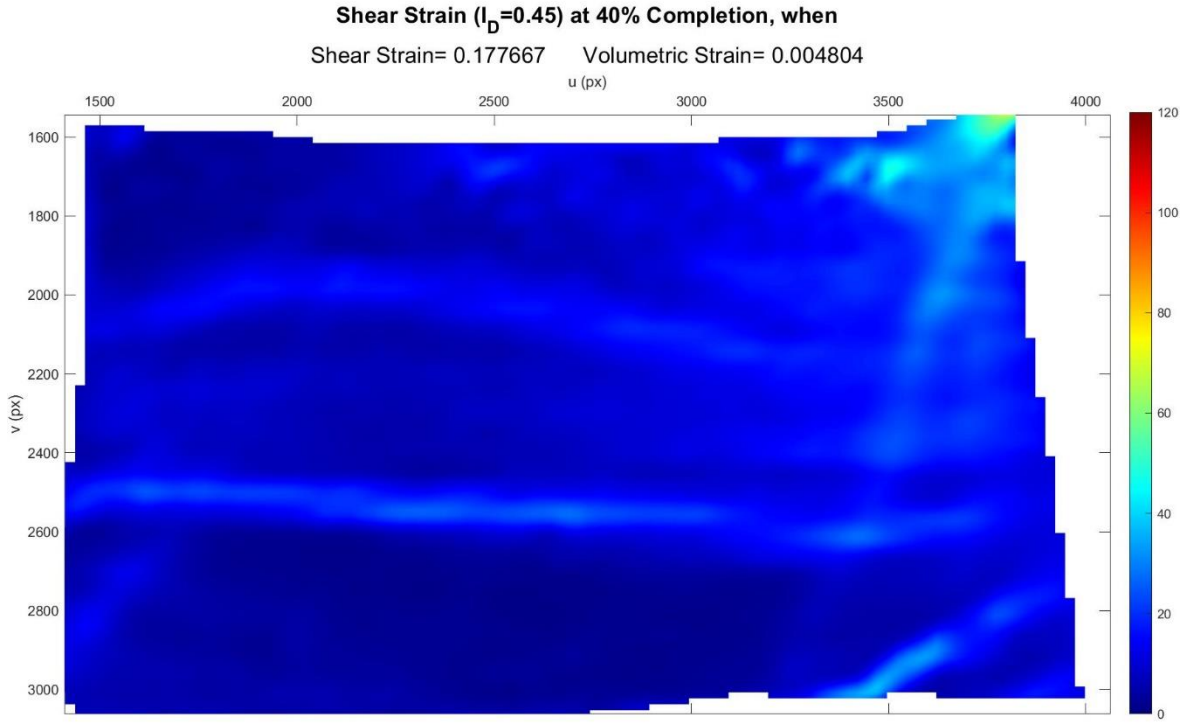

Figure C.82. Shear Strain Field at 40% Completion ($I_D = 0.45$ & $\sigma' = 0.88\,kPa$).

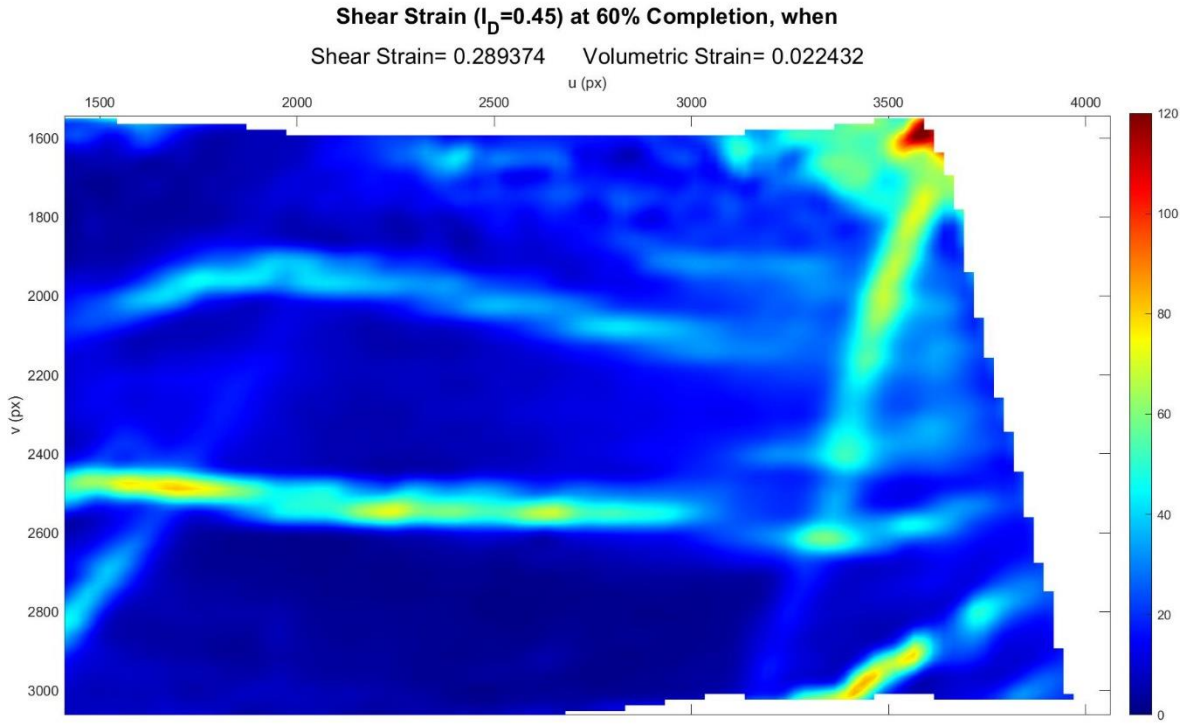

Figure C.83. Shear Strain Field at 60% Completion ($I_D = 0.45$ & $\sigma' = 0.88\,kPa$).

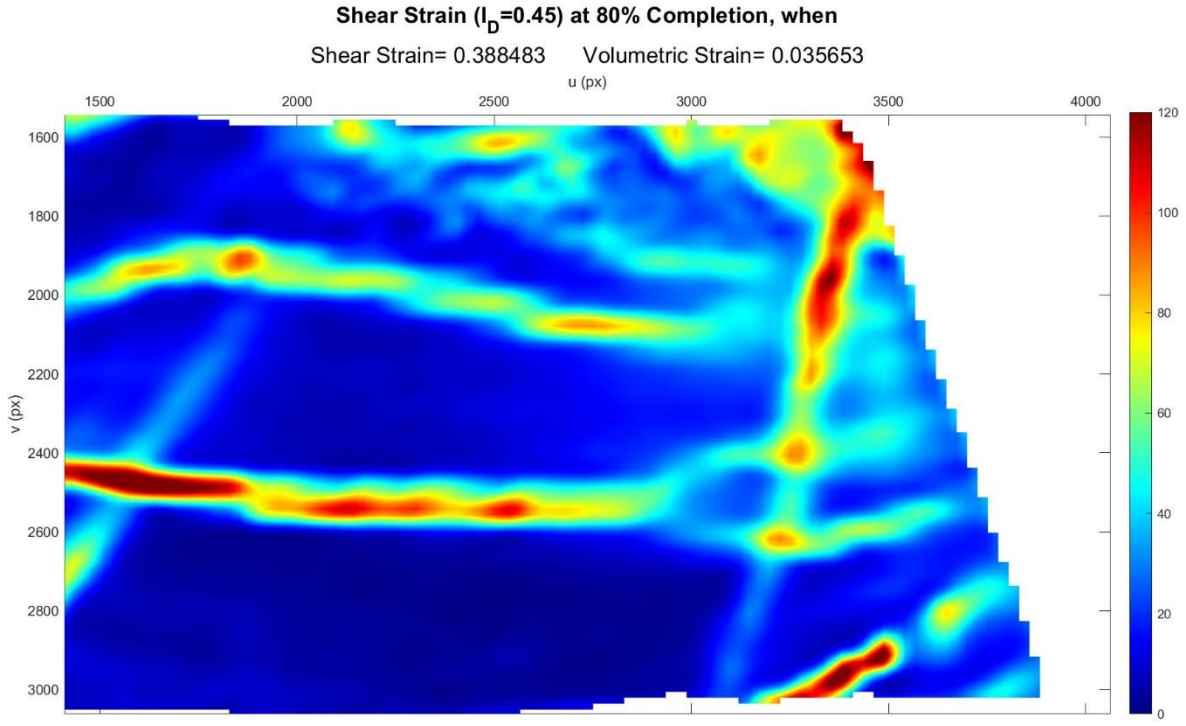

Figure C.84. Shear Strain Field at 80% Completion ($I_D = 0.45$ & $\sigma' = 0.88\,kPa$).

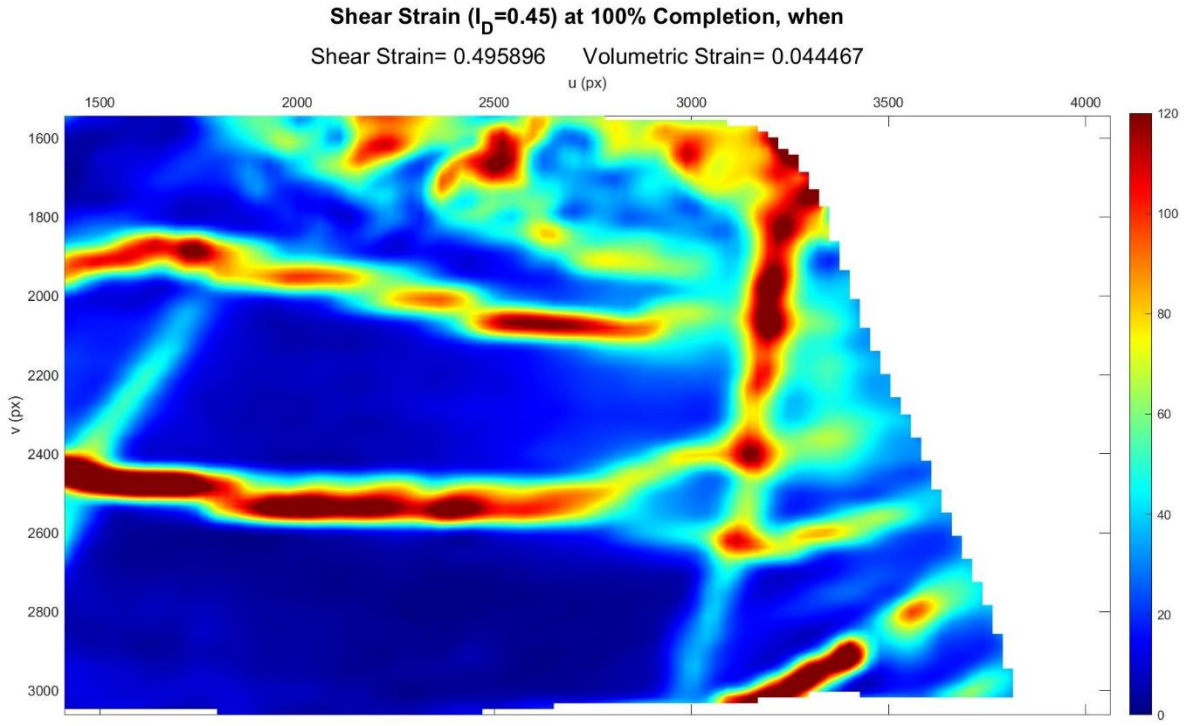

Figure C.85. Shear Strain Field at 100% Completion ($I_D = 0.45$ & $\sigma' = 0.88\ kPa$).

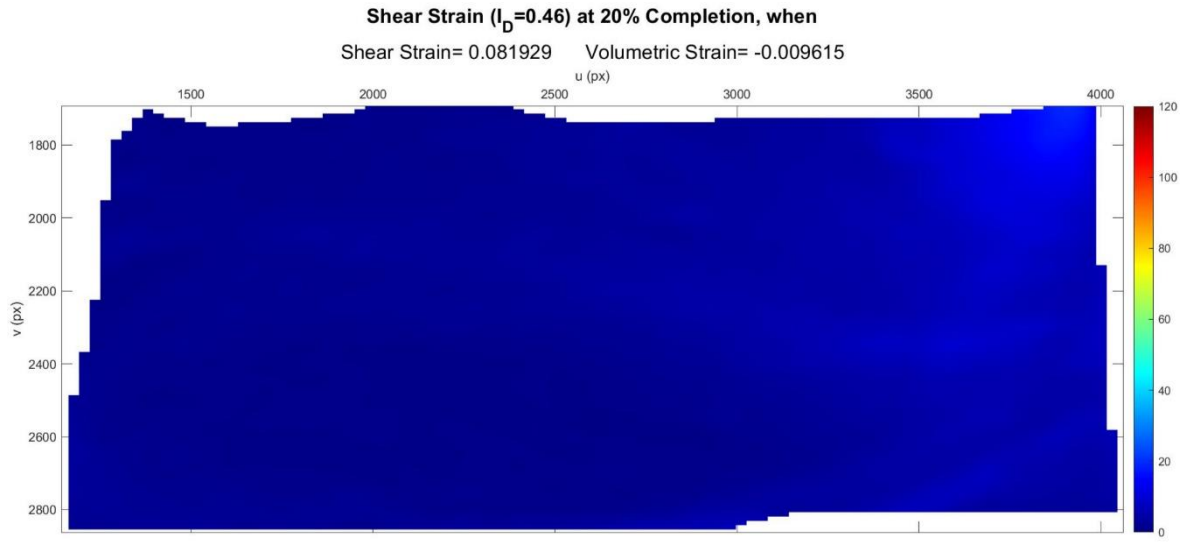

Figure C.86. Shear Strain Field at 20% Completion ($I_D = 0.46$ & $\sigma' = 0.71\ kPa$).

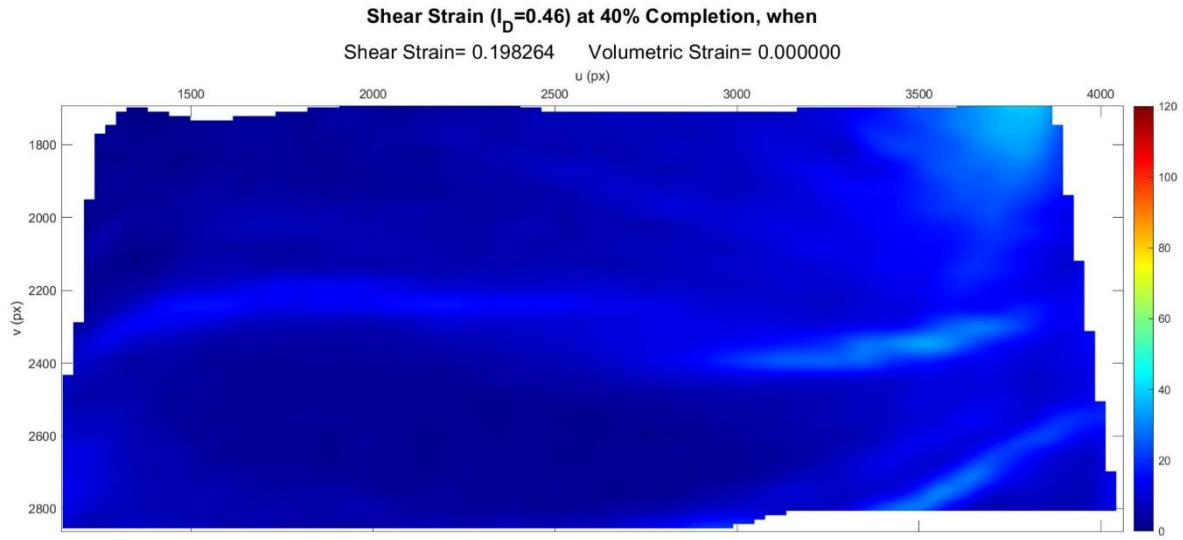

Figure C.87. Shear Strain Field at 40% Completion ($I_D = 0.46$ & $\sigma' = 0.71\ kPa$).

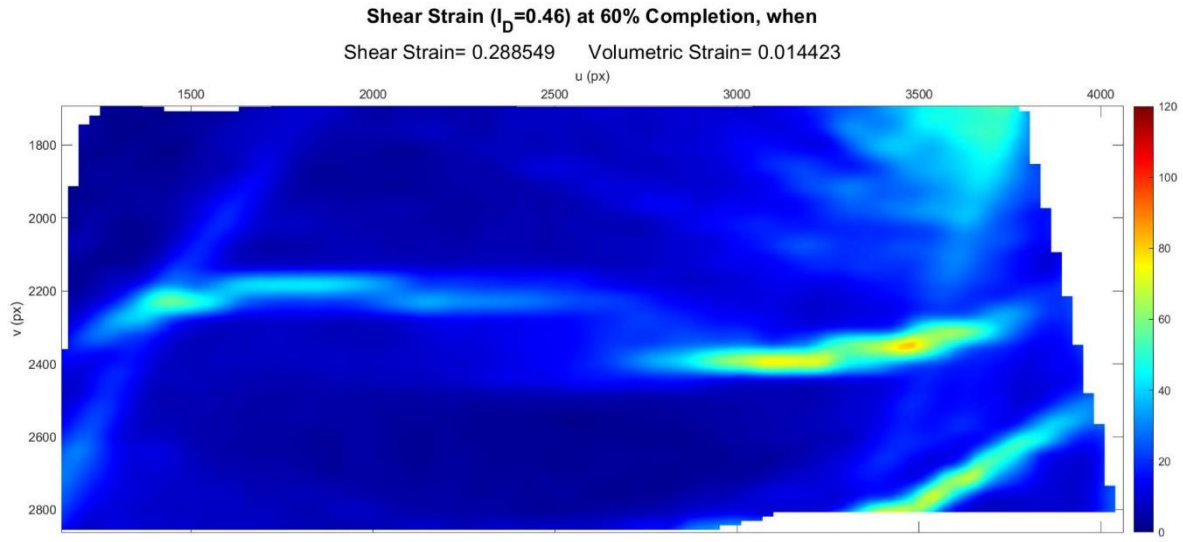

Figure C.88. Shear Strain Field at 60% Completion ($I_D = 0.46$ & $\sigma' = 0.71\ kPa$).

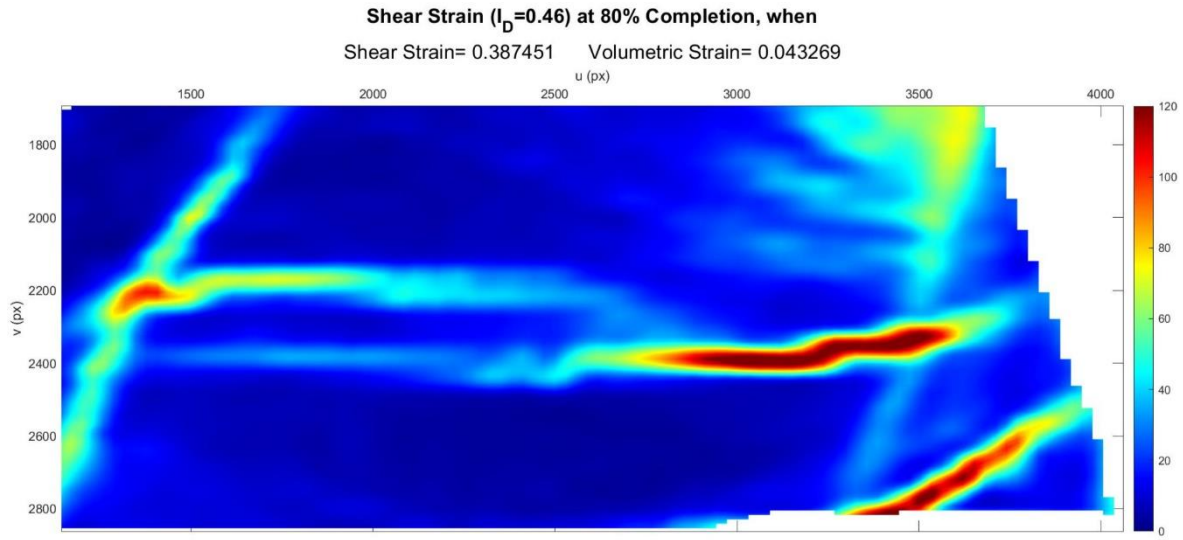

Figure C.89. Shear Strain Field at 80% Completion ($I_D = 0.46$ & $\sigma' = 0.71\ kPa$).

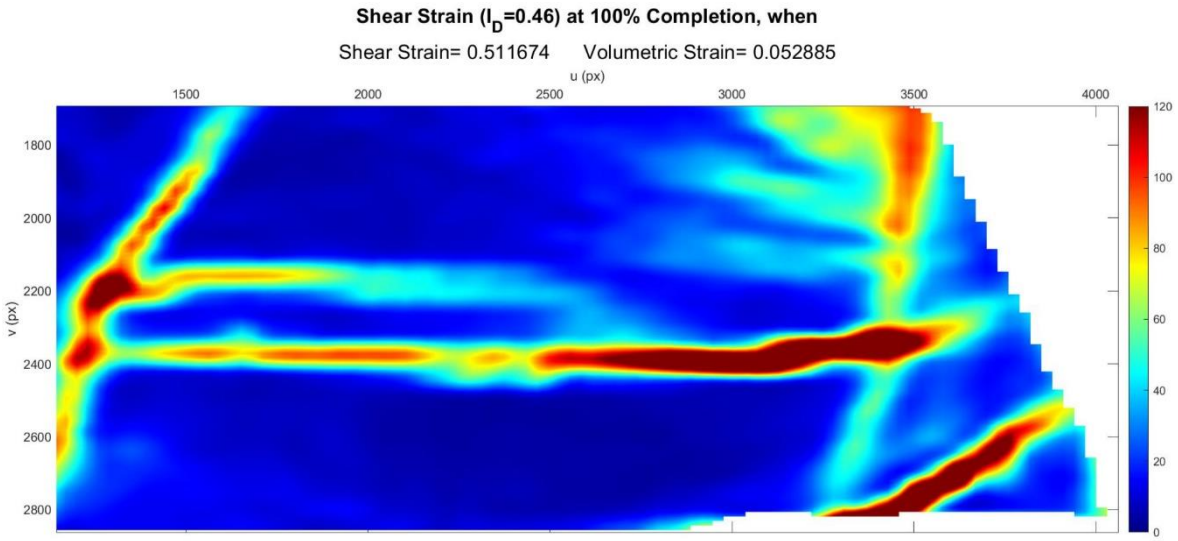

Figure C.90. Shear Strain Field at 100% Completion ($I_D = 0.46$ & $\sigma' = 0.71\ kPa$).

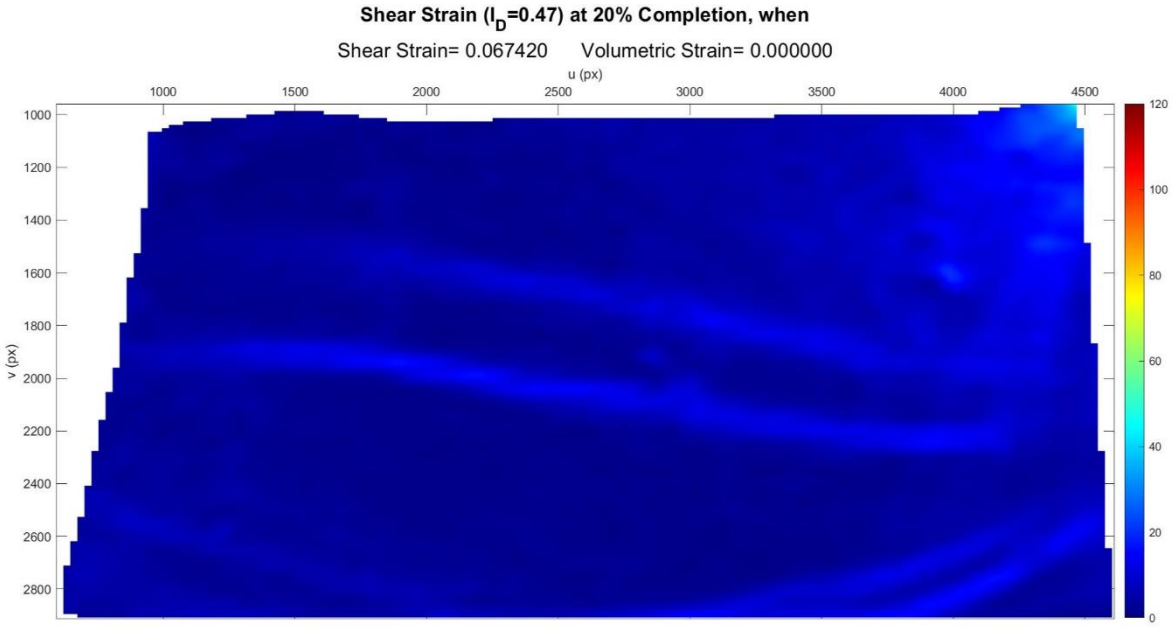

Figure C.91. Shear Strain Field at 20% Completion ($I_D = 0.47$ & $\sigma' = 0.84\ kPa$).

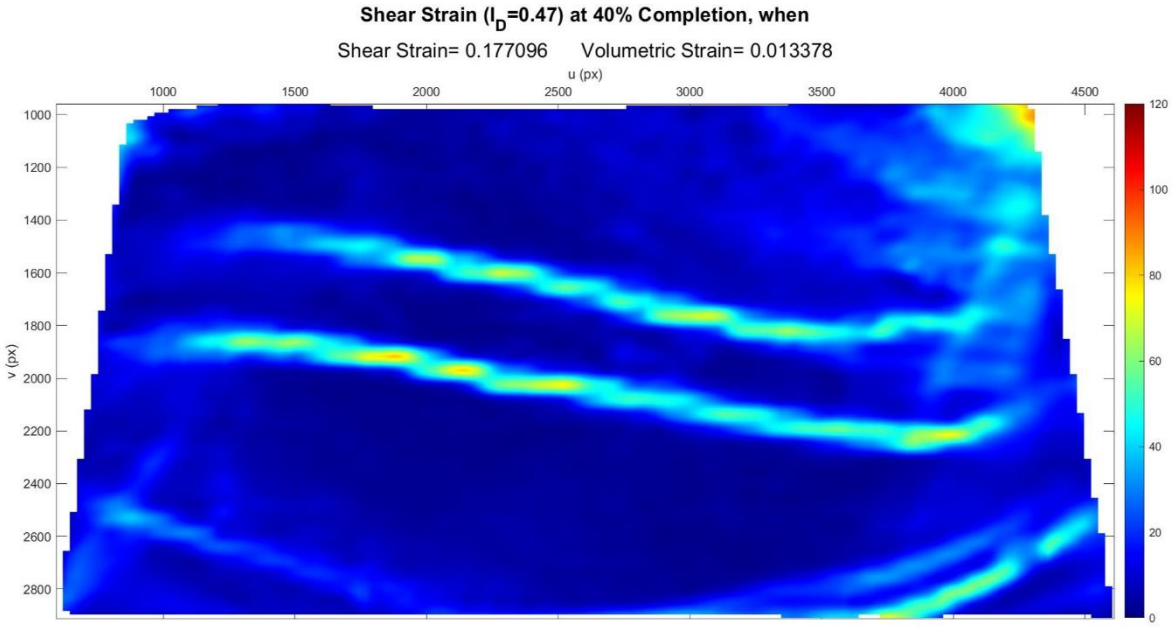

Figure C.92. Shear Strain Field at 40% Completion ($I_D = 0.47$ & $\sigma' = 0.84\ kPa$).

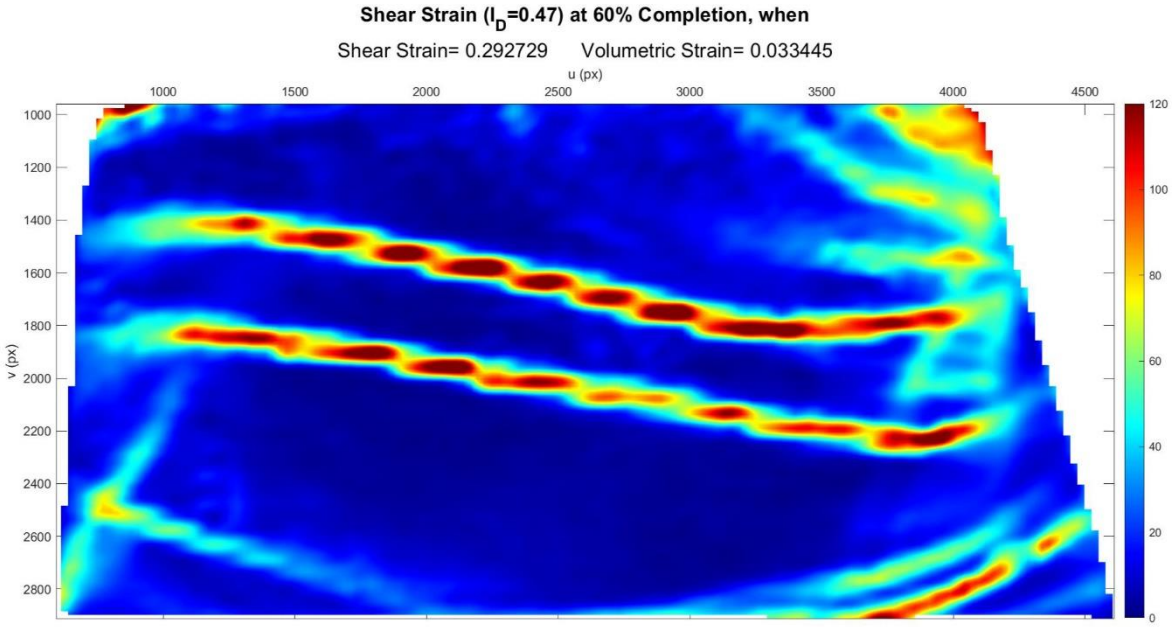

Figure C.93. Shear Strain Field at 60% Completion ($I_D = 0.47$ & $\sigma' = 0.84\ kPa$).

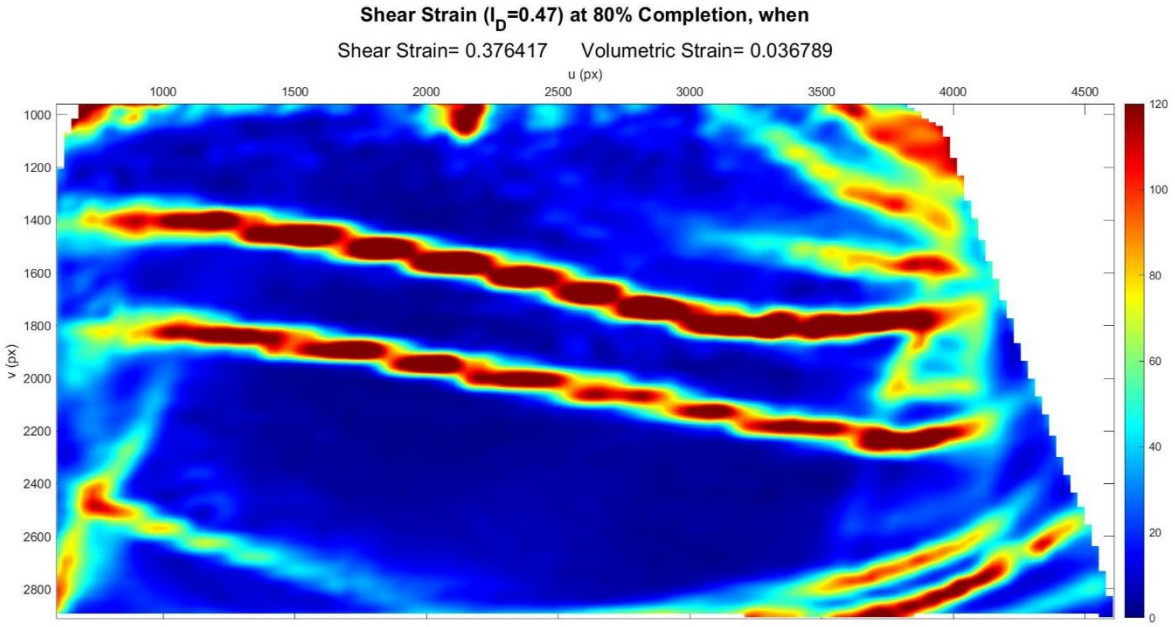

Figure C.94. Shear Strain Field at 80% Completion ($I_D = 0.47$ & $\sigma' = 0.84\ kPa$).

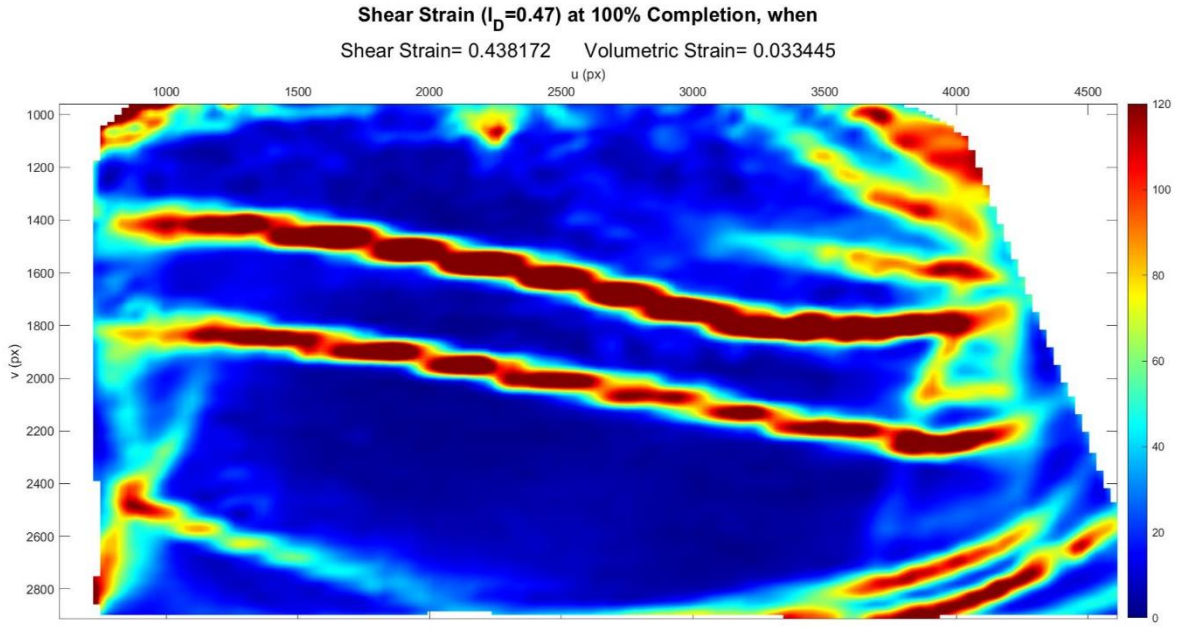

Figure C.95. Shear Strain Field at 100% Completion ($I_D = 0.47$ & $\sigma' = 0.84\ kPa$).

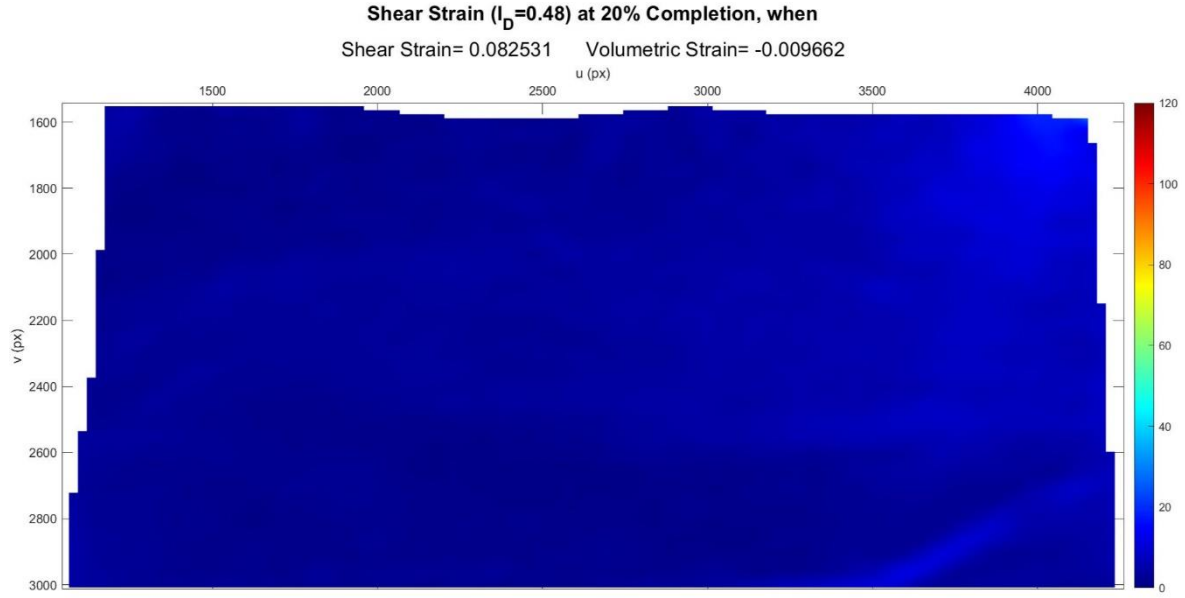

Figure C.96. Shear Strain Field at 20% Completion ($I_D = 0.48$ & $\sigma' = 0.81\ kPa$).

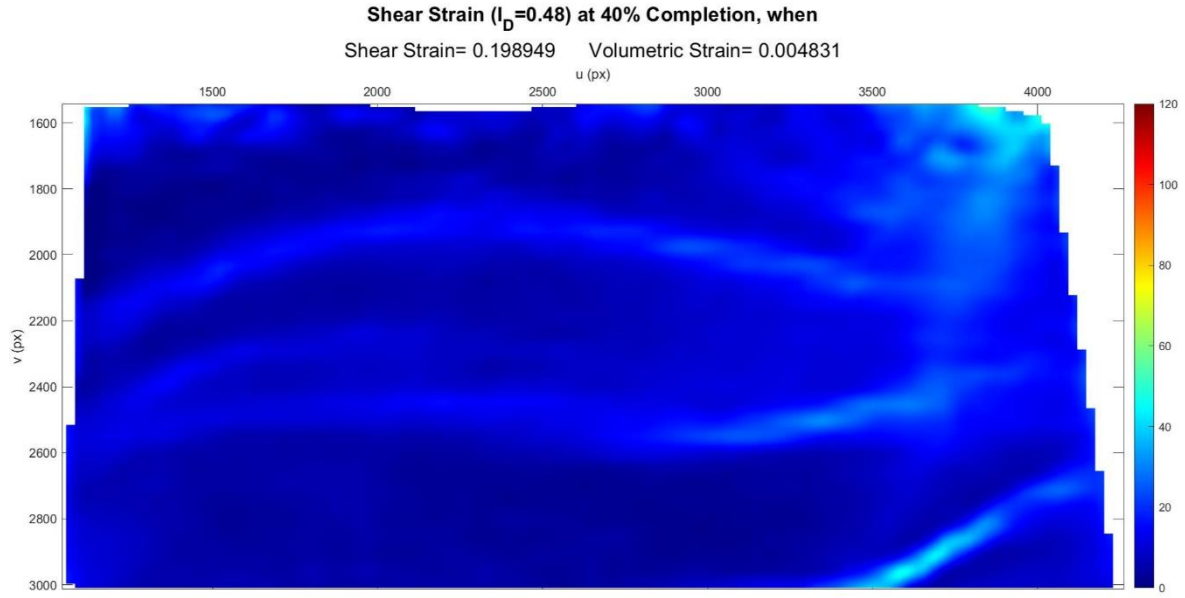

Figure C.97. Shear Strain Field at 40% Completion ($I_D = 0.48$ & $\sigma' = 0.81\ kPa$).

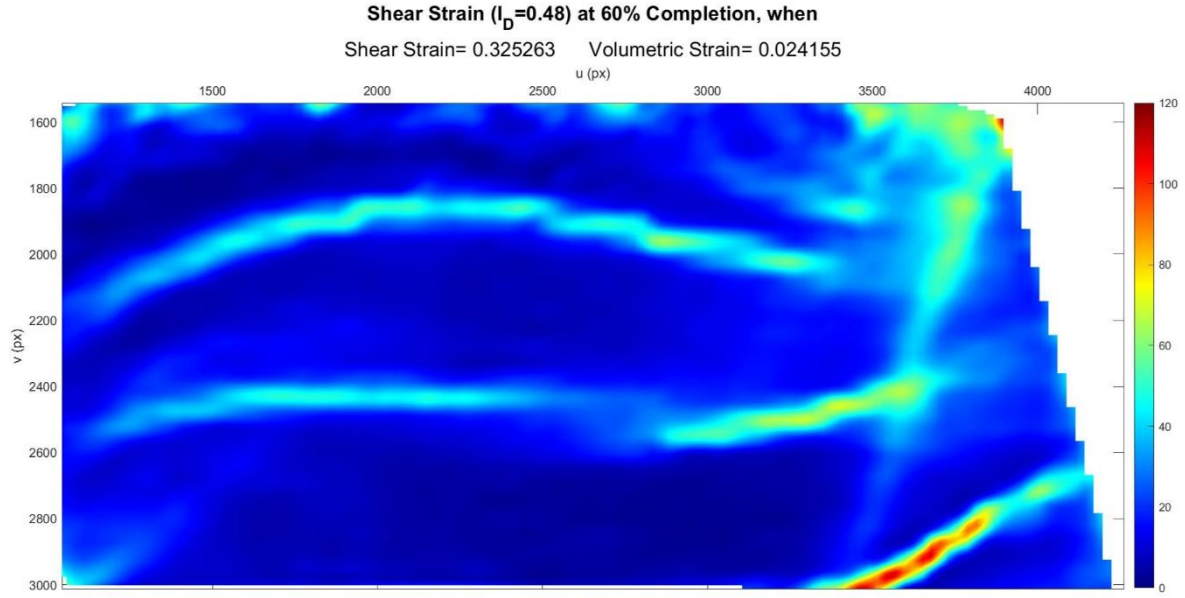

Figure C.98. Shear Strain Field at 60% Completion ($I_D = 0.48$ & $\sigma' = 0.81\ kPa$).

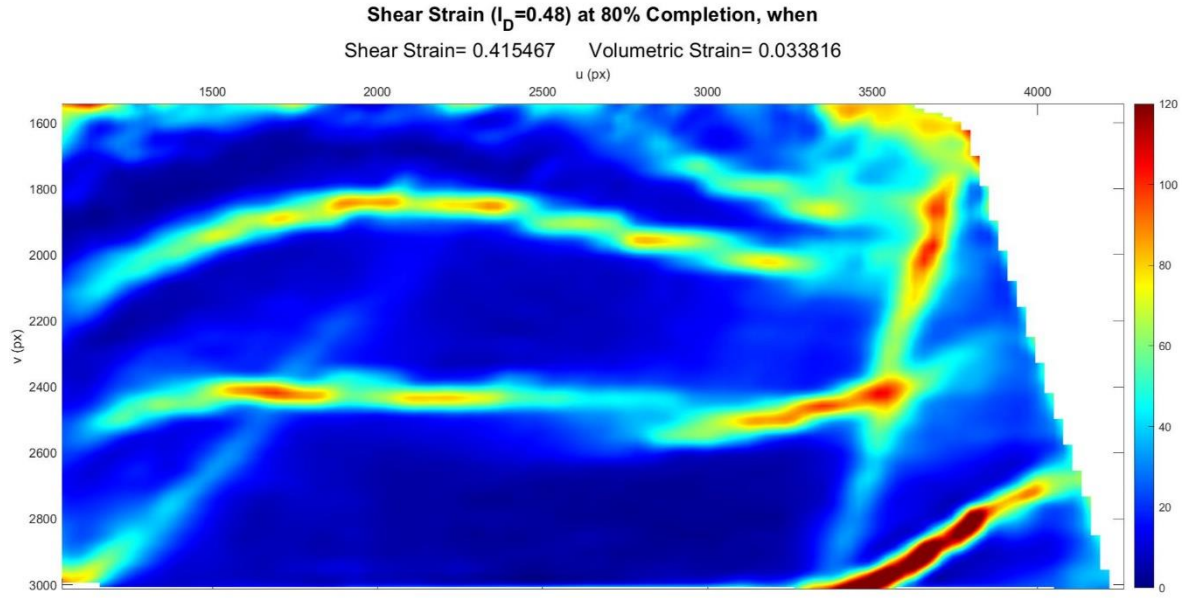

Figure C.99. Shear Strain Field at 80% Completion ($I_D = 0.48$ & $\sigma' = 0.81\ kPa$).

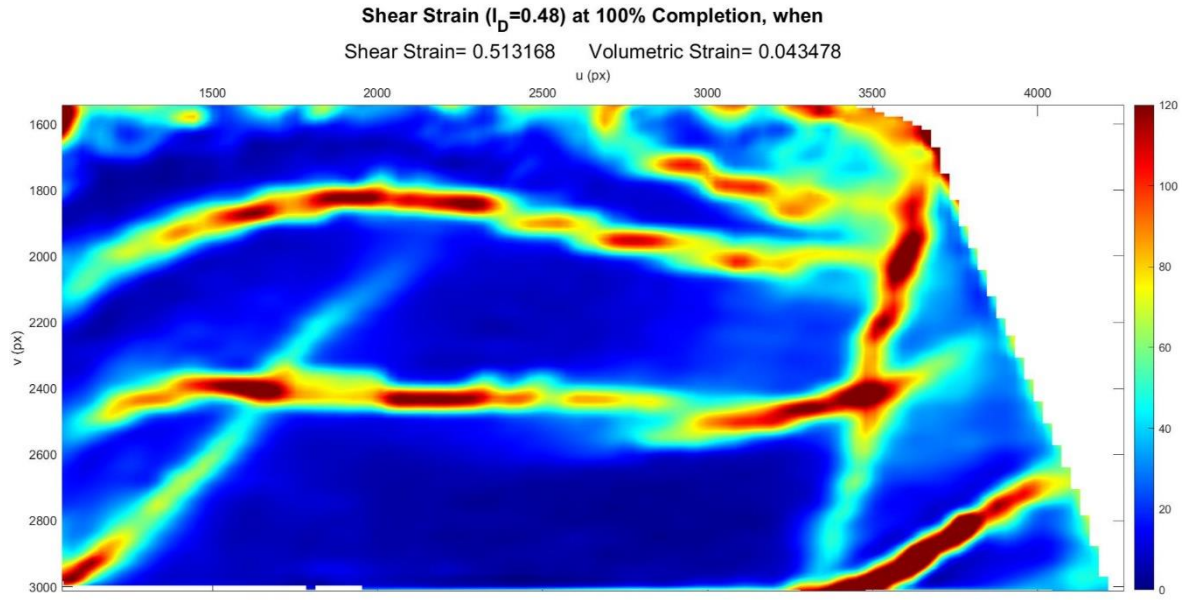

Figure C.100. Shear Strain Field at 100% Completion ($I_D = 0.48$ & $\sigma' = 0.81\ kPa$).

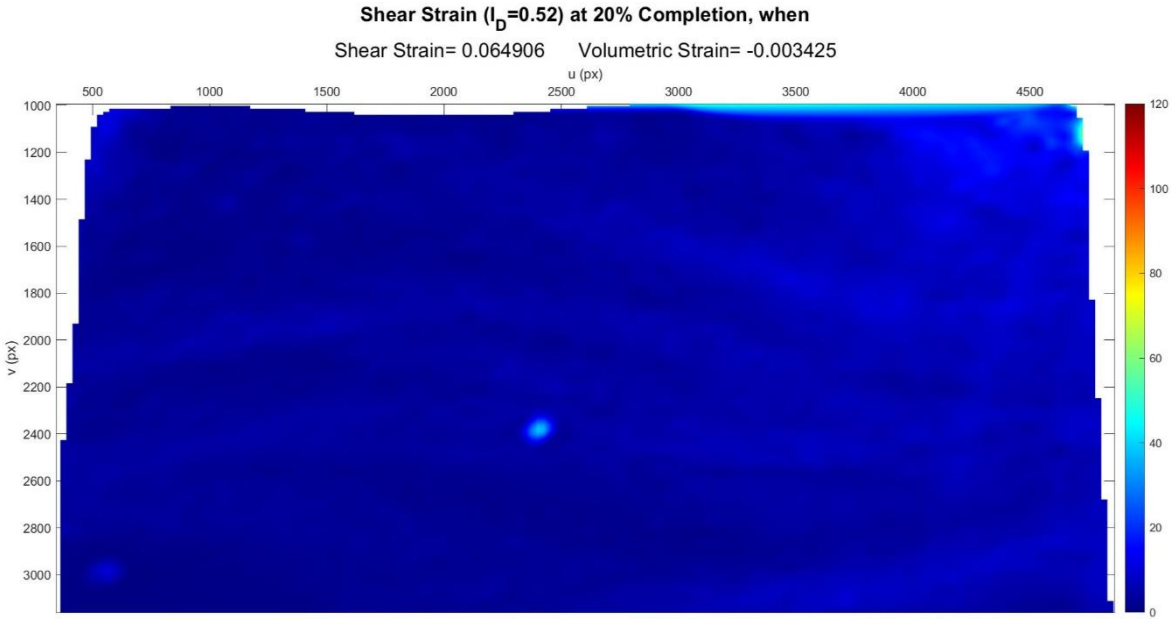

Figure C.101. Shear Strain Field at 20% Completion ($I_D = 0.52$ & $\sigma' = 0.88\ kPa$).

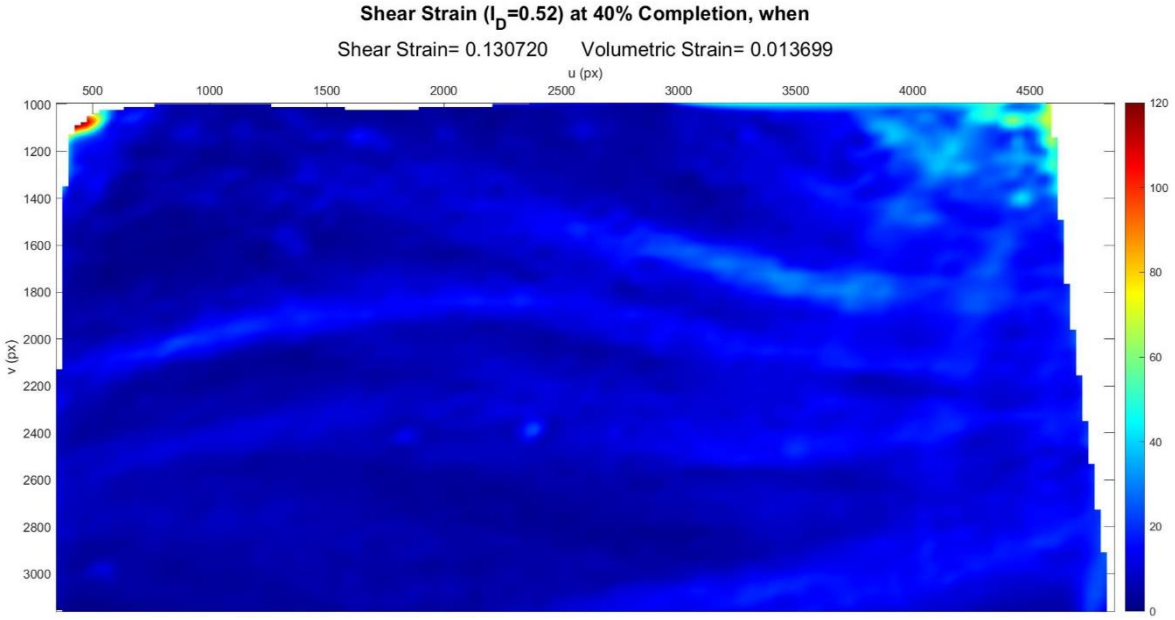

Figure C.102. Shear Strain Field at 40% Completion ($I_D = 0.52$ & $\sigma' = 0.88\ kPa$).

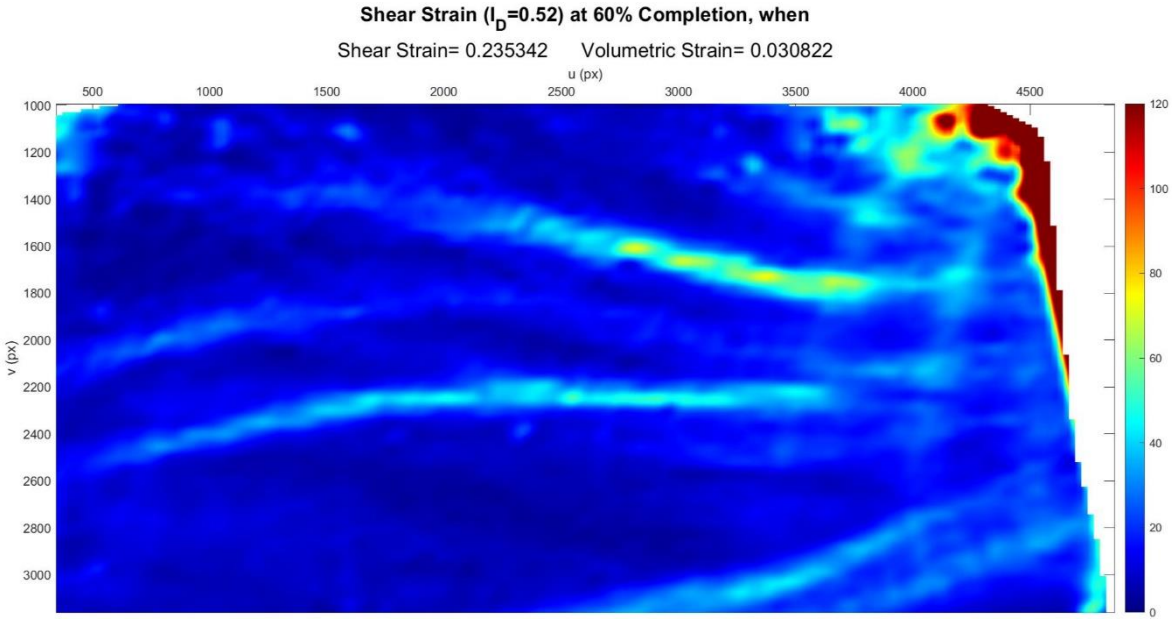

Figure C.103. Shear Strain Field at 60% Completion ($I_D = 0.52$ & $\sigma' = 0.88\ kPa$).

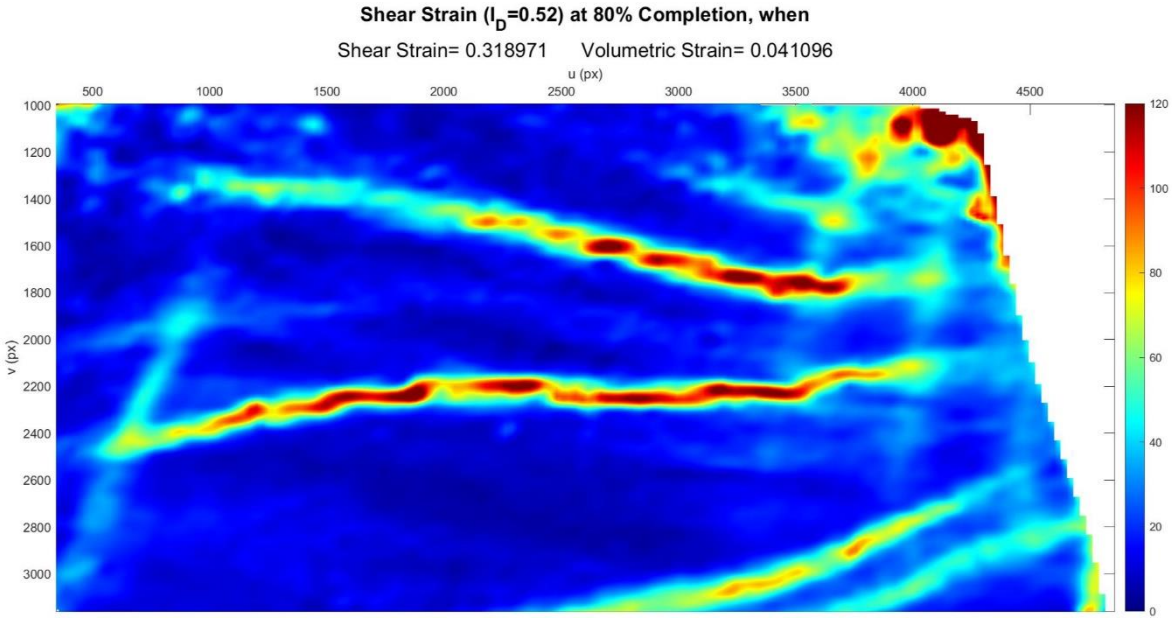

Figure C.104. Shear Strain Field at 80% Completion ($I_D = 0.52$ & $\sigma' = 0.88\ kPa$).

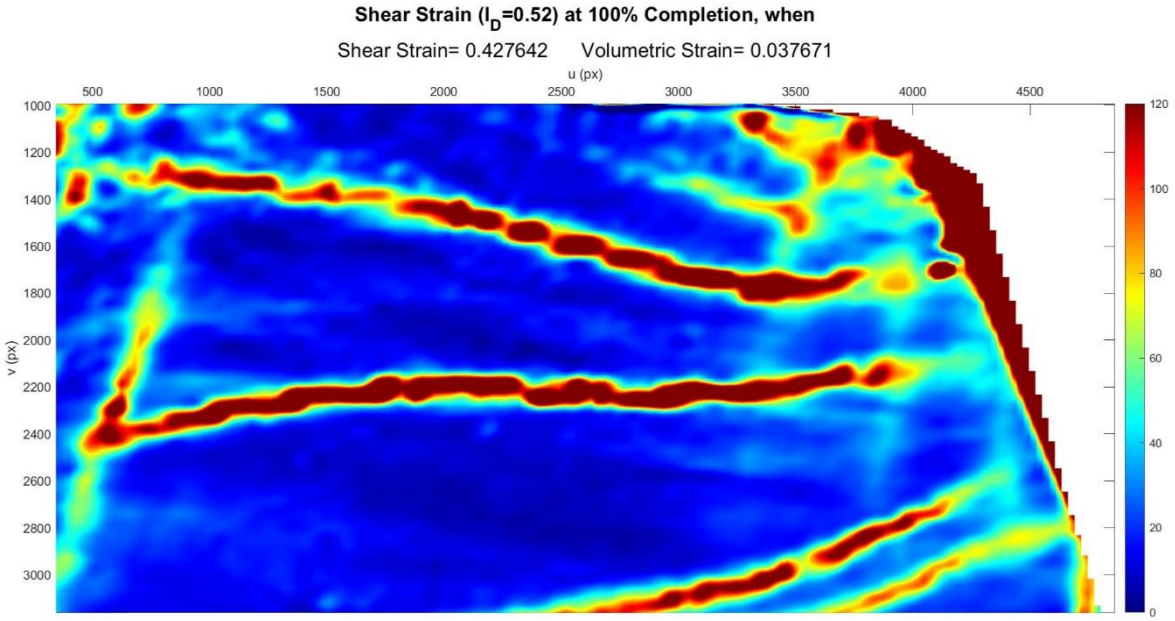

Figure C.105. Shear Strain Field at 100% Completion ($I_D = 0.52$ & $\sigma' = 0.88\,kPa$).

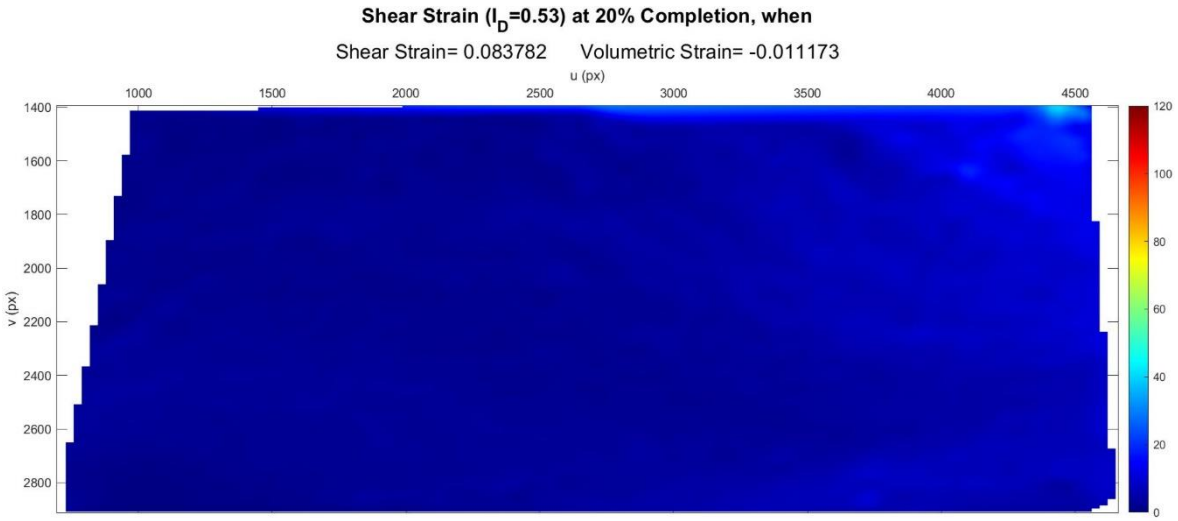

Figure C.106. Shear Strain Field at 20% Completion ($I_D = 0.53$ & $\sigma' = 0.69\ kPa$).

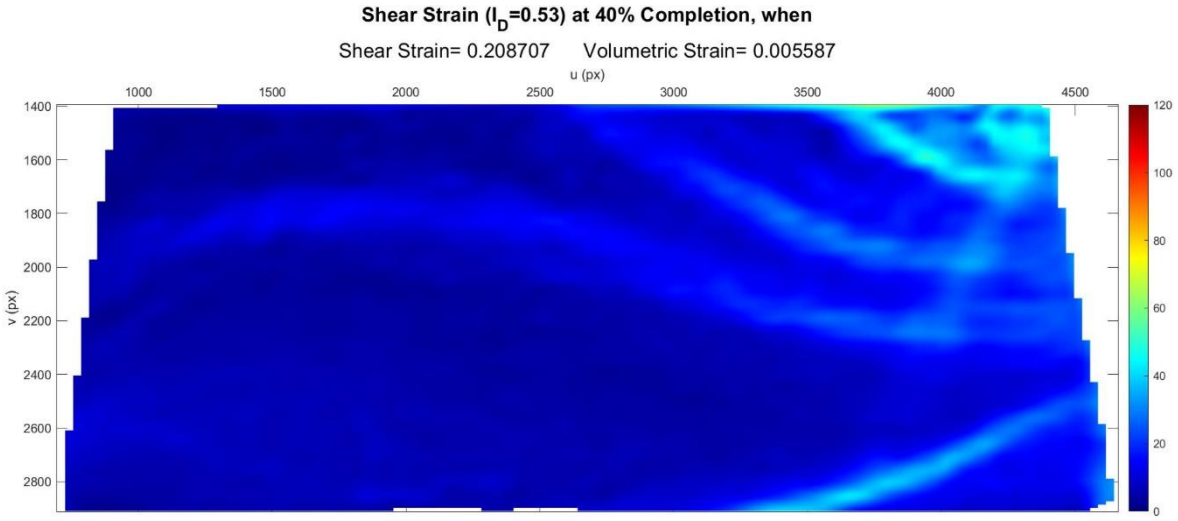

Figure C.107. Shear Strain Field at 40% Completion ($I_D = 0.53$ & $\sigma' = 0.69\ kPa$).

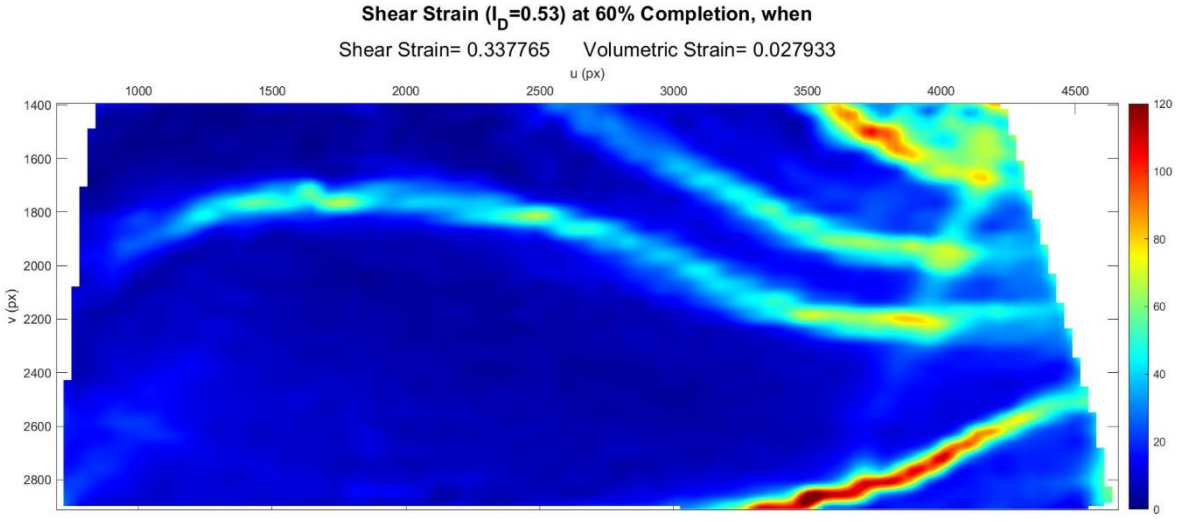

Figure C.108. Shear Strain Field at 60% Completion ($I_D = 0.53$ & $\sigma' = 0.69\ kPa$).

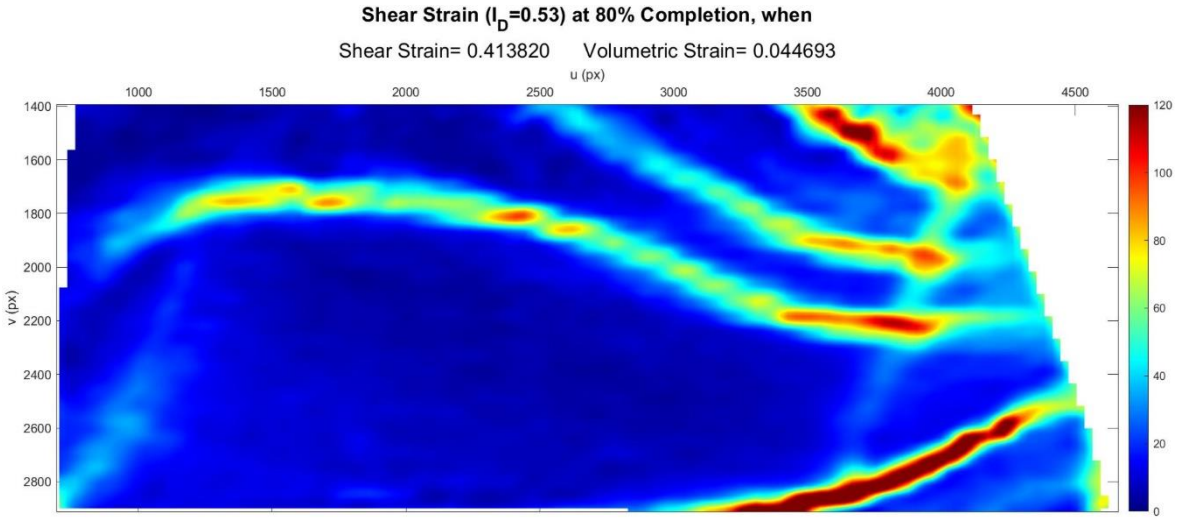

Figure C.109. Shear Strain Field at 80% Completion ($I_D = 0.53$ & $\sigma' = 0.69\ kPa$).

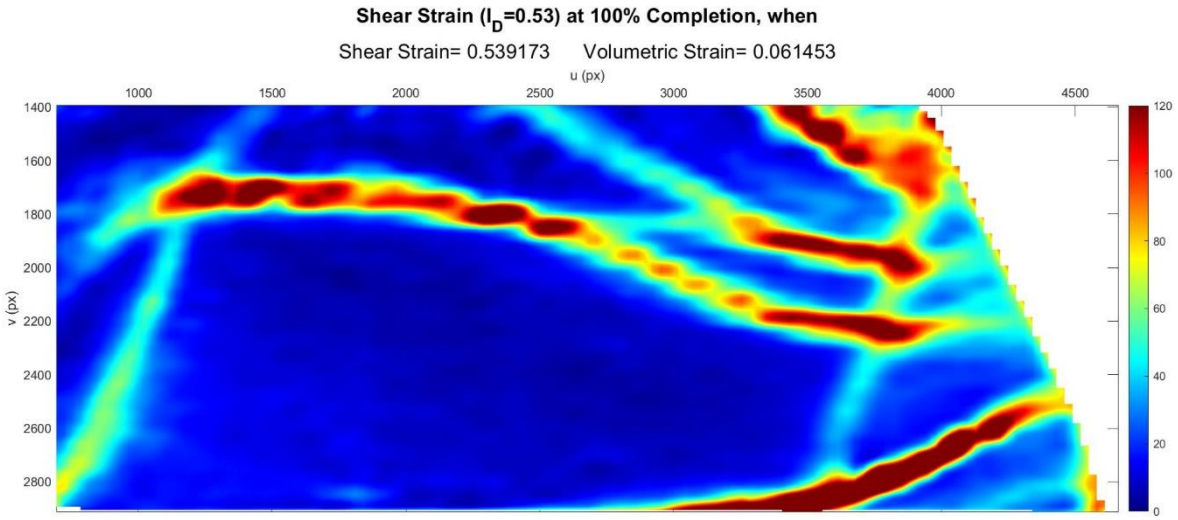

Figure C.110. Shear Strain Field at 100% Completion ($I_D = 0.53$ & $\sigma' = 0.69\ kPa$).

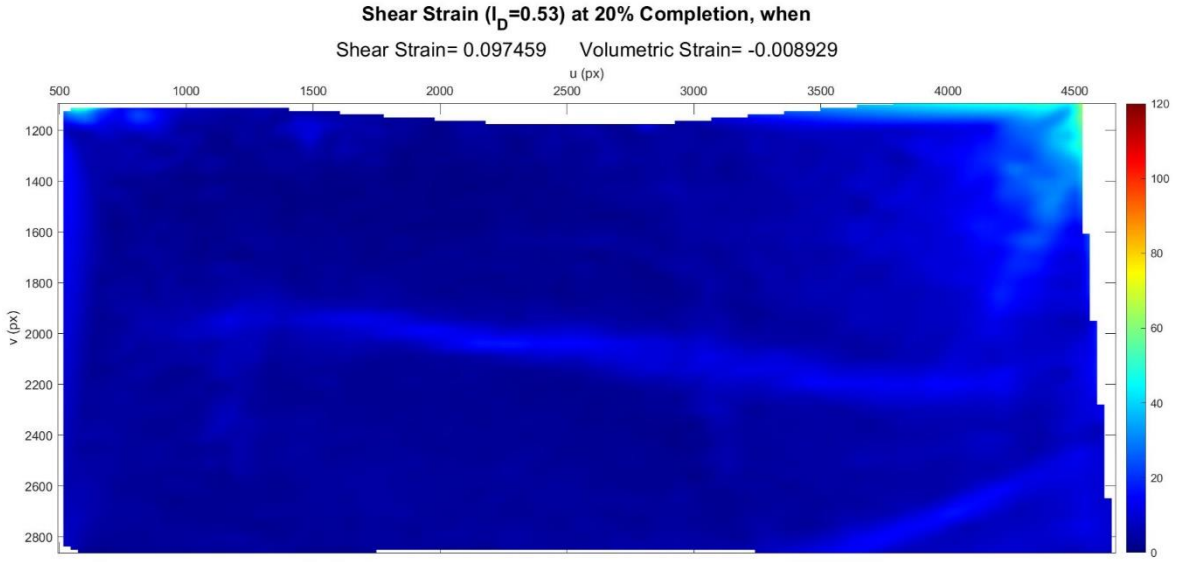

Figure C.111. Shear Strain Field at 20% Completion ($I_D = 0.53$ & $\sigma' = 0.72\ kPa$).

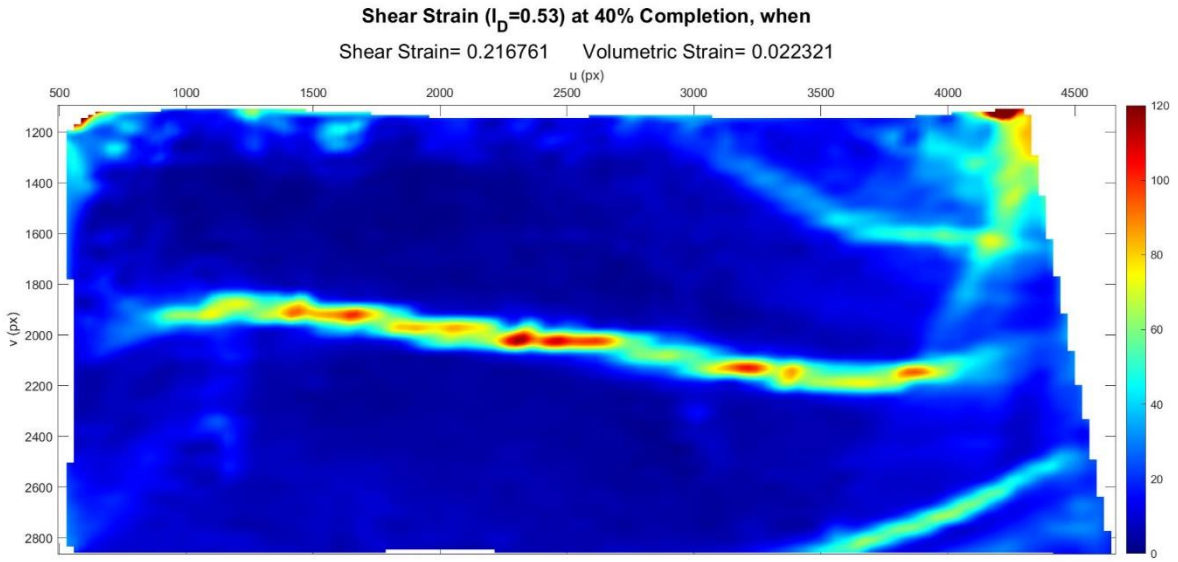

Figure C.112. Shear Strain Field at 40% Completion ($I_D = 0.53$ & $\sigma' = 0.72\ kPa$).

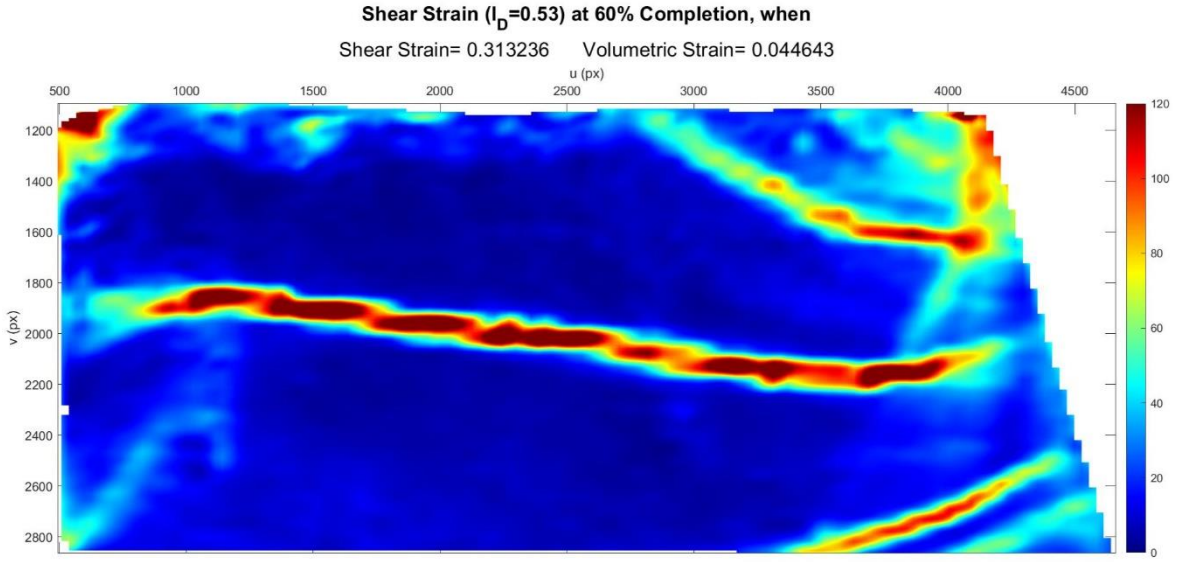

Figure C.113. Shear Strain Field at 60% Completion ($I_D = 0.53$ & $\sigma' = 0.72\ kPa$).

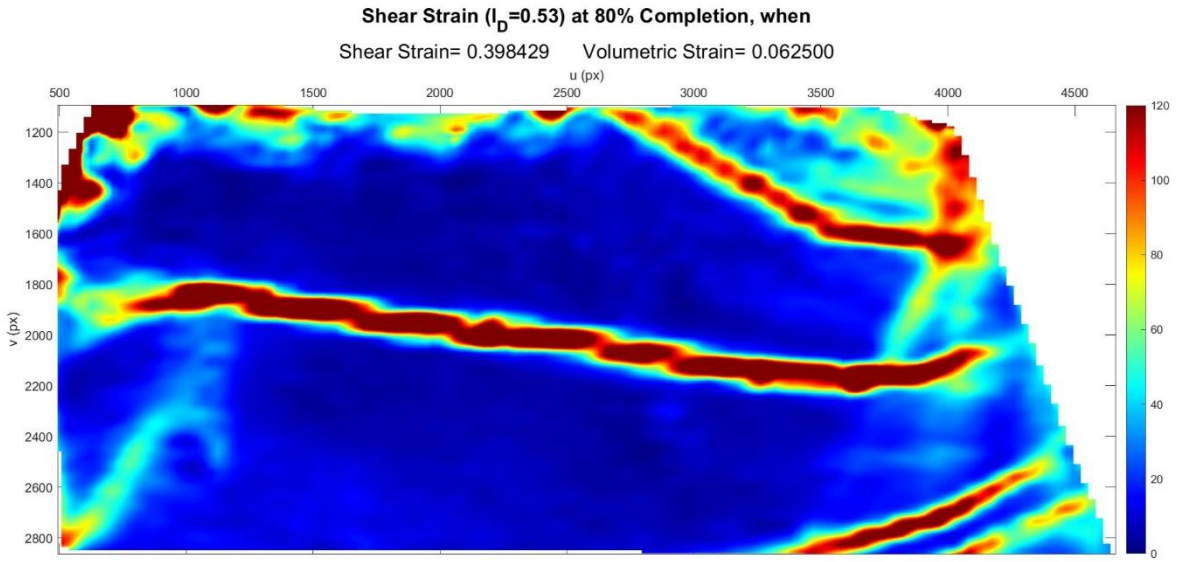

Figure C.114. Shear Strain Field at 80% Completion ($I_D = 0.53$ & $\sigma' = 0.72\ kPa$).

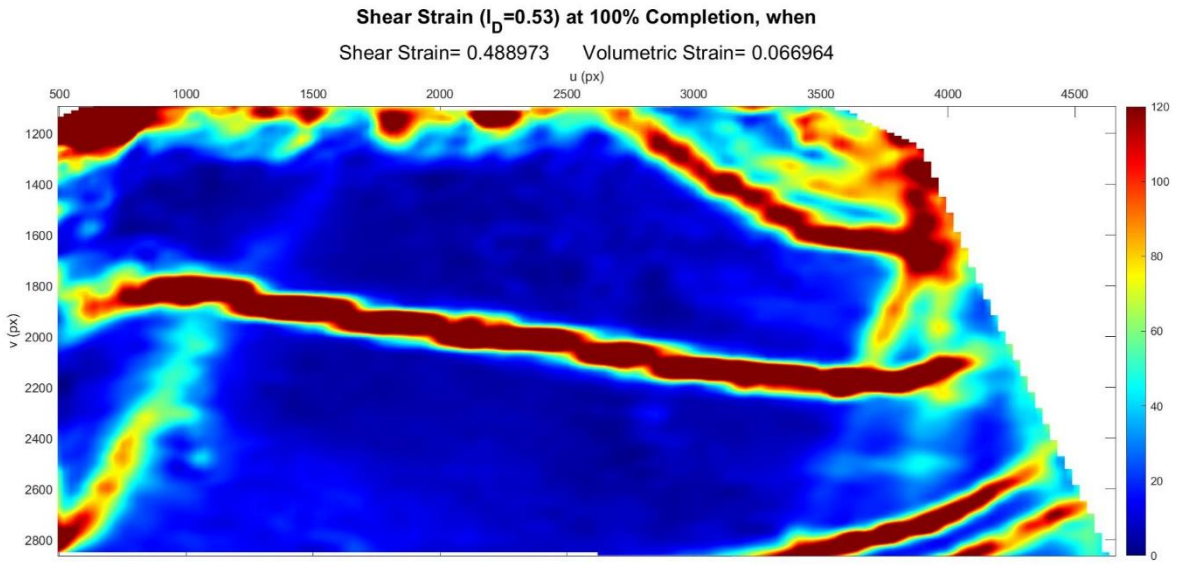

Figure C.115. Shear Strain Field at 100% Completion ($I_D = 0.53$ & $\sigma' = 0.72\ kPa$).

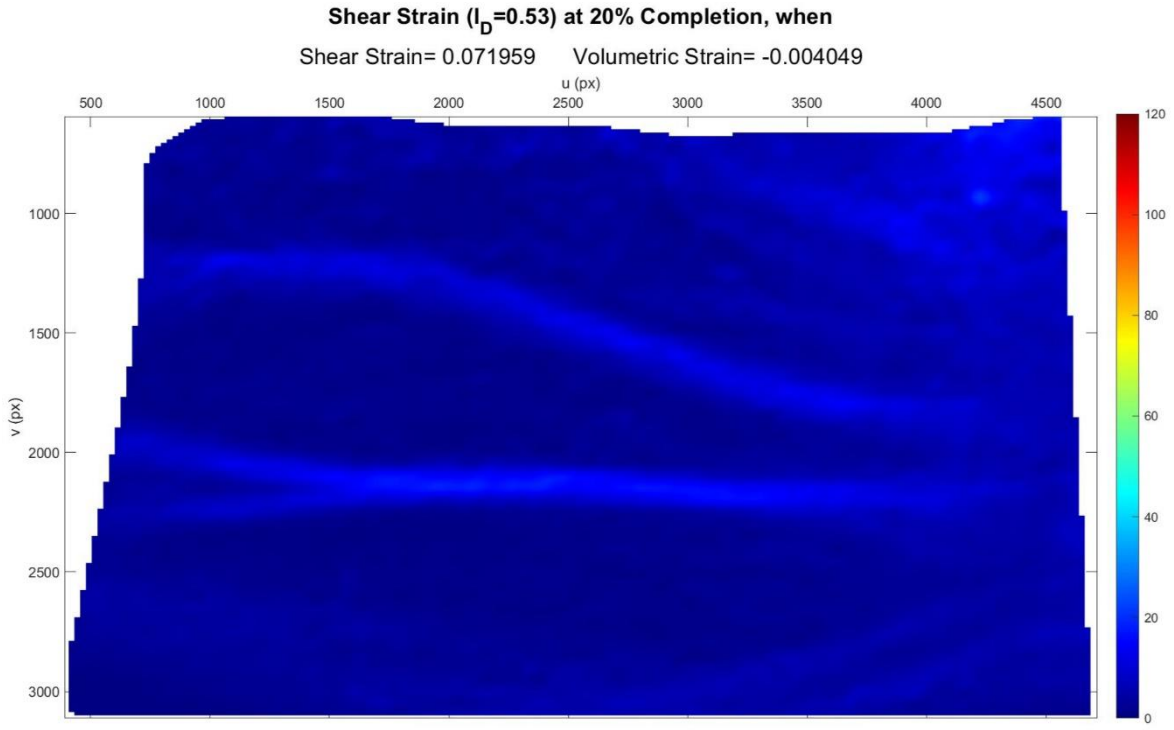

Figure C.116. Shear Strain Field at 20% Completion ($I_D = 0.53$ & $\sigma' = 0.96\ kPa$).

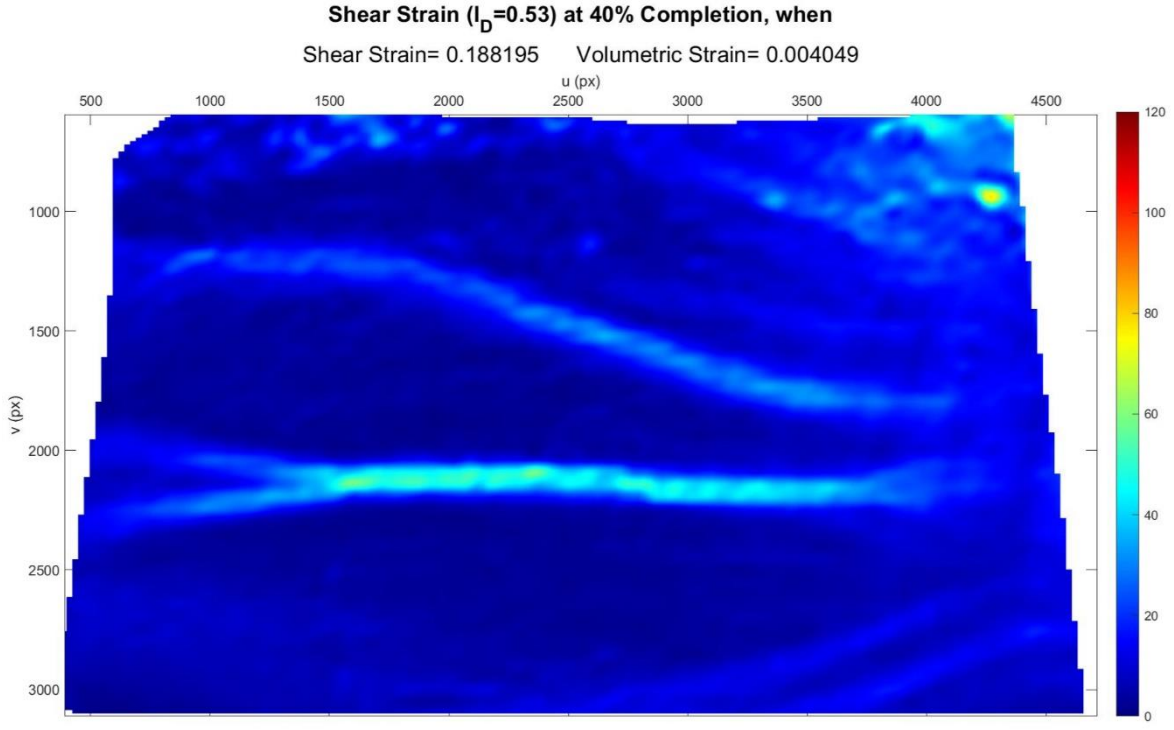

Figure C.117. Shear Strain Field at 40% Completion ($I_D = 0.53$ & $\sigma' = 0.96\ kPa$).

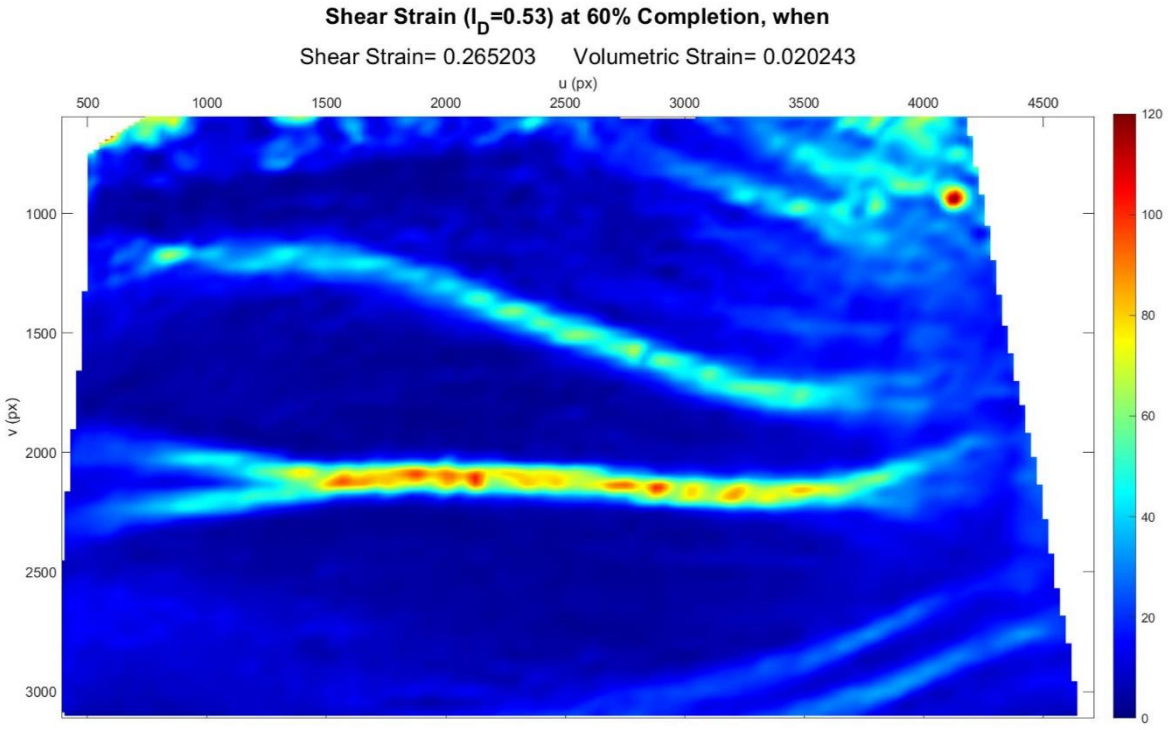

Figure C.118. Shear Strain Field at 60% Completion ($I_D = 0.53$ & $\sigma' = 0.96\ kPa$).

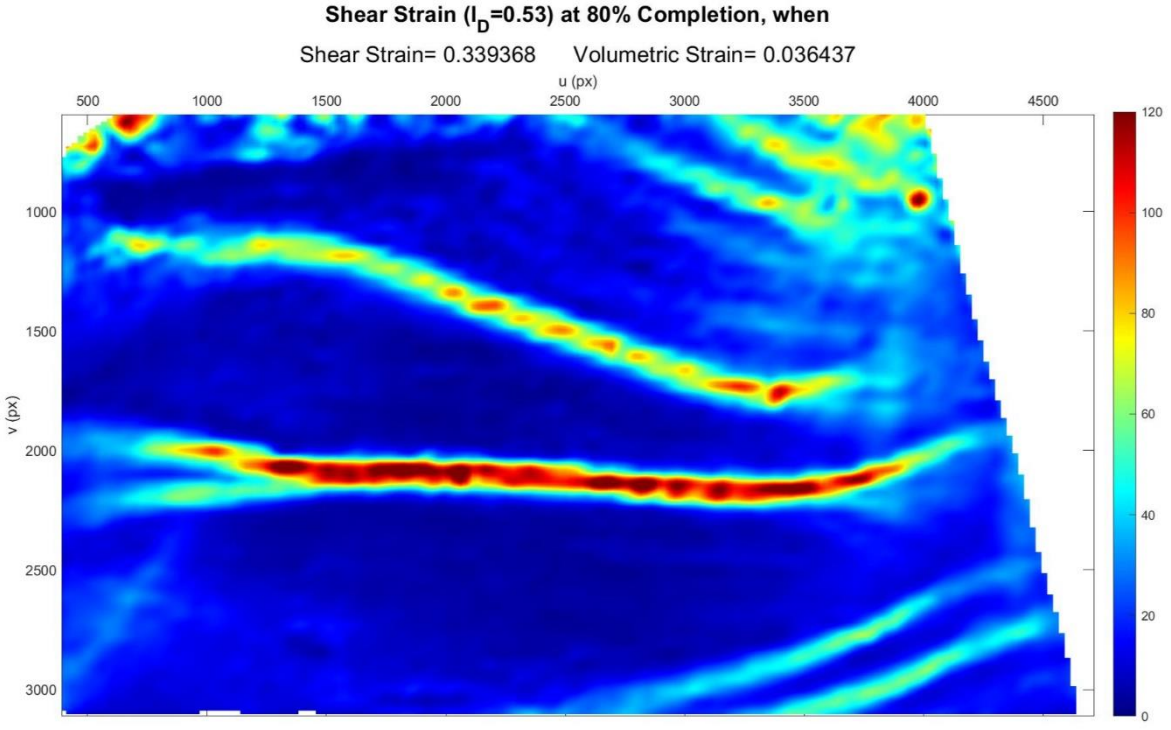

Figure C.119. Shear Strain Field at 80% Completion ($I_D = 0.53$ & $\sigma' = 0.96\ kPa$).

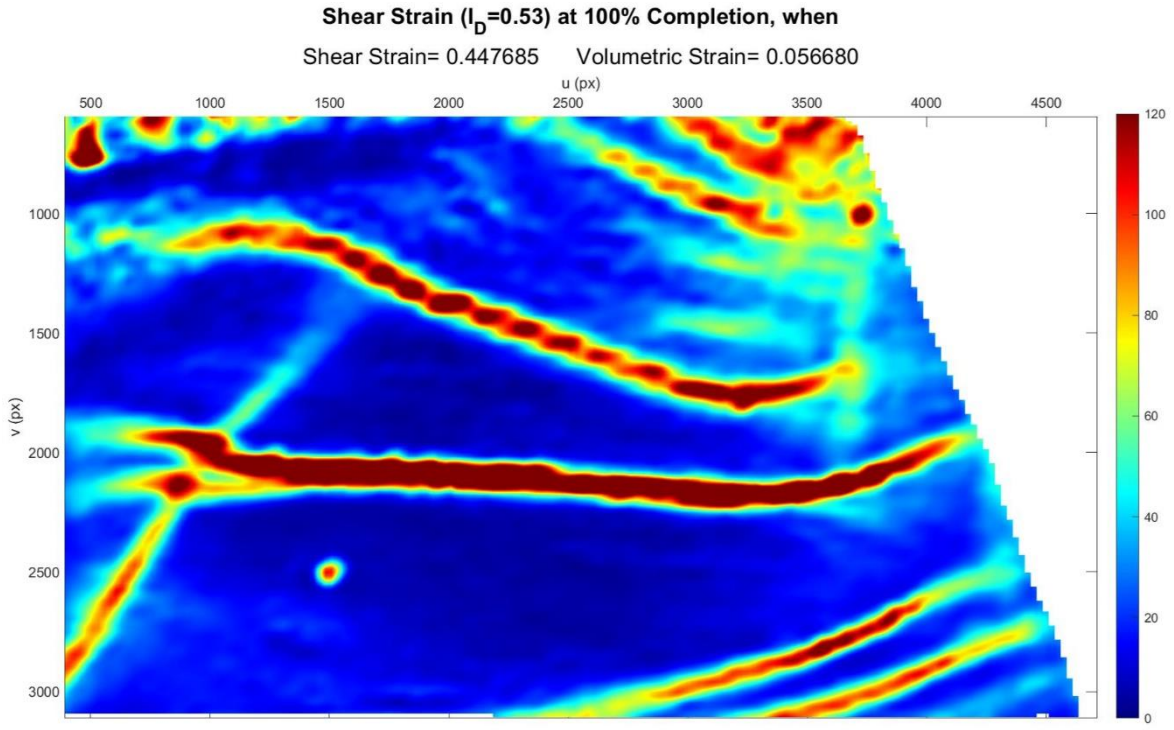

Figure C.120. Shear Strain Field at 100% Completion ($I_D = 0.53$ & $\sigma' = 0.96\ kPa$).

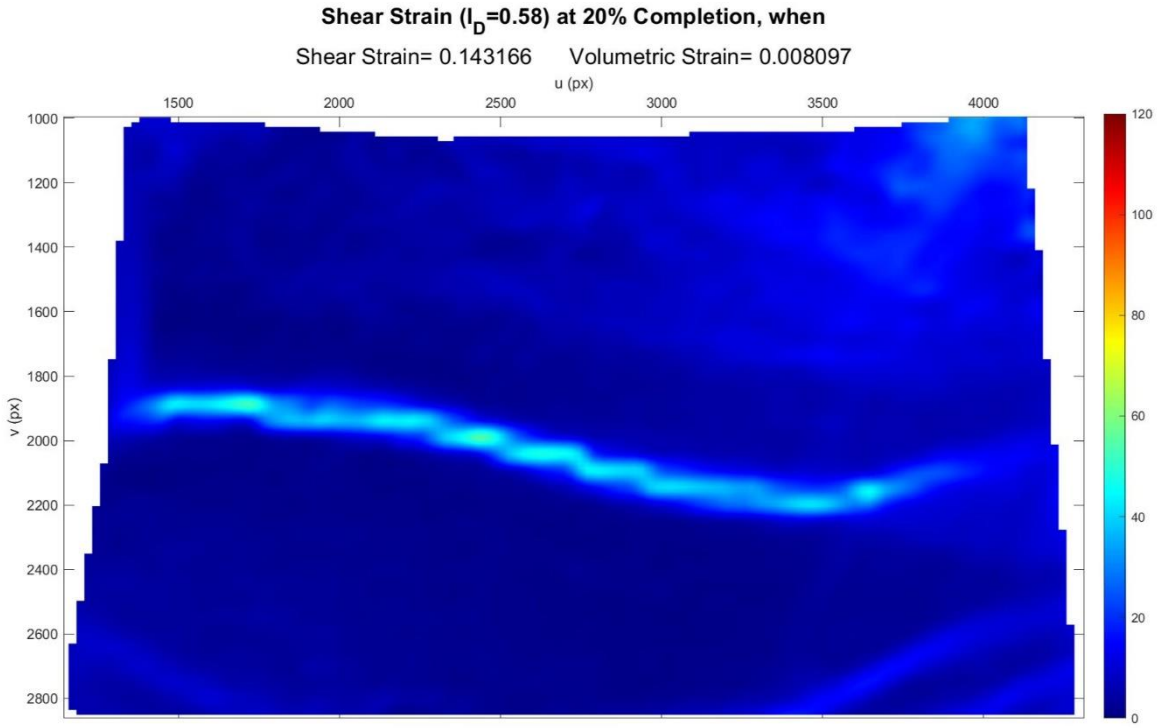

Figure C.121. Shear Strain Field at 20% Completion ($I_D = 0.58$ & $\sigma' = 0.79\ kPa$).

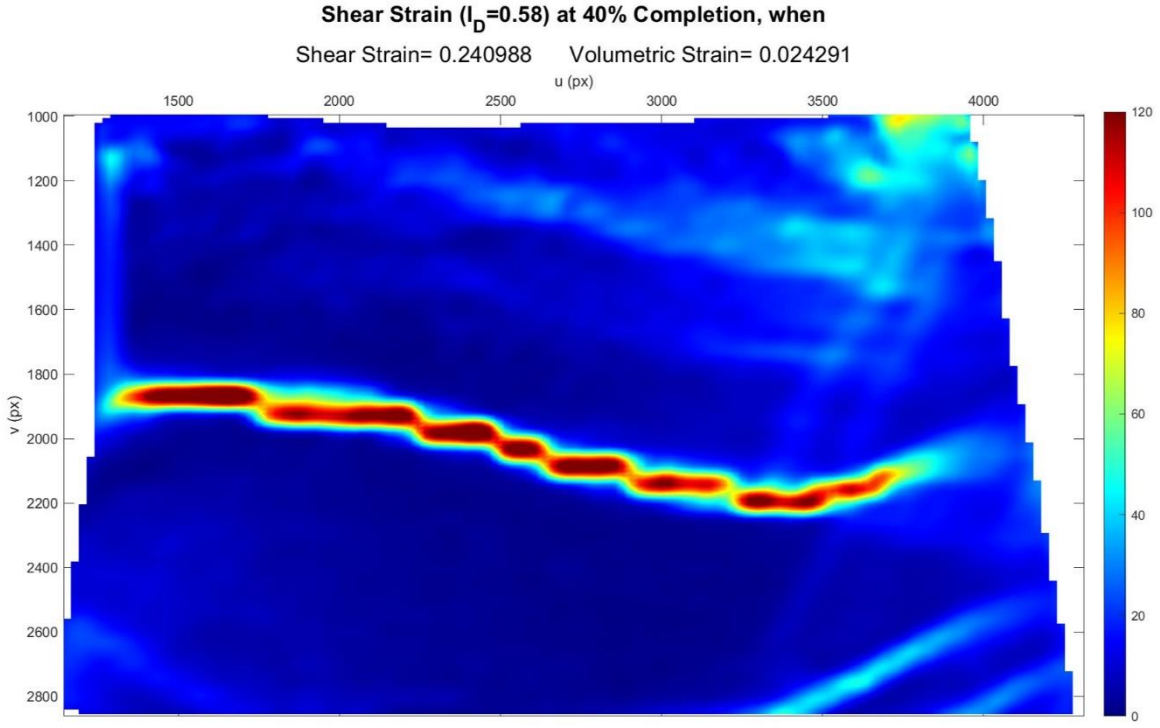

Figure C.122. Shear Strain Field at 40% Completion ($I_D = 0.58$ & $\sigma' = 0.79\ kPa$).

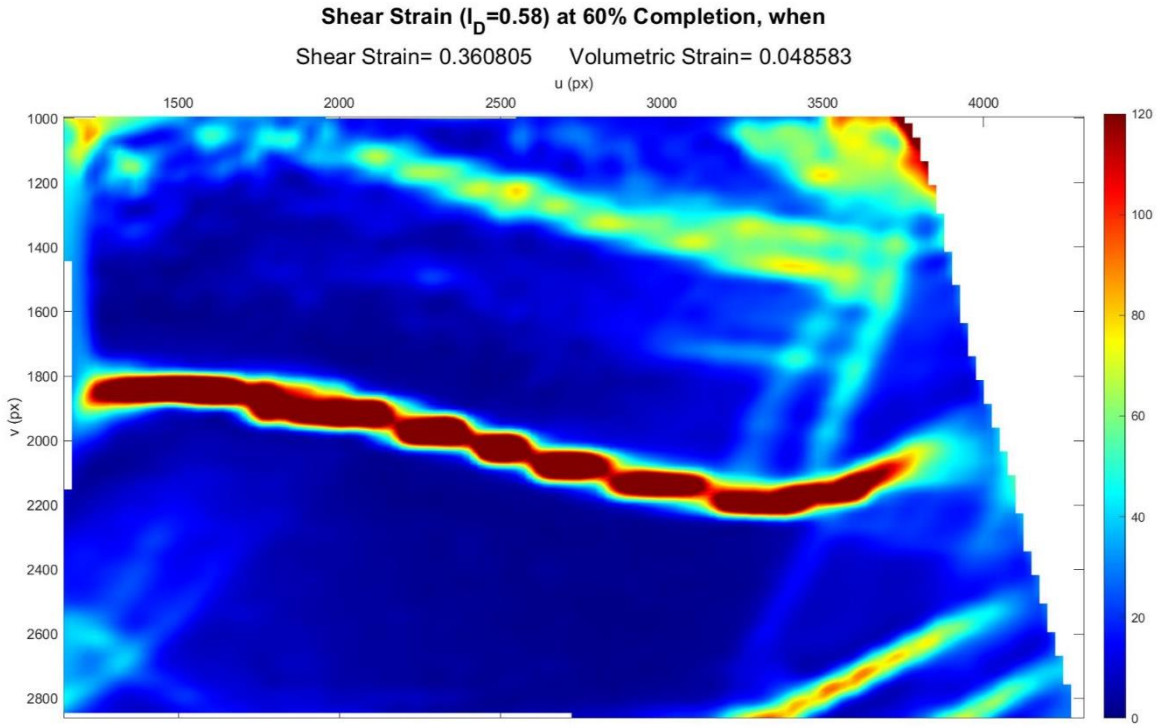

Figure C.123. Shear Strain Field at 60% Completion ($I_D = 0.58$ & $\sigma' = 0.79\ kPa$).

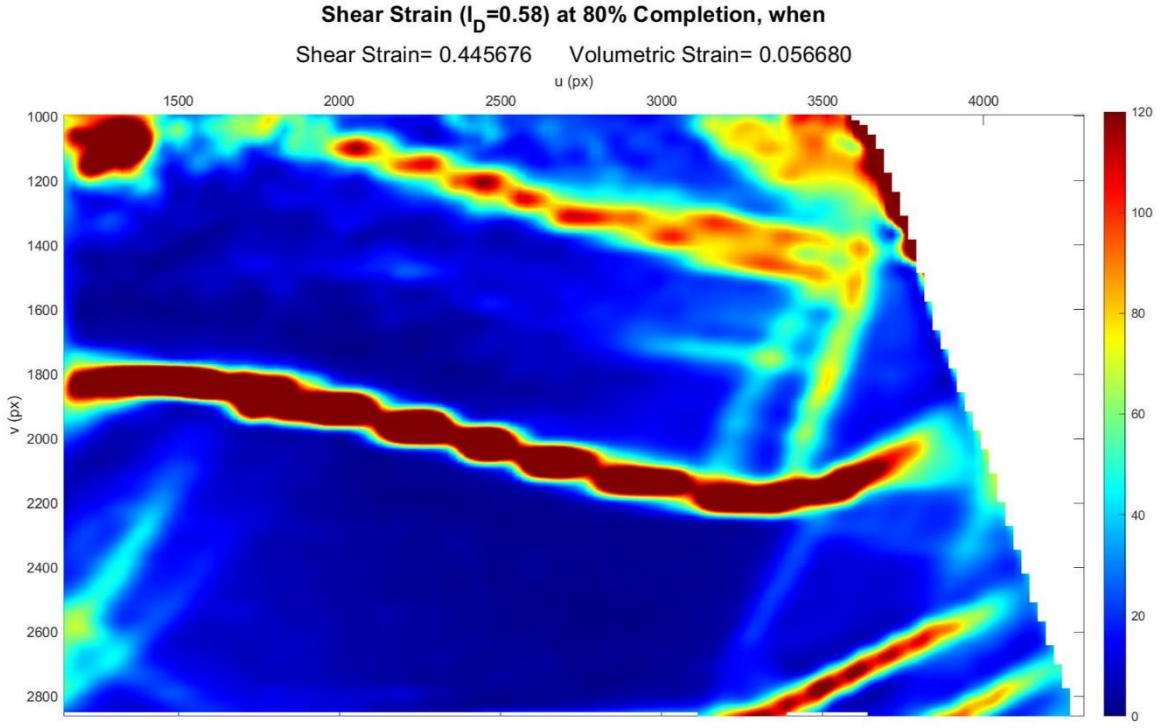

Figure C.124. Shear Strain Field at 80% Completion ($I_D = 0.58$ & $\sigma' = 0.79\ kPa$).

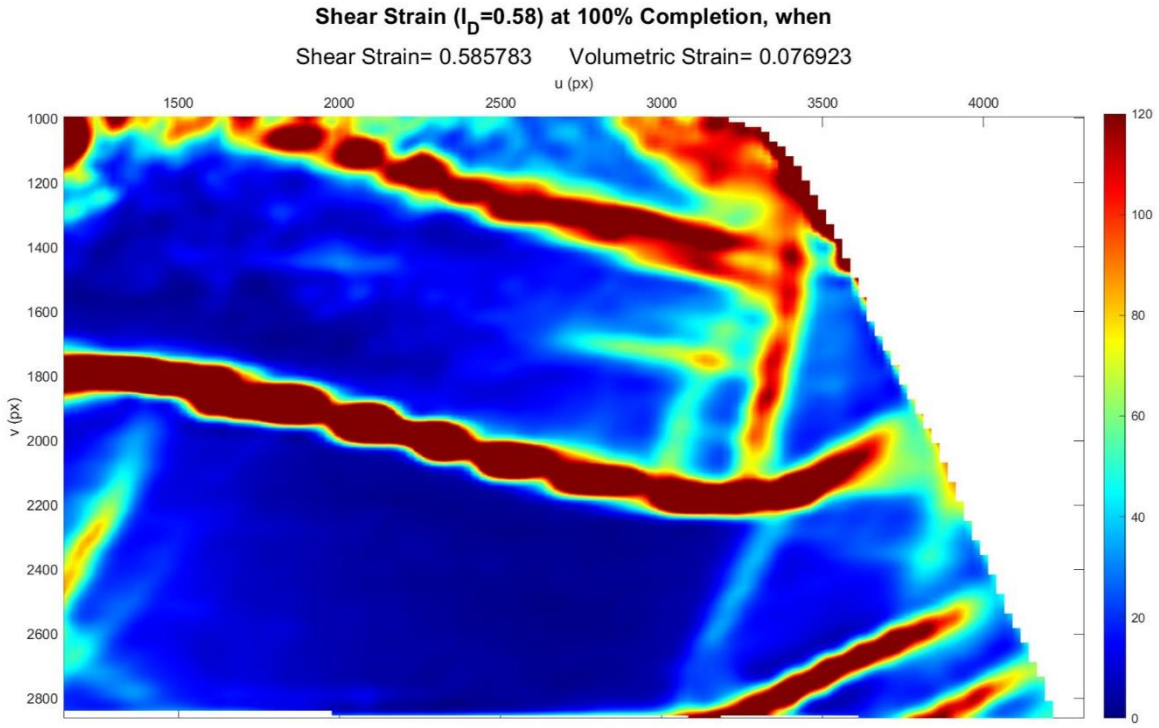

Figure C.125. Shear Strain Field at 100% Completion ($I_D = 0.58$ & $\sigma' = 0.79\ kPa$).

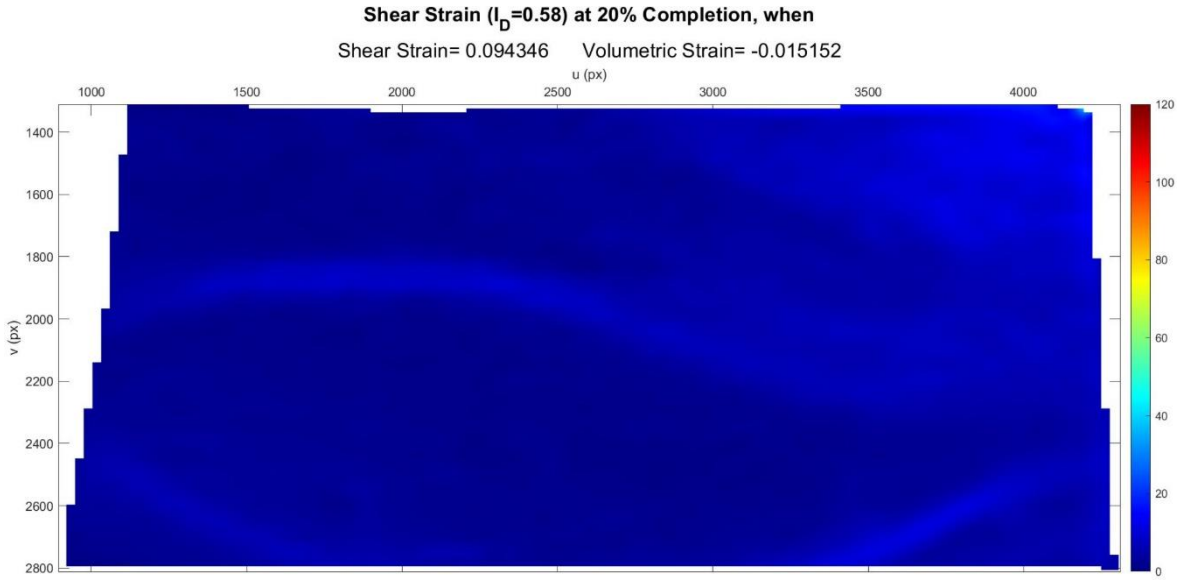

Figure C.126. Shear Strain Field at 20% Completion ($I_D = 0.58$ & $\sigma' = 0.80\ kPa$).

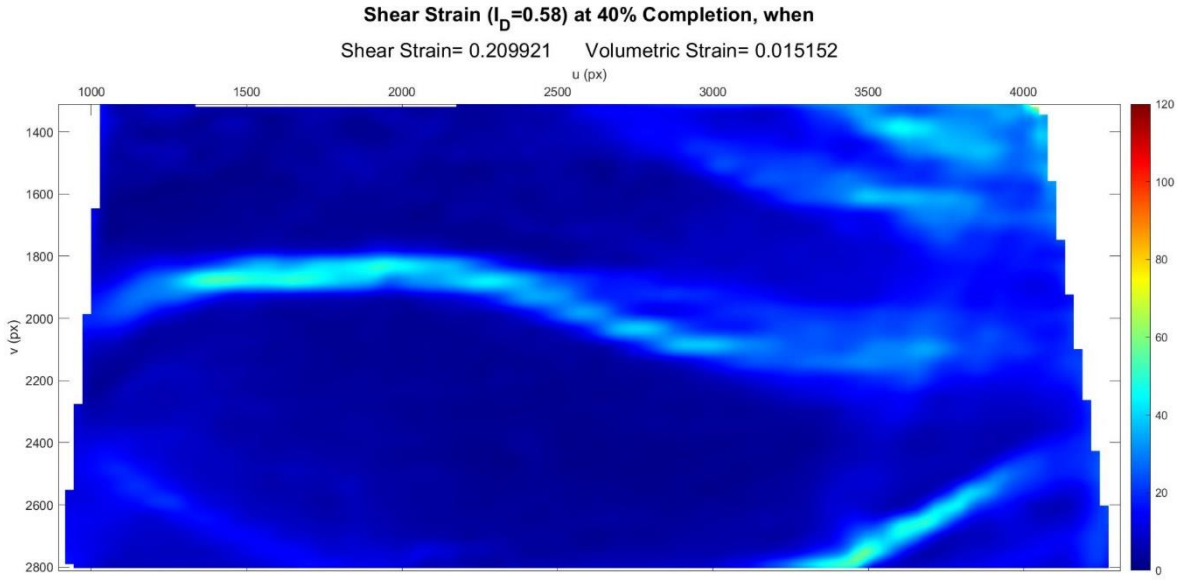

Figure C.127. Shear Strain Field at 40% Completion ($I_D = 0.58$ & $\sigma' = 0.80\ kPa$).

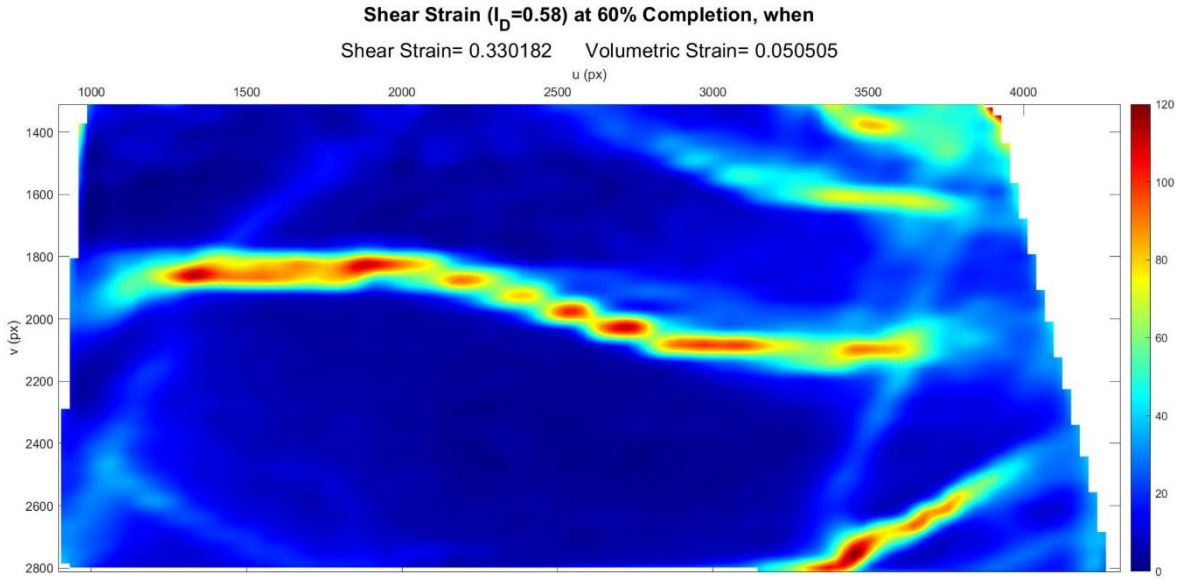

Figure C.128. Shear Strain Field at 60% Completion ($I_D = 0.58$ & $\sigma' = 0.80\ kPa$).

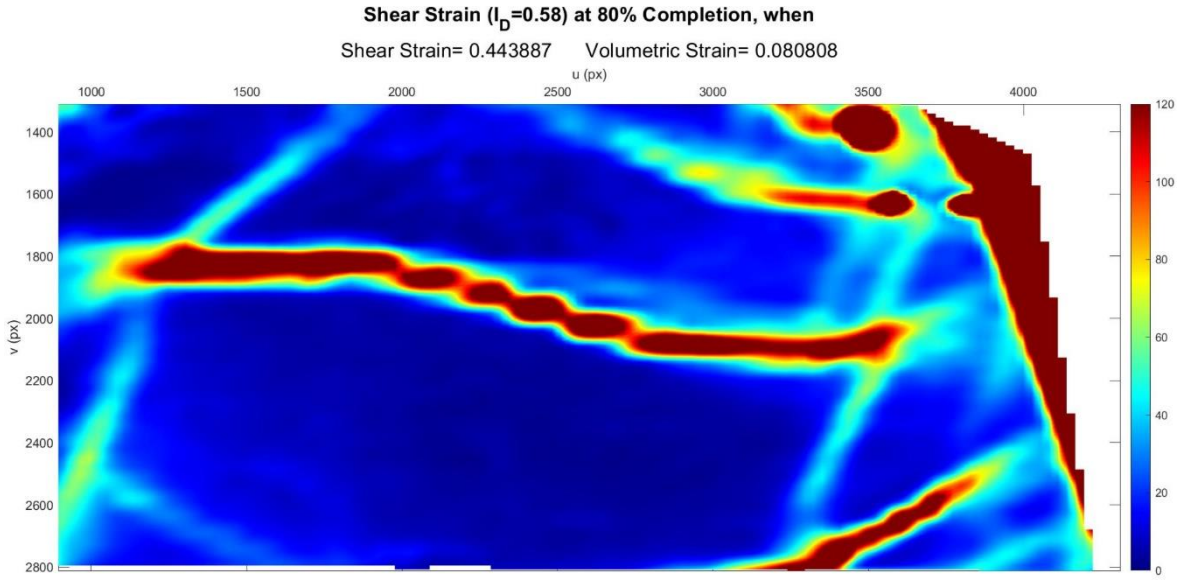

Figure C.129. Shear Strain Field at 80% Completion ($I_D = 0.58$ & $\sigma' = 0.80\ kPa$).

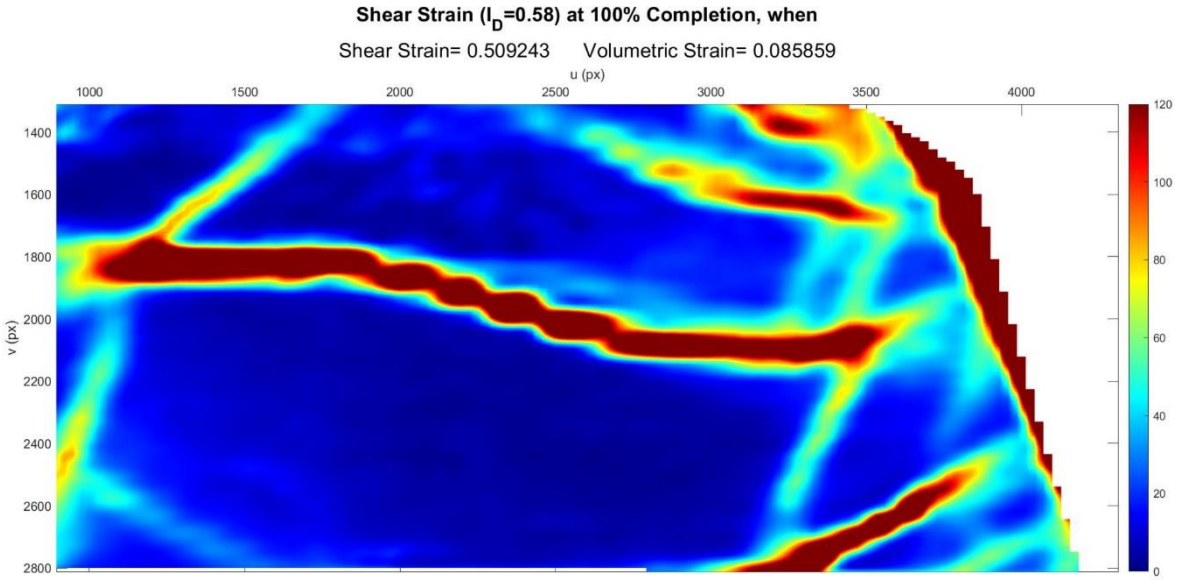

Figure C.130. Shear Strain Field at 100% Completion ($I_D = 0.58$ & $\sigma' = 0.80\ kPa$).

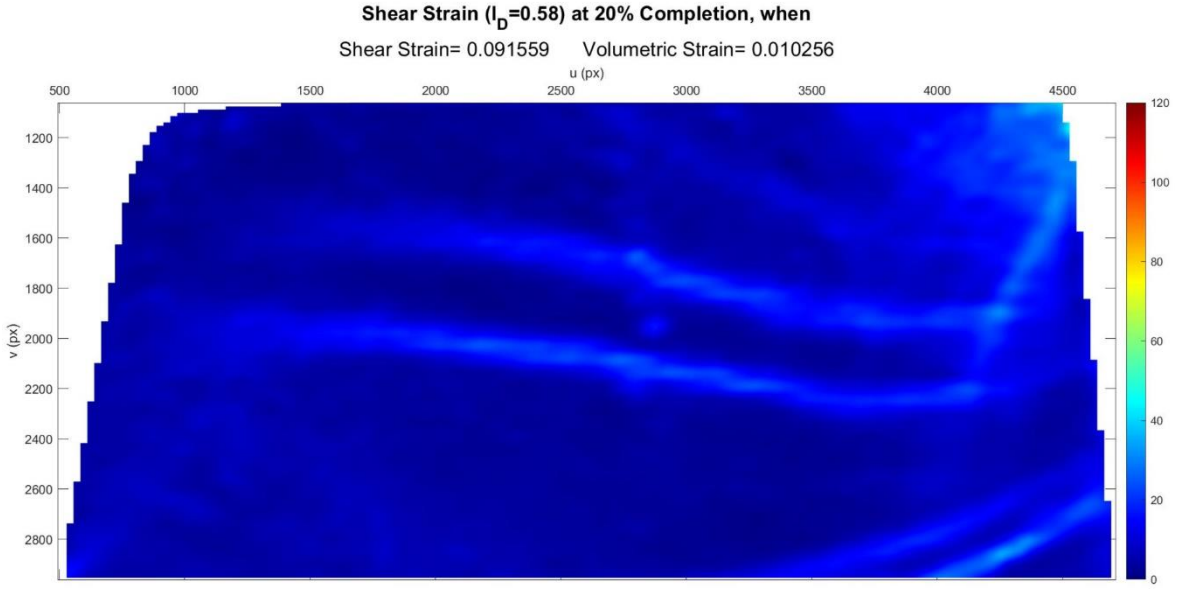

Figure C.131. Shear Strain Field at 20% Completion ($I_D = 0.58$ & $\sigma' = 0.96\ kPa$).

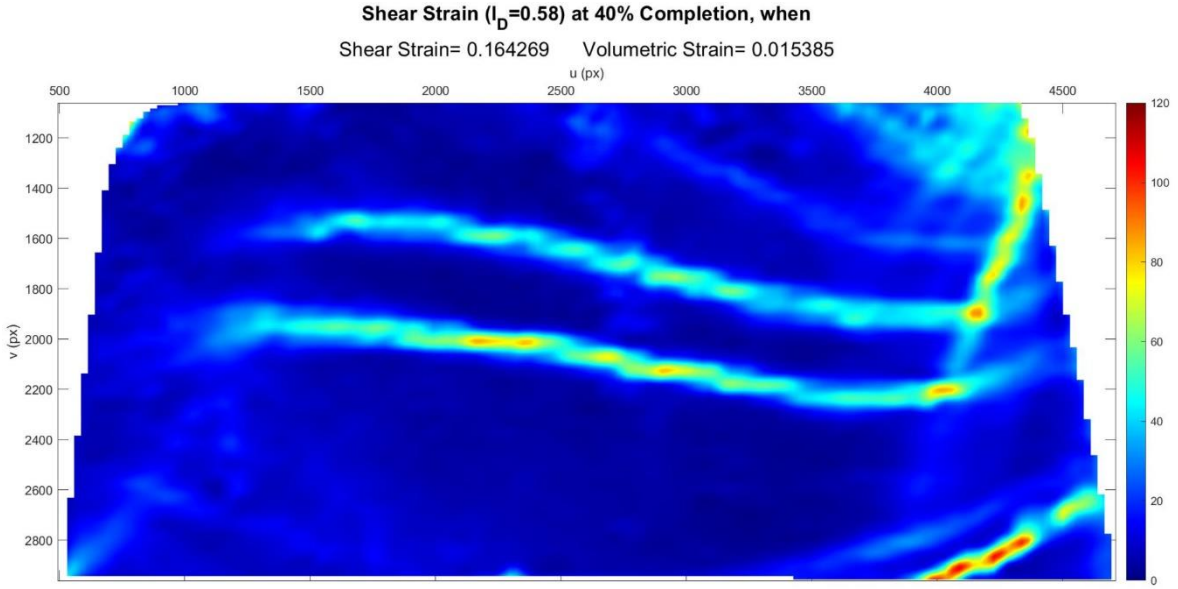

Figure C.132. Shear Strain Field at 40% Completion ($I_D = 0.58$ & $\sigma' = 0.96\ kPa$).

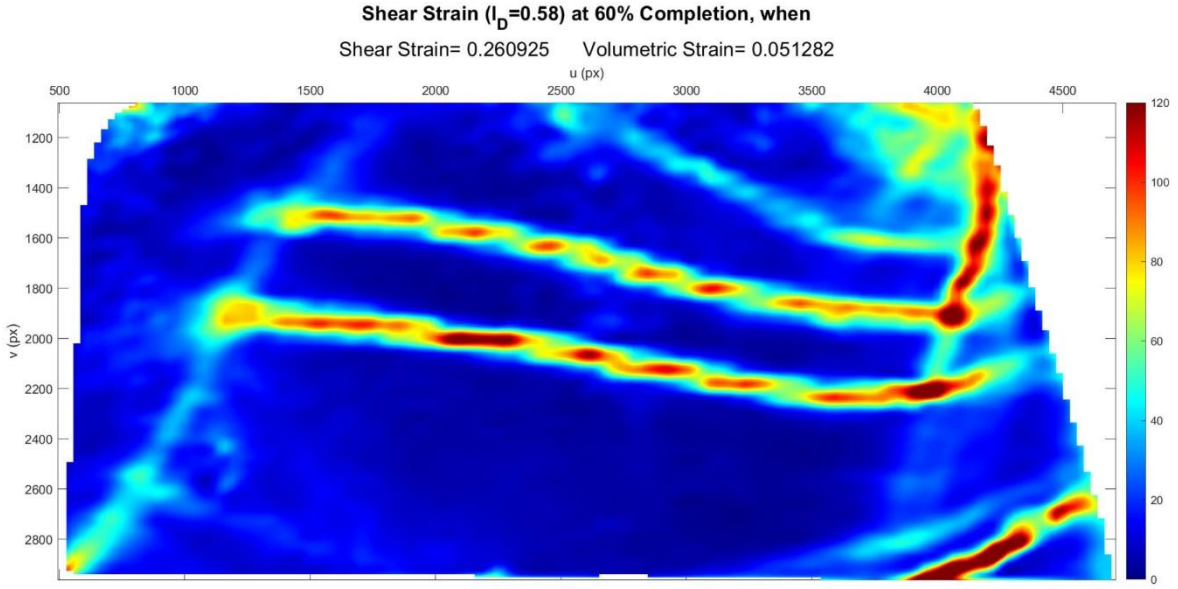

Figure C.133. Shear Strain Field at 60% Completion ($I_D = 0.58$ & $\sigma' = 0.96\ kPa$).

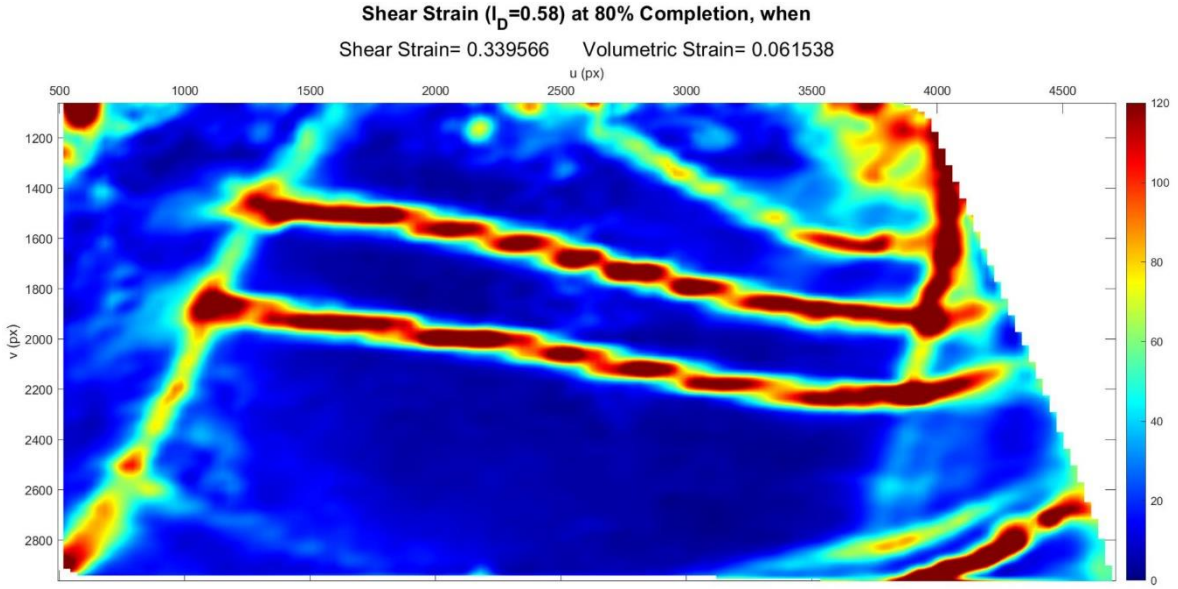

Figure C.134. Shear Strain Field at 80% Completion ($I_D = 0.58$ & $\sigma' = 0.96\ kPa$).

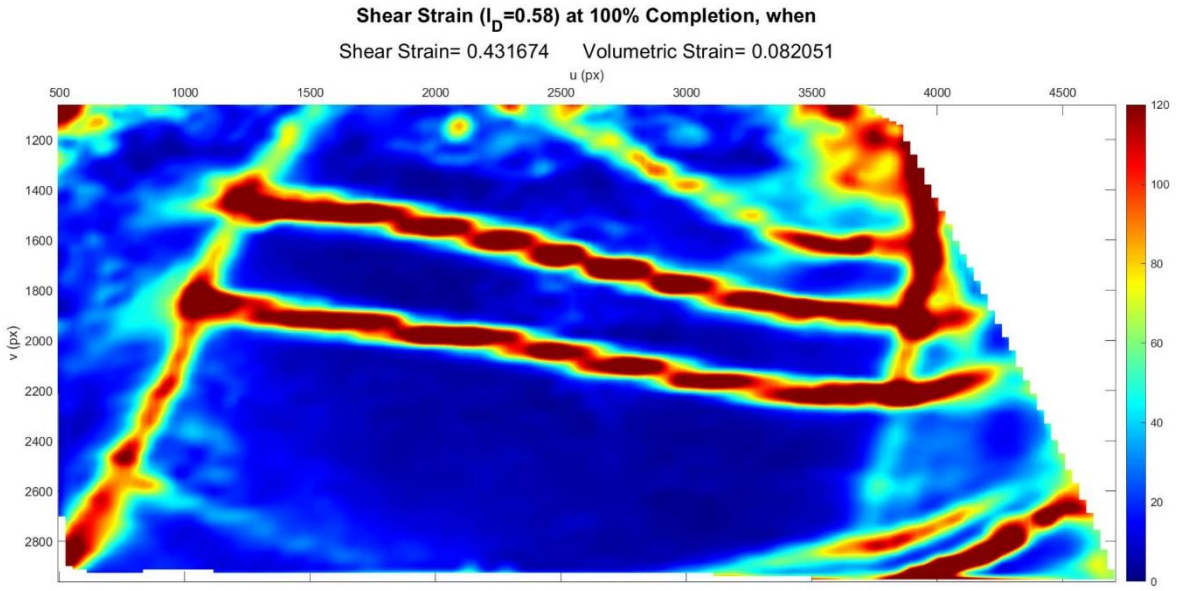

Figure C.135. Shear Strain Field at 100% Completion ($I_D = 0.58$ & $\sigma' = 0.96\ kPa$).

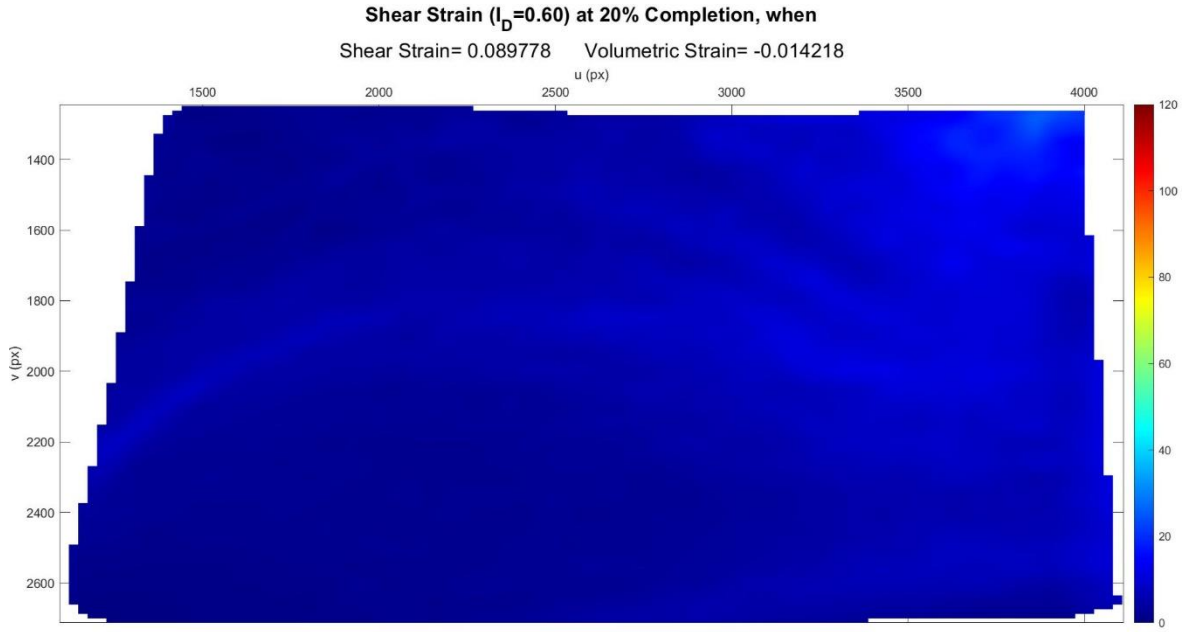

Figure C.136. Shear Strain Field at 20% Completion ($I_D = 0.60$ & $\sigma' = 0.84\ kPa$).

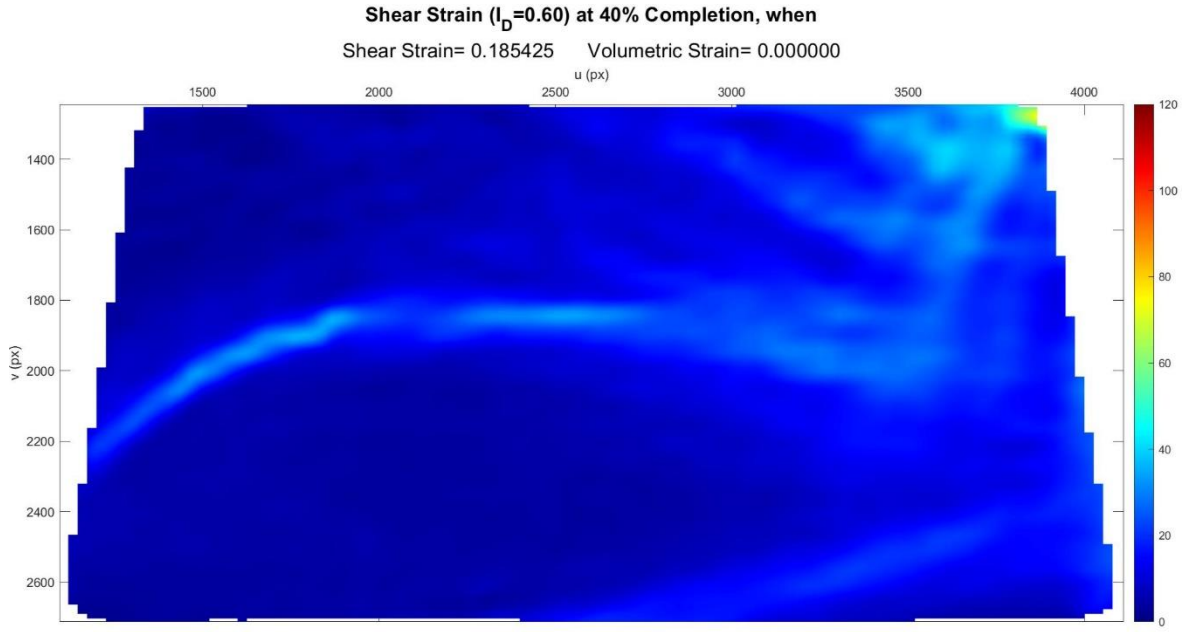

Figure C.137. Shear Strain Field at 40% Completion ($I_D = 0.60$ & $\sigma' = 0.84\ kPa$).

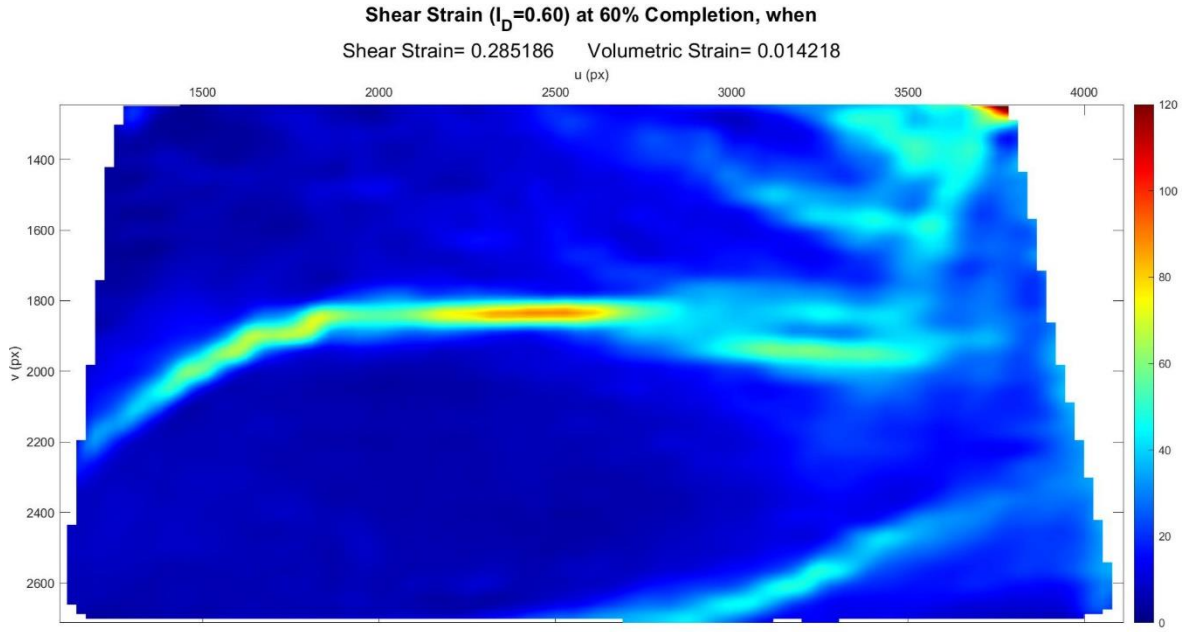

Figure C.138. Shear Strain Field at 60% Completion ($I_D = 0.60$ & $\sigma' = 0.84\ kPa$).

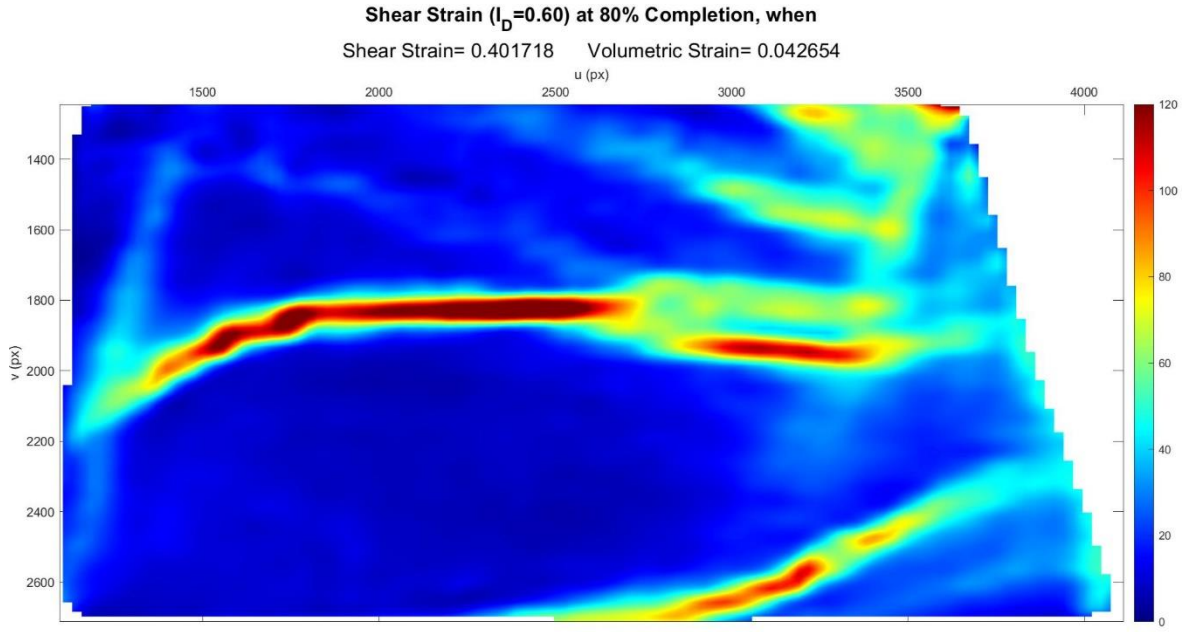

Figure C.139. Shear Strain Field at 80% Completion ($I_D = 0.60$ & $\sigma' = 0.84\ kPa$).

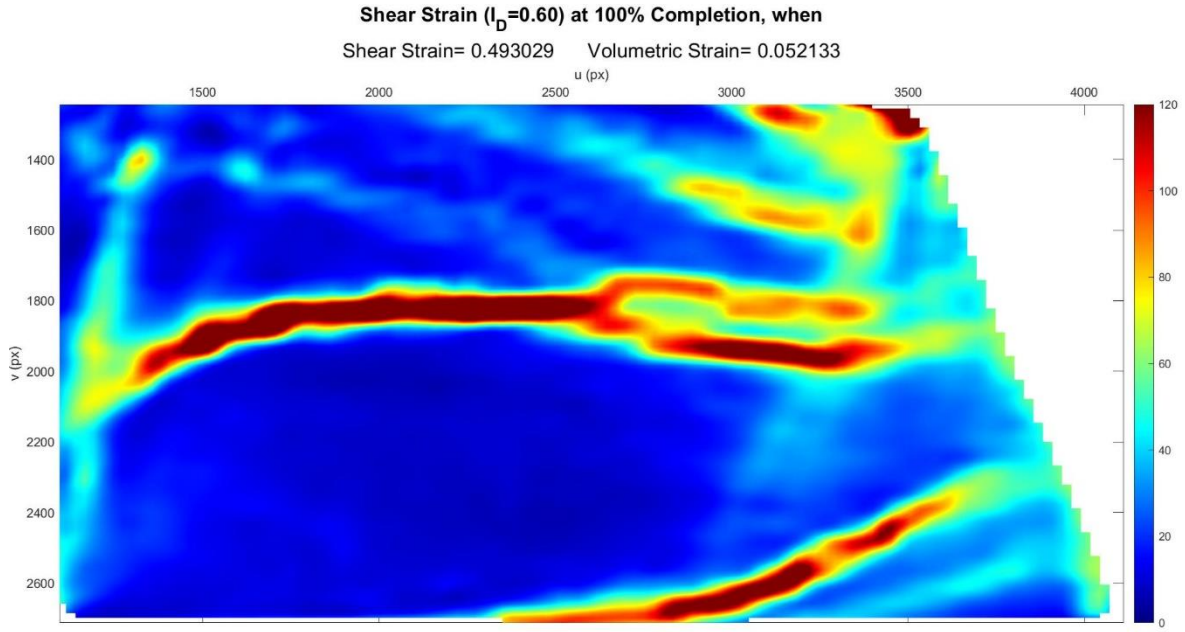

Figure C.140. Shear Strain Field at 100% Completion ($I_D = 0.60$ & $\sigma' = 0.84\ kPa$).

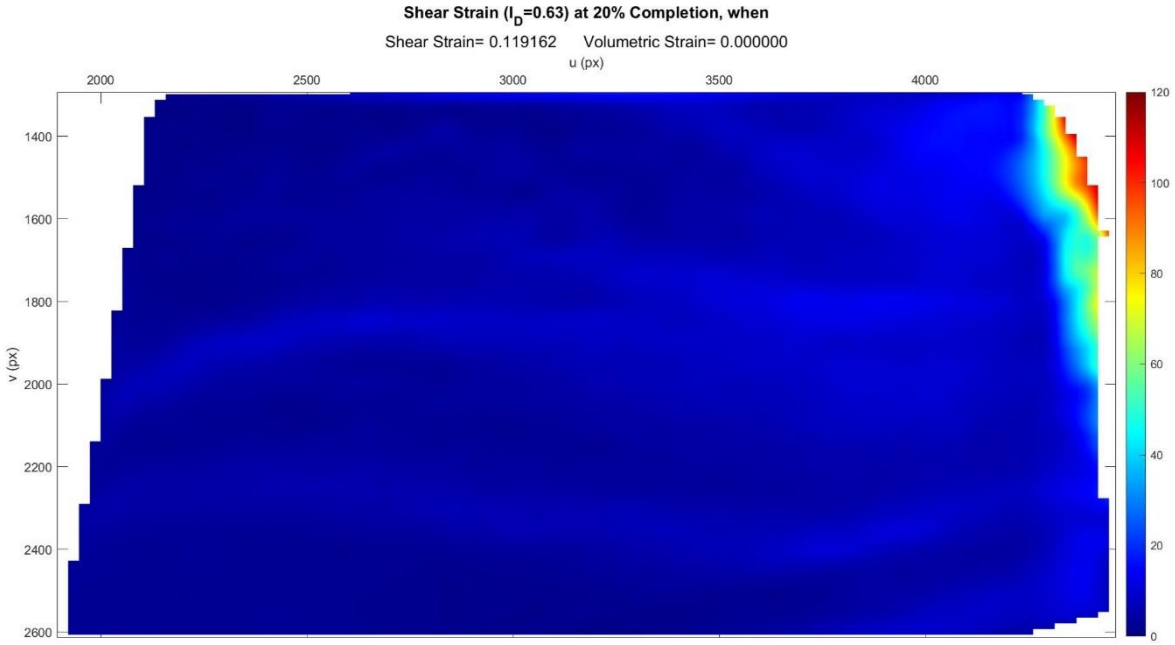

Figure C.141. Shear Strain Field at 20% Completion ($I_D = 0.63$ & $\sigma' = 0.56\ kPa$).

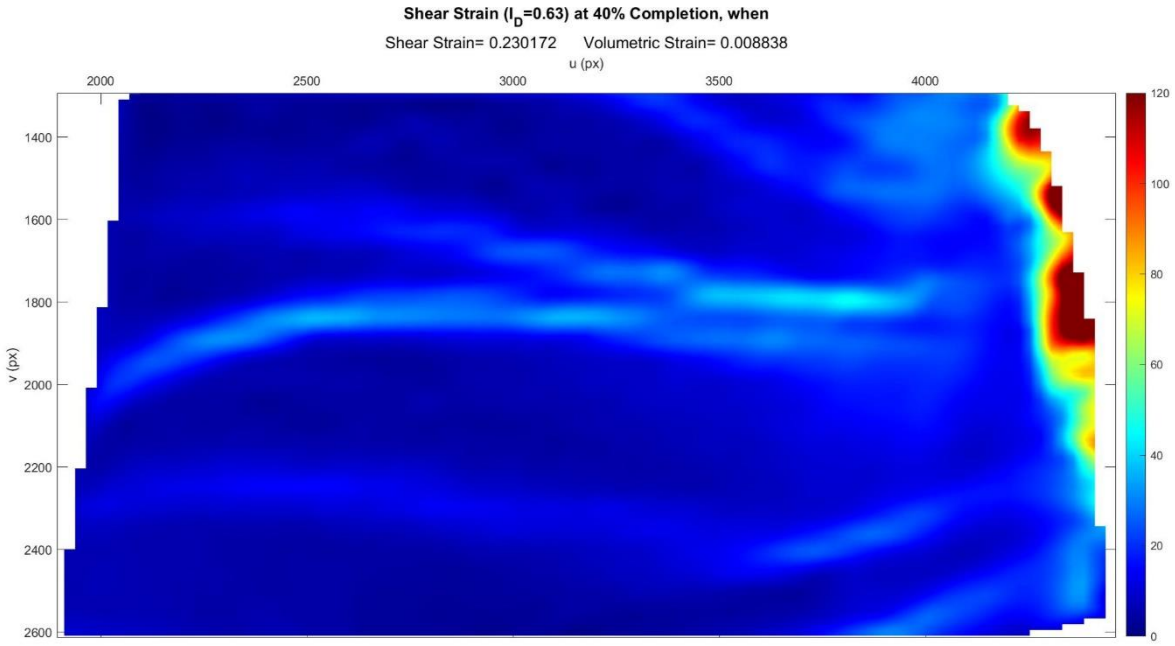

Figure C.142. Shear Strain Field at 40% Completion ($I_D = 0.63$ & $\sigma' = 0.56\ kPa$).

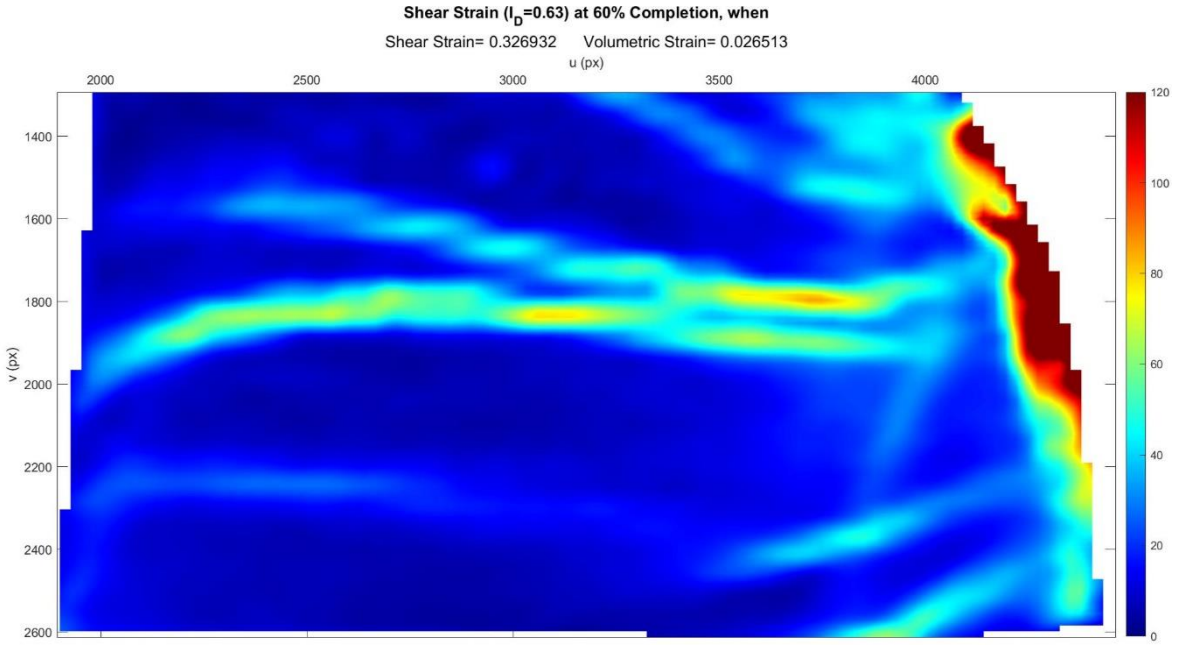

Figure C.143. Shear Strain Field at 60% Completion ($I_D = 0.63$ & $\sigma' = 0.56\ kPa$).

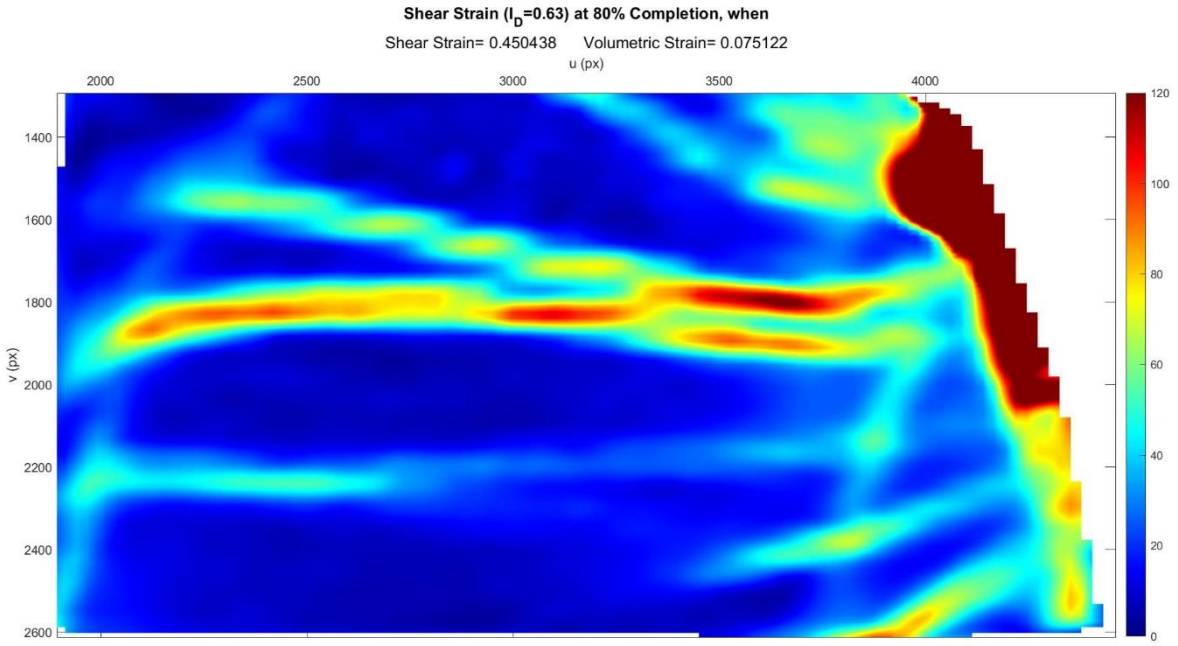

Figure C.144. Shear Strain Field at 80% Completion ($I_D = 0.63$ & $\sigma' = 0.56\ kPa$).

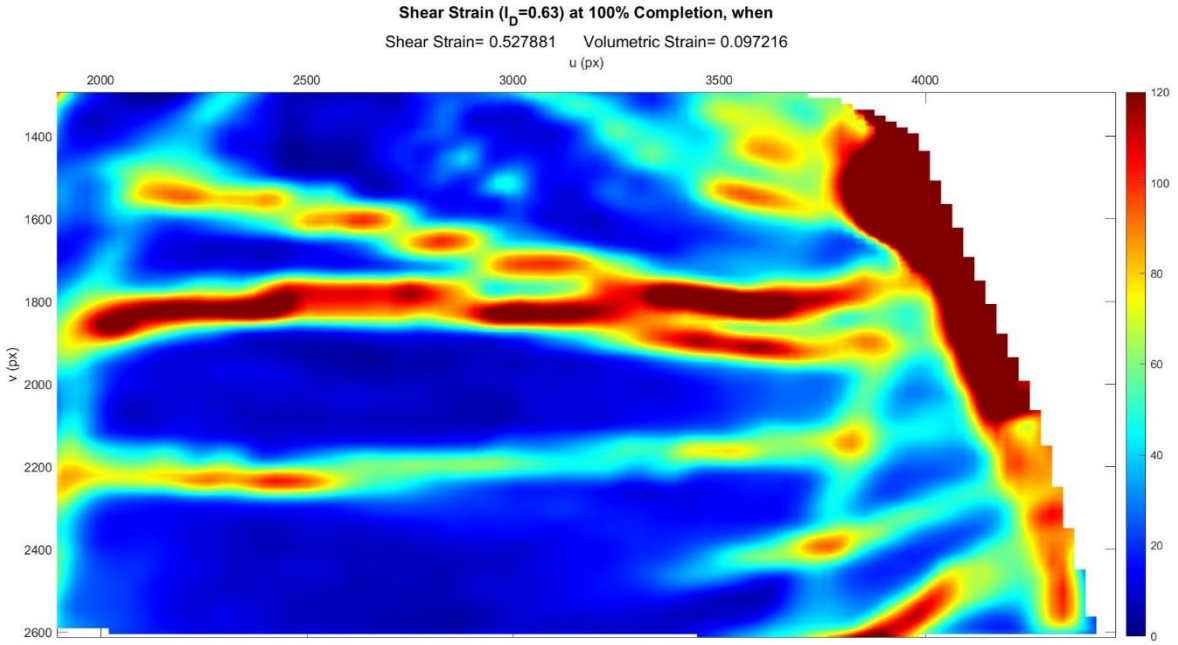

Figure C.145. Shear Strain Field at 100% Completion ($I_D = 0.63$ & $\sigma' = 0.56\,kPa$).

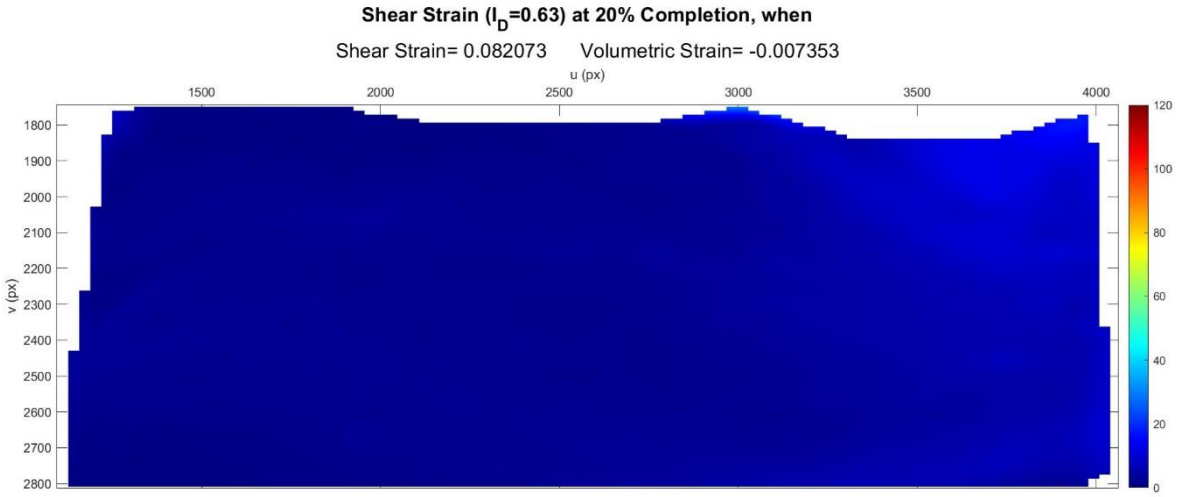

Figure C.146. Shear Strain Field at 20% Completion ($I_D = 0.63$ & $\sigma' = 0.66\ kPa$).

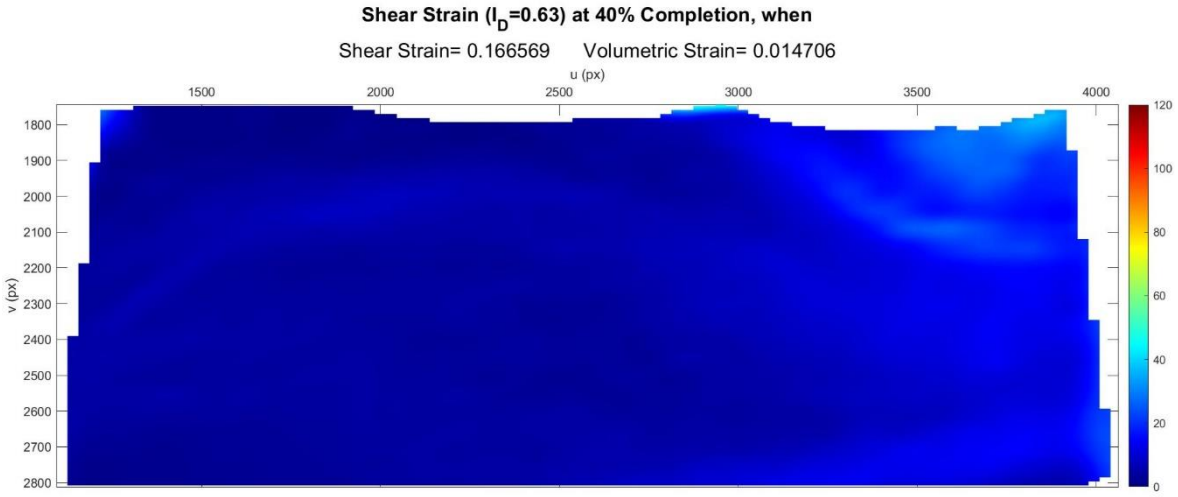

Figure C.147. Shear Strain Field at 40% Completion ($I_D = 0.63$ & $\sigma' = 0.66\ kPa$).

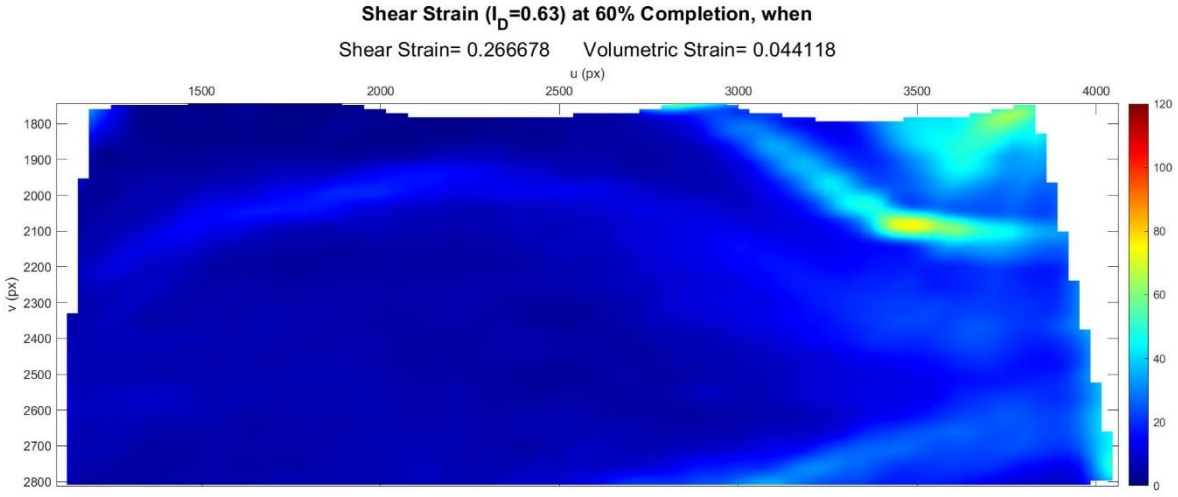

Figure C.148. Shear Strain Field at 60% Completion ($I_D = 0.63$ & $\sigma' = 0.66\ kPa$).

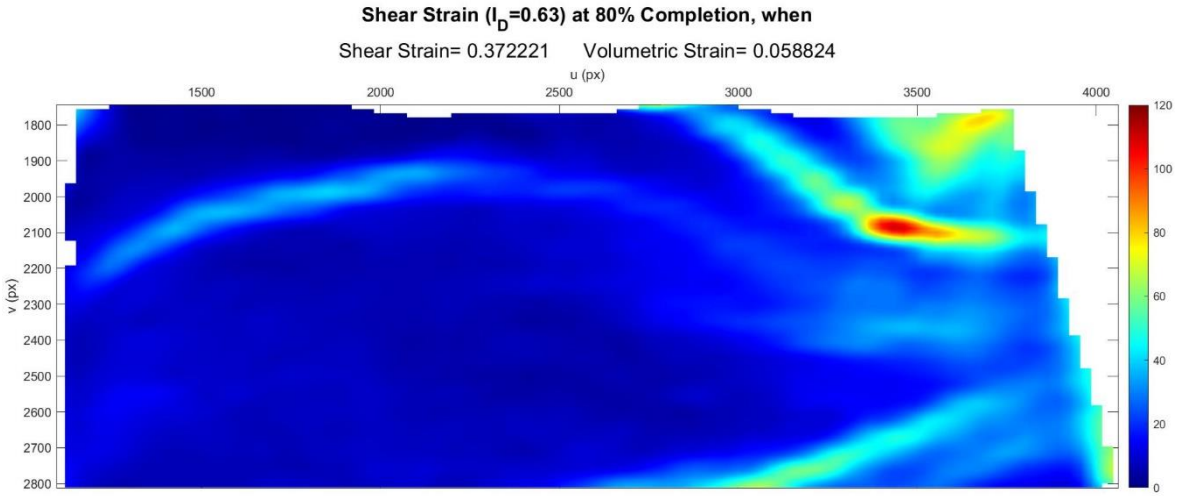

Figure C.149. Shear Strain Field at 80% Completion ($I_D = 0.63$ & $\sigma' = 0.66\ kPa$).

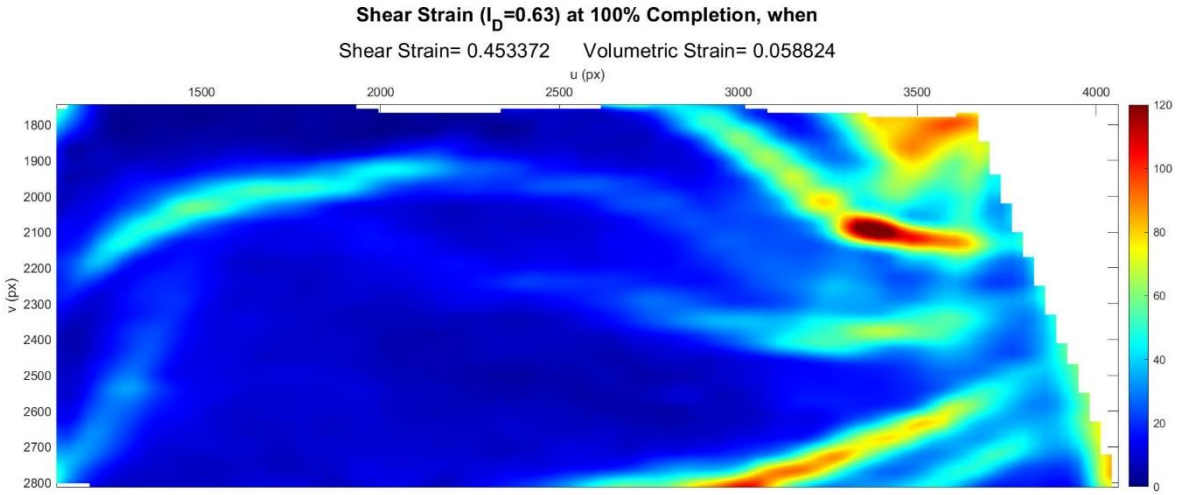

Figure C.150. Shear Strain Field at 100% Completion ($I_D = 0.63$ & $\sigma' = 0.66\ kPa$).

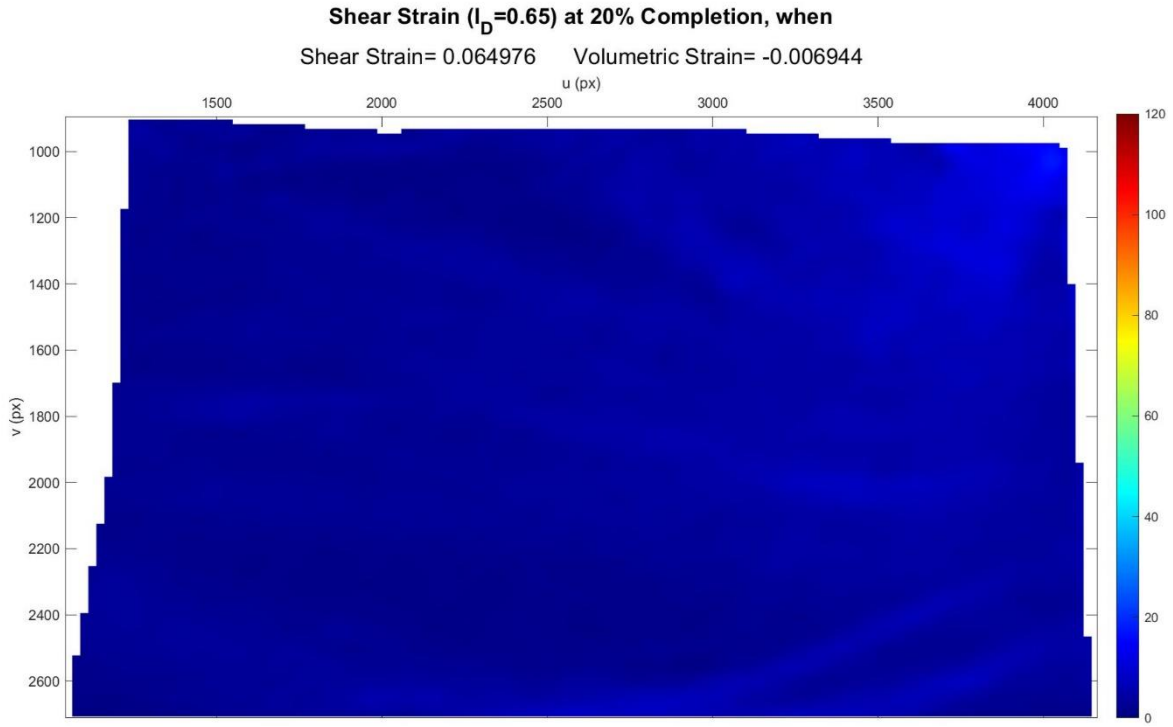

Figure C.151. Shear Strain Field at 20% Completion ($I_D = 0.65$ & $\sigma' = 0.96\ kPa$).

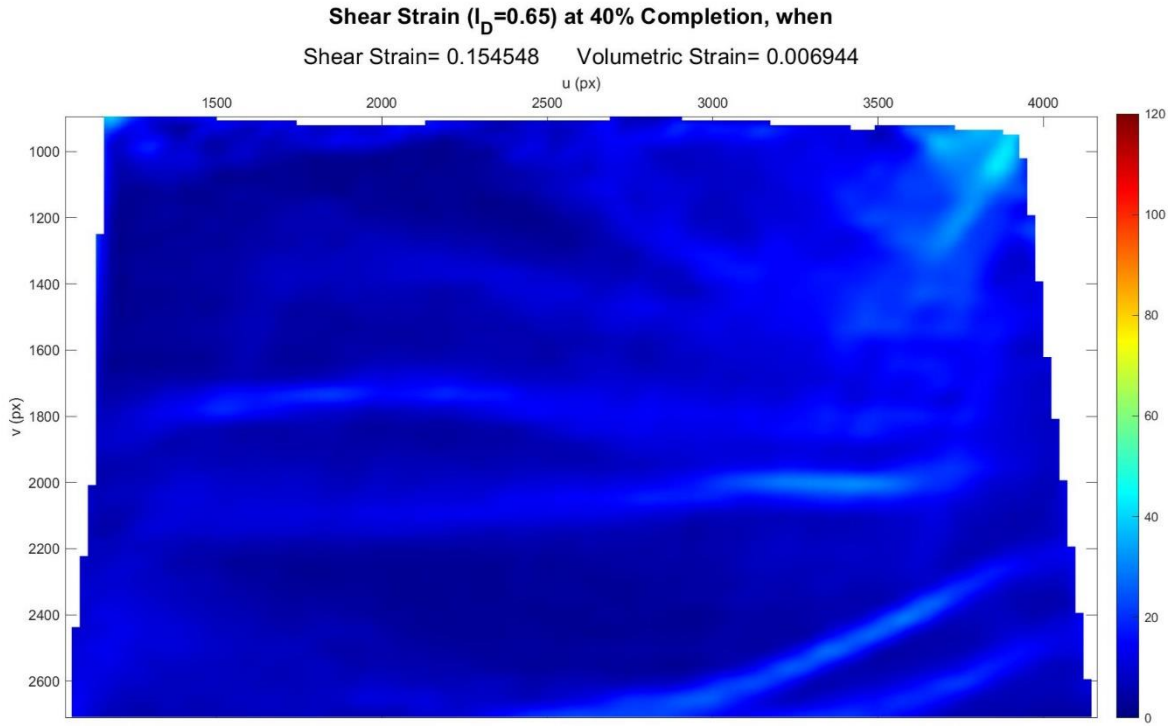

Figure C.152. Shear Strain Field at 40% Completion ($I_D = 0.65$ & $\sigma' = 0.96\ kPa$).

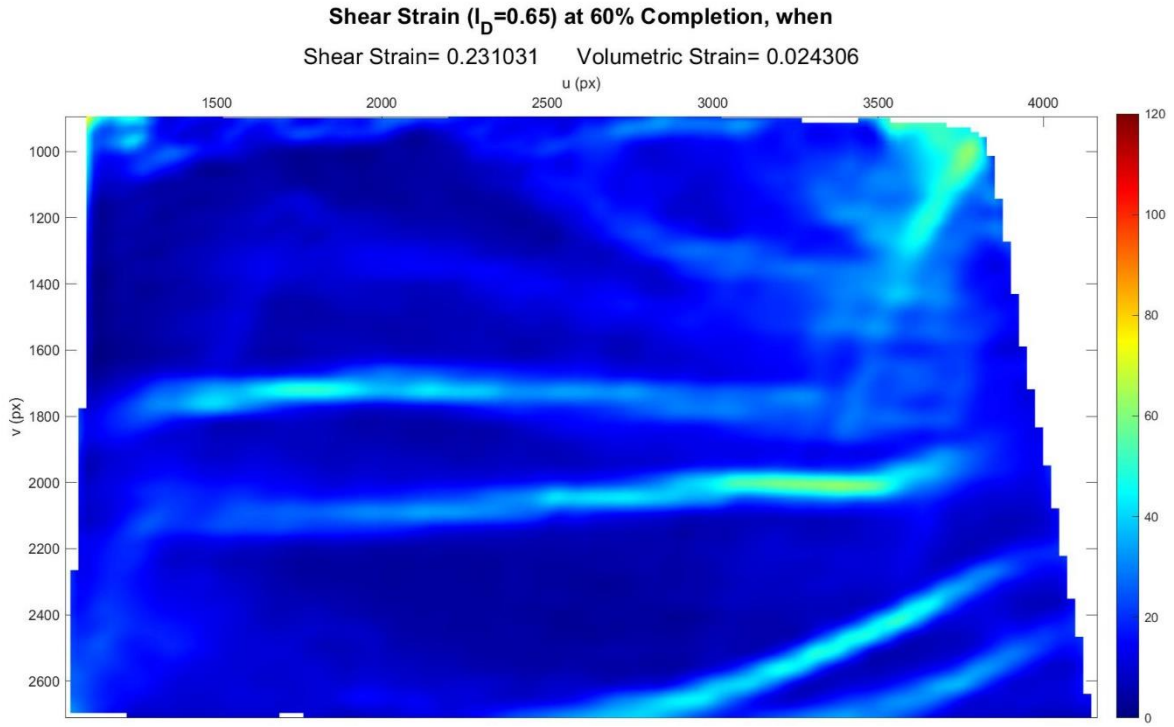

Figure C.153. Shear Strain Field at 60% Completion ($I_D = 0.65$ & $\sigma' = 0.96\ kPa$).

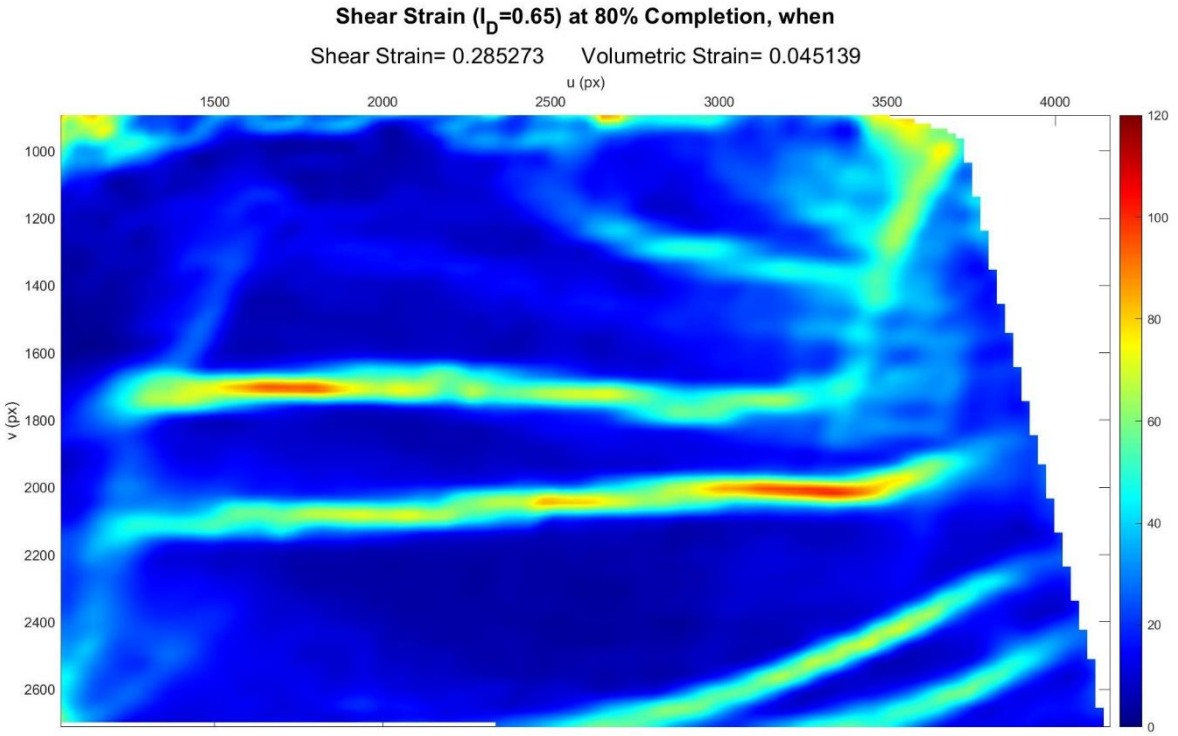

Figure C.154. Shear Strain Field at 80% Completion ($I_D = 0.65$ & $\sigma' = 0.96\ kPa$).

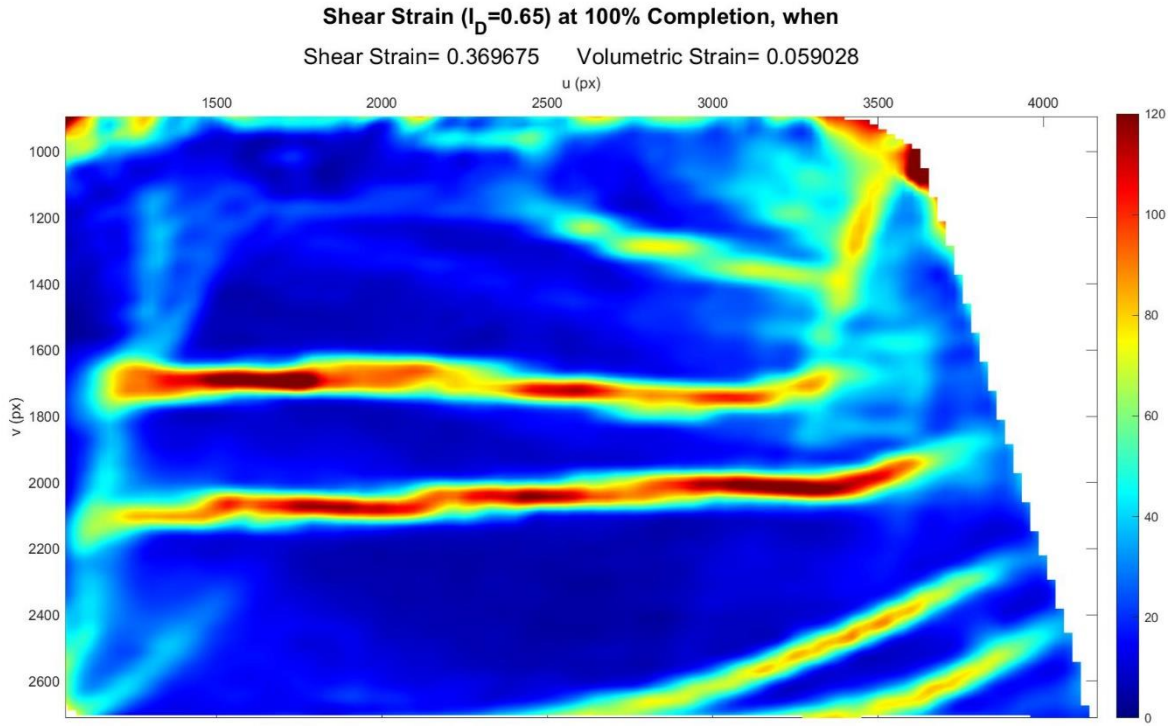

Figure C.155. Shear Strain Field at 100% Completion ($I_D = 0.65$ & $\sigma' = 0.96\,kPa$).

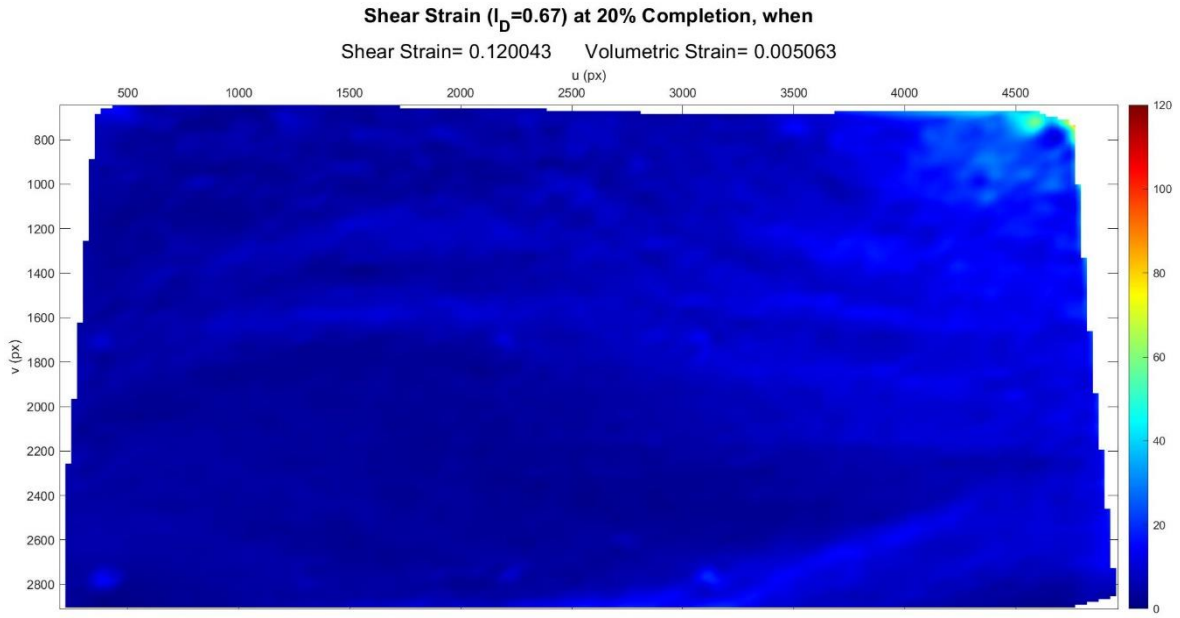

Figure C.156. Shear Strain Field at 20% Completion ($I_D = 0.67$ & $\sigma' = 0.83\ kPa$).

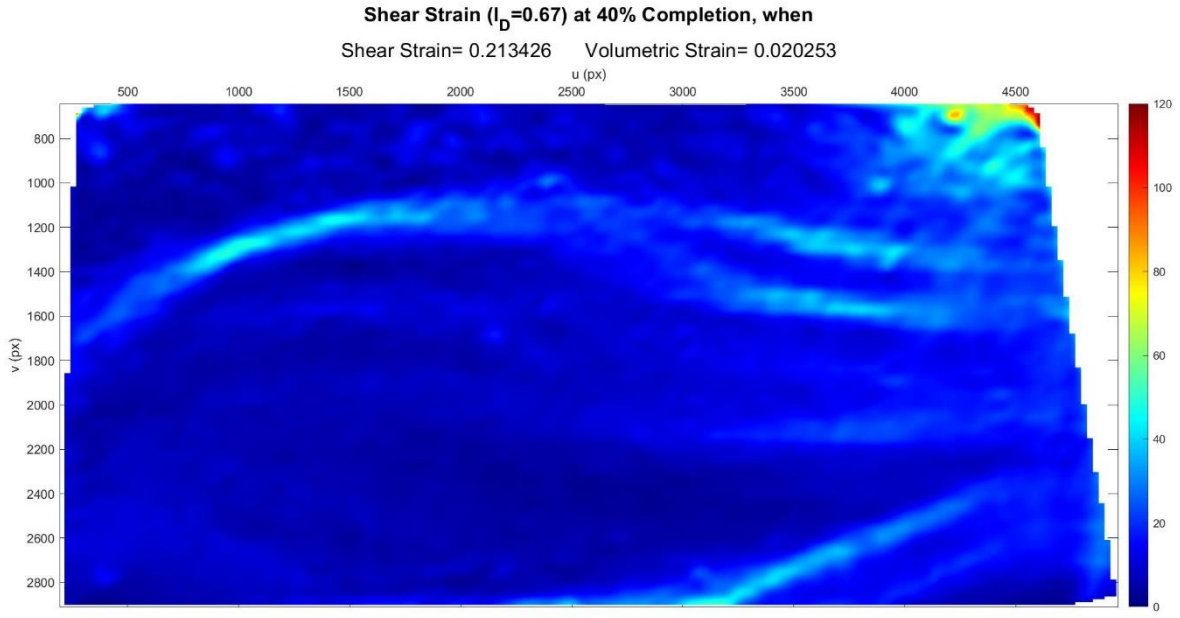

Figure C.157. Shear Strain Field at 40% Completion ($I_D = 0.67$ & $\sigma' = 0.83\ kPa$).

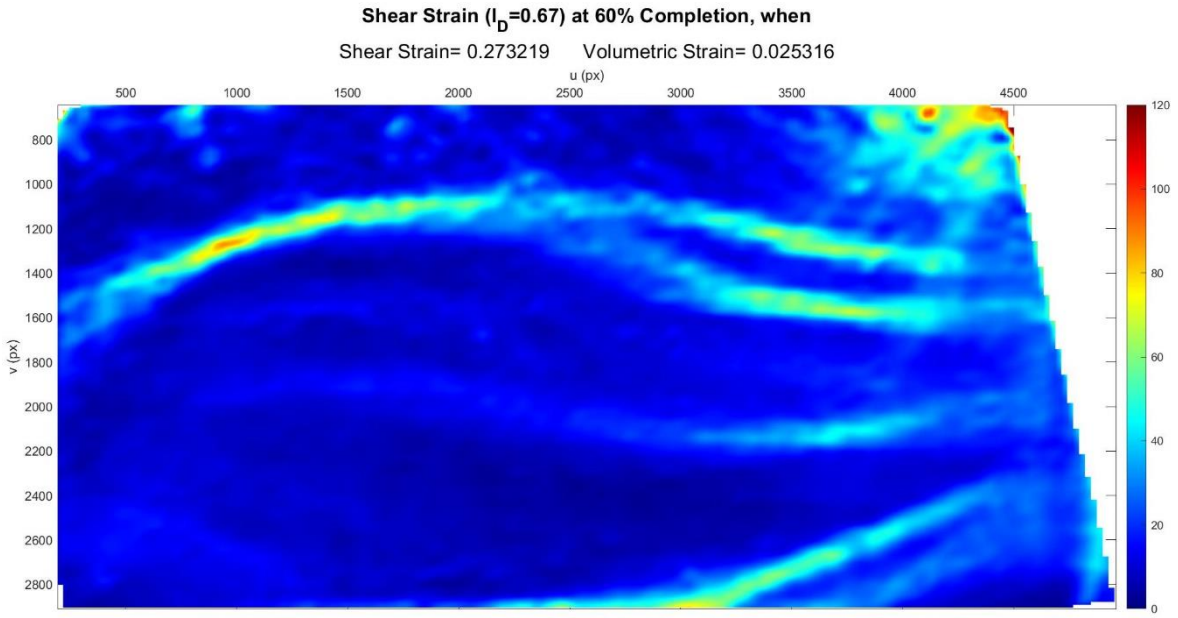

Figure C.158. Shear Strain Field at 60% Completion ($I_D = 0.67$ & $\sigma' = 0.83\ kPa$).

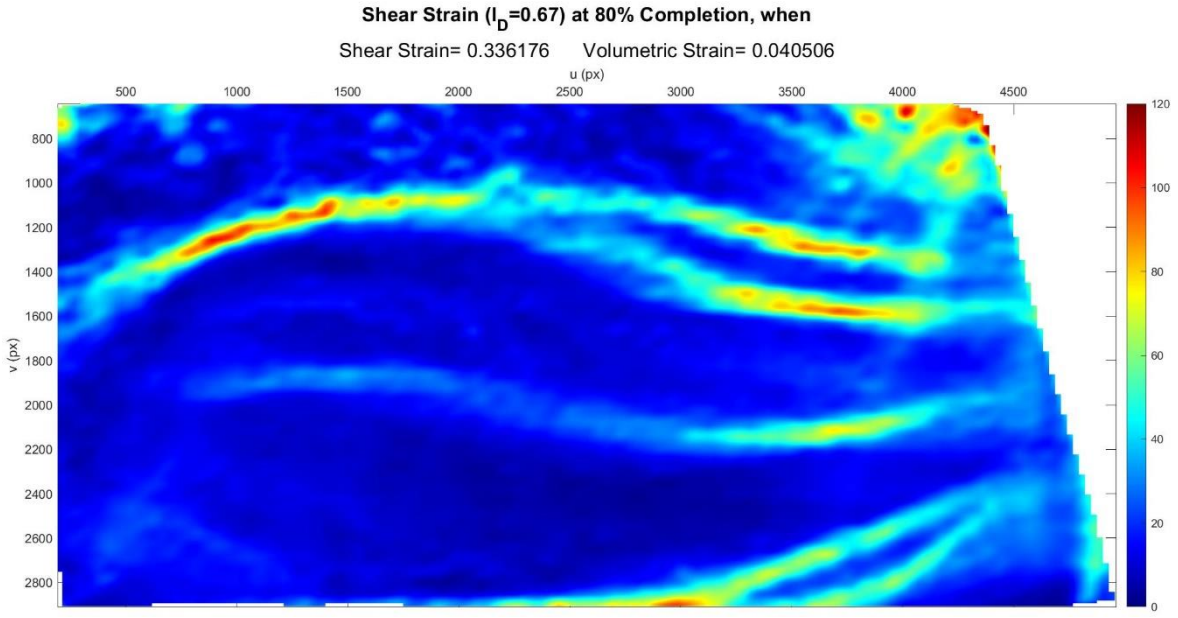

Figure C.159. Shear Strain Field at 80% Completion ($I_D = 0.67$ & $\sigma' = 0.83\ kPa$).

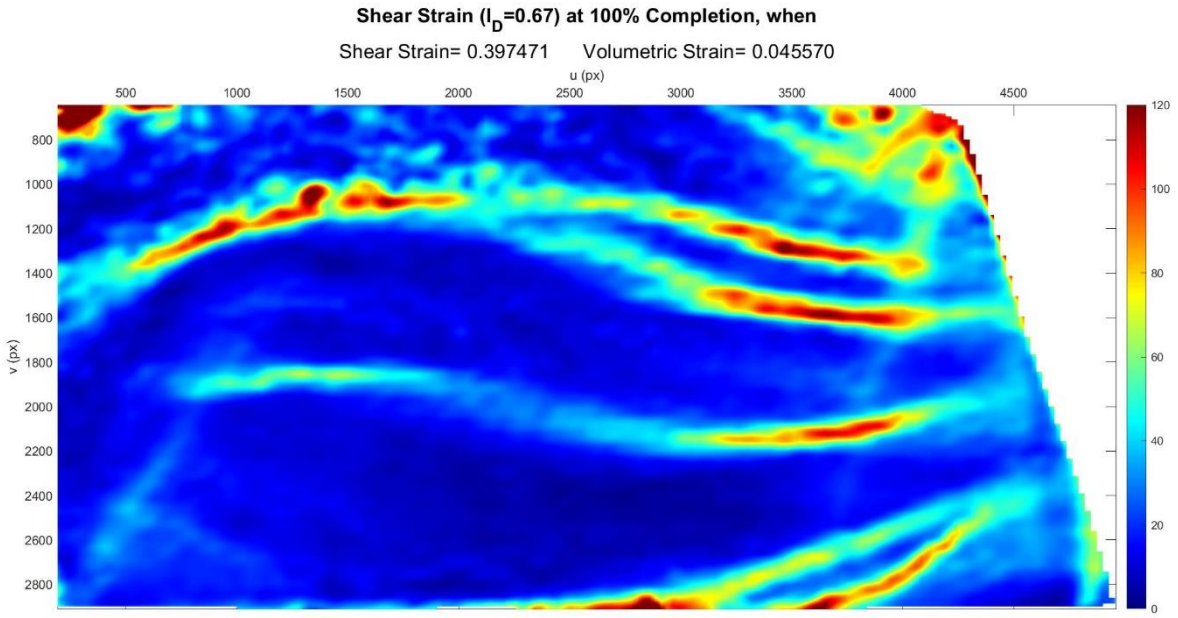

Figure C.160. Shear Strain Field at 100% Completion ($I_D = 0.67$ & $\sigma' = 0.83\ kPa$).

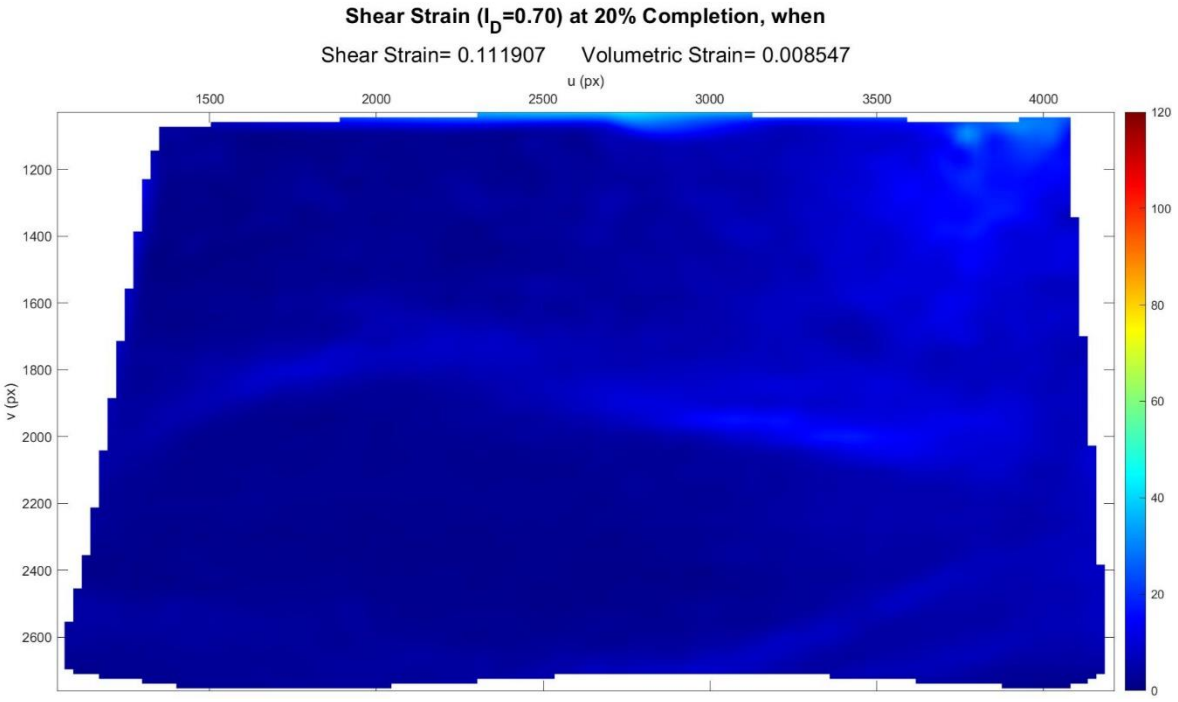

Figure C.161. Shear Strain Field at 20% Completion ($I_D = 0.70$ & $\sigma' = 0.92\ kPa$).

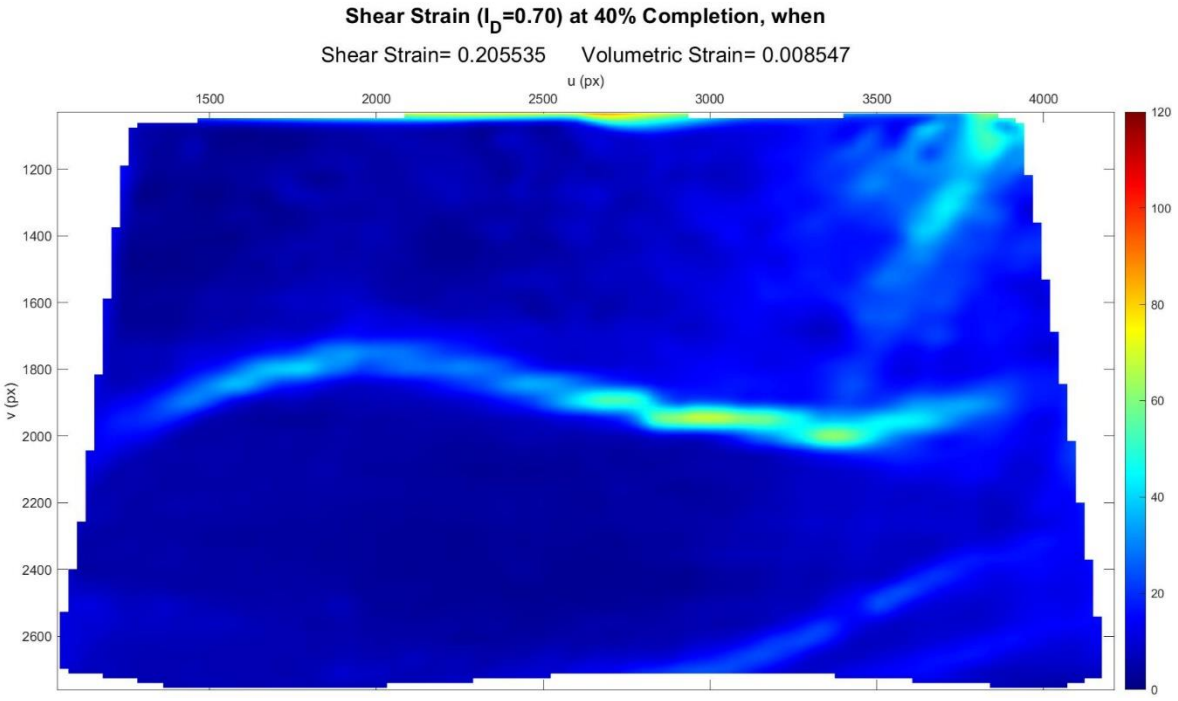

Figure C.162. Shear Strain Field at 40% Completion ($I_D = 0.70$ & $\sigma' = 0.92\ kPa$).

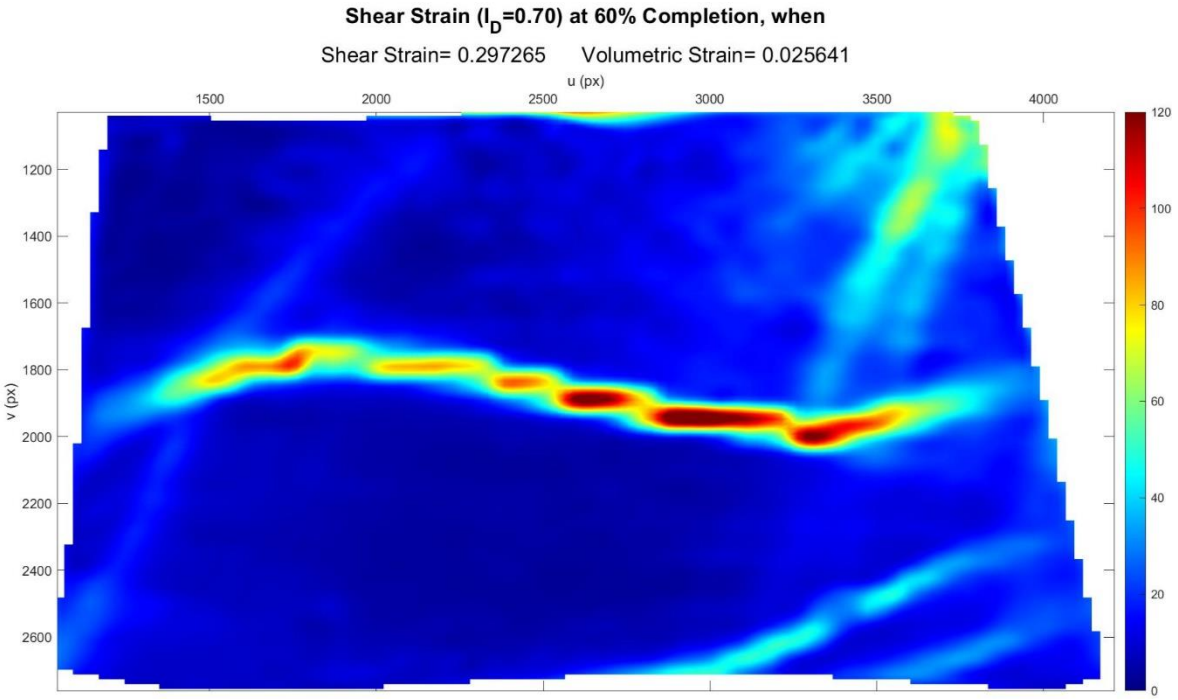

Figure C.163. Shear Strain Field at 60% Completion ($I_D = 0.70$ & $\sigma' = 0.92\ kPa$).

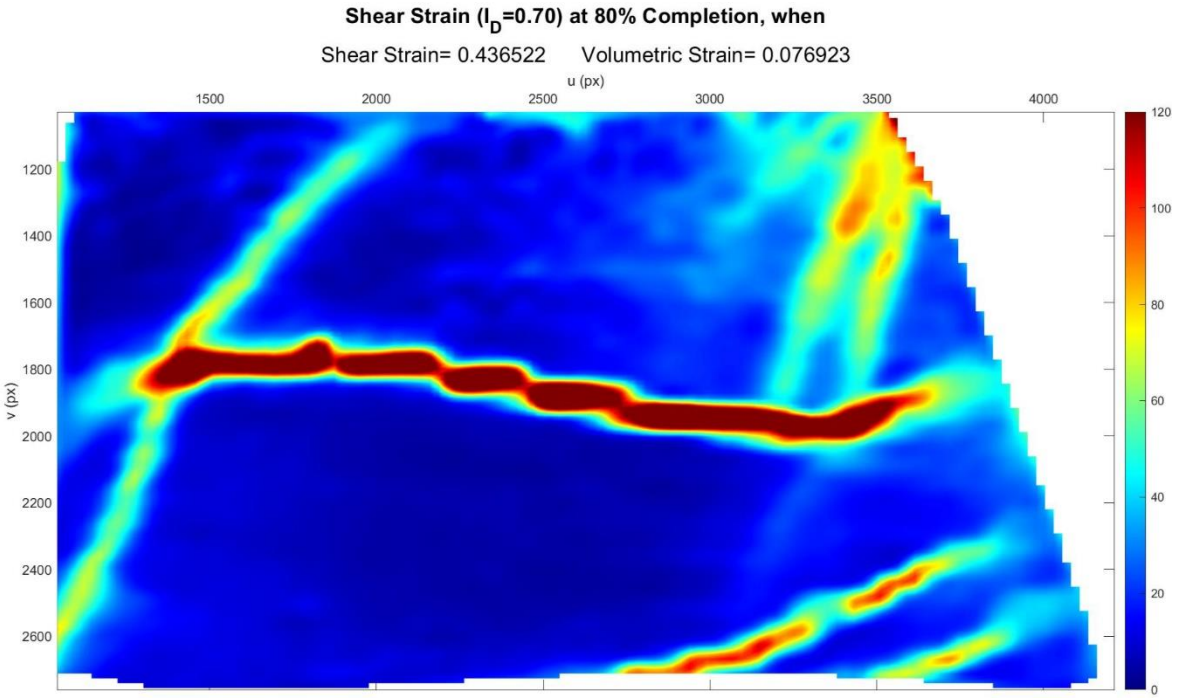

Figure C.164. Shear Strain Field at 80% Completion ($I_D = 0.70$ & $\sigma' = 0.92\ kPa$).

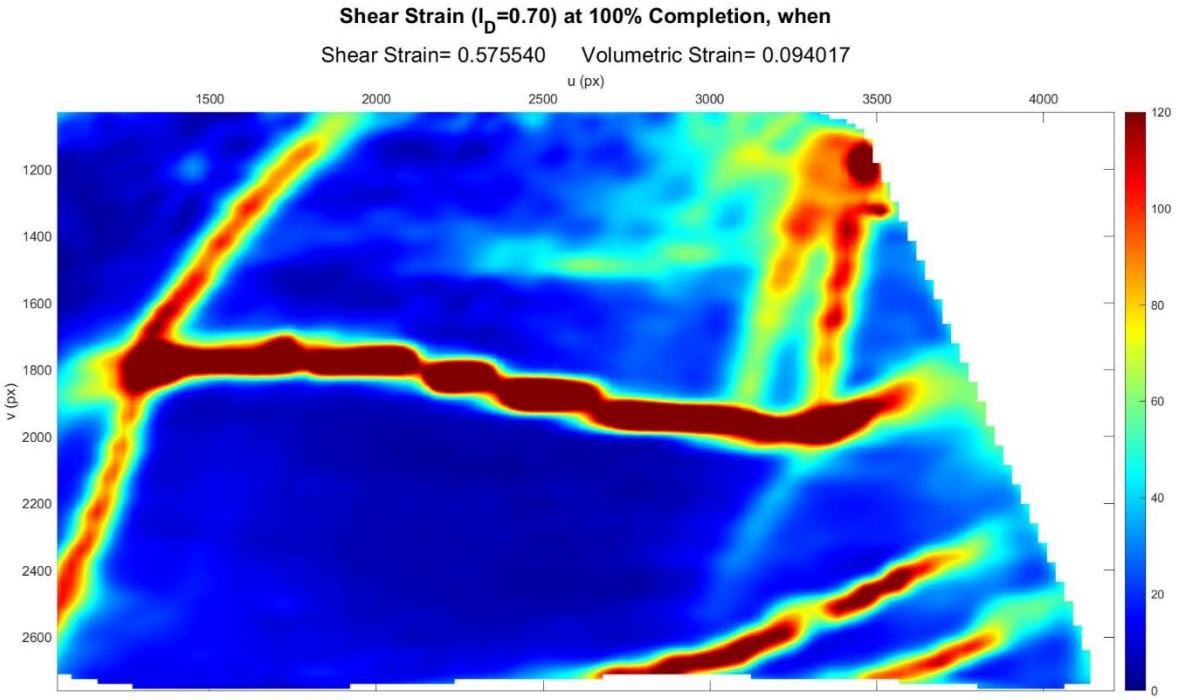

Figure C.165. Shear Strain Field at 100% Completion ($I_D = 0.70$ & $\sigma' = 0.92\ kPa$).

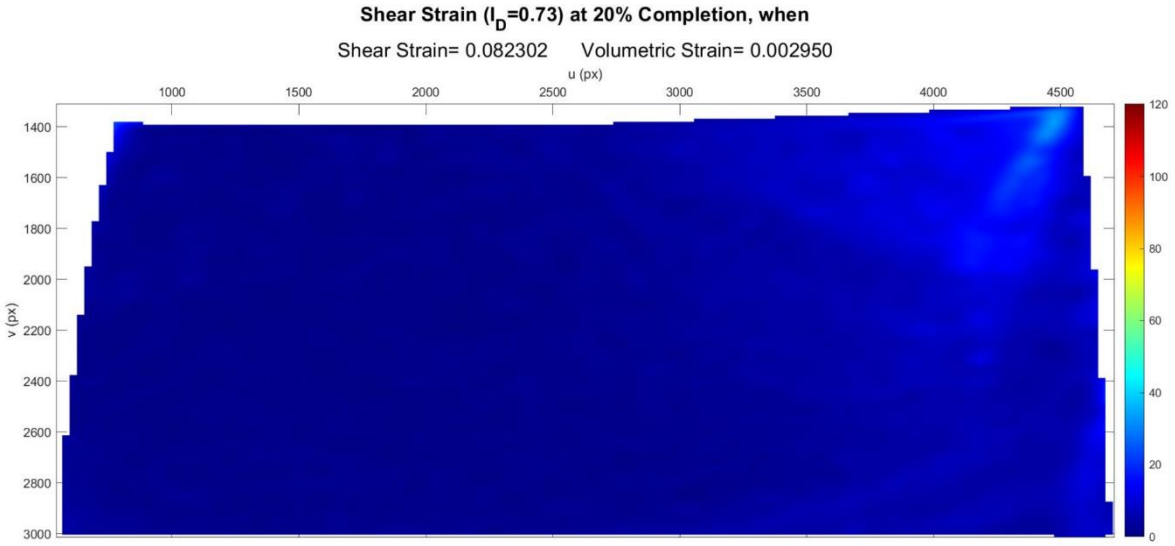

Figure C.166. Shear Strain Field at 20% Completion ($I_D = 0.73$ & $\sigma' = 0.78\,kPa$).

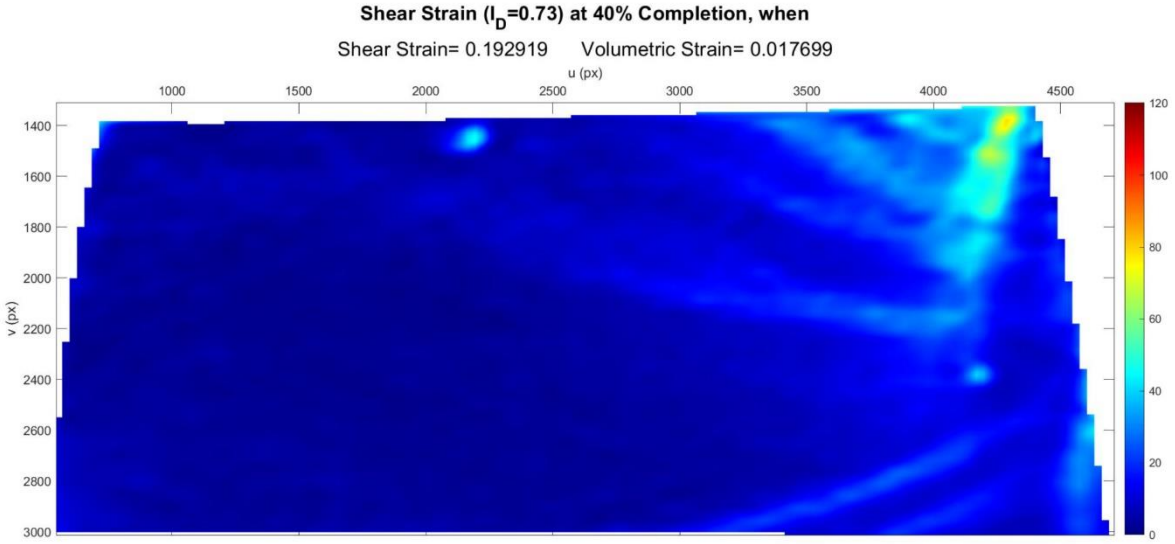

Figure C.167. Shear Strain Field at 40% Completion ($I_D = 0.73$ & $\sigma' = 0.78\,kPa$).

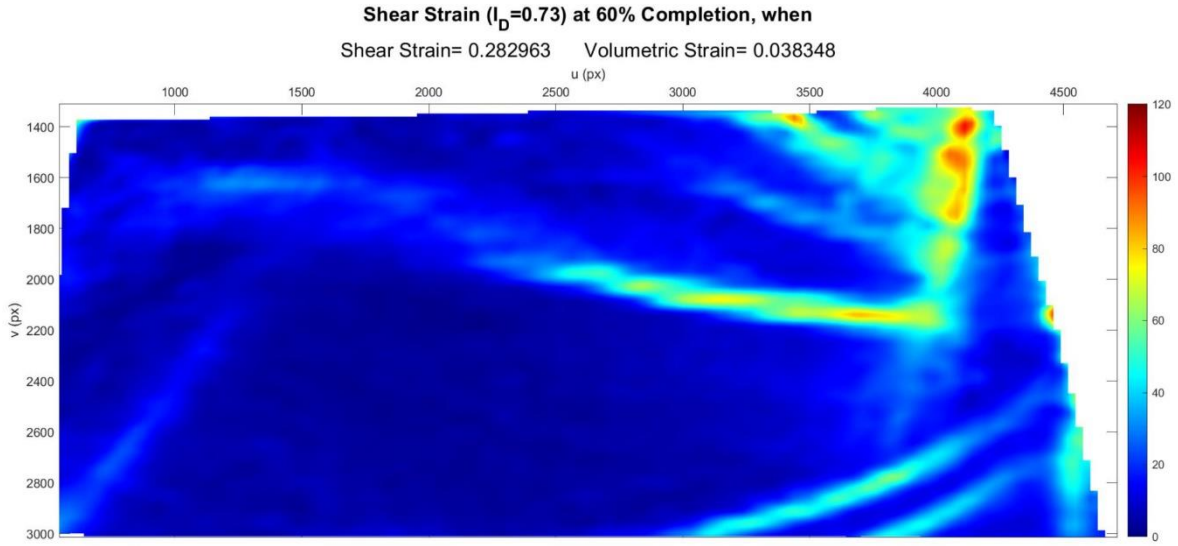

Figure C.168. Shear Strain Field at 60% Completion ($I_D = 0.73$ & $\sigma' = 0.78\ kPa$).

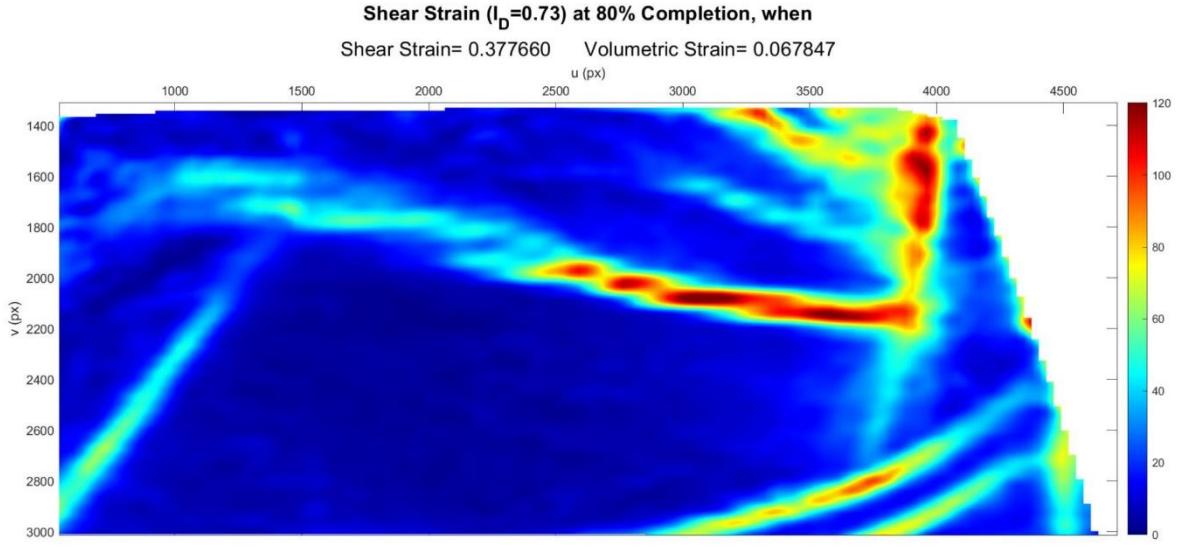

Figure C.169. Shear Strain Field at 80% Completion ($I_D = 0.73$ & $\sigma' = 0.78\ kPa$).

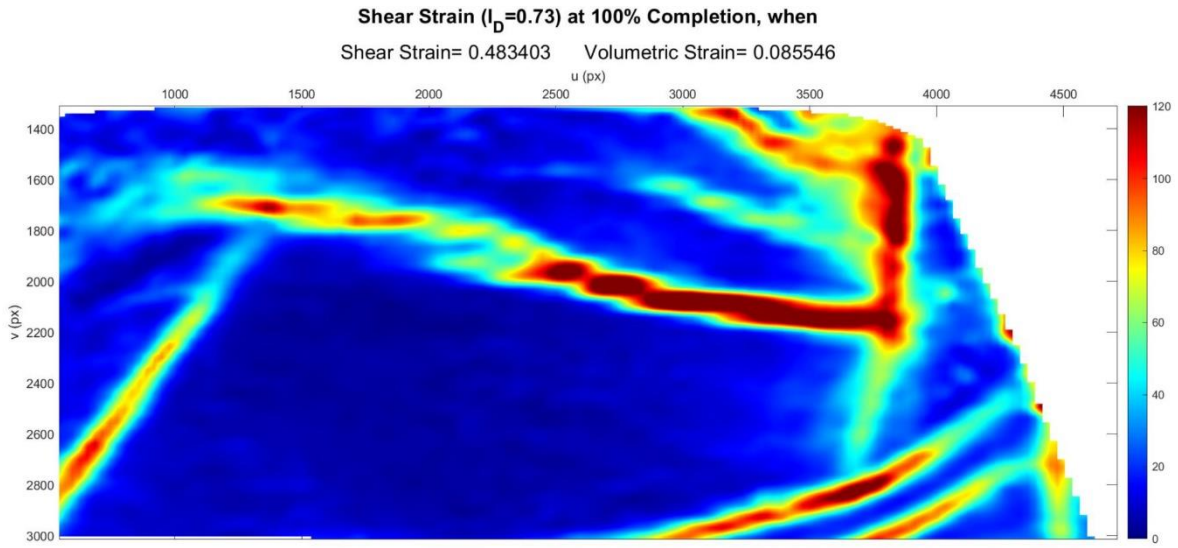

Figure C.170. Shear Strain Field at 100% Completion ($I_D = 0.73$ & $\sigma' = 0.78\ kPa$).

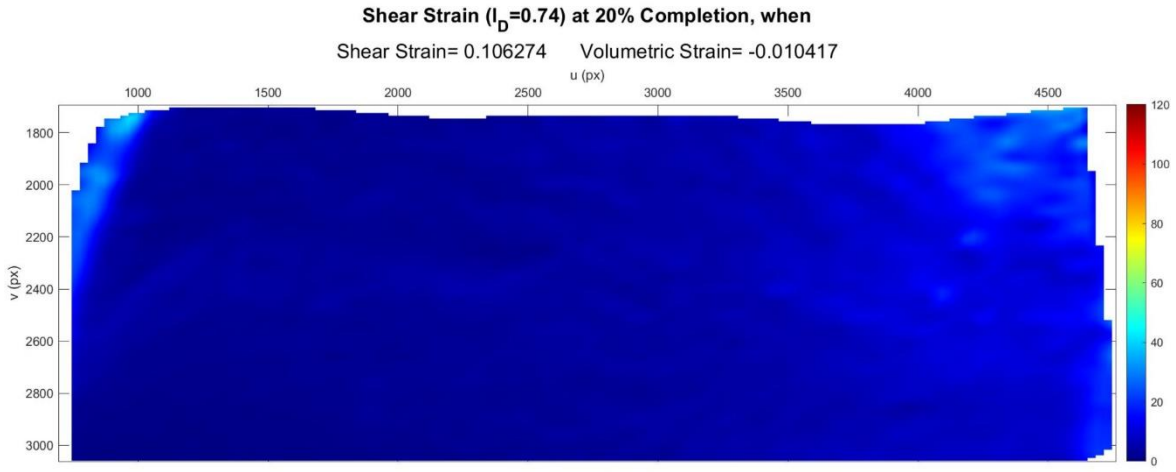

Figure C.171. Shear Strain Field at 20% Completion ($I_D = 0.74$ & $\sigma' = 0.66\ kPa$).

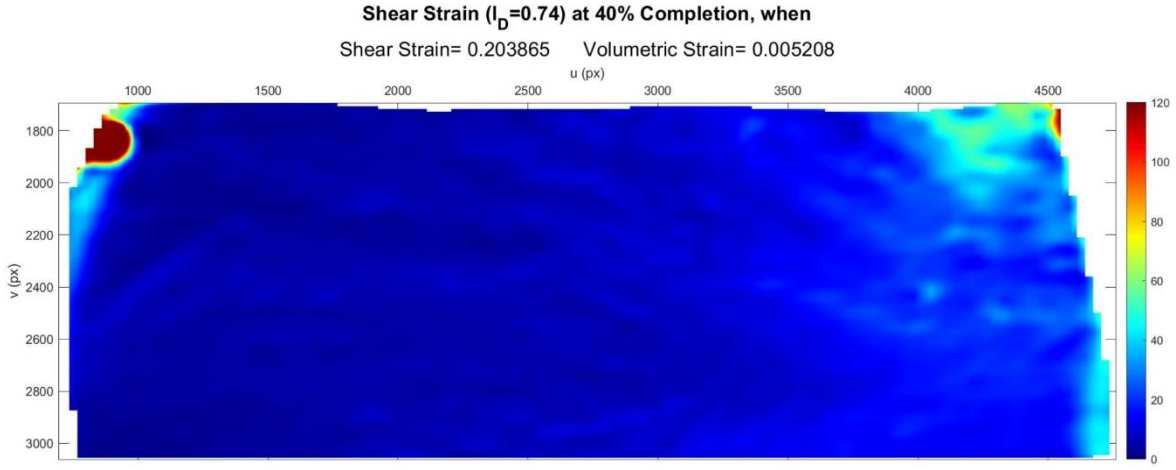

Figure C.172. Shear Strain Field at 40% Completion ($I_D = 0.74$ & $\sigma' = 0.66\ kPa$).

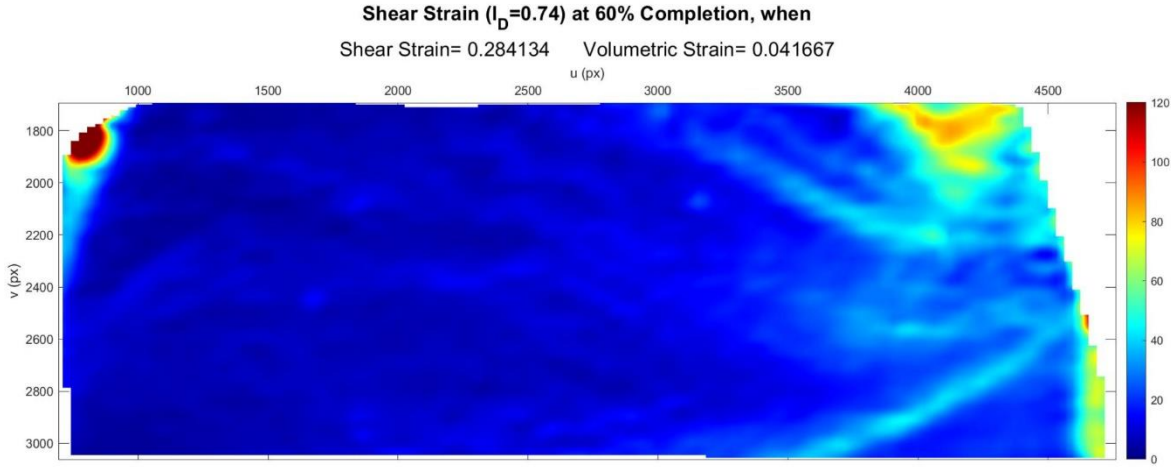

Figure C.173. Shear Strain Field at 60% Completion ($I_D = 0.74$ & $\sigma' = 0.66\ kPa$).

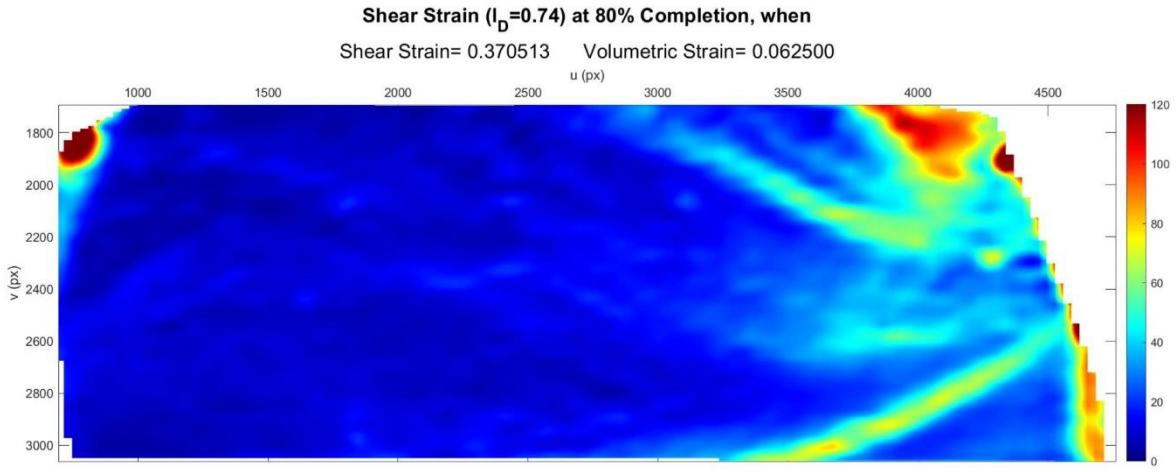

Figure C.174. Shear Strain Field at 80% Completion ($I_D = 0.74$ & $\sigma' = 0.66\ kPa$).

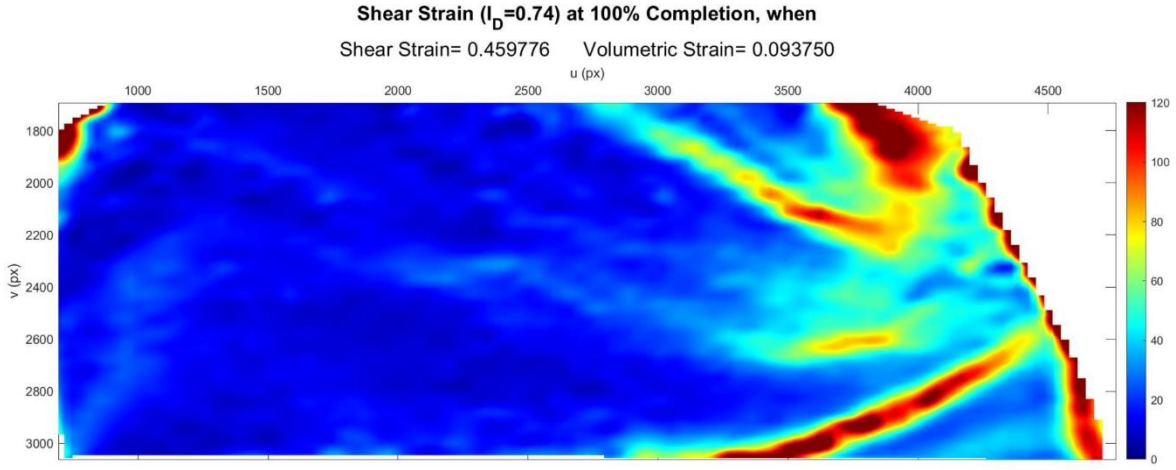

Figure C.175. Shear Strain Field at 100% Completion ($I_D = 0.74$ & $\sigma' = 0.66\ kPa$).

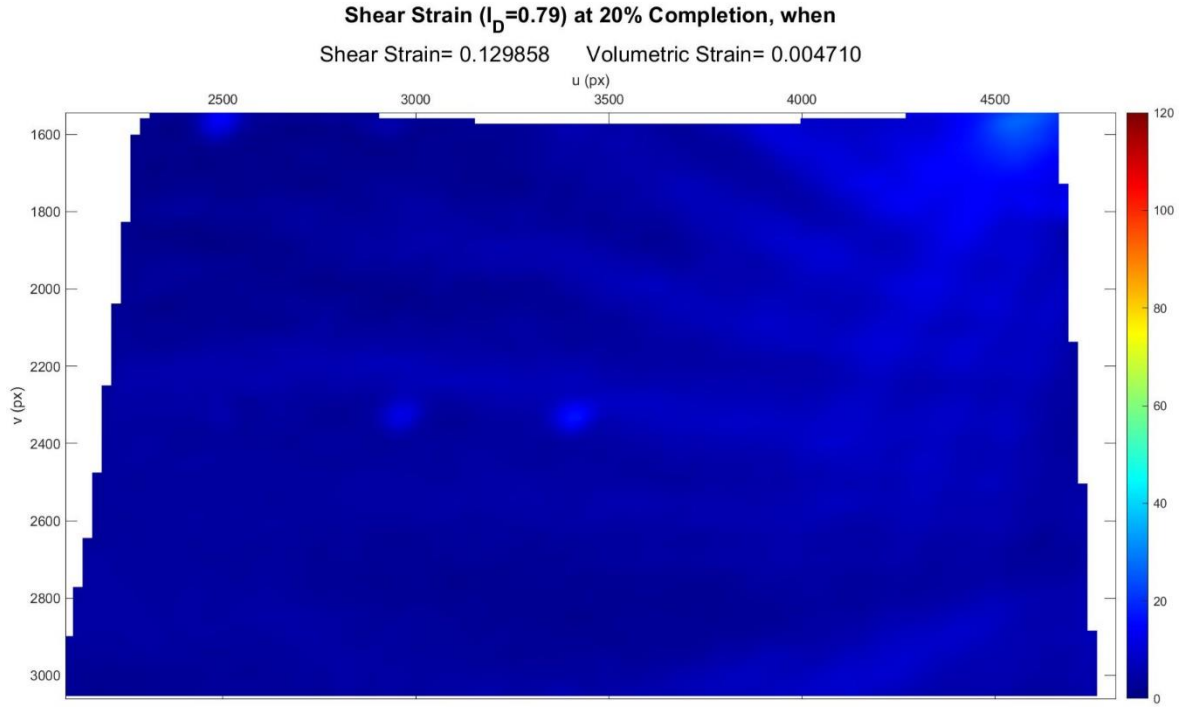

Figure C.176. Shear Strain Field at 20% Completion ($I_D = 0.79$ & $\sigma' = 0.91\ kPa$).

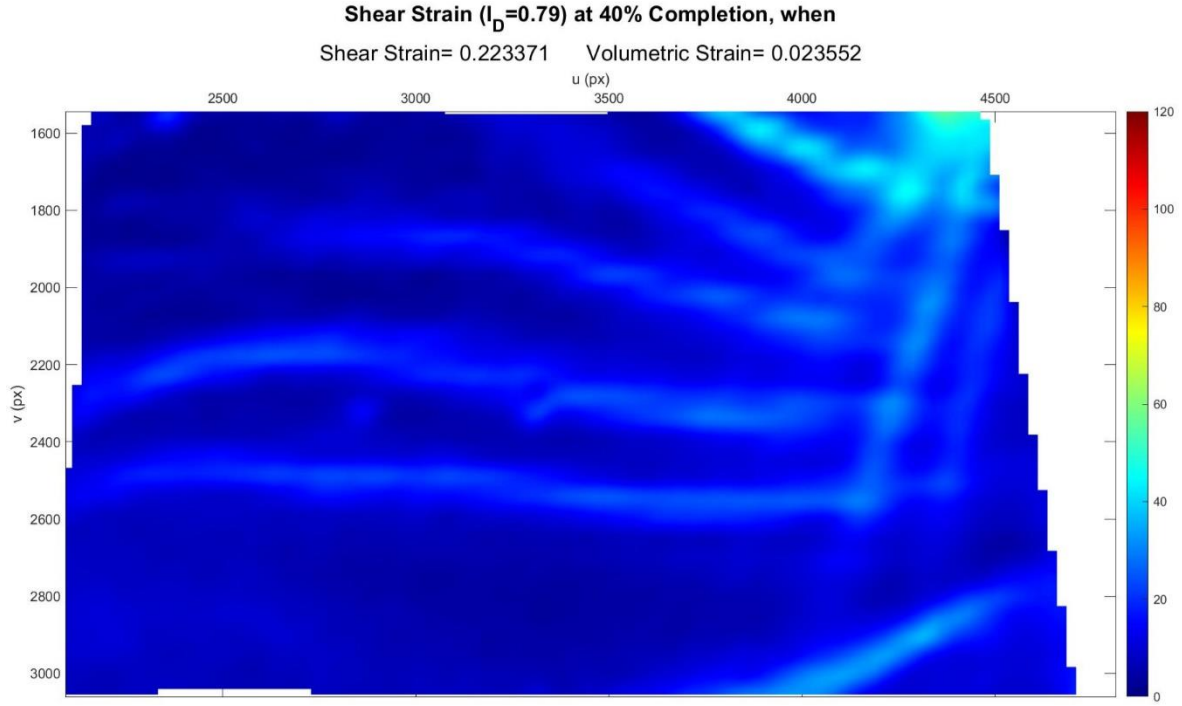

Figure C.177. Shear Strain Field at 40% Completion ($I_D = 0.79$ & $\sigma' = 0.91\ kPa$).

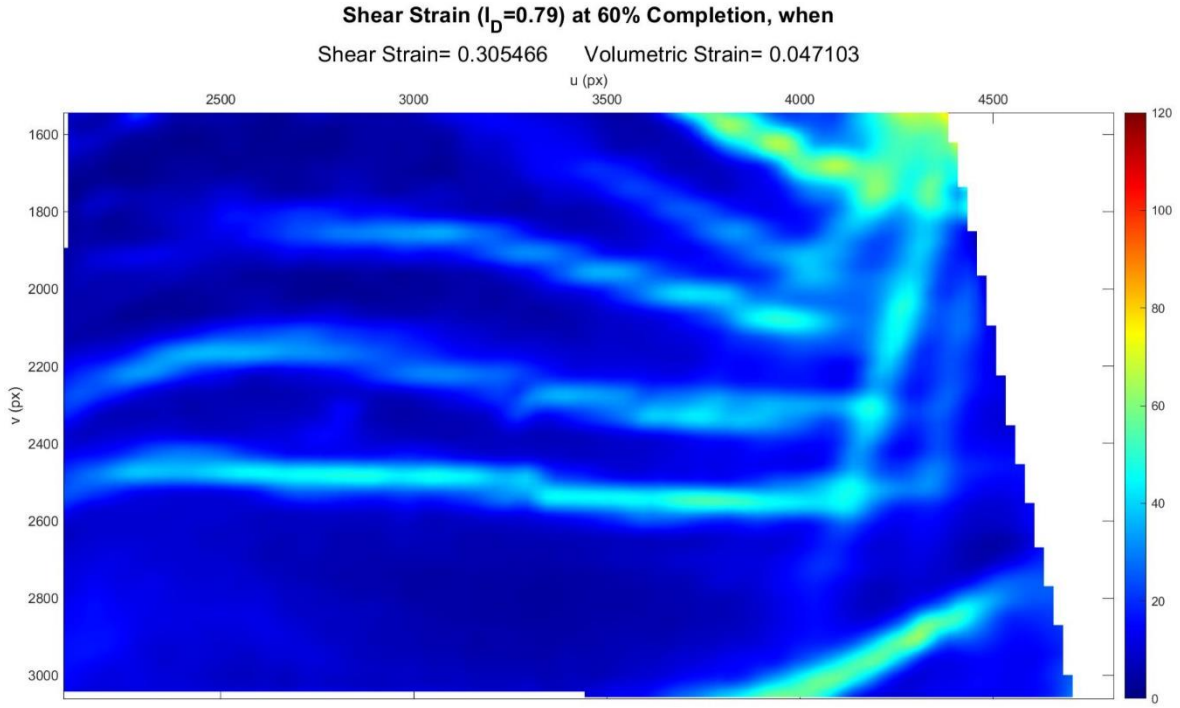

Figure C.178. Shear Strain Field at 60% Completion ($I_D = 0.79$ & $\sigma' = 0.91\ kPa$).

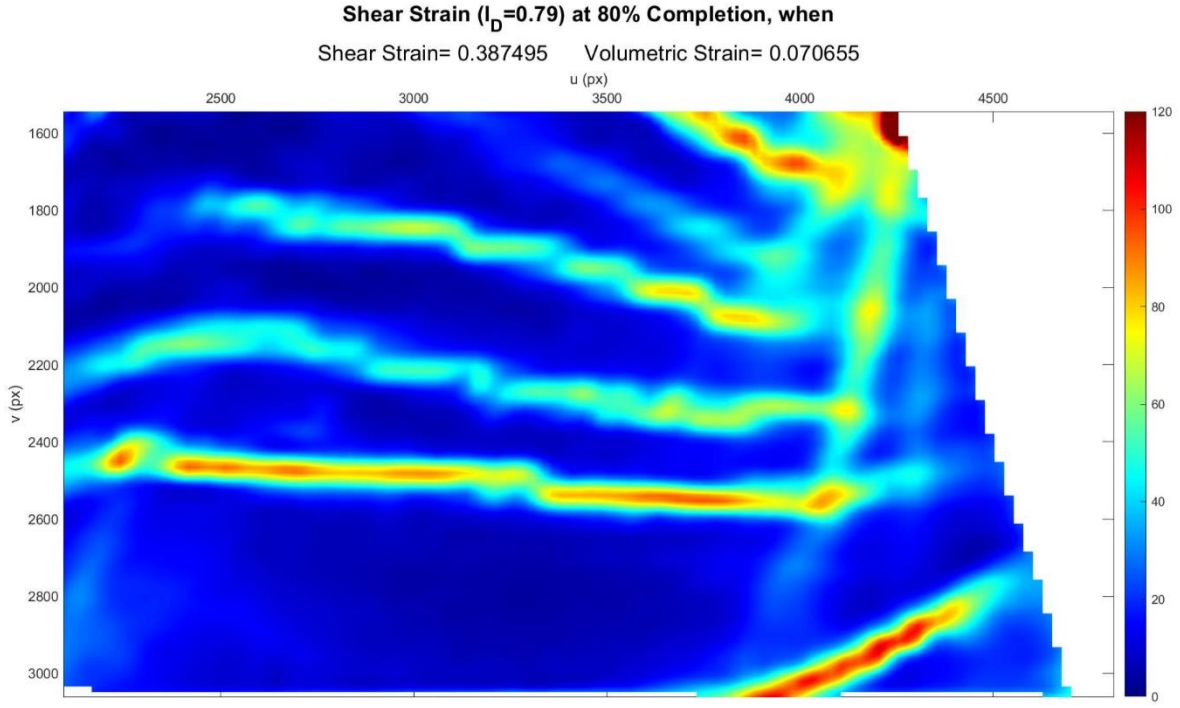

Figure C.179. Shear Strain Field at 80% Completion ($I_D = 0.79$ & $\sigma' = 0.91\ kPa$).

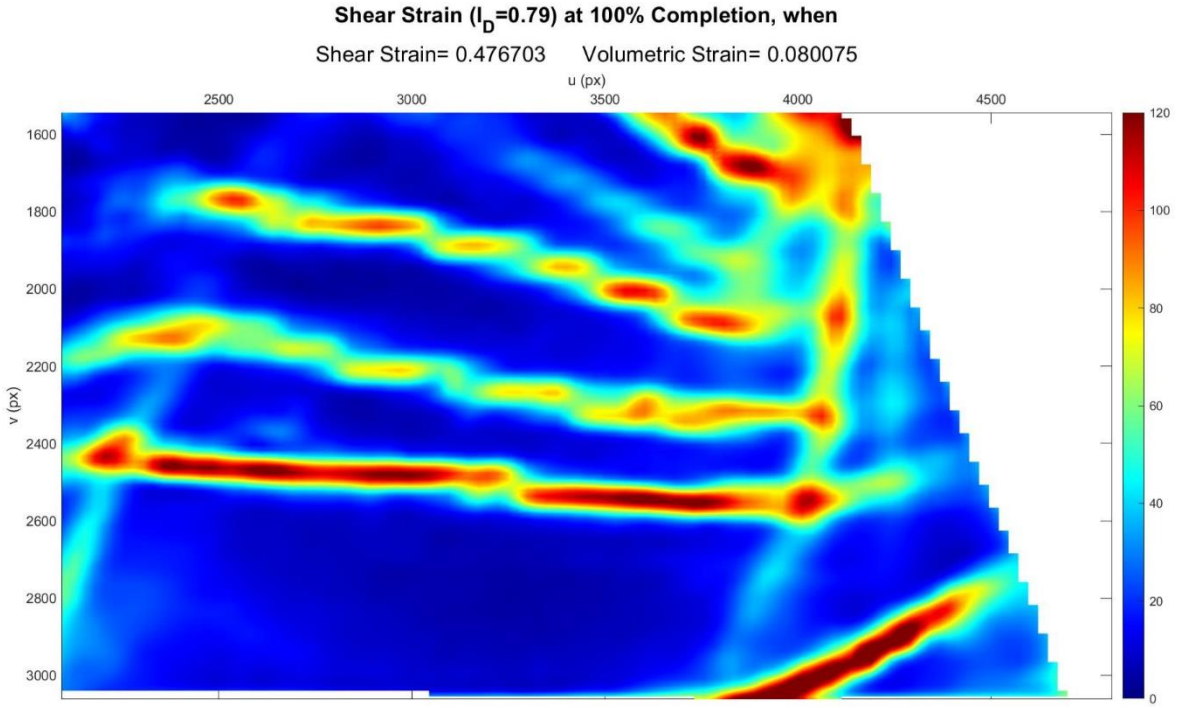

Figure C.180. Shear Strain Field at 100% Completion ($I_D = 0.79$ & $\sigma' = 0.91\ kPa$).

APPENDIX D: VOLUMETRIC STRAIN PLOTS AGAINST SHEAR STRAIN EXTRACTED FROM GEOPIV-RG ANALYSES

Volumetric strain versus shear strain diagrams of the points with maximum and minimum shear strain for all analyses are presented in the following figures.

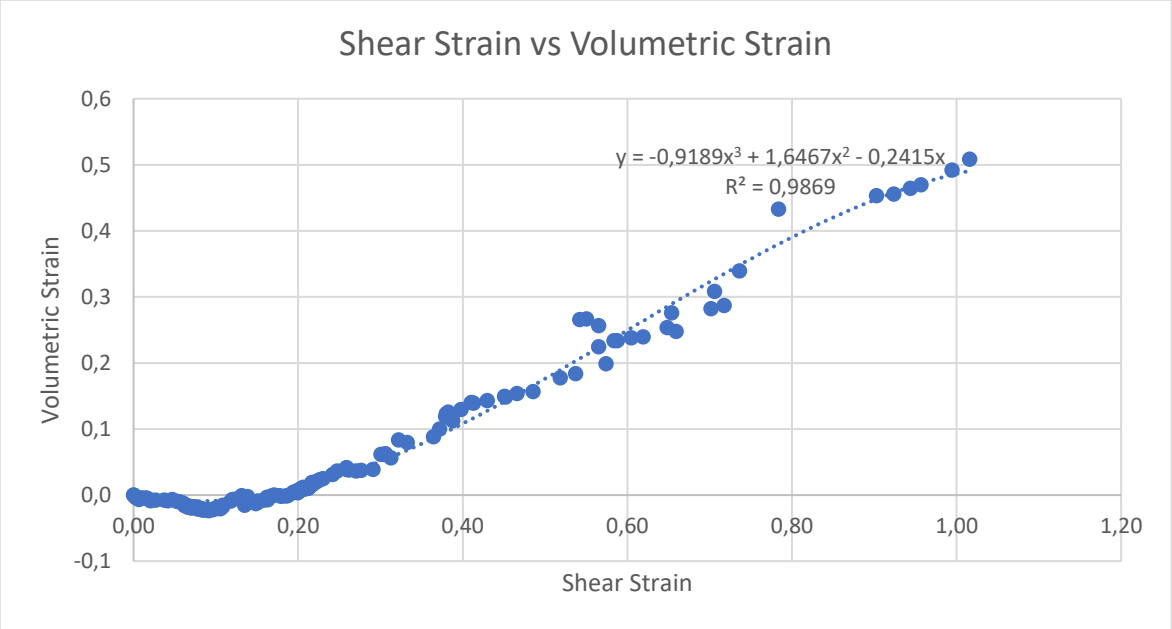

Figure D.1. Volumetric vs Shear Strain Diagram of the Point with Maximum Shear Strain ($I_D = 0.14$ & $\sigma' = 0.49\ kPa$).

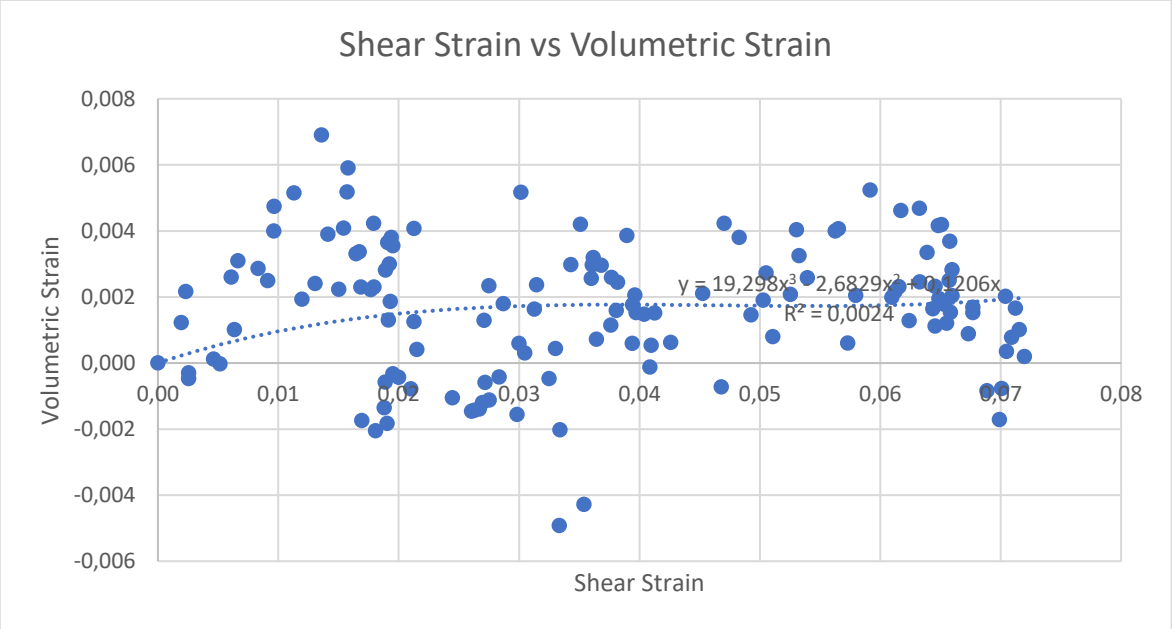

Figure D.2. Volumetric vs Shear Strain Diagram of the Point with Minimum Shear Strain ($I_D = 0.14$ & $\sigma' = 0.49\ kPa$).

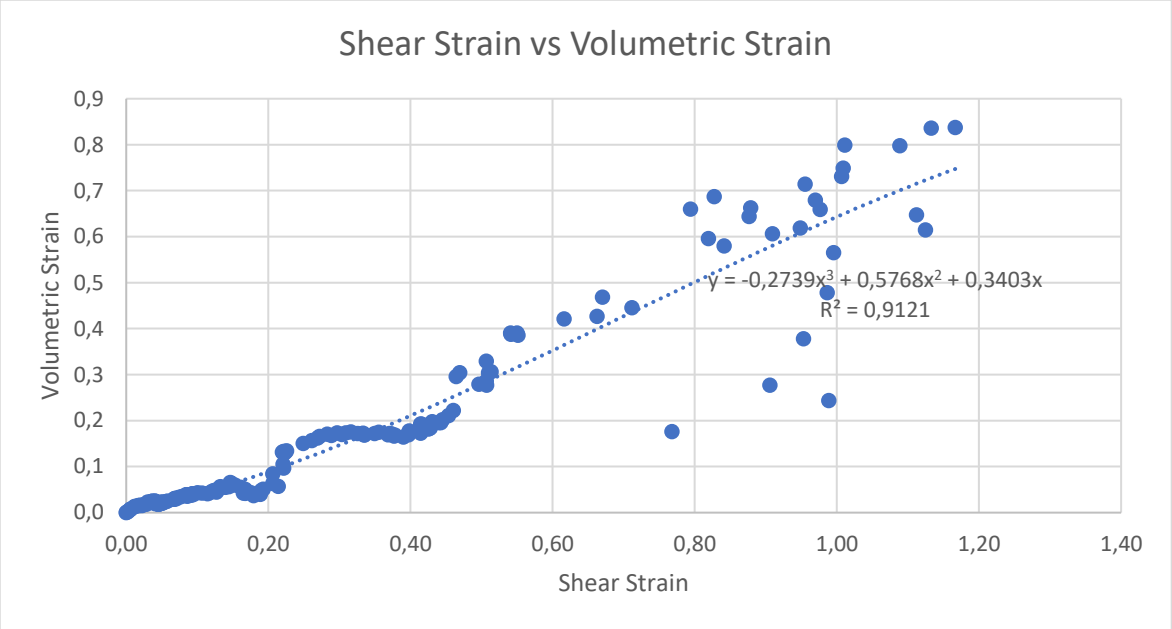

Figure D.3. Volumetric vs Shear Strain Diagram of the Point with Maximum Shear Strain ($I_D = 0.16$ & $\sigma' = 0.61\ kPa$).

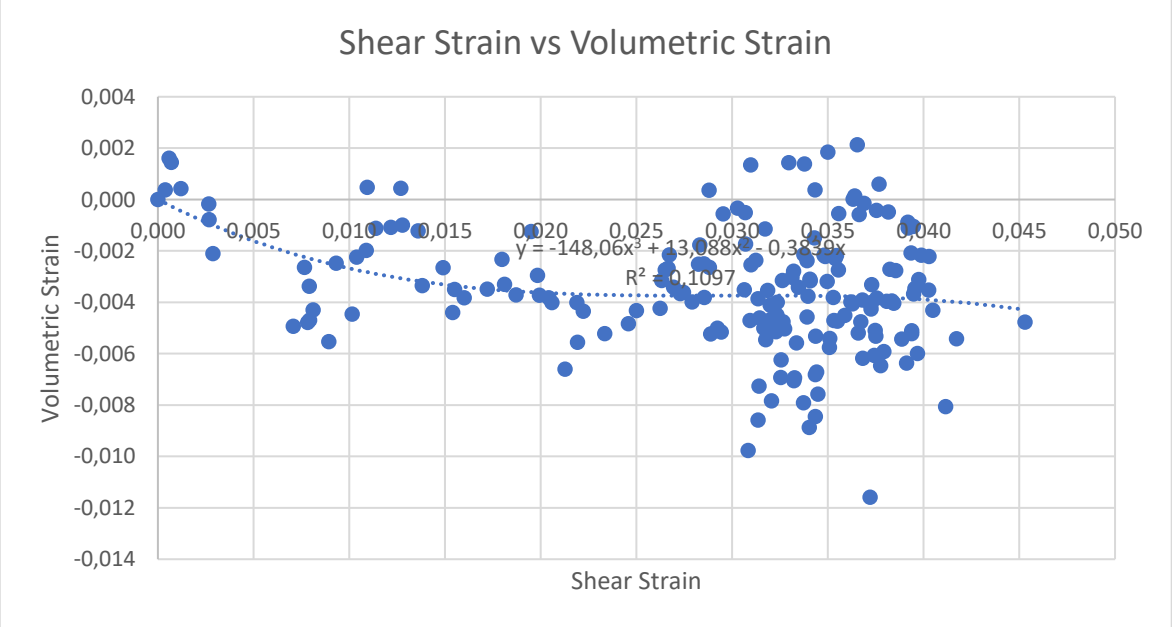

Figure D.4. Volumetric vs Shear Strain Diagram of the Point with Minimum Shear Strain ($I_D = 0.16$ & $\sigma' = 0.61\ kPa$).

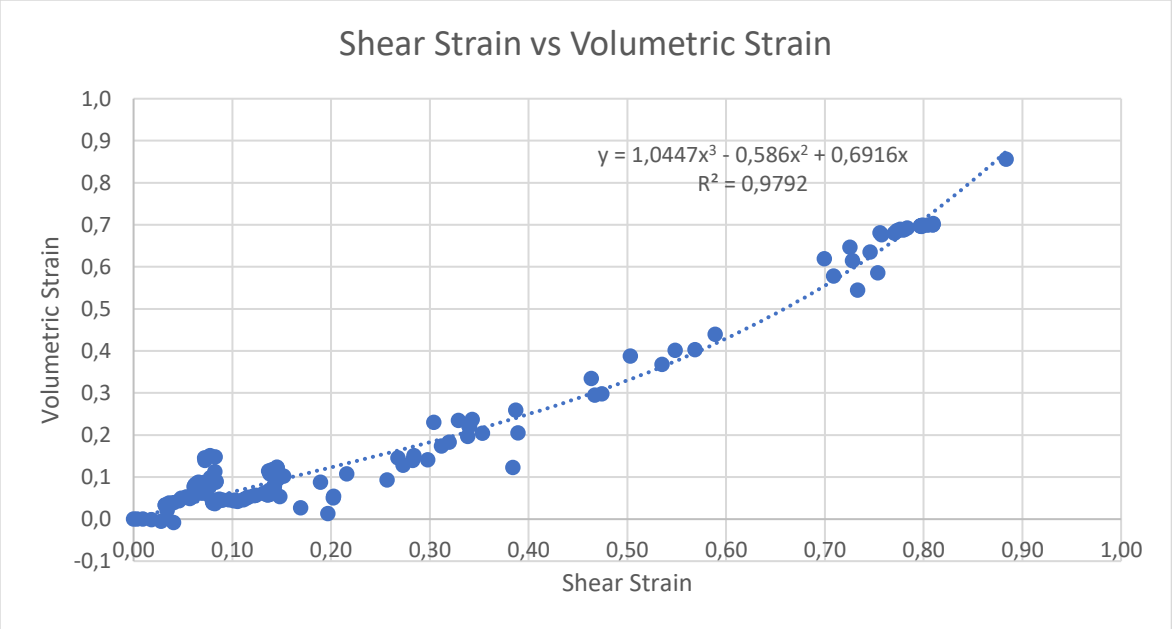

Figure D.5. Volumetric vs Shear Strain Diagram of the Point with Maximum Shear Strain ($I_D = 0.17$ & $\sigma' = 0.44\ kPa$).

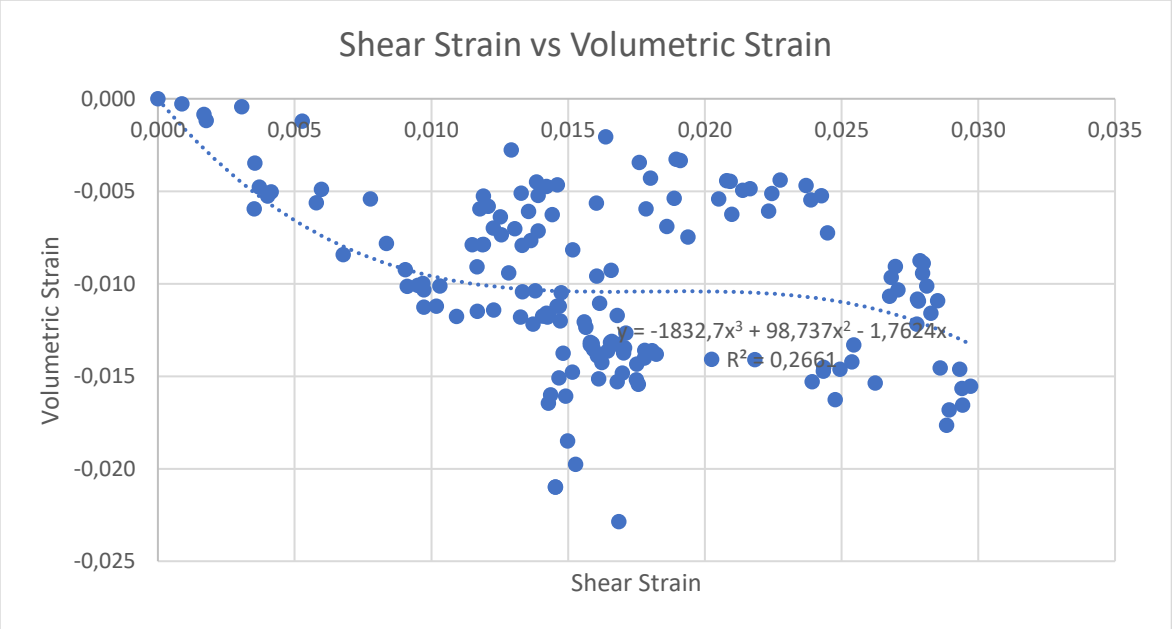

Figure D.6. Volumetric vs Shear Strain Diagram of the Point with Minimum Shear Strain ($I_D = 0.17$ & $\sigma' = 0.44\ kPa$).

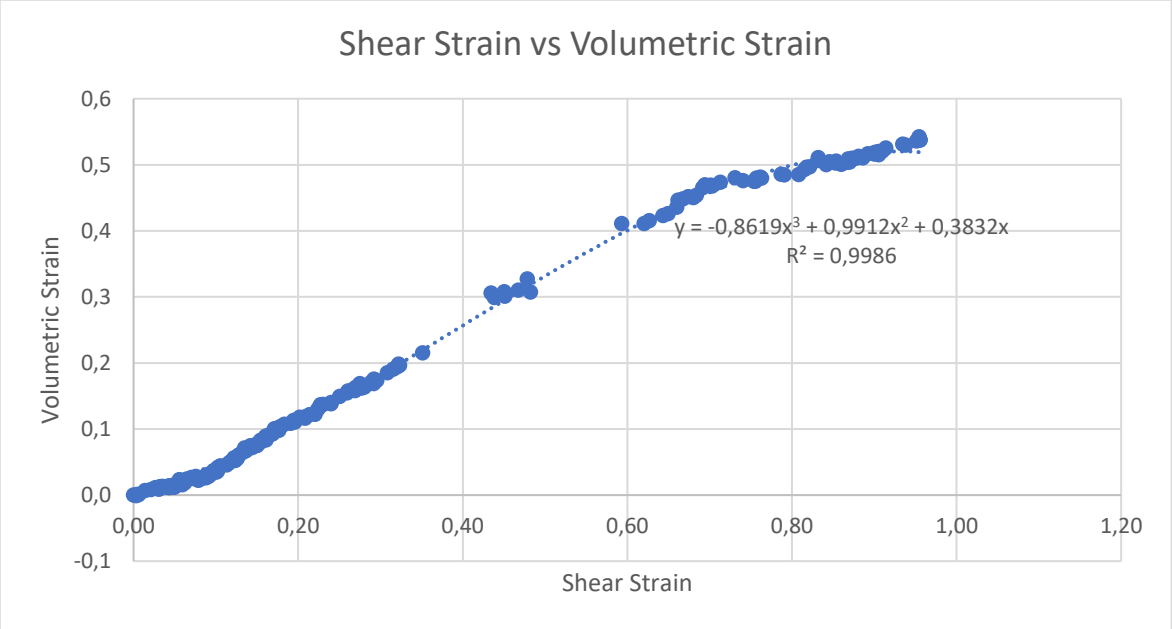

Figure D.7. Volumetric vs Shear Strain Diagram of the Point with Maximum Shear Strain ($I_D = 0.17$ & $\sigma' = 0.52\ kPa$).

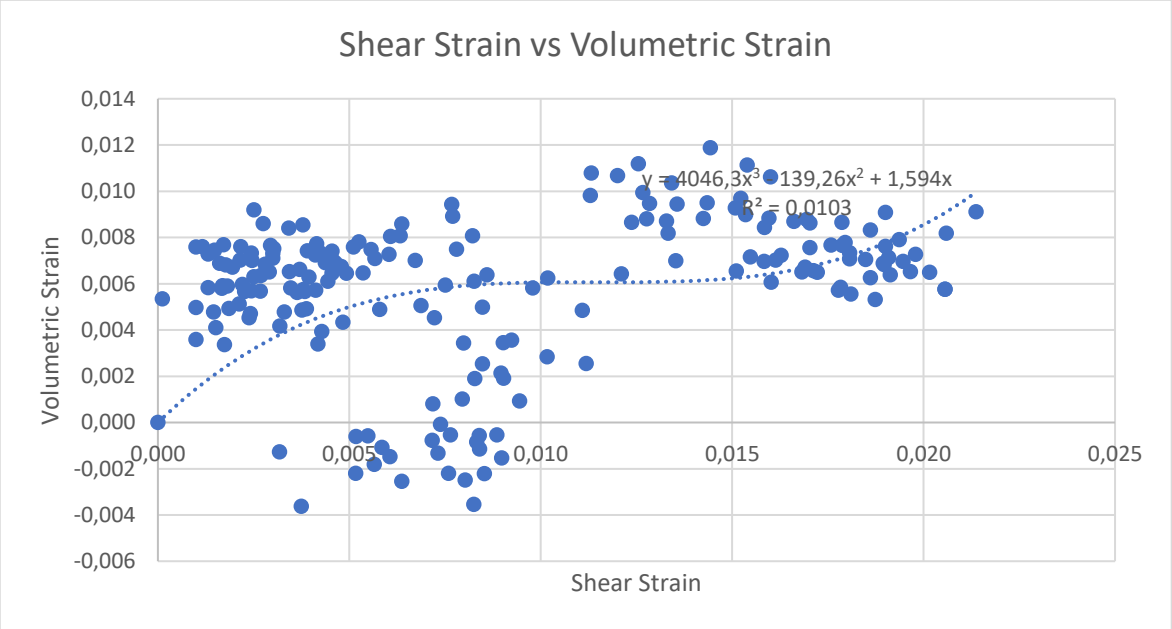

Figure D.8. Volumetric vs Shear Strain Diagram of the Point with Minimum Shear Strain ($I_D = 0.17$ & $\sigma' = 0.52\ kPa$).

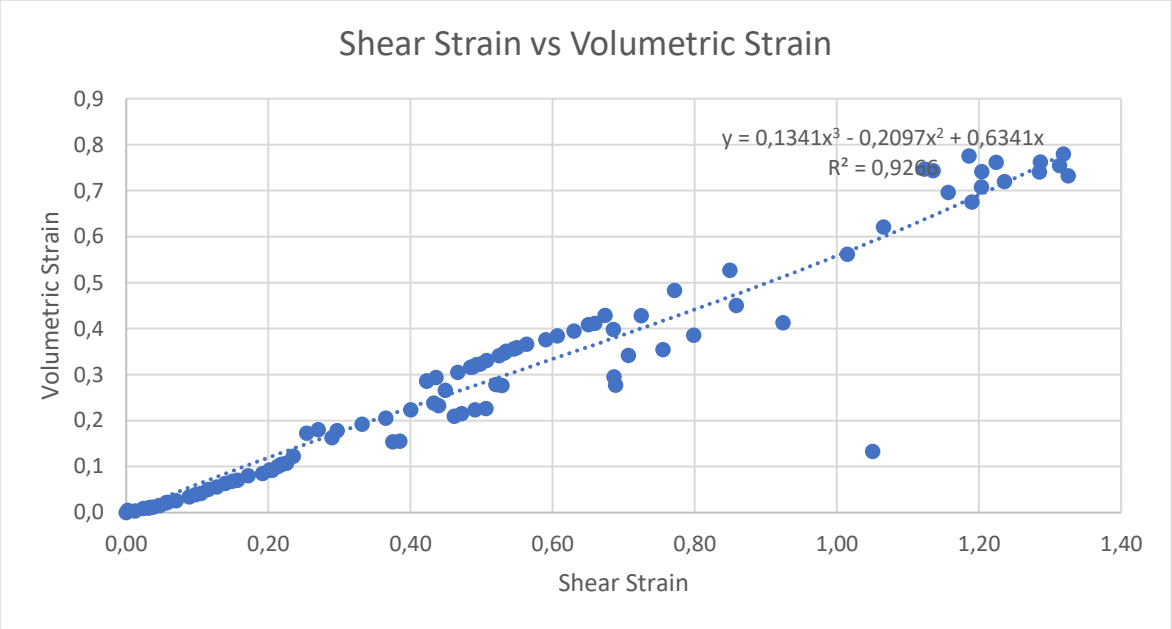

Figure D.9. Volumetric vs Shear Strain Diagram of the Point with Maximum Shear Strain ($I_D = 0.20$ & $\sigma' = 0.49\ kPa$).

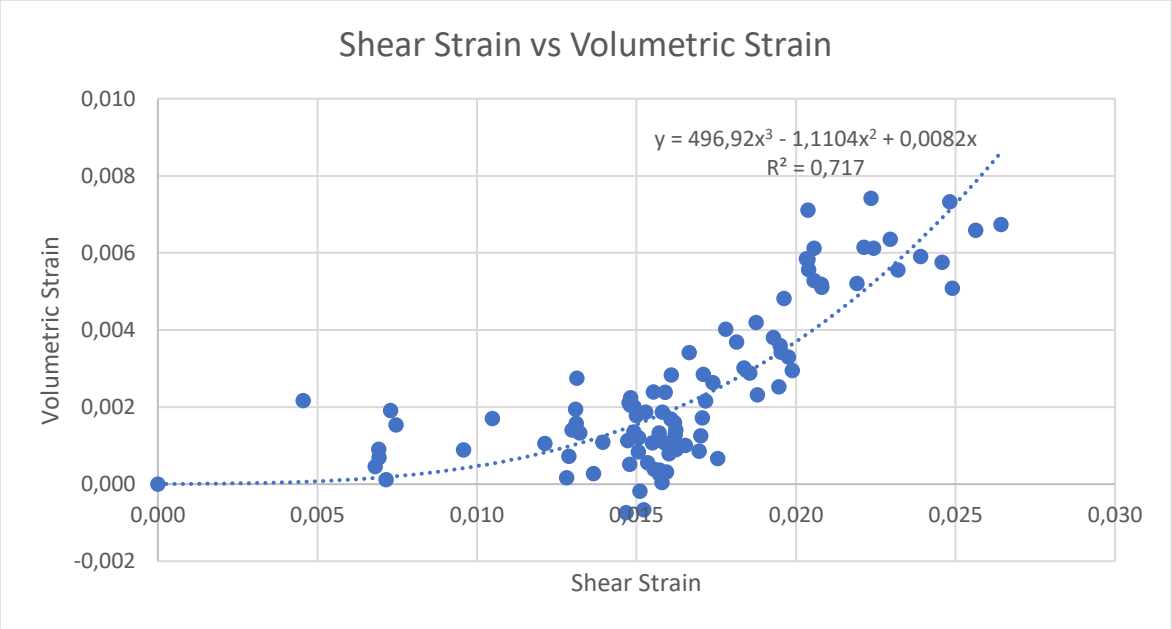

Figure D.10. Volumetric vs Shear Strain Diagram of the Point with Minimum Shear Strain ($I_D = 0.20$ & $\sigma' = 0.49\ kPa$).

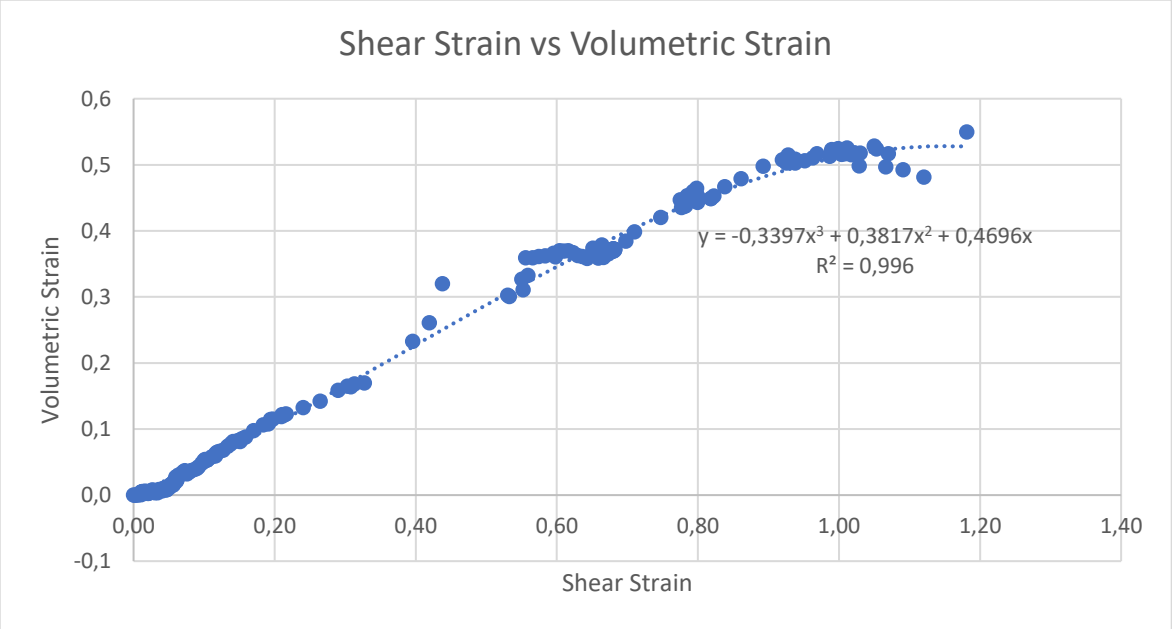

Figure D.11. Volumetric vs Shear Strain Diagram of the Point with Maximum Shear Strain ($I_D = 0.24$ & $\sigma' = 0.58\,kPa$).

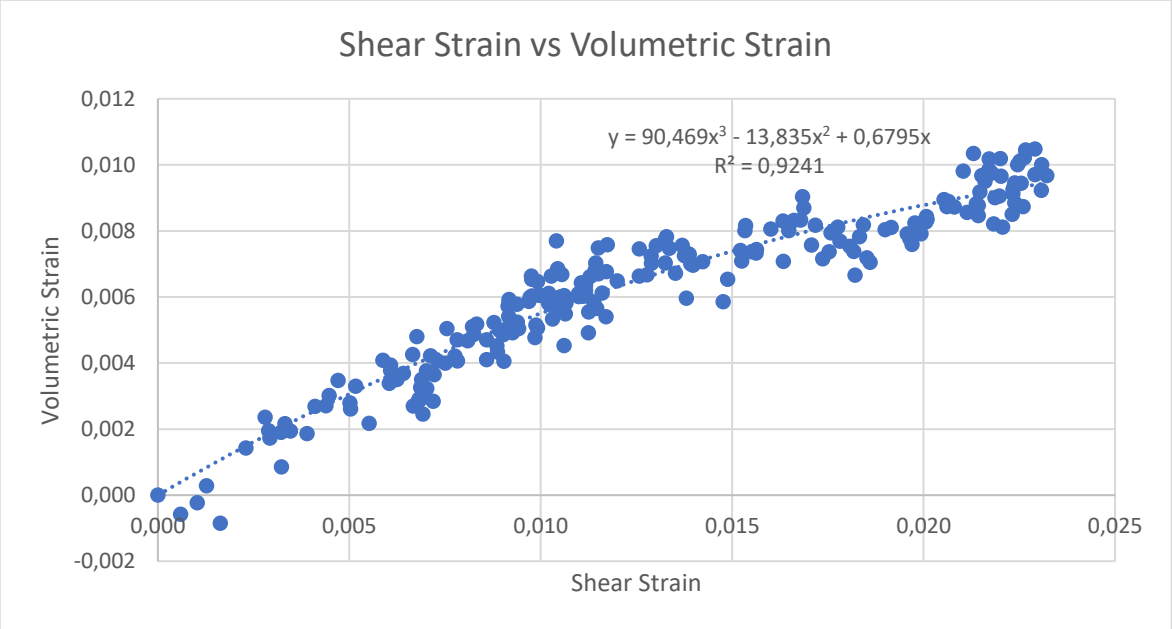

Figure D.12. Volumetric vs Shear Strain Diagram of the Point with Minimum Shear Strain ($I_D = 0.24$ & $\sigma' = 0.58\,kPa$).

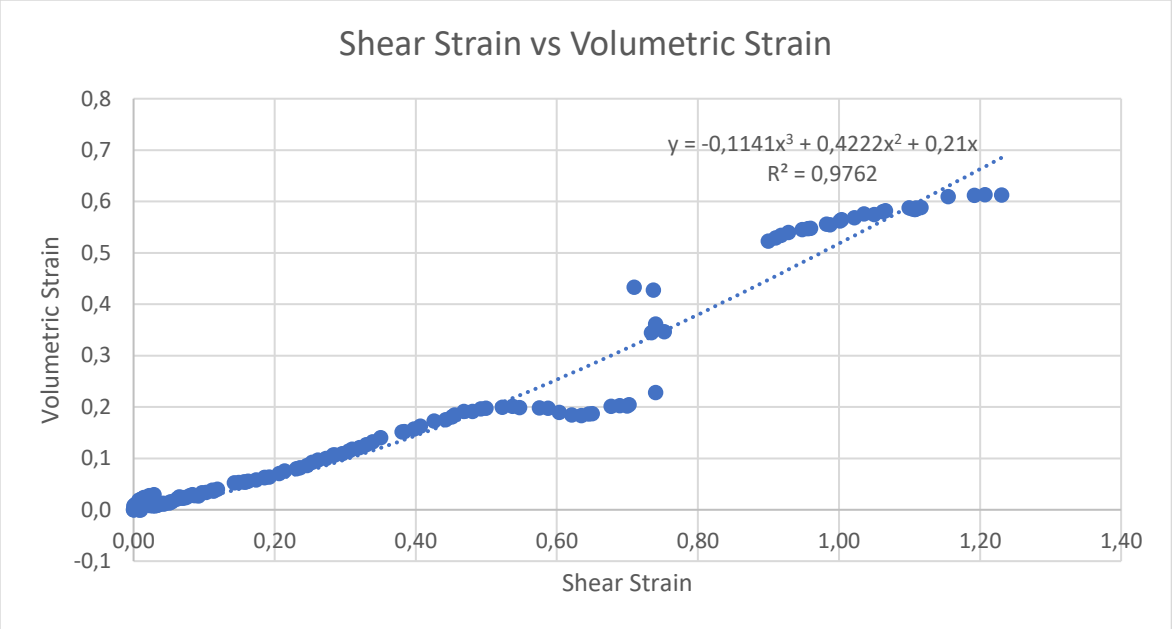

Figure D.13. Volumetric vs Shear Strain Diagram of the Point with Maximum Shear Strain ($I_D = 0.24$ & $\sigma' = 0.59\ kPa$).

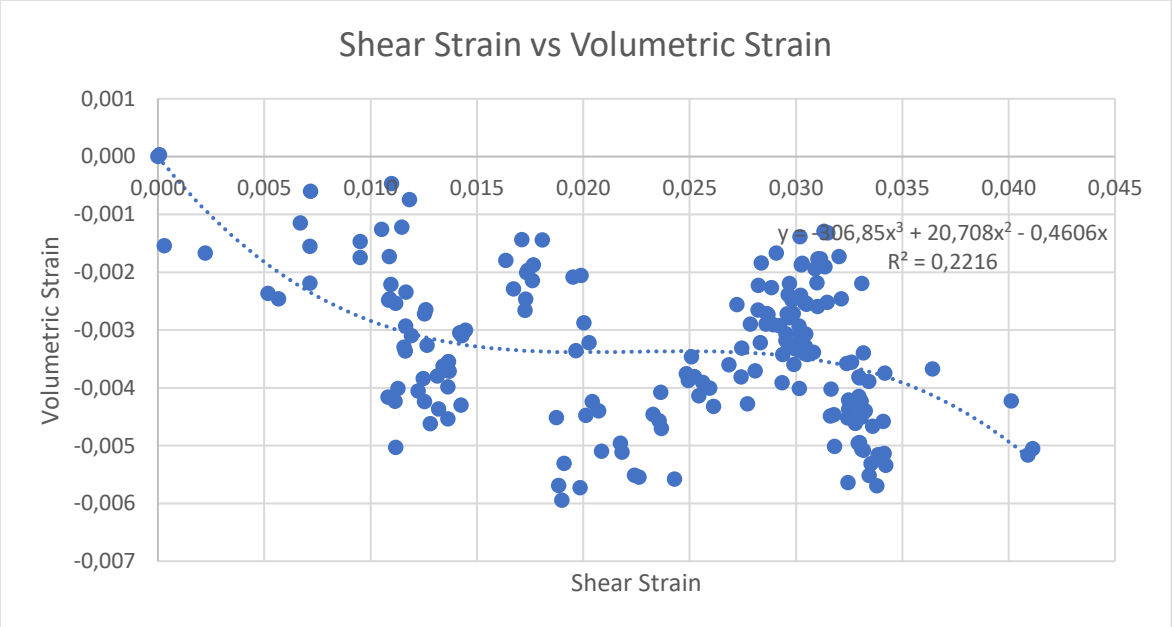

Figure D.14. Volumetric vs Shear Strain Diagram of the Point with Minimum Shear Strain ($I_D = 0.24$ & $\sigma' = 0.59\ kPa$).

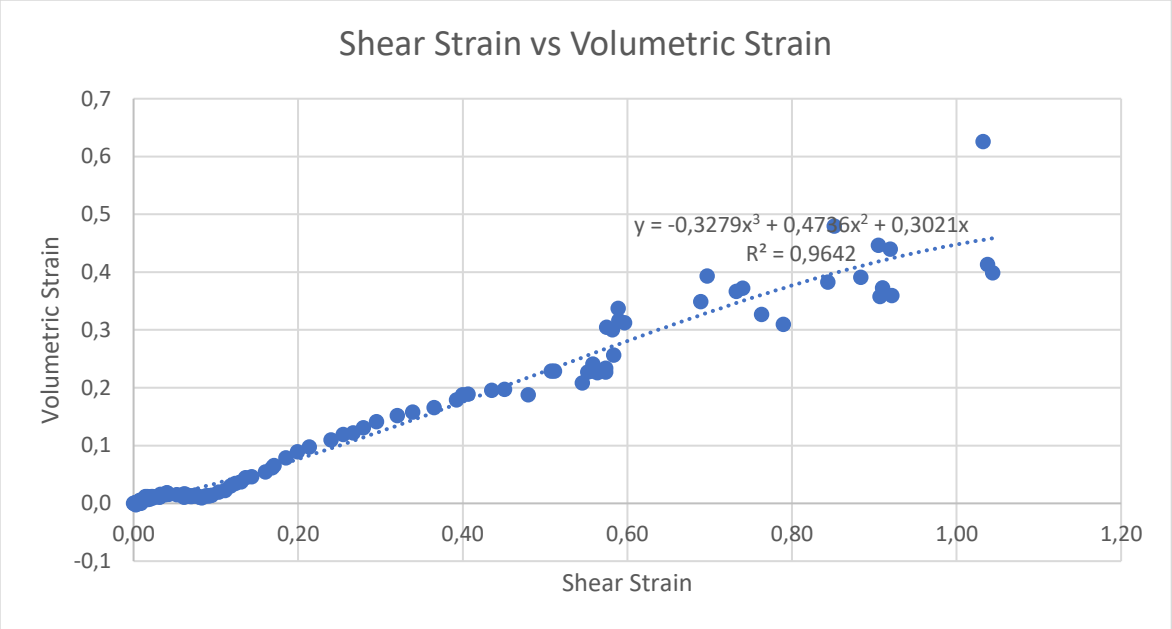

Figure D.15. Volumetric vs Shear Strain Diagram of the Point with Maximum Shear Strain ($I_D = 0.27$ & $\sigma' = 0.53\ kPa$).

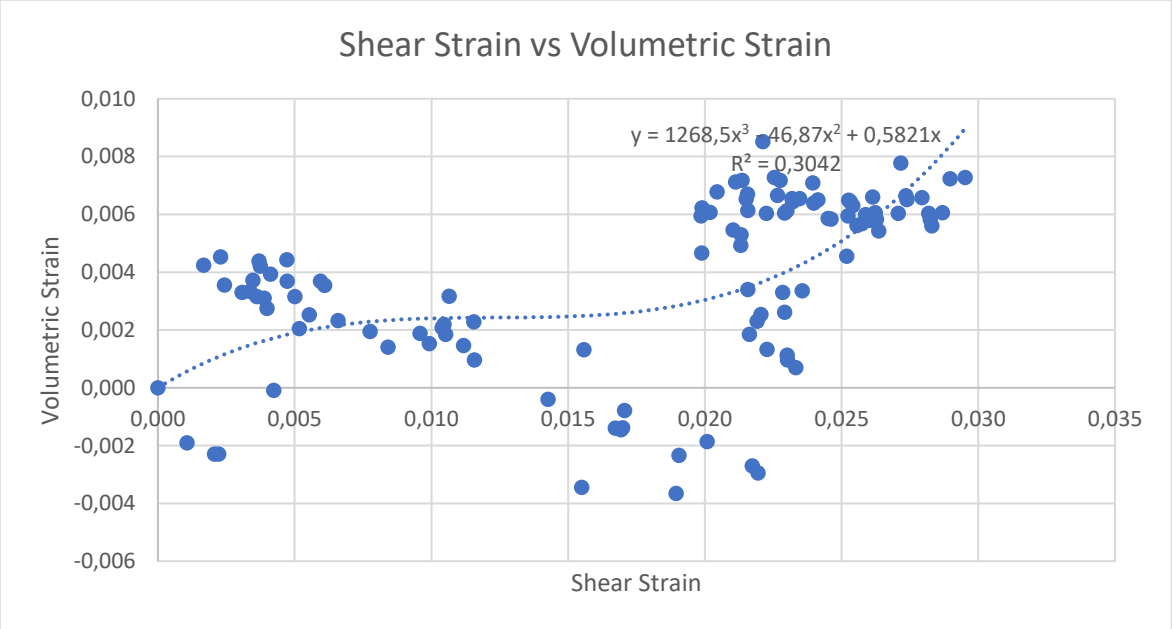

Figure D.16. Volumetric vs Shear Strain Diagram of the Point with Minimum Shear Strain ($I_D = 0.27$ & $\sigma' = 0.53\ kPa$).

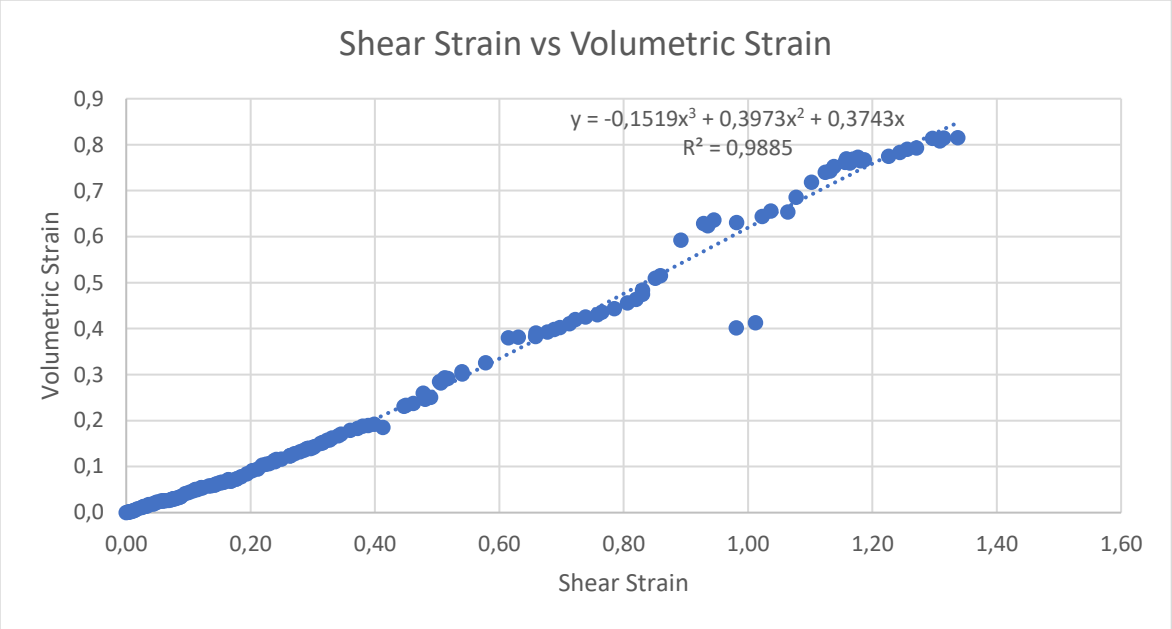

Figure D.17. Volumetric vs Shear Strain Diagram of the Point with Maximum Shear Strain ($I_D = 0.27$ & $\sigma' = 0.77\ kPa$).

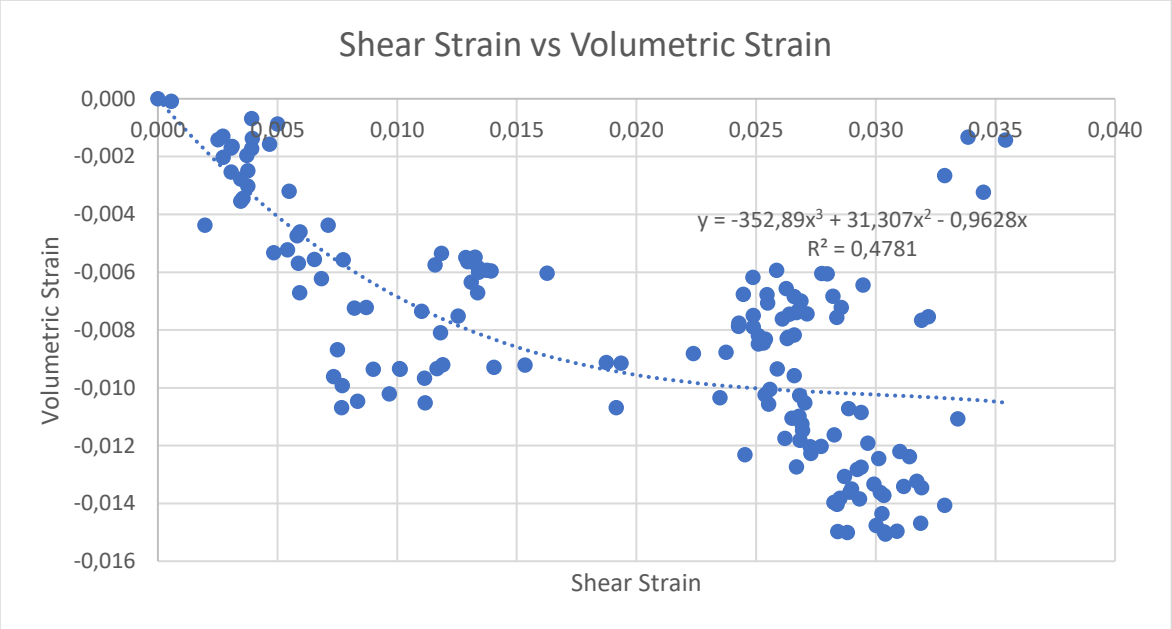

Figure D.18. Volumetric vs Shear Strain Diagram of the Point with Minimum Shear Strain ($I_D = 0.27$ & $\sigma' = 0.77\ kPa$).

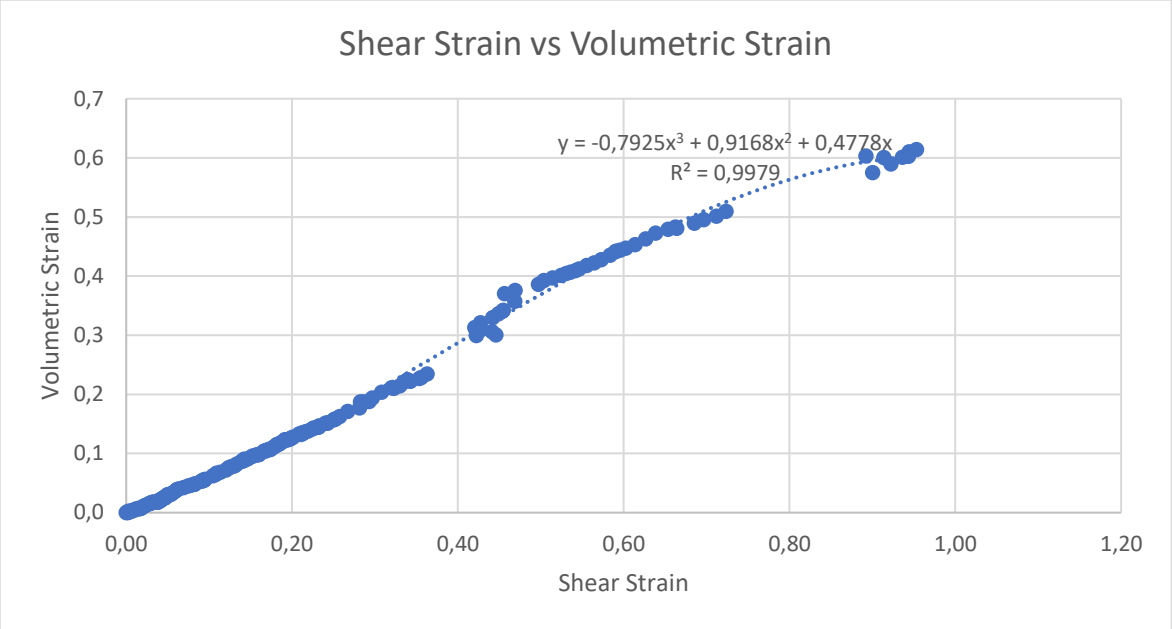

Figure D.19. Volumetric vs Shear Strain Diagram of the Point with Maximum Shear Strain ($I_D = 0.29$ & $\sigma' = 0.72\ kPa$).

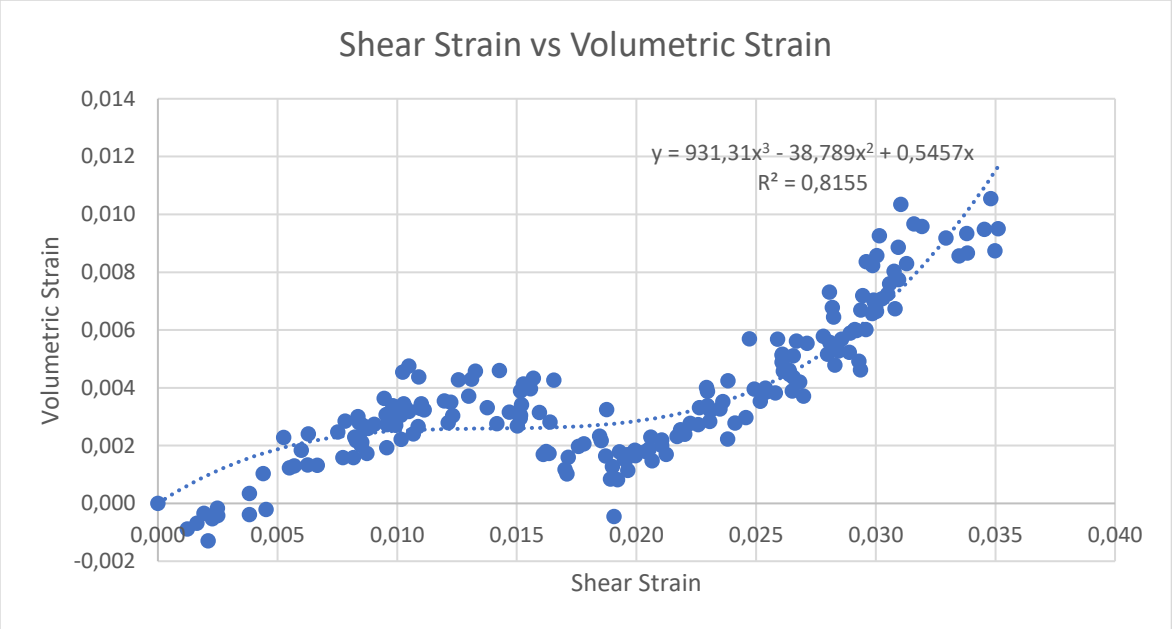

Figure D.20. Volumetric vs Shear Strain Diagram of the Point with Minimum Shear Strain ($I_D = 0.29$ & $\sigma' = 0.72\ kPa$).

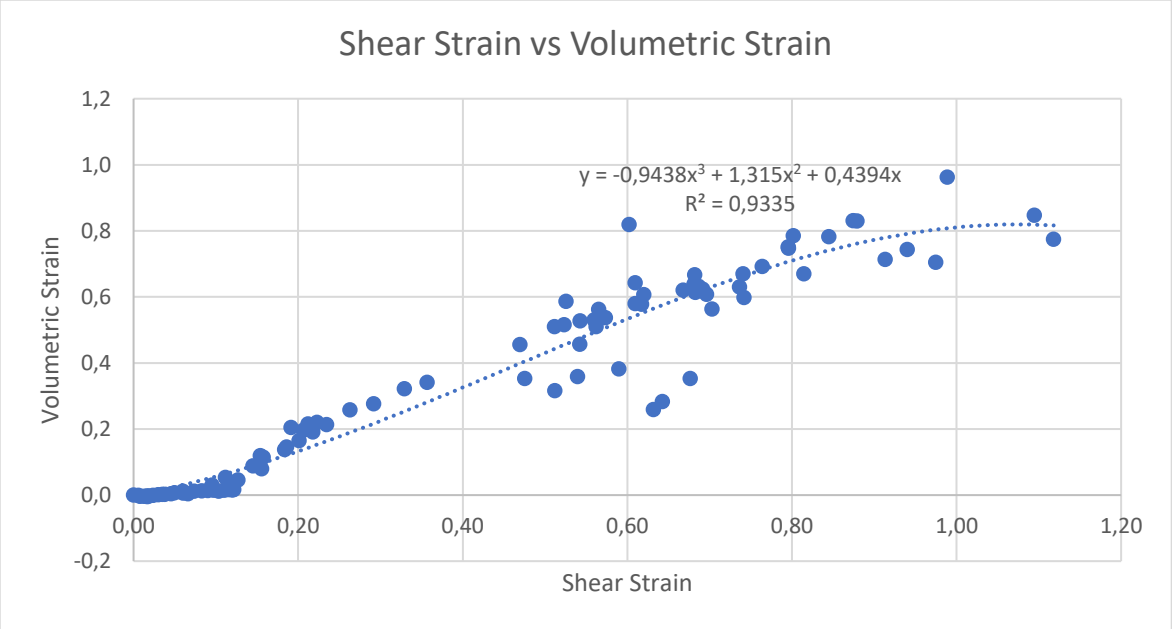

Figure D.21. Volumetric vs Shear Strain Diagram of the Point with Maximum Shear Strain ($I_D = 0.32$ & $\sigma' = 0.94\ kPa$).

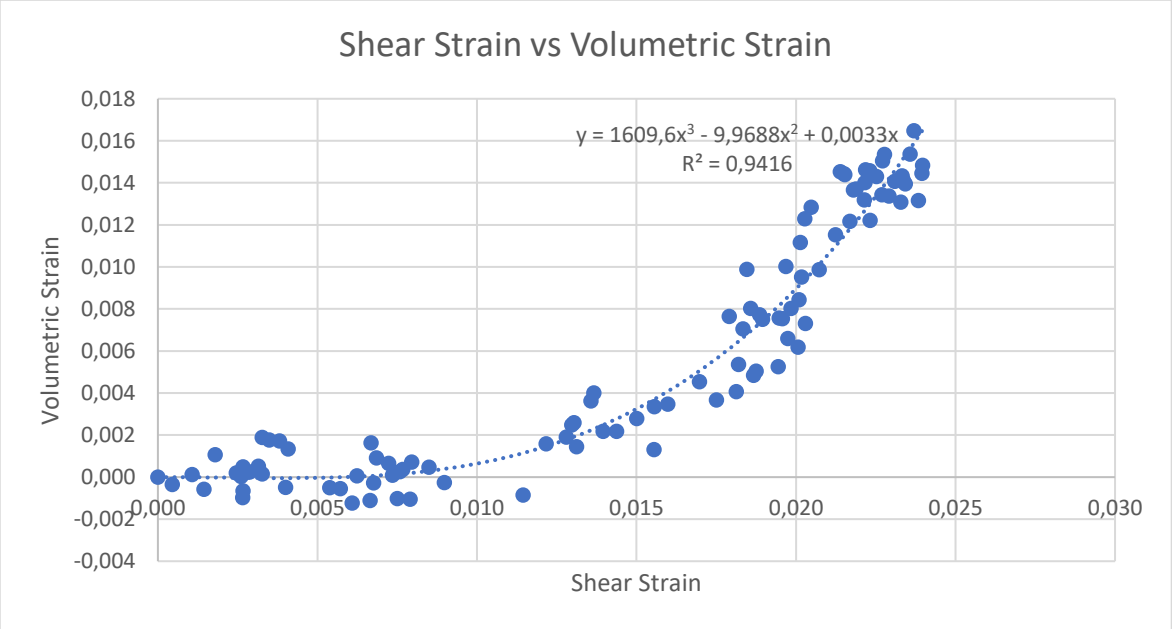

Figure D.22. Volumetric vs Shear Strain Diagram of the Point with Minimum Shear Strain ($I_D = 0.32$ & $\sigma' = 0.94\ kPa$).

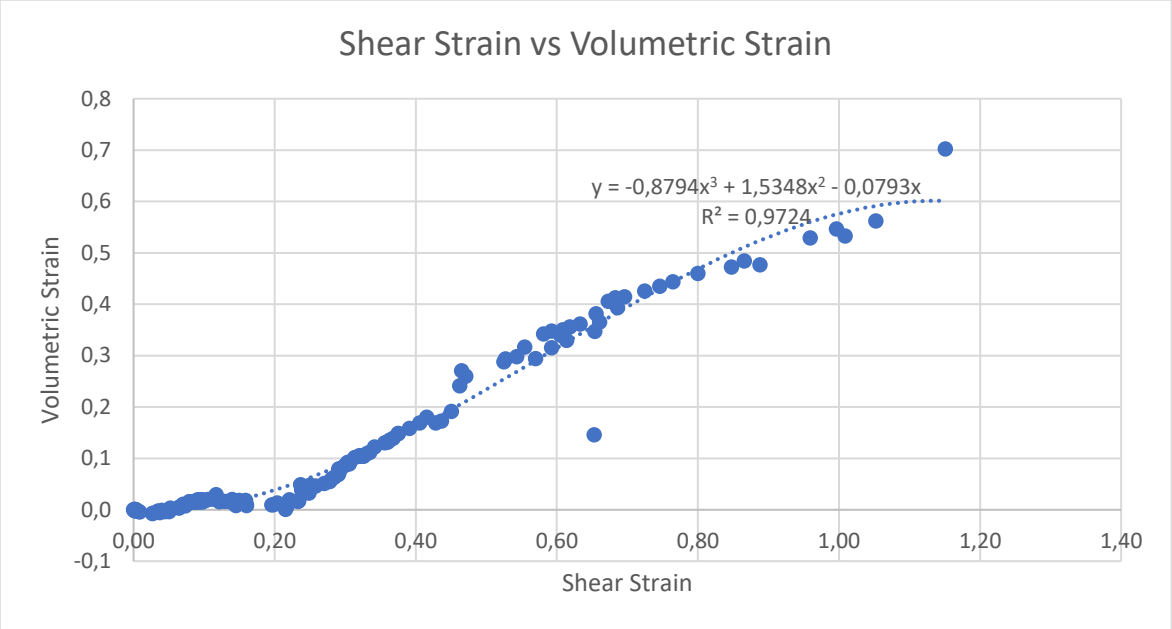

Figure D.23. Volumetric vs Shear Strain Diagram of the Point with Maximum Shear Strain ($I_D = 0.33$ & $\sigma' = 0.85\ kPa$).

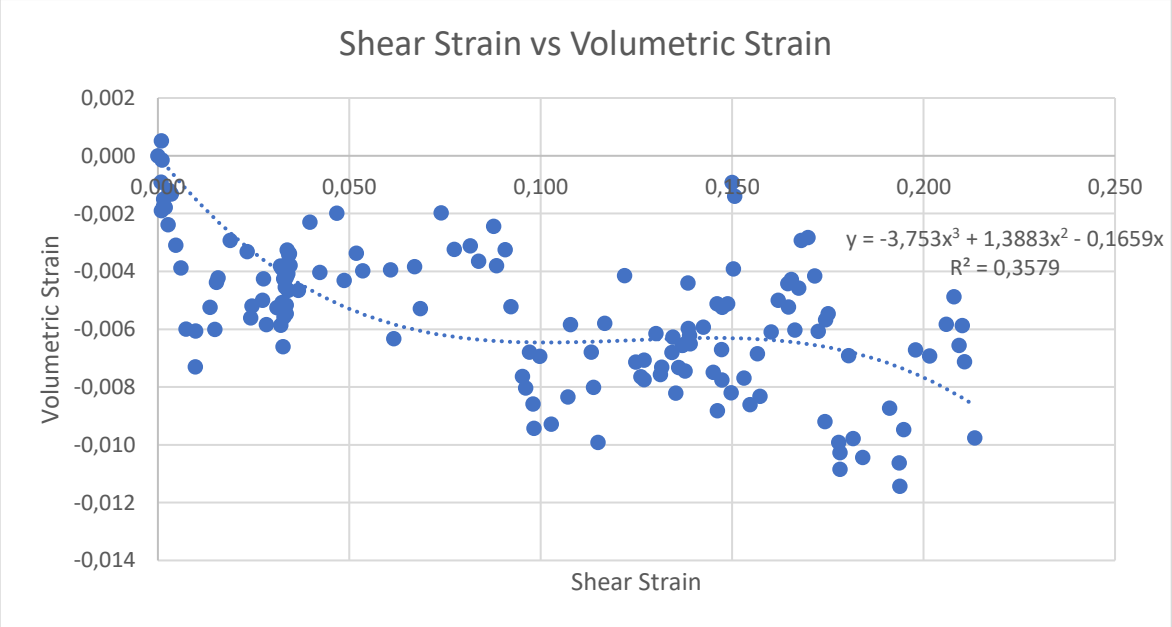

Figure D.24. Volumetric vs Shear Strain Diagram of the Point with Minimum Shear Strain ($I_D = 0.33$ & $\sigma' = 0.85\ kPa$).

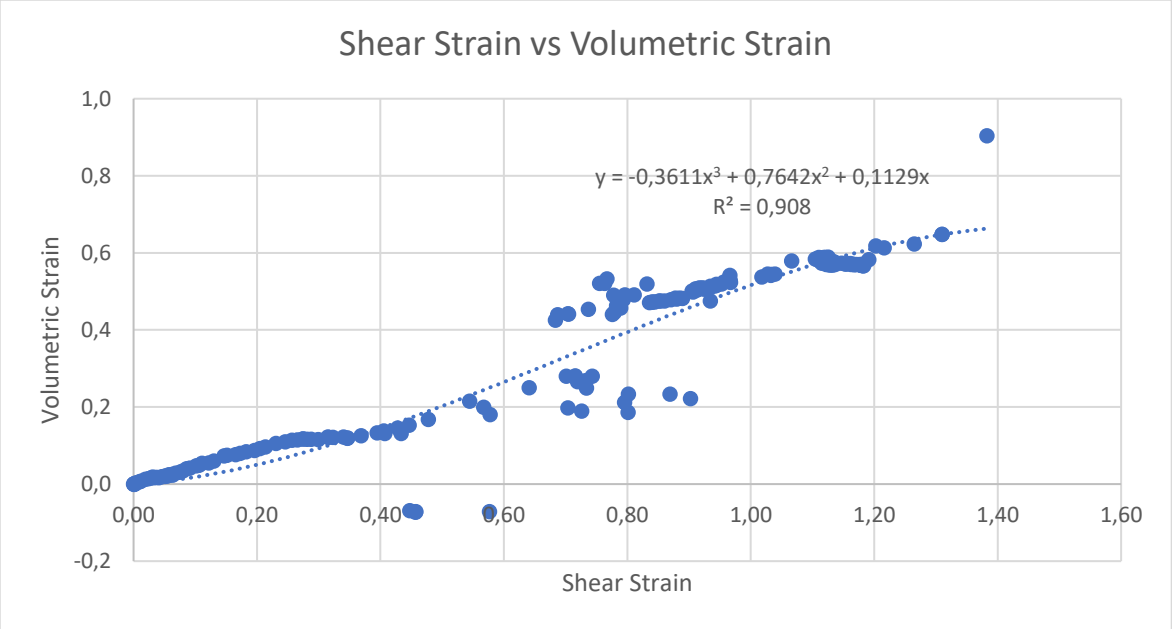

Figure D.25. Volumetric vs Shear Strain Diagram of the Point with Maximum Shear Strain ($I_D = 0.36$ & $\sigma' = 0.71\ kPa$).

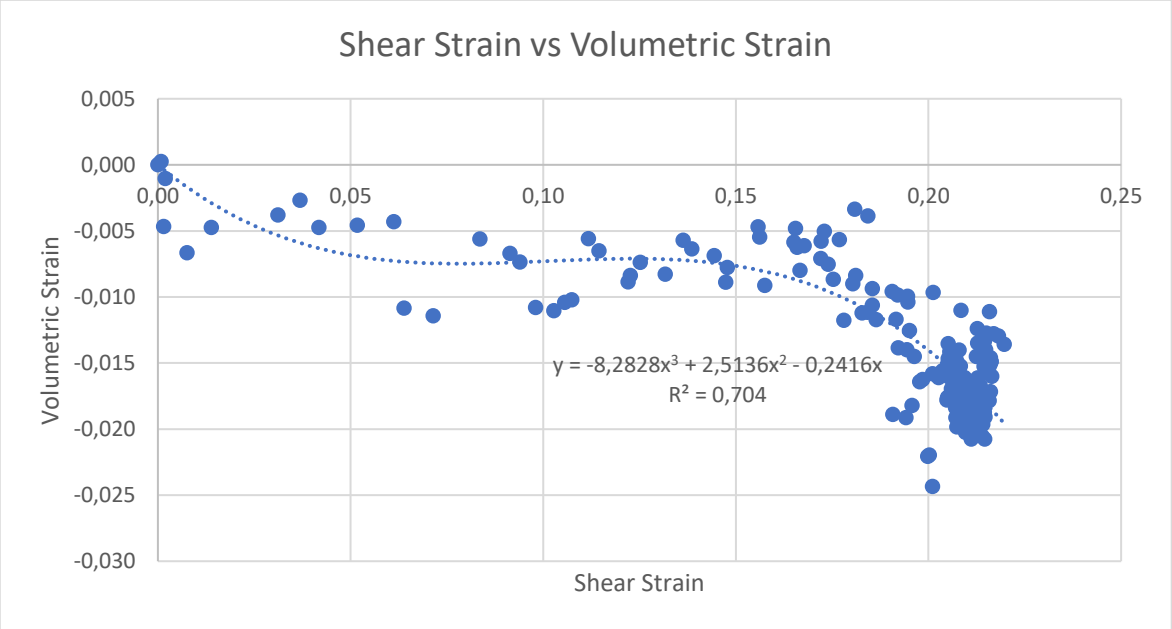

Figure D.26. Volumetric vs Shear Strain Diagram of the Point with Minimum Shear Strain ($I_D = 0.36$ & $\sigma' = 0.71\ kPa$).

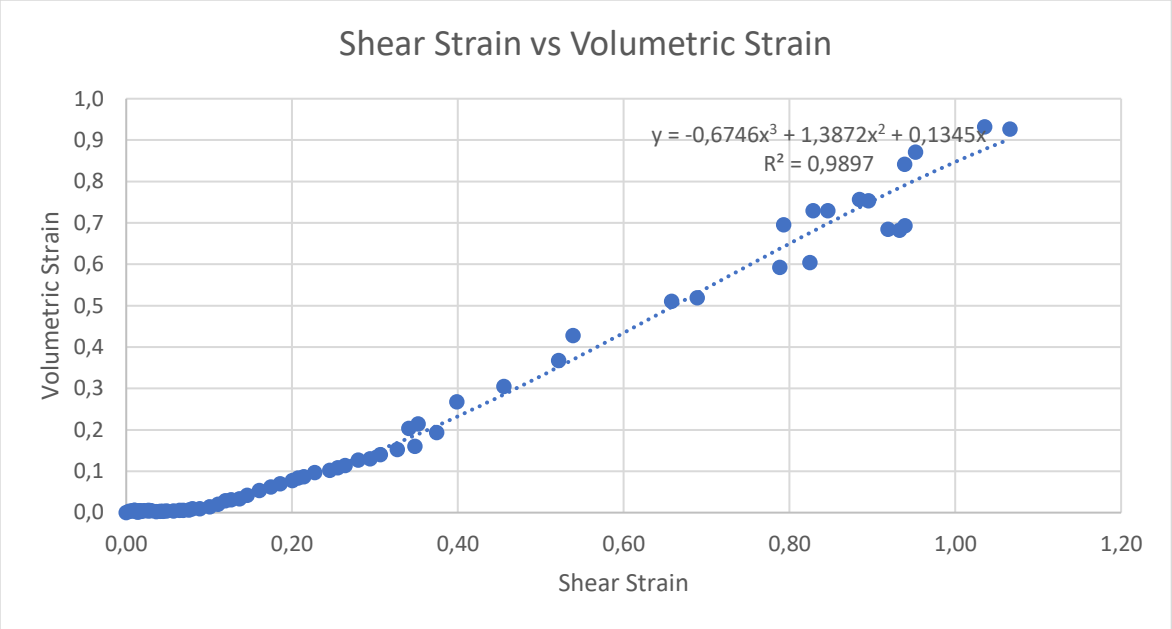

Figure D.27. Volumetric vs Shear Strain Diagram of the Point with Maximum Shear Strain ($I_D = 0.39$ & $\sigma' = 0.58\,kPa$).

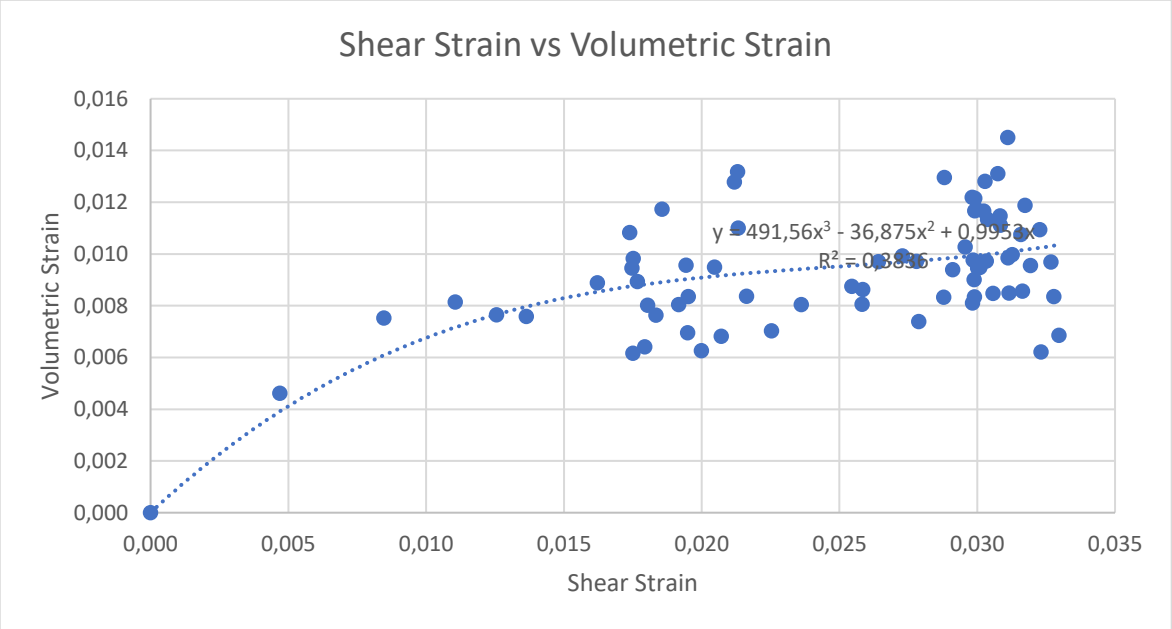

Figure D.28. Volumetric vs Shear Strain Diagram of the Point with Minimum Shear Strain ($I_D = 0.39$ & $\sigma' = 0.58\,kPa$).

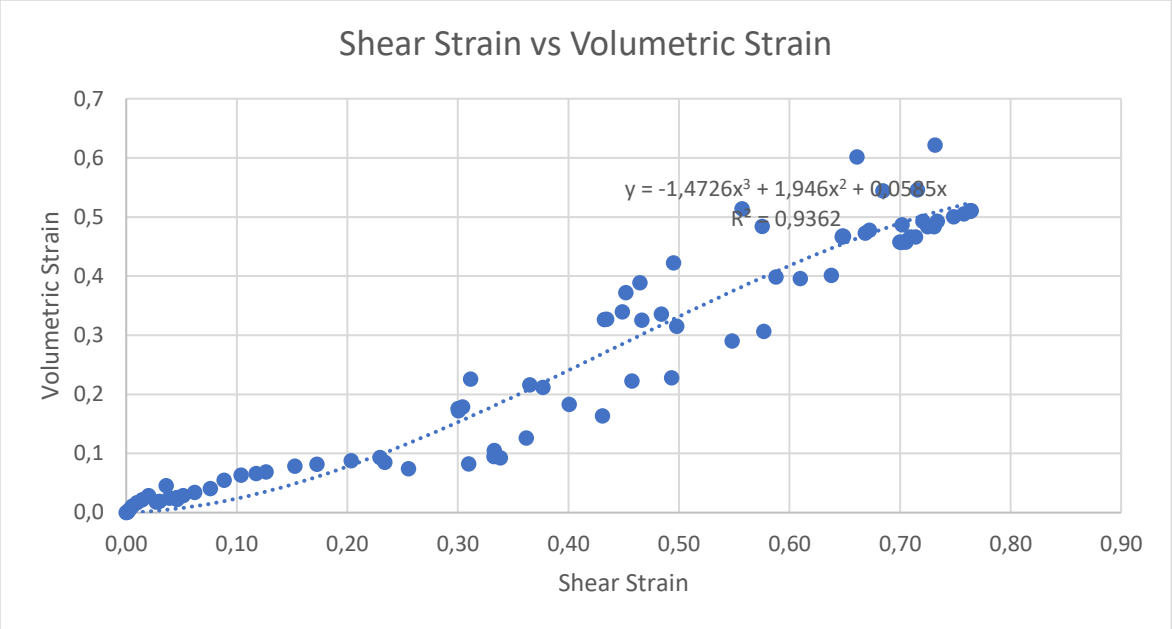

Figure D.29. Volumetric vs Shear Strain Diagram of the Point with Maximum Shear Strain ($I_D = 0.41$ & $\sigma' = 0.87\ kPa$).

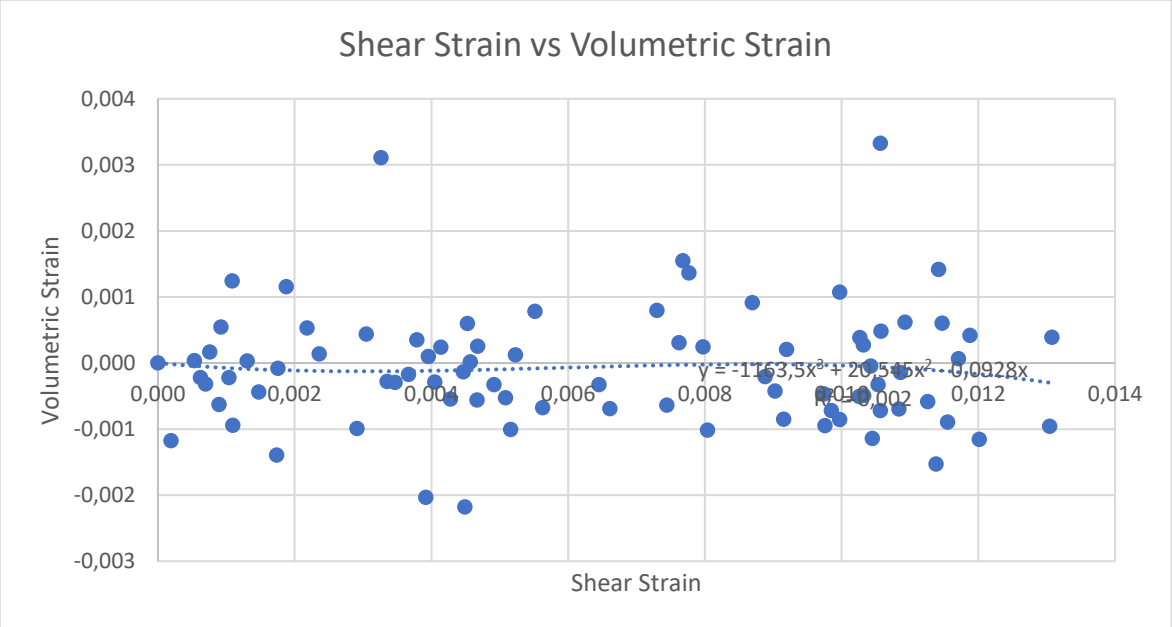

Figure D.30. Volumetric vs Shear Strain Diagram of the Point with Minimum Shear Strain ($I_D = 0.41$ & $\sigma' = 0.87\ kPa$).

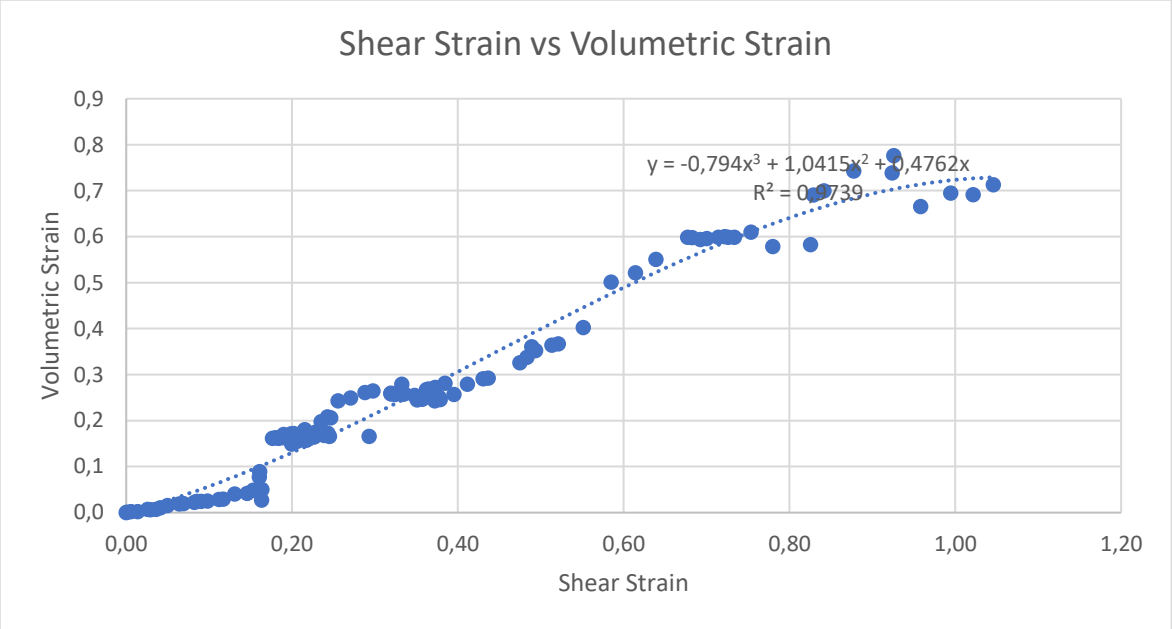

Figure D.31. Volumetric vs Shear Strain Diagram of the Point with Maximum Shear Strain ($I_D = 0.41$ & $\sigma' = 0.96\ kPa$).

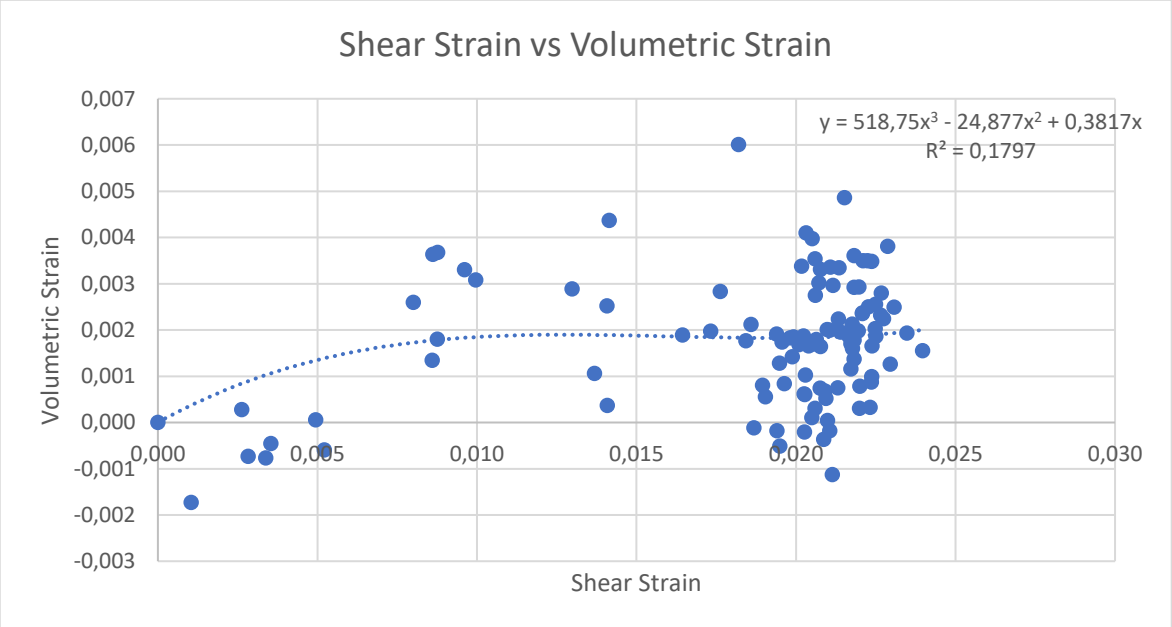

Figure D.32. Volumetric vs Shear Strain Diagram of the Point with Minimum Shear Strain ($I_D = 0.41$ & $\sigma' = 0.96\ kPa$).

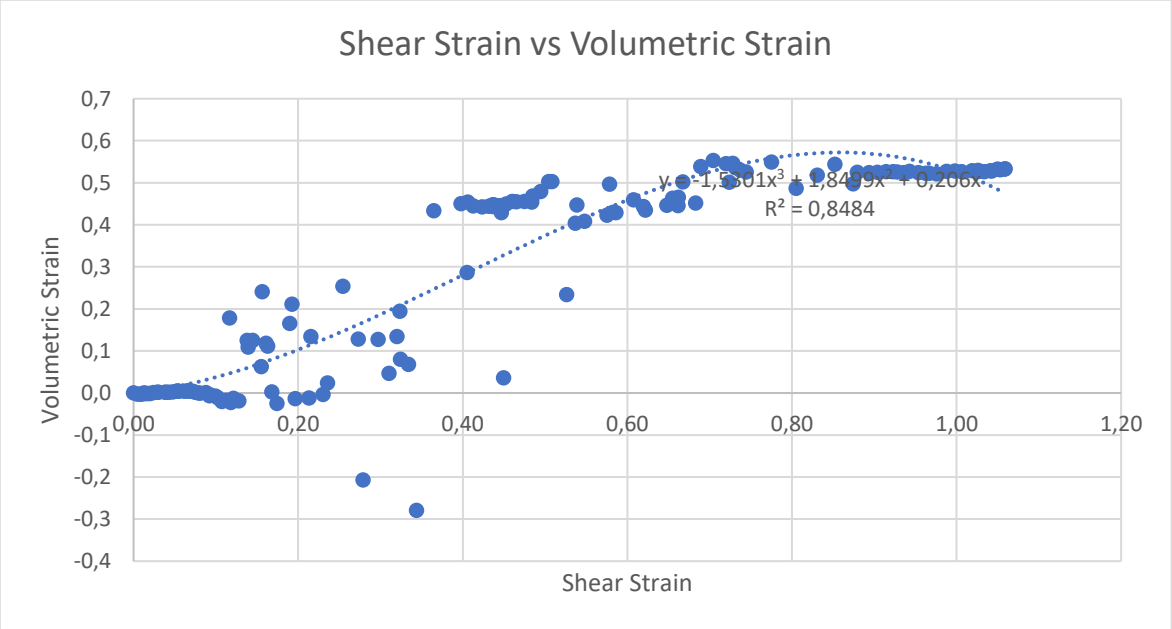

Figure D.33. Volumetric vs Shear Strain Diagram of the Point with Maximum Shear Strain ($I_D = 0.45$ & $\sigma' = 0.88\,kPa$).

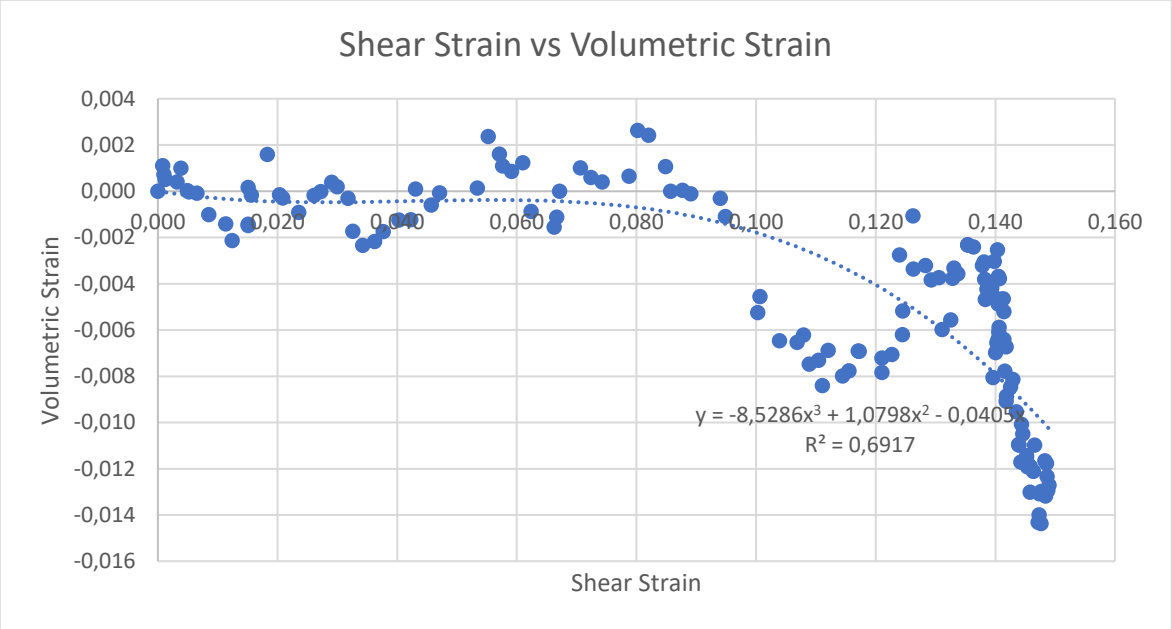

Figure D.34. Volumetric vs Shear Strain Diagram of the Point with Minimum Shear Strain ($I_D = 0.45$ & $\sigma' = 0.88\,kPa$).

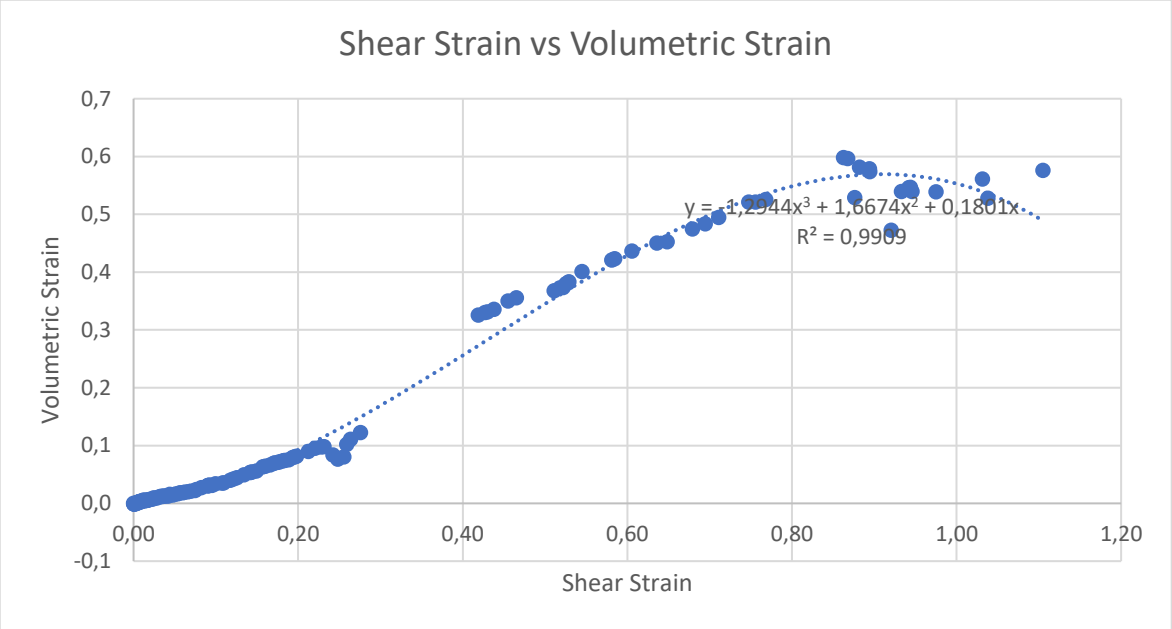

Figure D.35. Volumetric vs Shear Strain Diagram of the Point with Maximum Shear Strain ($I_D = 0.46$ & $\sigma' = 0.71\ kPa$).

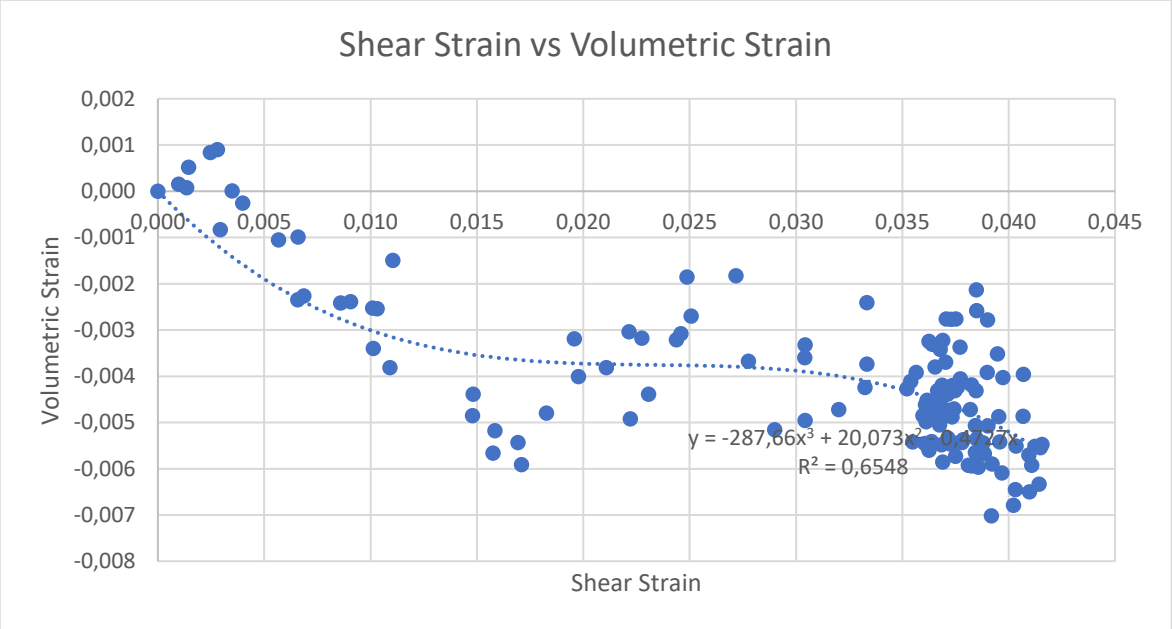

Figure D.36. Volumetric vs Shear Strain Diagram of the Point with Minimum Shear Strain ($I_D = 0.46$ & $\sigma' = 0.71\ kPa$).

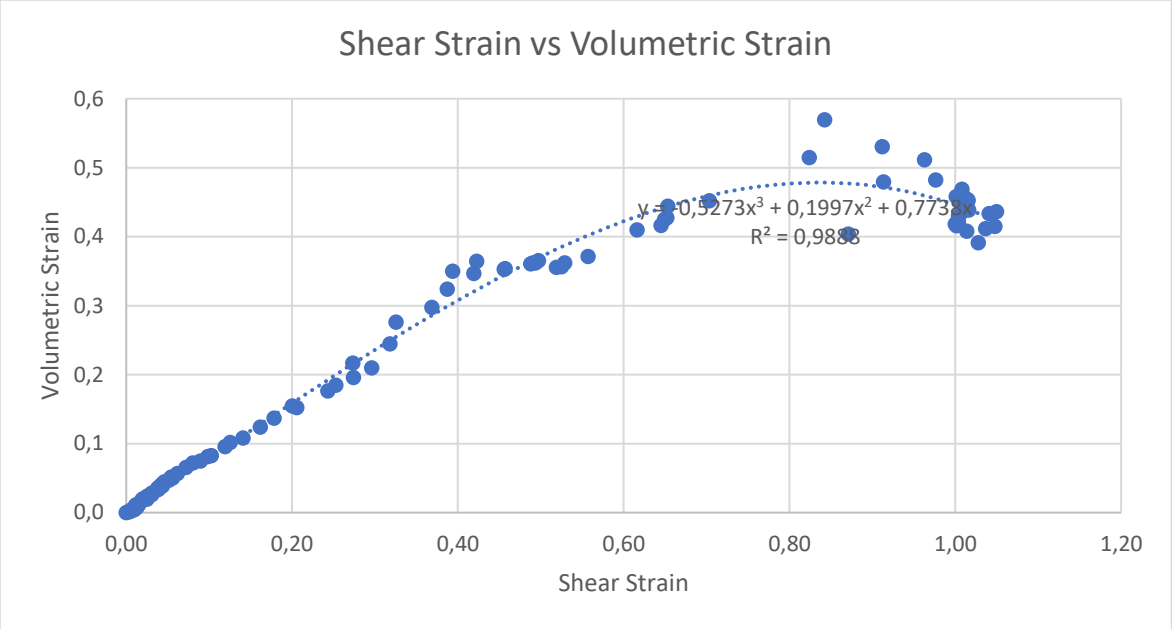

Figure D.37. Volumetric vs Shear Strain Diagram of the Point with Maximum Shear Strain ($I_D = 0.47$ & $\sigma' = 0.84\ kPa$).

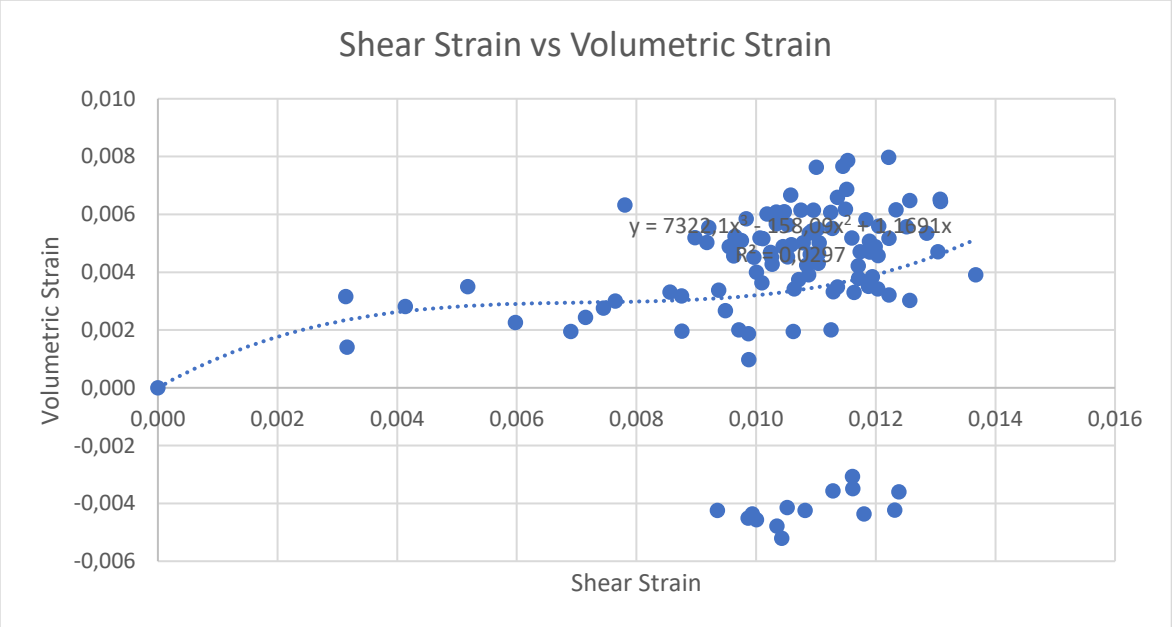

Figure D.38. Volumetric vs Shear Strain Diagram of the Point with Minimum Shear Strain ($I_D = 0.47$ & $\sigma' = 0.84\ kPa$).

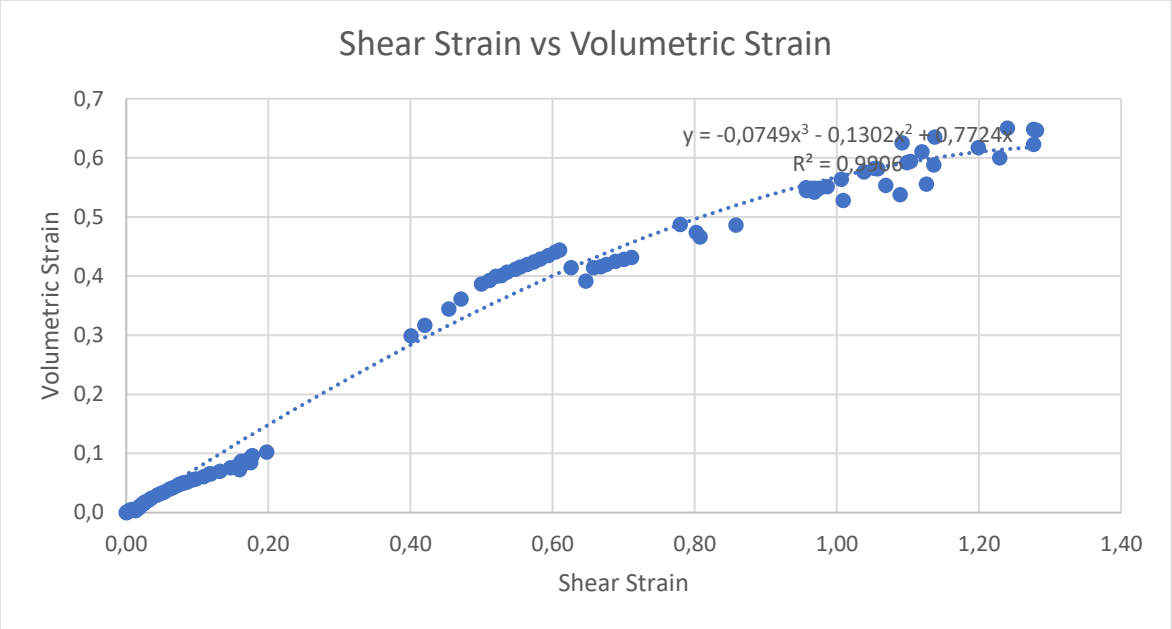

Figure D.39. Volumetric vs Shear Strain Diagram of the Point with Maximum Shear Strain ($I_D = 0.48$ & $\sigma' = 0.81\ kPa$).

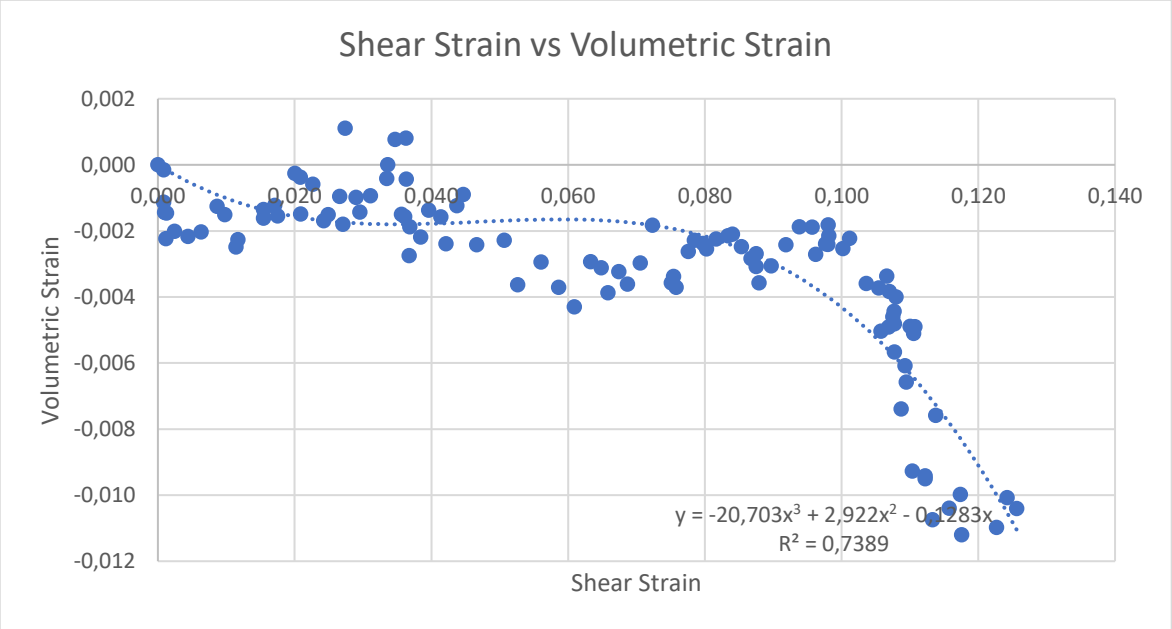

Figure D.40. Volumetric vs Shear Strain Diagram of the Point with Minimum Shear Strain ($I_D = 0.48$ & $\sigma' = 0.81\ kPa$).

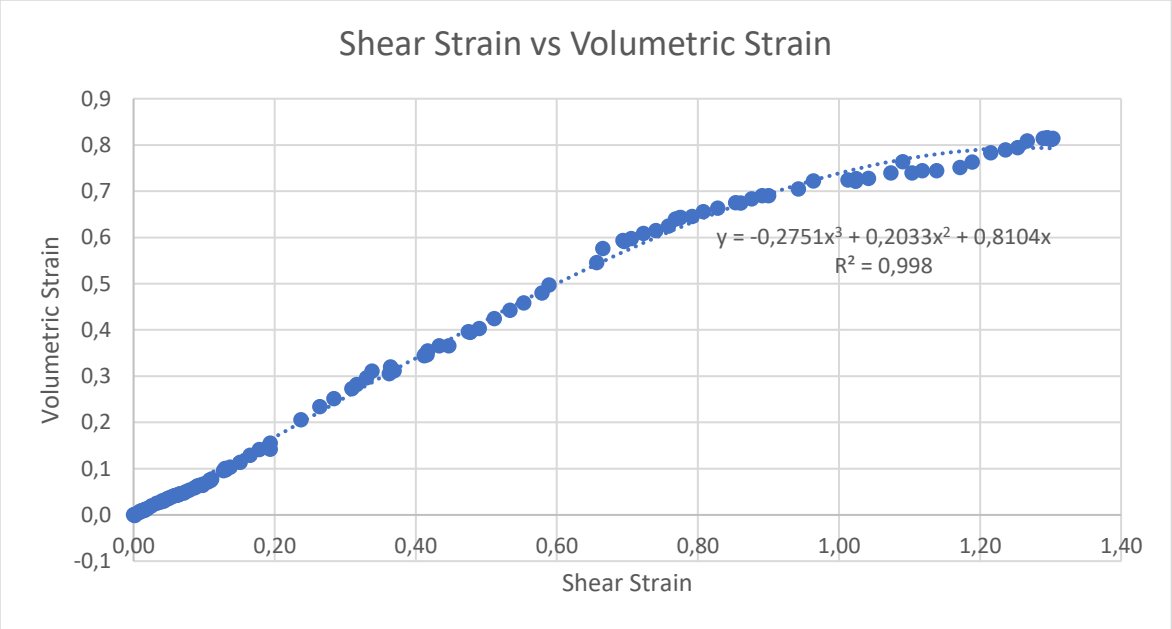

Figure D.41. Volumetric vs Shear Strain Diagram of the Point with Maximum Shear Strain ($I_D = 0.52$ & $\sigma' = 0.88\,kPa$).

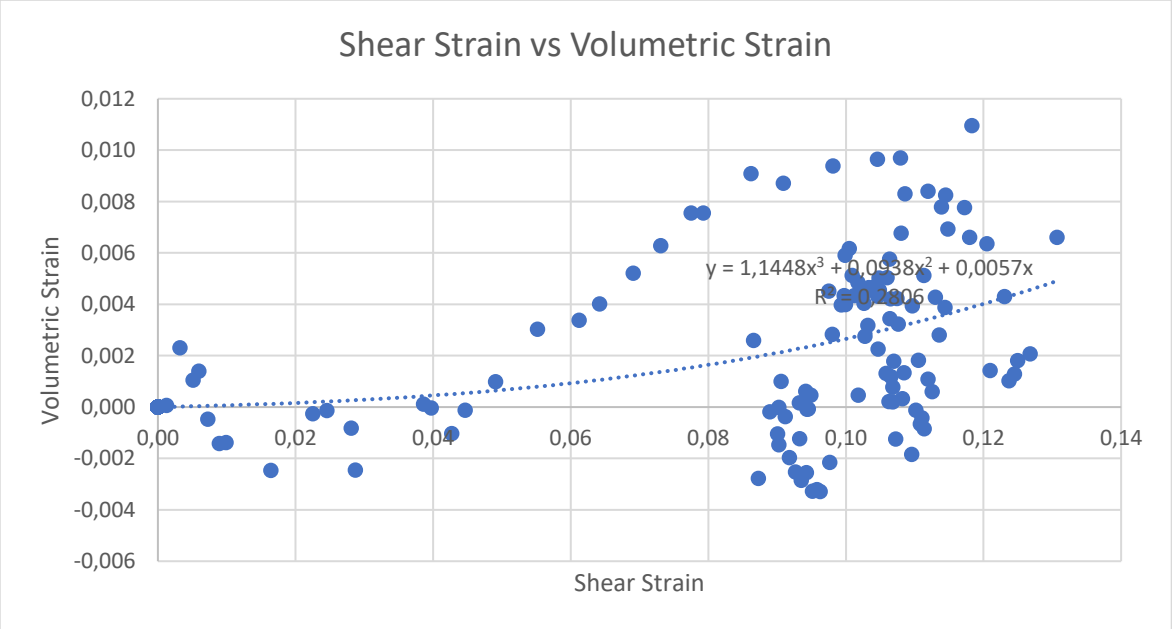

Figure D.42. Volumetric vs Shear Strain Diagram of the Point with Minimum Shear Strain ($I_D = 0.52$ & $\sigma' = 0.88\,kPa$).

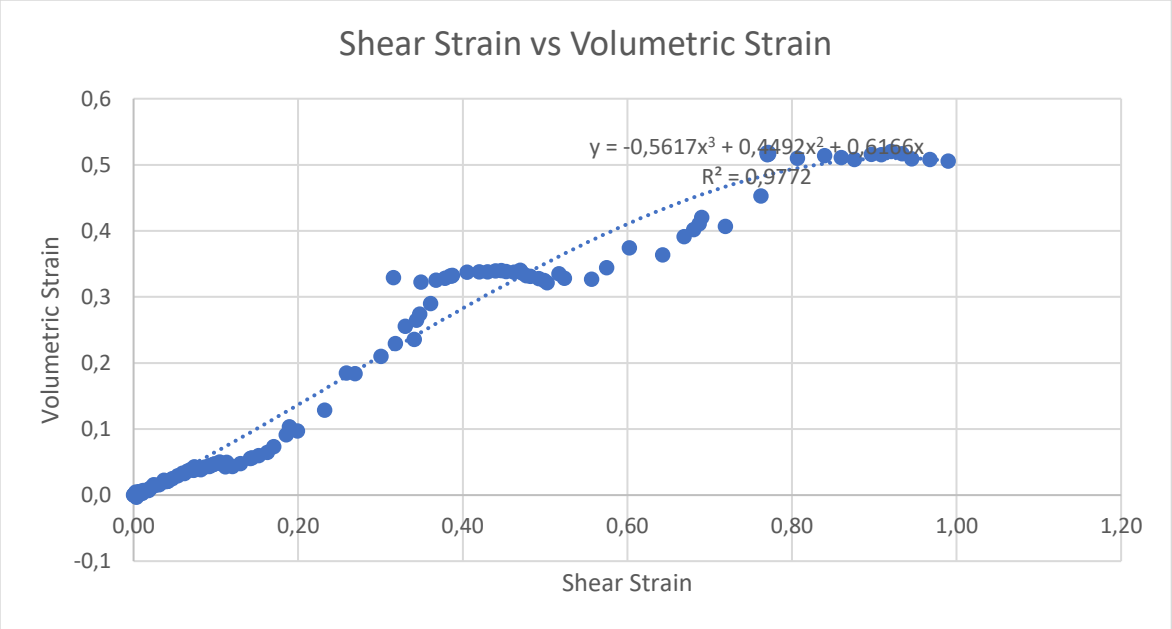

Figure D.43. Volumetric vs Shear Strain Diagram of the Point with Maximum Shear Strain ($I_D = 0.53$ & $\sigma' = 0.69\ kPa$).

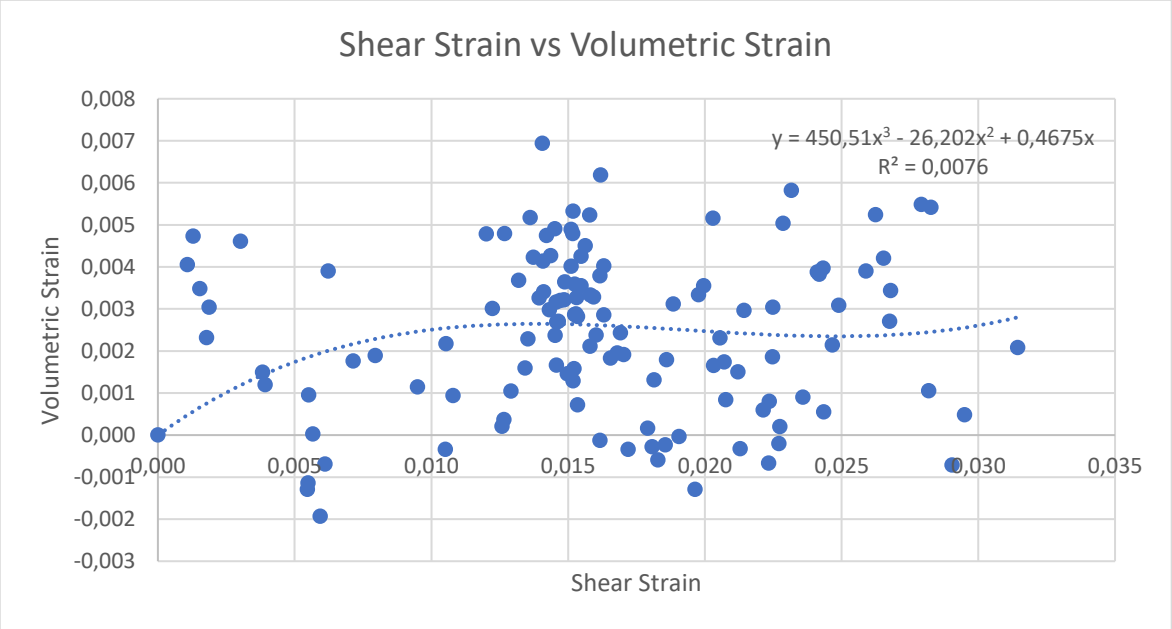

Figure D.44. Volumetric vs Shear Strain Diagram of the Point with Minimum Shear Strain ($I_D = 0.53$ & $\sigma' = 0.69\ kPa$).

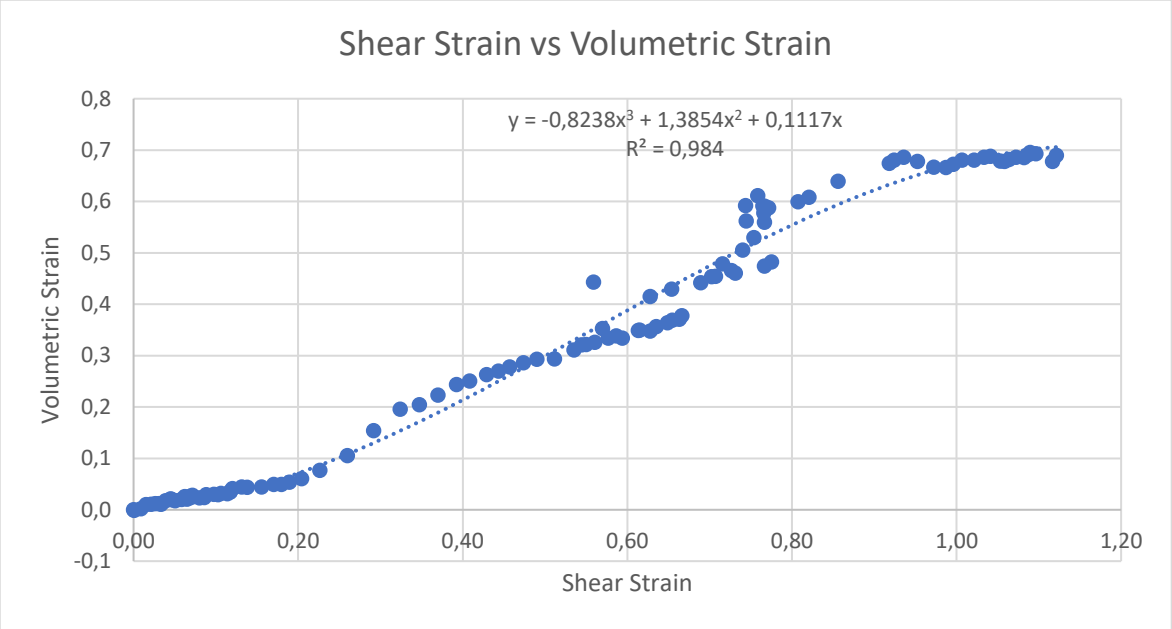

Figure D.45. Volumetric vs Shear Strain Diagram of the Point with Maximum Shear Strain ($I_D = 0.53$ & $\sigma' = 0.72\ kPa$).

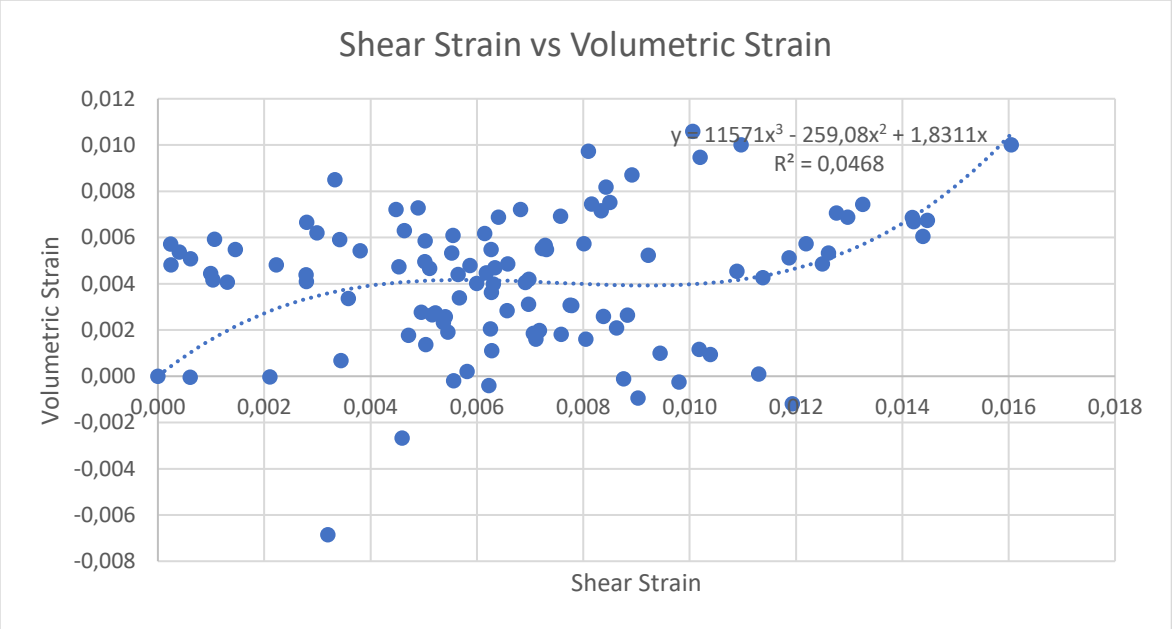

Figure D.46. Volumetric vs Shear Strain Diagram of the Point with Minimum Shear Strain ($I_D = 0.53$ & $\sigma' = 0.72\ kPa$).

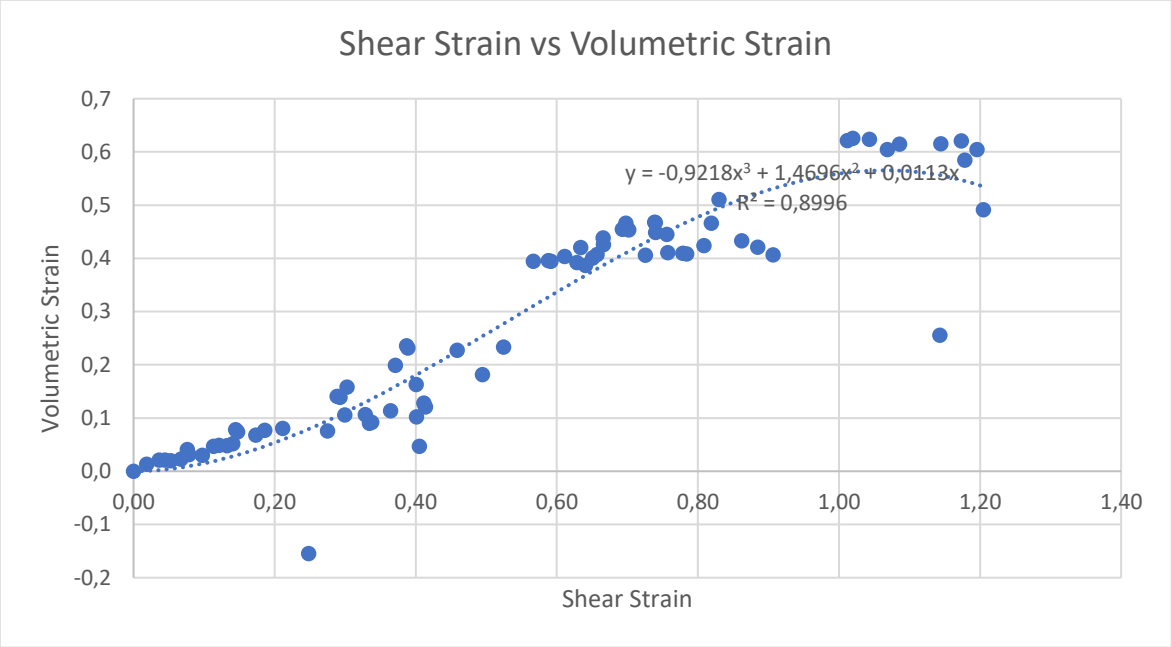

Figure D.47. Volumetric vs Shear Strain Diagram of the Point with Maximum Shear Strain ($I_D = 0.53$ & $\sigma' = 0.96\ kPa$).

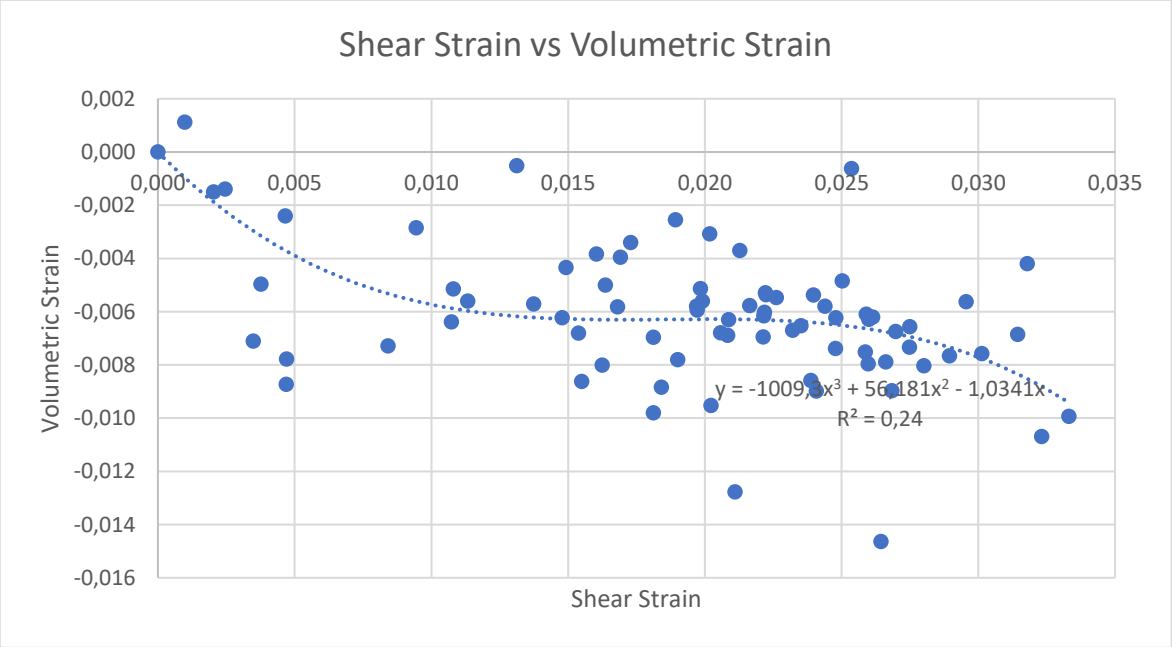

Figure D.48. Volumetric vs Shear Strain Diagram of the Point with Minimum Shear Strain ($I_D = 0.53$ & $\sigma' = 0.96\ kPa$).

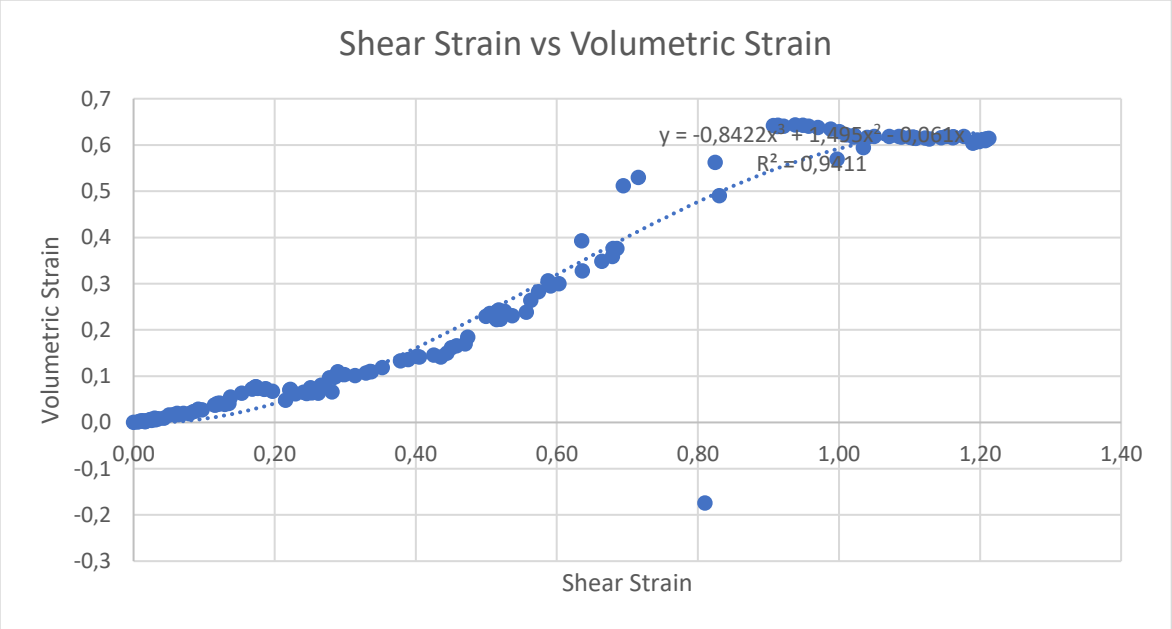

Figure D.49. Volumetric vs Shear Strain Diagram of the Point with Maximum Shear Strain ($I_D = 0.58$ & $\sigma' = 0.79\ kPa$).

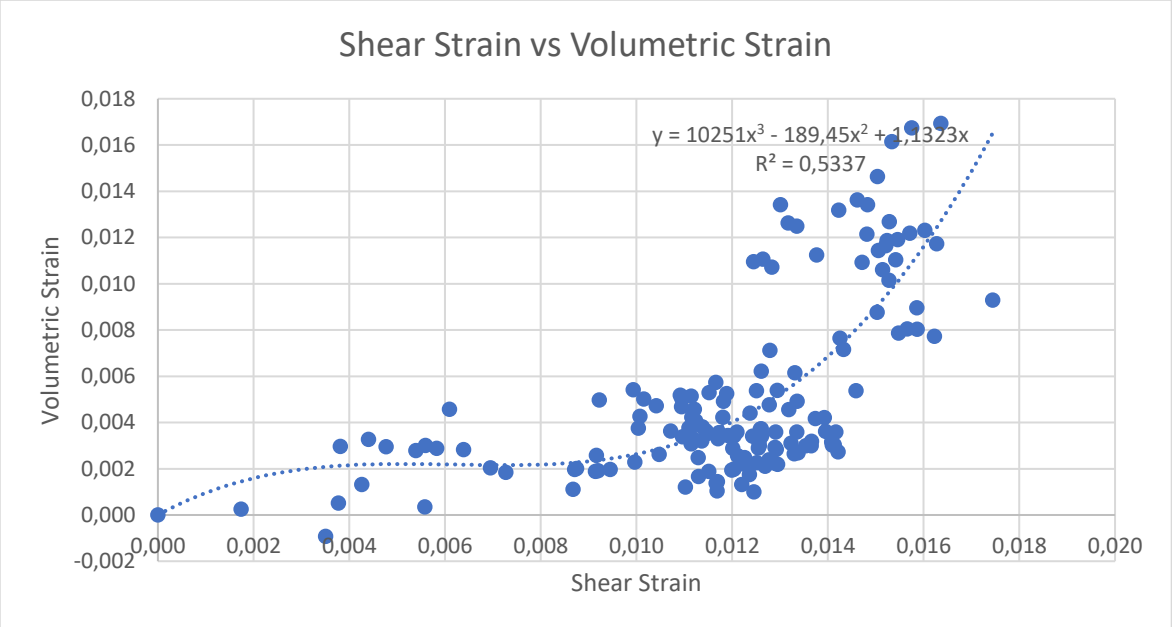

Figure D.50. Volumetric vs Shear Strain Diagram of the Point with Minimum Shear Strain ($I_D = 0.58$ & $\sigma' = 0.79\ kPa$).

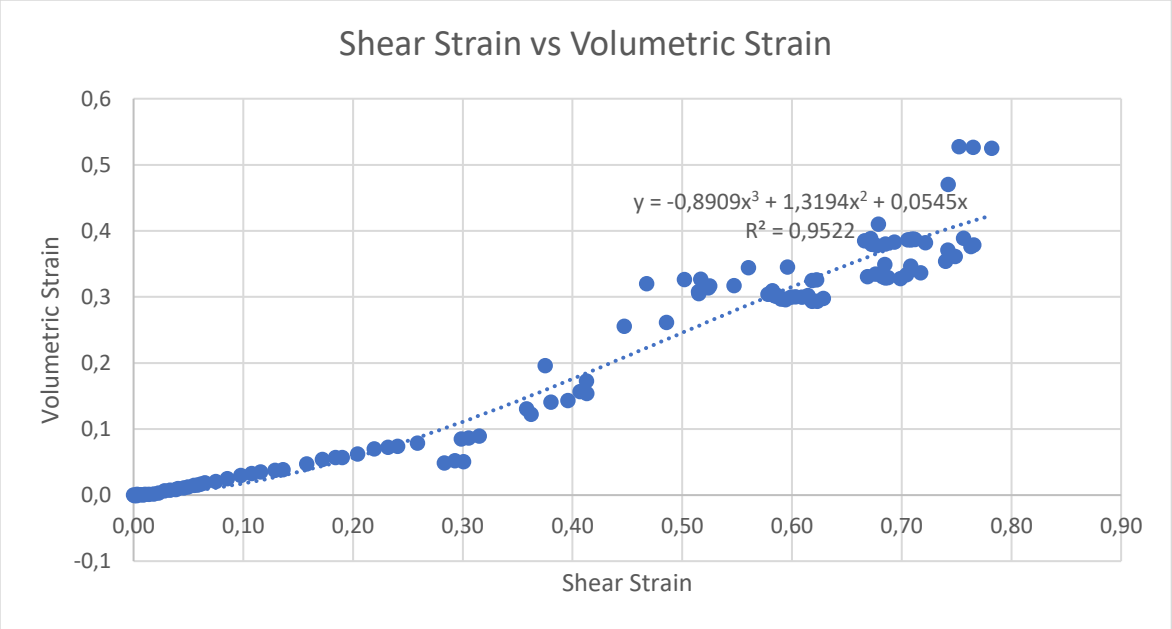

Figure D.51. Volumetric vs Shear Strain Diagram of the Point with Maximum Shear Strain ($I_D = 0.58$ & $\sigma' = 0.80\ kPa$).

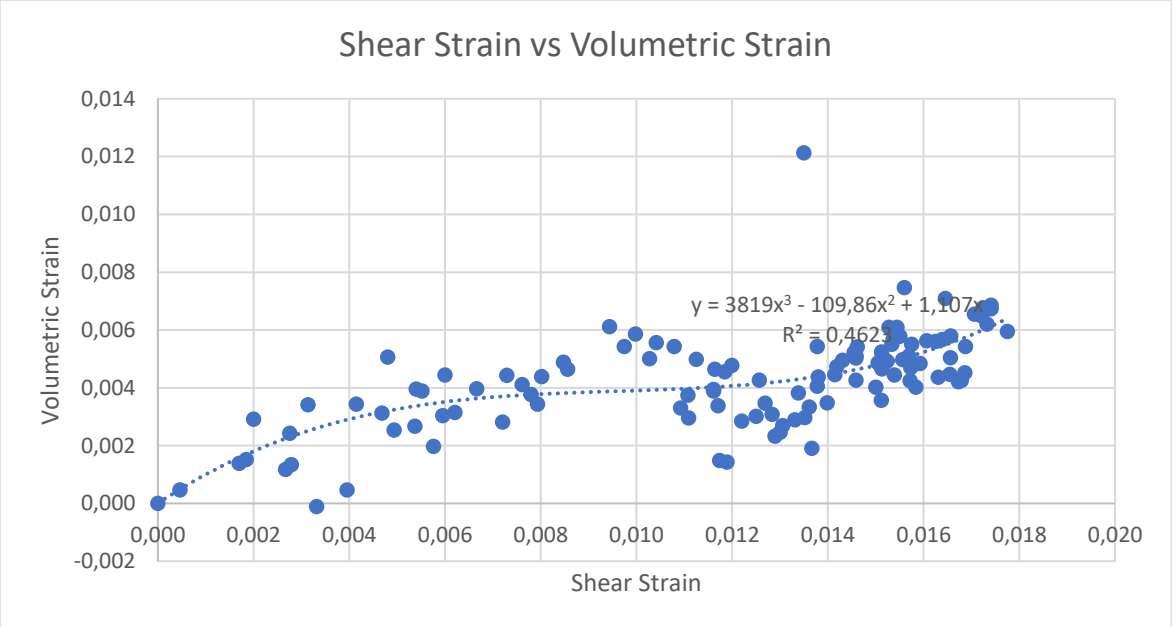

Figure D.52. Volumetric vs Shear Strain Diagram of the Point with Minimum Shear Strain ($I_D = 0.58$ & $\sigma' = 0.80\ kPa$).

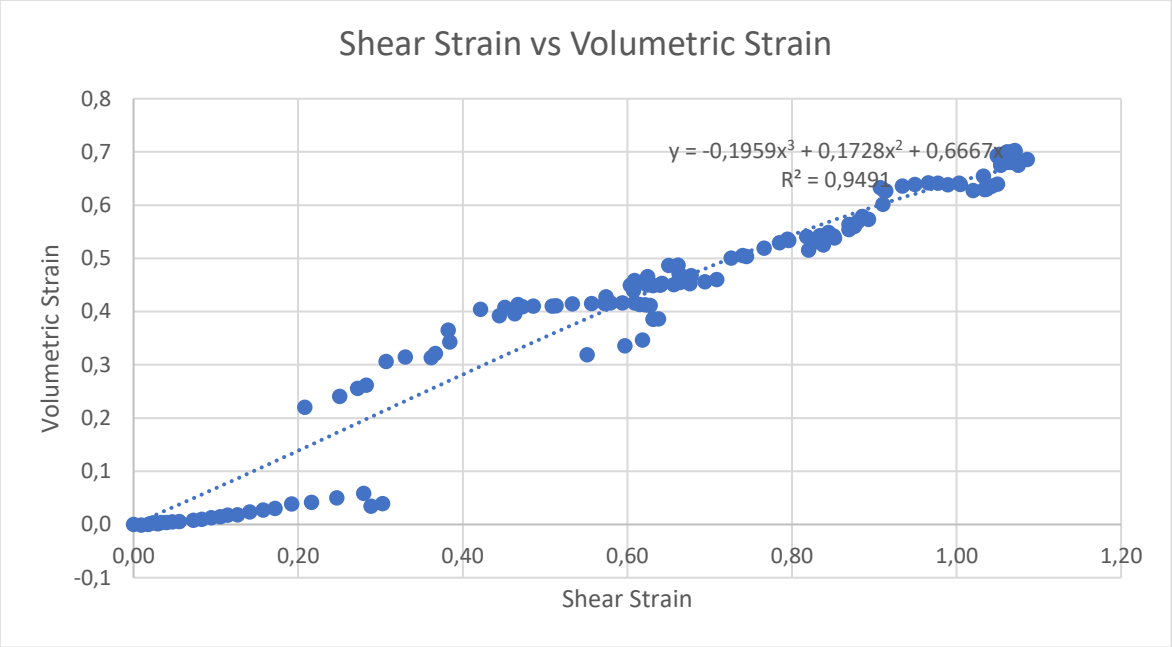

Figure D.53. Volumetric vs Shear Strain Diagram of the Point with Maximum Shear Strain ($I_D = 0.58$ & $\sigma' = 0.96\ kPa$).

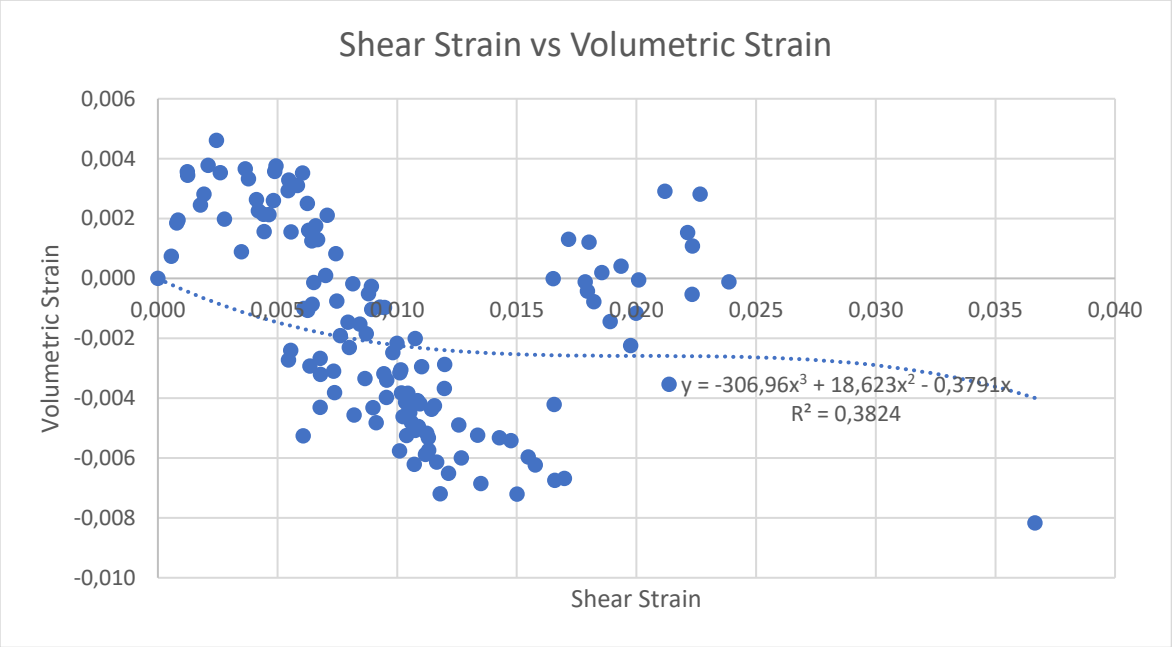

Figure D.54. Volumetric vs Shear Strain Diagram of the Point with Minimum Shear Strain ($I_D = 0.58$ & $\sigma' = 0.96\ kPa$).

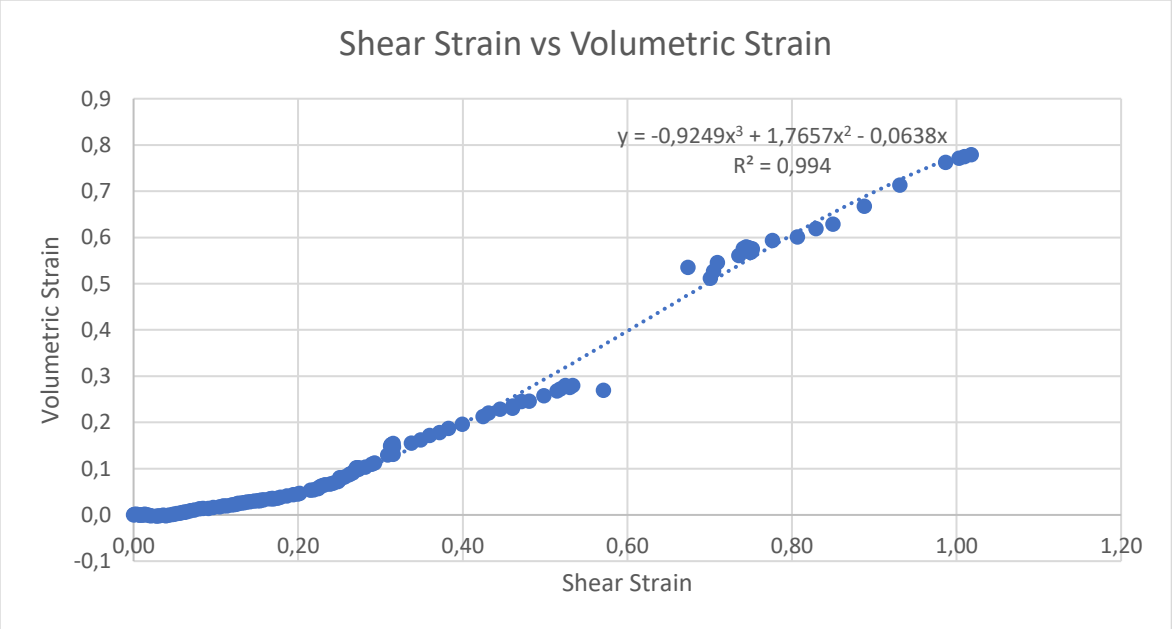

Figure D.55. Volumetric vs Shear Strain Diagram of the Point with Maximum Shear Strain ($I_D = 0.60$ & $\sigma' = 0.84\ kPa$).

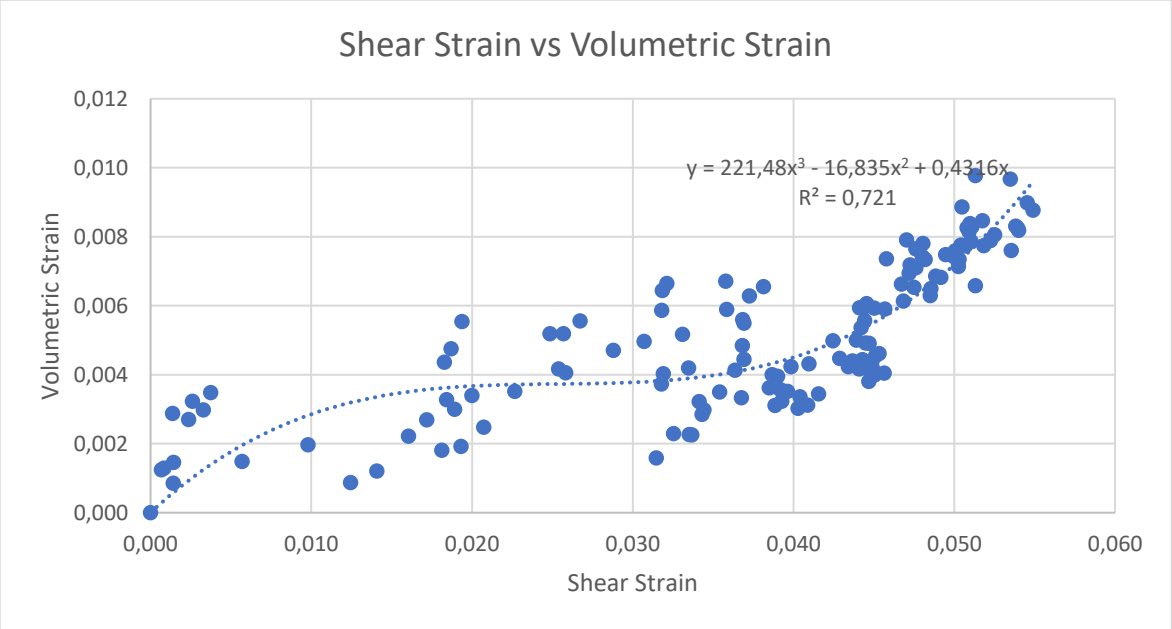

Figure D.56. Volumetric vs Shear Strain Diagram of the Point with Minimum Shear Strain ($I_D = 0.60$ & $\sigma' = 0.84\ kPa$).

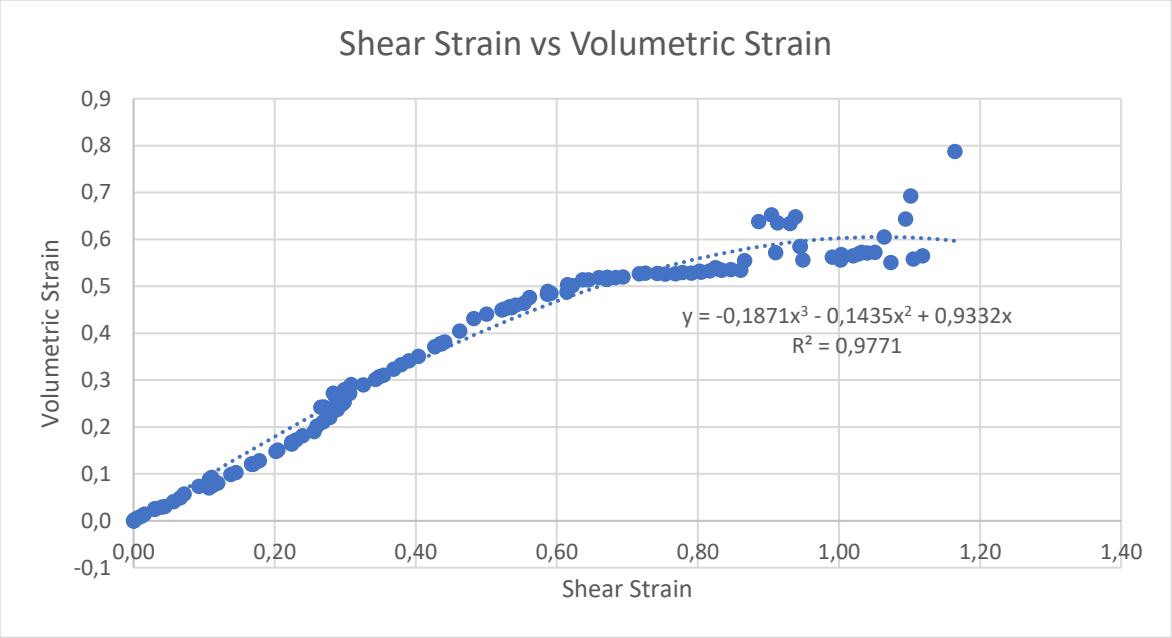

Figure D.57. Volumetric vs Shear Strain Diagram of the Point with Maximum Shear Strain ($I_D = 0.63$ & $\sigma' = 0.56kPa$).

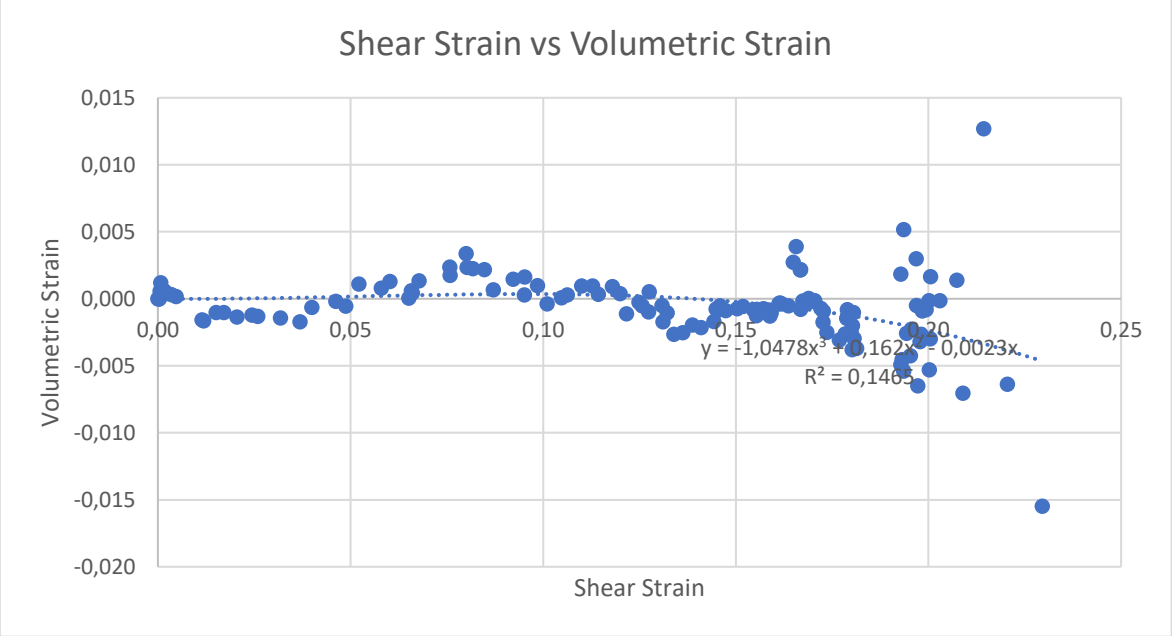

Figure D.58. Volumetric vs Shear Strain Diagram of the Point with Minimum Shear Strain ($I_D = 0.63$ & $\sigma' = 0.56kPa$).

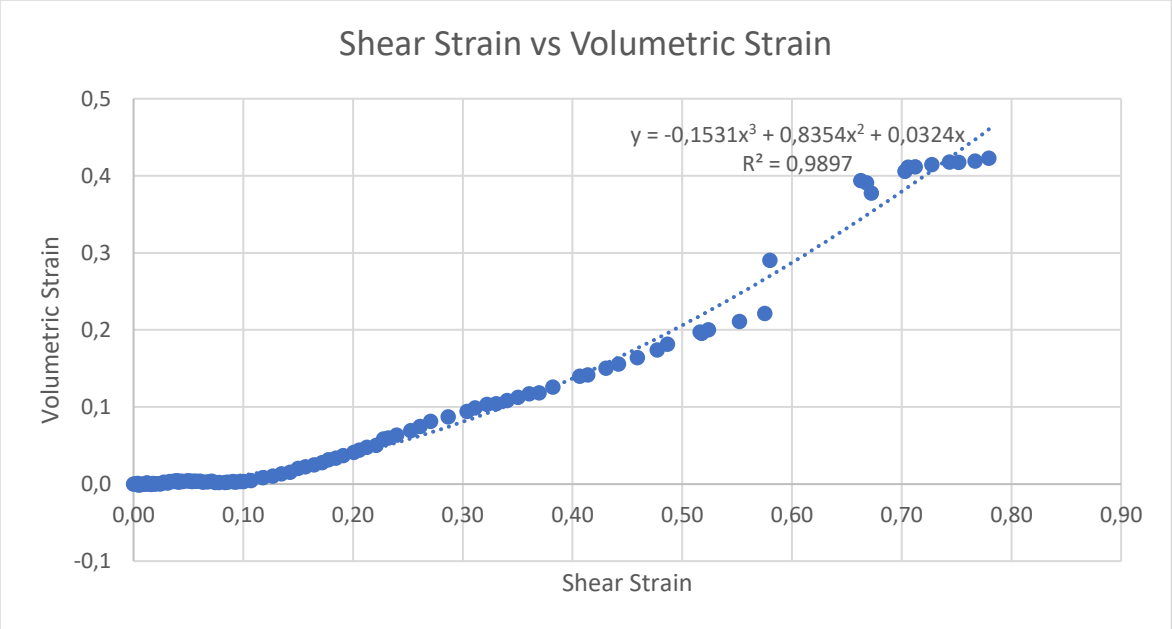

Figure D.59. Volumetric vs Shear Strain Diagram of the Point with Maximum Shear Strain ($I_D = 0.63$ & $\sigma' = 0.66\ kPa$).

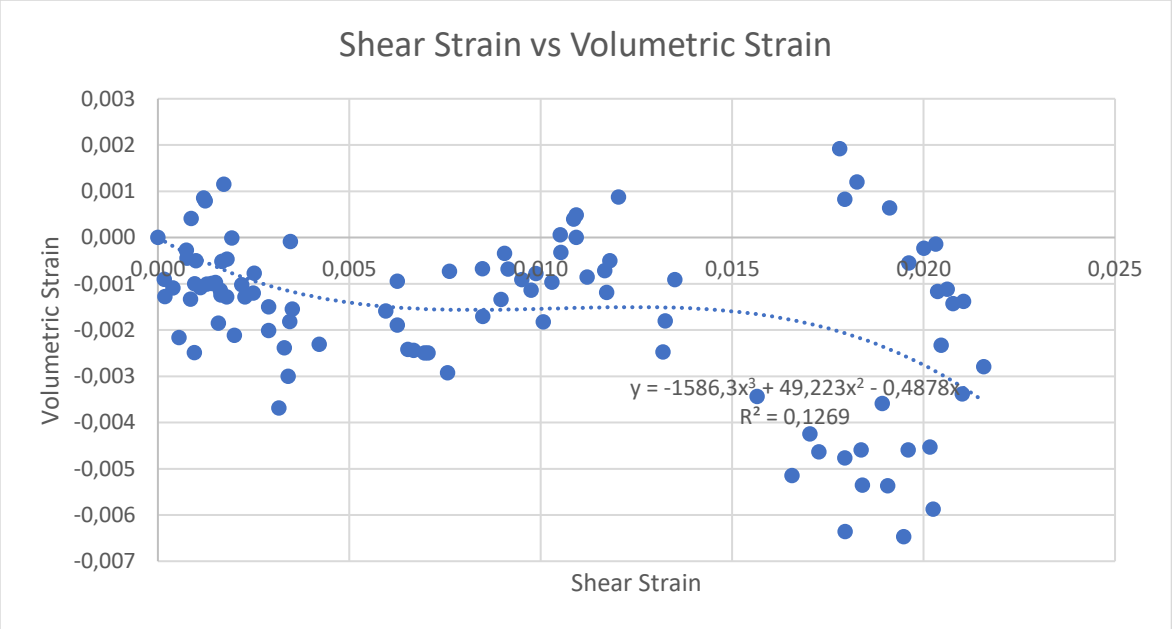

Figure D.60. Volumetric vs Shear Strain Diagram of the Point with Minimum Shear Strain ($I_D = 0.63$ & $\sigma' = 0.66\ kPa$).

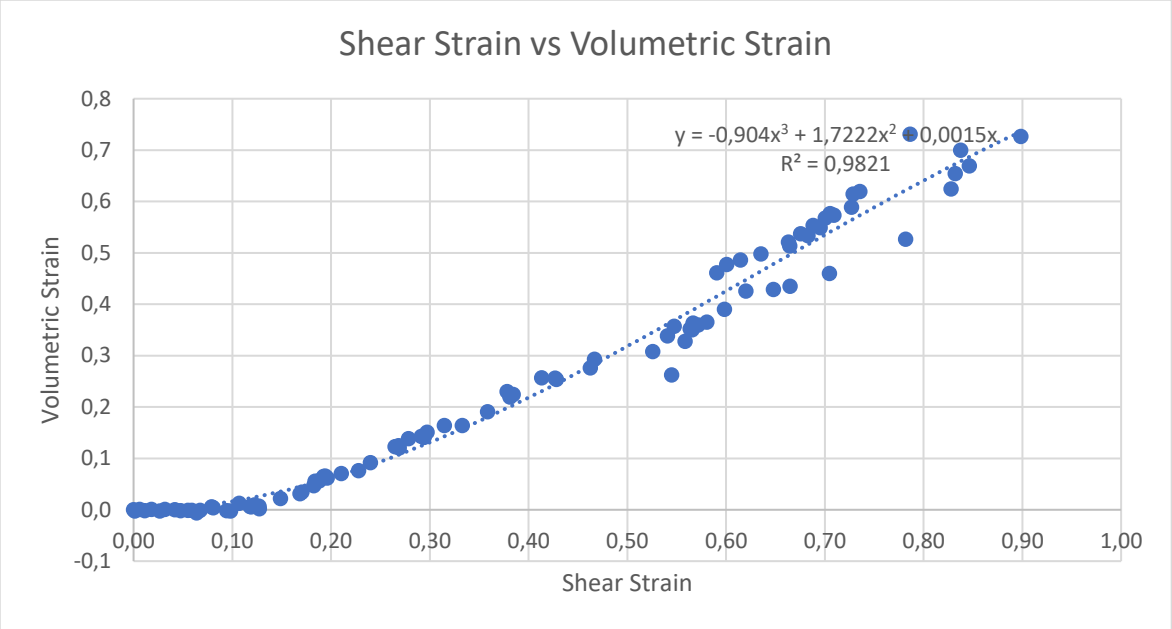

Figure D.61. Volumetric vs Shear Strain Diagram of the Point with Maximum Shear Strain ($I_D = 0.65$ & $\sigma' = 0.96\ kPa$).

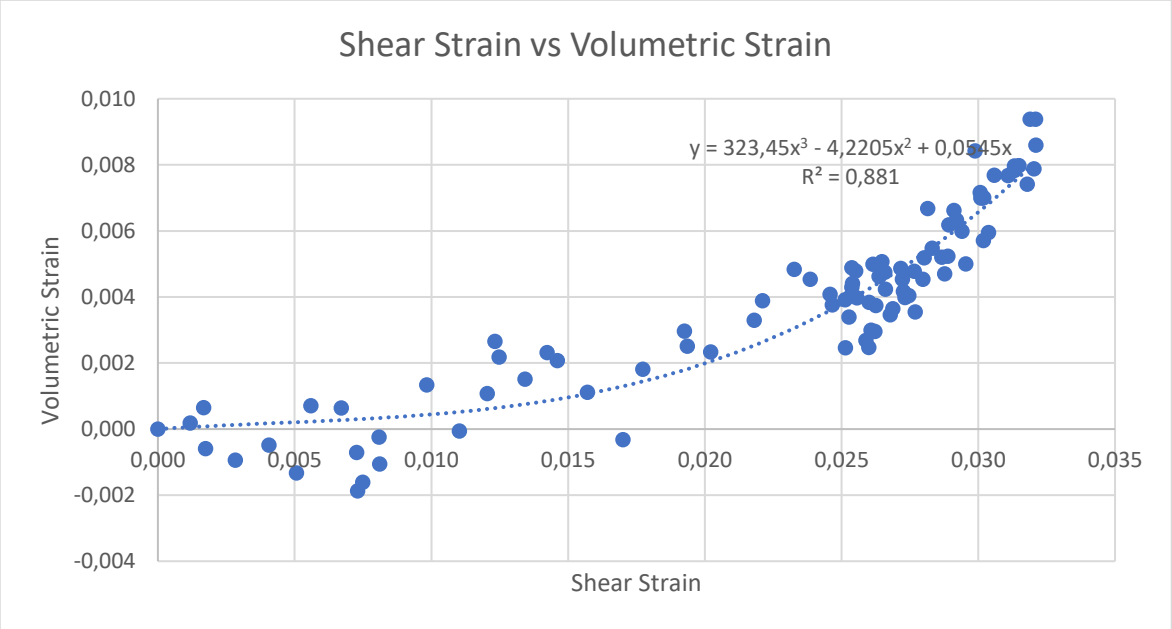

Figure D.62. Volumetric vs Shear Strain Diagram of the Point with Minimum Shear Strain ($I_D = 0.65$ & $\sigma' = 0.96\ kPa$).

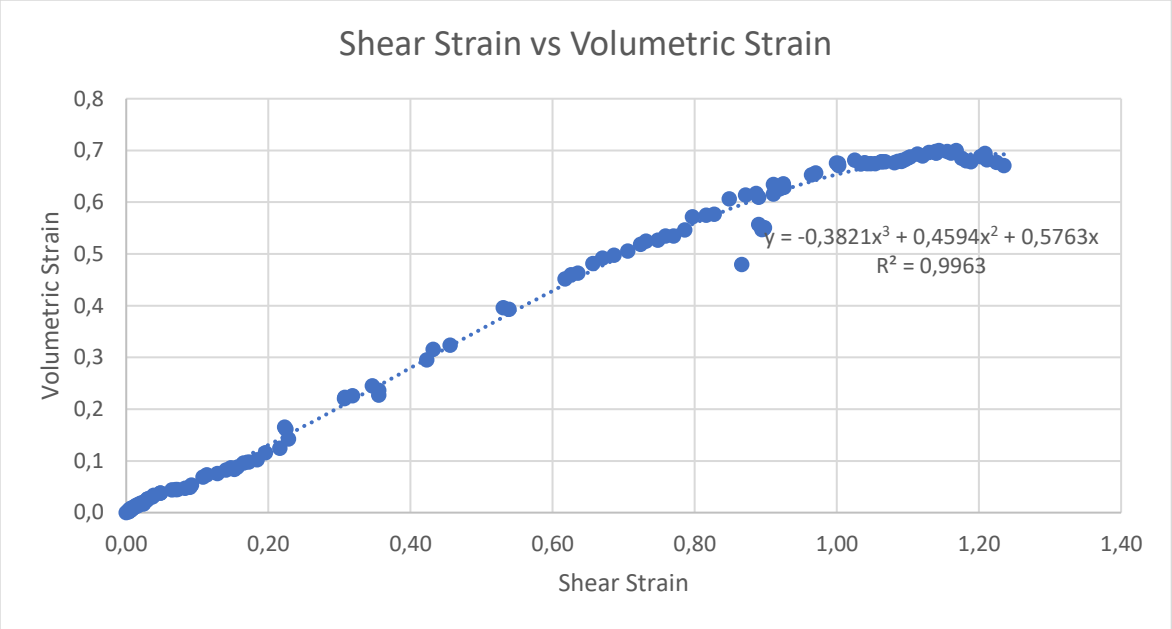

Figure D.63. Volumetric vs Shear Strain Diagram of the Point with Maximum Shear Strain ($I_D = 0.67$ & $\sigma' = 0.83\ kPa$).

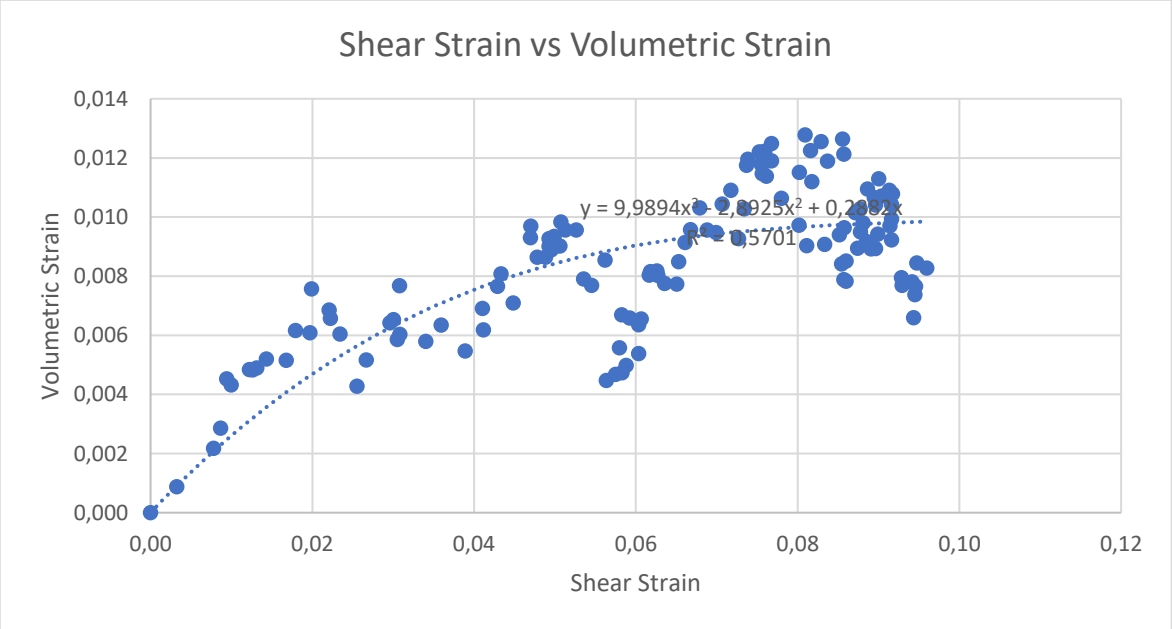

Figure D.64. Volumetric vs Shear Strain Diagram of the Point with Minimum Shear Strain ($I_D = 0.67$ & $\sigma' = 0.83\ kPa$).

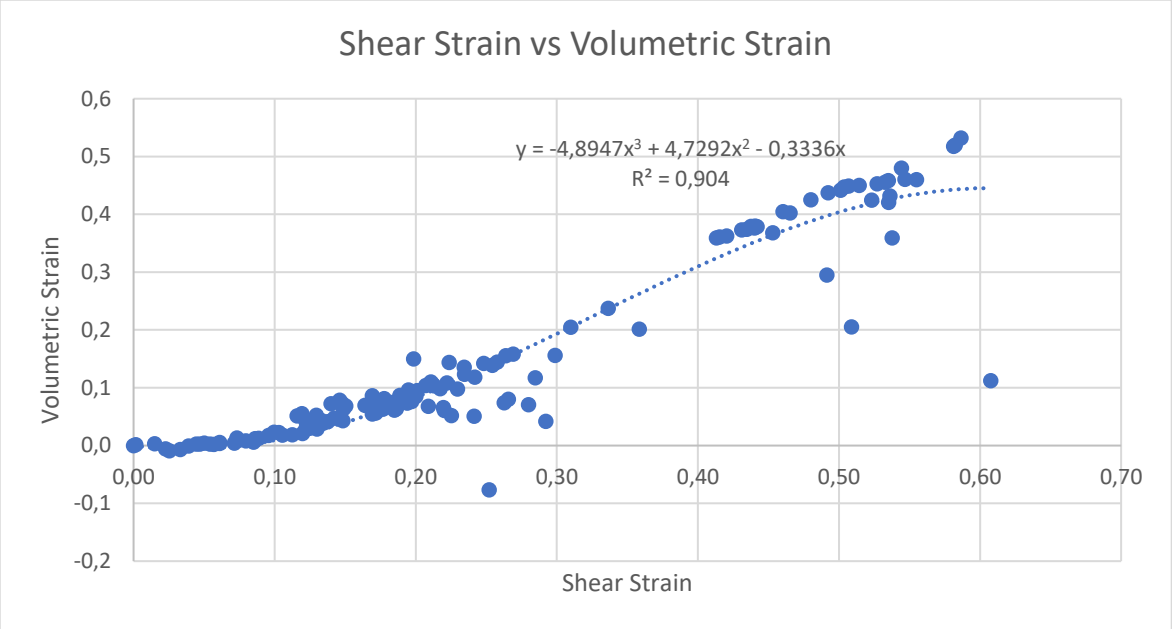

Figure D.65. Volumetric vs Shear Strain Diagram of the Point with Maximum Shear Strain ($I_D = 0.70$ & $\sigma' = 0.92\ kPa$).

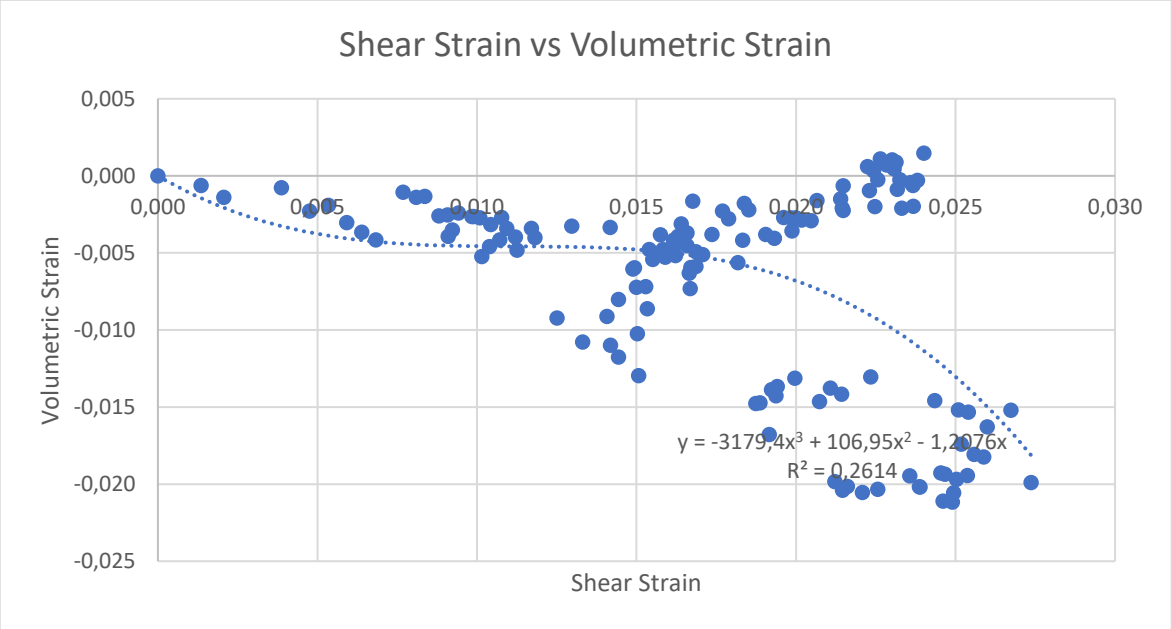

Figure D.66. Volumetric vs Shear Strain Diagram of the Point with Minimum Shear Strain ($I_D = 0.70$ & $\sigma' = 0.92\ kPa$).

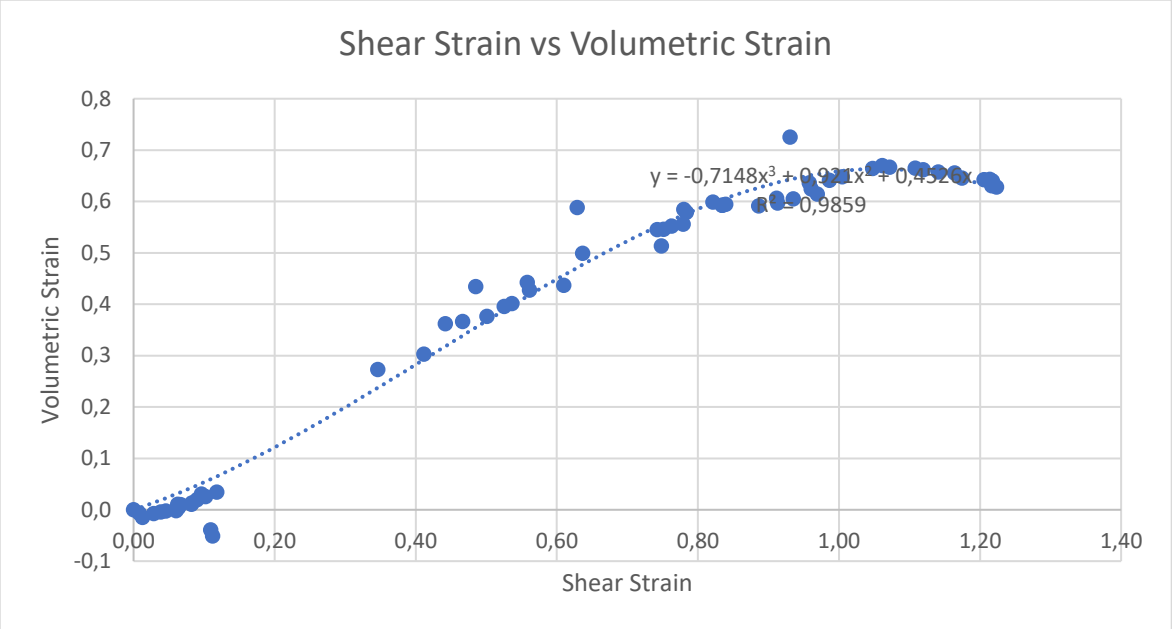

Figure D.67. Volumetric vs Shear Strain Diagram of the Point with Minimum Shear Strain ($I_D = 0.73$ & $\sigma' = 0.78\ kPa$).

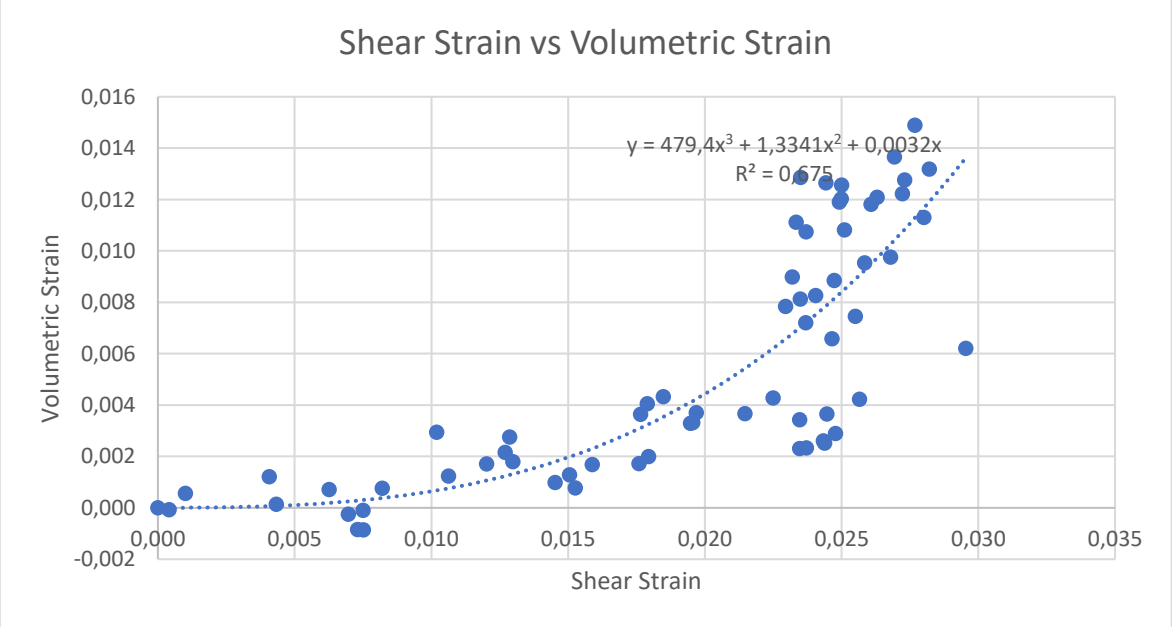

Figure D.68. Volumetric vs Shear Strain Diagram of the Point with Minimum Shear Strain ($I_D = 0.73$ & $\sigma' = 0.78\ kPa$).

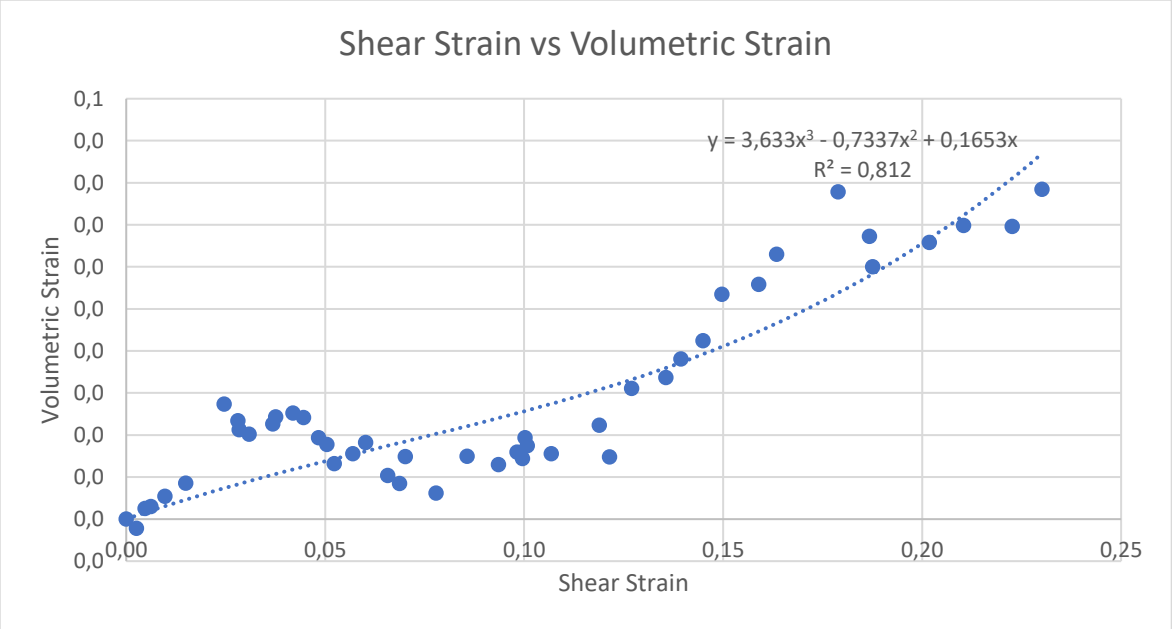

Figure D.69. Volumetric vs Shear Strain Diagram of the Point with Minimum Shear Strain ($I_D = 0.74$ & $\sigma' = 0.66\ kPa$).

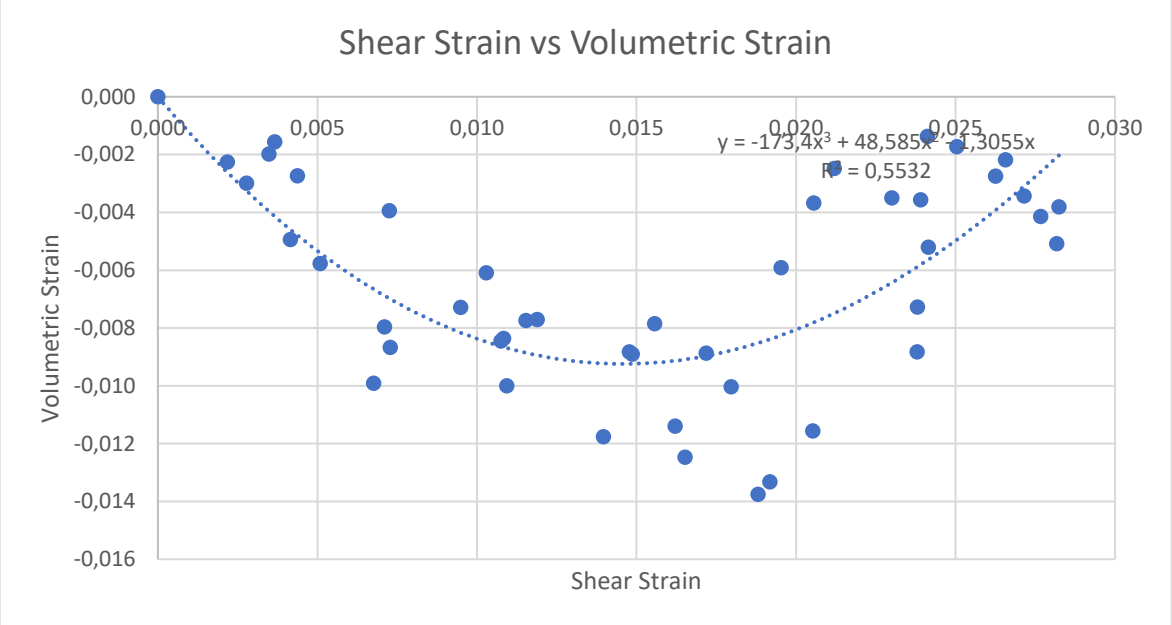

Figure D.70. Volumetric vs Shear Strain Diagram of the Point with Minimum Shear Strain ($I_D = 0.74$ & $\sigma' = 0.66\ kPa$).

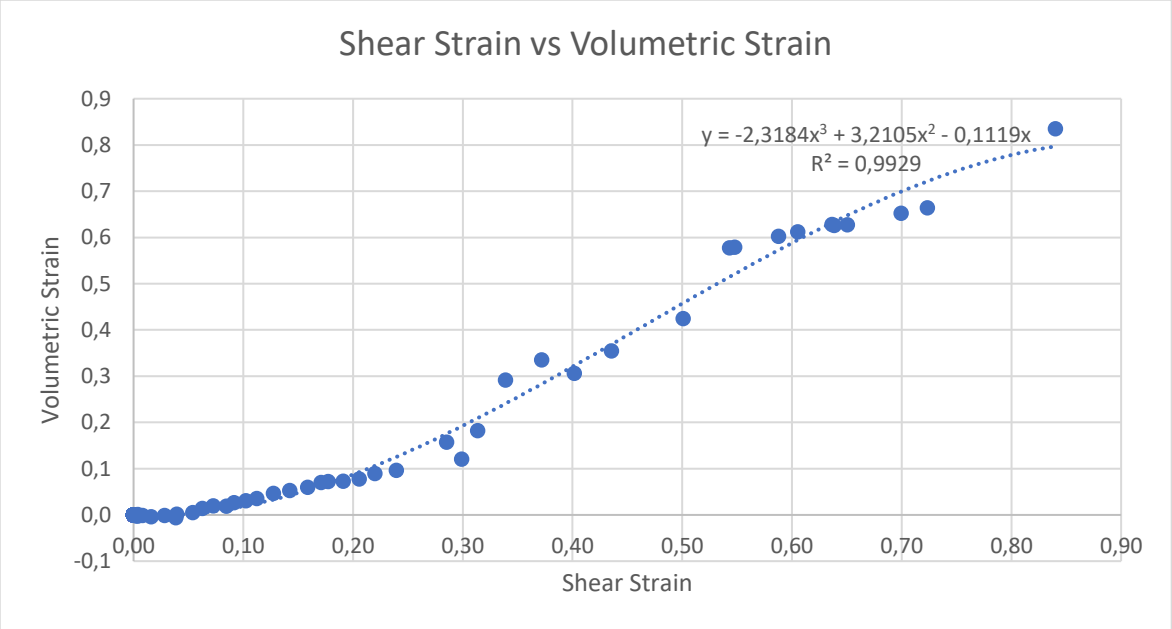

Figure D.71. Volumetric vs Shear Strain Diagram of the Point with Minimum Shear Strain ($I_D = 0.79$ & $\sigma' = 0.91\ kPa$).

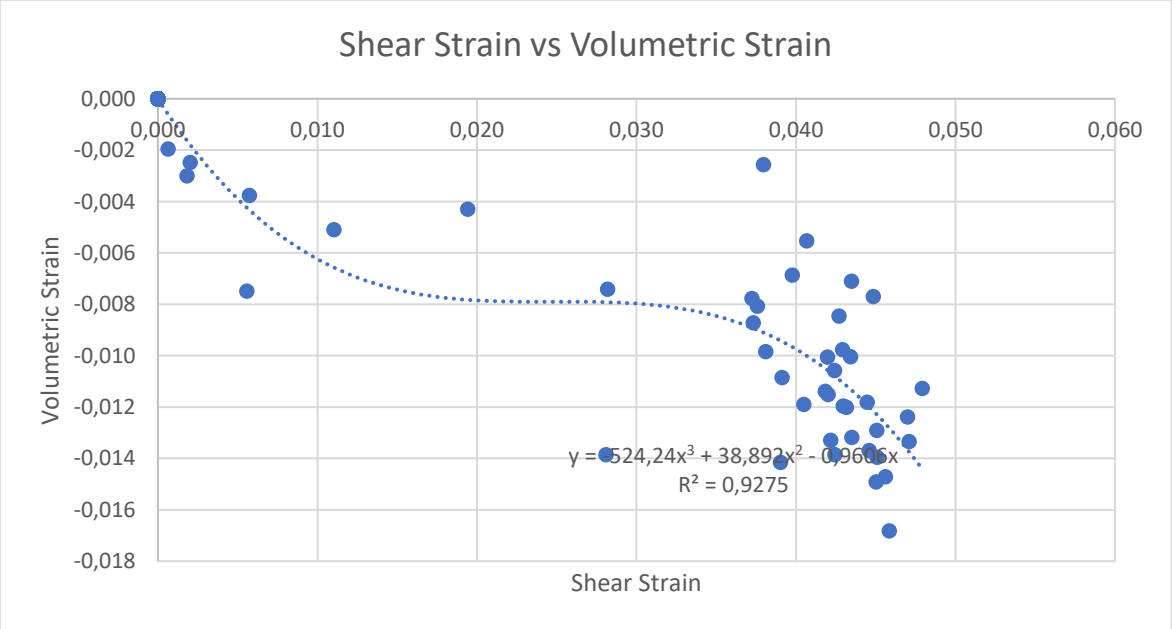

Figure D.72. Volumetric vs Shear Strain Diagram of the Point with Minimum Shear Strain ($I_D = 0.79$ & $\sigma' = 0.91\ kPa$).